LOCKHEED MARTIN ENERGY RESEARCH LIBRARIES
3 4456 0514193 1

TRAL RESEARCH LIBRARY
CUMENT COLLECTION

OAK RIDGE NATIONAL LABORATORY
operated by
UNION CARBIDE CORPORATION • NUCLEAR DIVISION
for the
U. S. ATOMIC ENERGY COMMISSION

ORNL - TM - 3550
cy 2

OAK RIDGE NATIONAL LABORATORY
CENTRAL RESEARCH LIBRARY
DOCUMENT COLLECTION
LIBRARY LOAN COPY
DO NOT TRANSFER TO ANOTHER PERSON
If you wish someone else to see this document, send in name with document and the library will arrange a loan.
UCN-7969
(3 3-67)

FUELS AND MATERIALS DEVELOPMENT PROGRAM QUARTERLY PROGRESS REPORT FOR PERIOD ENDING SEPTEMBER 30, 1971

P. Patriarca

NOTICE This document contains information of a preliminary nature and was prepared primarily for internal use at the Oak Ridge National Laboratory. It is subject to revision or correction and therefore does not represent a final report.

This report was prepared as an account of work sponsored by the United States Government. Neither the United States nor the United States Atomic Energy Commission, nor any of their employees, nor any of their contractors, subcontractors, or their employees, makes any warranty, express or implied, or assumes any legal liability or responsibility for the accuracy, completeness or usefulness of any information, apparatus, product or process disclosed, or represents that its use would not infringe privately owned rights.

ORNL-TM-3550

Contract No. W-7405-eng-26

METALS AND CERAMICS DIVISION

FUELS AND MATERIALS DEVELOPMENT PROGRAM QUARTERLY PROGRESS REPORT FOR PERIOD ENDING SEPTEMBER 30, 1971

P. Patriarca

DECEMBER 1971

OAK RIDGE NATIONAL LABORATORY
Oak Ridge, Tennessee 37830
operated by
UNION CARBIDE CORPORATION
for the
U.S. ATOMIC ENERGY COMMISSION

LOCKHEED MARTIN ENERGY RESEARCH LIBRARIES

3 4456 0514193 1

HIGHLIGHTS

PART I. FAST REACTOR TECHNOLOGY

FUELS

The statistical analysis of the large quantity of data obtained from the SG-3 thermal performance test for $(U,Pu)O_2$ confirms that the pellet fuel pin had a higher central temperature than the Sphere-Pac pin operated at equivalent heat generation rates and provides additional evidence that Sphere-Pac fuel has a higher gap conductance than pellet fuel. (p. 19)

An analysis of fuel-clad chemical interaction data has led to the postulate that particulate $(U,Pu)O_2$ fuel may exhibit less attack than pellet fuel at the same heat rating because of the absence of cracks that lead from the interior of the fuel structure to the cladding. (p. 23)

A kinetic model has been developed for prediction of redistribution of actinides in fast reactor $(U,Pu)O_2$ fuel pins. (p. 34)

The sensitivity of the predicted LMFBR fuel pin performance to uncertainty in $(U,Pu)O_2$ fuel and cladding properties is being determined with the FMØDEL code, and the preliminary conclusion is that additional characterization to obtain some basic physical properties is necessary before performance of LMFBR fuel pins can be predicted by any model with confidence. (p. 35)

Fabrication of nine fuel pins containing (U,Pu)N for tests in EBR-II, an archive pin, and two dummies loaded with UN was completed. (p. 50)

ABSORBERS

A computerized performance code for absorber rods having boron carbide pellets clad on stainless steel has been developed. The code is called ABSORB and contains a model for pellet cracking. This code will be tested by analyzing the results of the X 099 EBR-II irradiation experiments. (p. 66)

Tantalum irradiated at 585°C in row 2 of the EBR-II to a fluence of 2.5×10^{22} neutrons/cm^2 swelled 2.4%. At temperatures above 950°C, the swelling was negligible for this magnitude of fluence. (p. 71)

CLADDINGS

Specimens of type 304 stainless steel from EBR-II thimbles exposed to a peak fluence of 1.5×10^{23} neutrons/cm^2 showed a peak density decrease of 11.0% at an irradiation temperature of 420°C, and data from these and other samples show that void nucleation ceases at some fluence, the exact value depending on the irradiation temperature. (p. 82)

Microstructural studies have been done on specimens of annealed type 304 stainless steel and annealed and cold-worked standard and titanium-modified type 316 stainless steel after irradiation at 450, 580, and 700°C at a fluence of 1.9×10^{22} neutrons/cm^2. Sigma phase and several types and morphologies of carbides were formed under various conditions, and voids and helium bubbles in these alloys were often associated with these particles. (p. 90)

Postirradiation tensile and creep properties of standard and titanium-modified type 316 stainless steel have been evaluated after irradiation to fluences in the range of 1 to 3×10^{22} neutrons/cm^2. Irradiation alters most mechanical properties with the magnitude of the changes depending strongly upon irradiation and test temperatures. The titanium-modified type 316 stainless steel has higher ductility than the standard alloy under all conditions studied. (p. 98)

The potential of producing tubing with a very fine grain size and free of precipitates has been demonstrated for type 316 stainless steel. (p. 110)

A theory with mathematical formulation has been developed that predicts the fracture time of notched and unirradiated tubes, and experimental data have been correlated by use of the equations. It is significant that for 20% cold-worked type 316 stainless steel at 650°C, the effect of a 10% notch on the time-to-rupture is greater than one would allow by using a single cladding thickness allowance of 10%. (p. 119)

FABRICATION DEVELOPMENT OF LMFBR COMPONENTS

The posttest examination of the ALCO/BLH steam generator is continuing. Many dissection operations have been conducted, and a detailed metallurgical examination of cracking in both the top and bottom tube sheets is under way. Tube failures in the top tube sheet region are also under study. Several possible failure mechanisms have been postulated. (p. 124)

A large number of specimens of ferritic steels and other steam generator materials have been prepared for isothermal general steam corrosion tests at 480 and 595°C. (p. 134)

A sixth stress-corrosion run was conducted in the chloride-injection loop, and it was determined that the ground surface preparation showed by far the highest susceptibility to cracking. Weldments of Inconel 625 and type 410 stainless steel did not crack in any surface condition. All other materials tested showed varying tendencies to crack. (p. 136)

Creep tests on stainless steel submerged-arc and shielded metal-arc welds have generated a large amount of data useful to designers. The data include stresses to provide a minimum strain rate (second-stage creep rate) of 10^{-6} hr^{-1}, stresses for rupture in 10^3 hr, stresses to provide 0.5% strain in 10^3 hr, stresses to cause onset of third-stage creep in 10^3 hr, and fracture strain in 10^3 hr. (p. 144)

We are assisting Aerojet Nuclear Corporation in obtaining ASME Code approval of Inconel 718, an age-hardenable, nickel-chromium alloy. (p. 151)

Metallographic examinations of Incoloy 800 welds indicate that substantial titanium is needed to avoid weld metal fissuring. (p. 153)

The weldability of the niobium-stabilized 2 1/4 Cr—1 Mo—1/2 Ni low-alloy steel is being determined. Fully restrained qualification welds have been made on 1/4-in.-thick plate and they have passed nondestructive and bend tests. (p. 156)

A program was outlined and begun for the nondestructive examination of tube-to-tube sheet joints for steam generators. The techniques include radiography, liquid penetrants, eddy currents and ultrasonics. (p. 160)

New, two-transducer techniques are being studied that will simplify application of ultrasonic frequency analysis for flaw characterization.

Improvements to both equipment and techniques for ultrasonic imaging with schlieren methods now allow optimum viewing of ultrasound at frequencies of 25 MHz and above. (p. 169)

Tensile tests on several heats of type 304 stainless steel show that the properties fall below the minimum expected values when the material is reannealed at the mill anneal temperature, thus indicating that the materials receive some cold working after the mill anneal. (p. 175)

Transmission electron microscopy of type 308 stainless steel weld metal deposited by the shielded metal-arc process shows that ferrite and carbides are present in samples creep tested at 650°C. Unexpectedly, much of the ferrite in the as-welded material transforms to carbides during testing instead of sigma phase. (p. 183)

Three heats of 2 1/4 Cr–1 Mo steel with variable carbon contents varying from 0.003 to 0.11% are being evaluated. Transverse and all weld metal samples have been tested and show that the transverse specimens fail in shorter times in creep than weld or base metal specimens. All specimens exhibited good fracture strains. (p. 193)

PART II. SPACE POWER TECHNOLOGY

We have now accumulated a combined total of over 8000 hr of irradiation time on capsules UN-4 and -5 at cladding temperatures near 1000°C, and both capsules are performing very satisfactorily. (p. 209)

We successfully extruded large diameter W–2% ThO_2 tubing and bars for use as high-strength thermionic emitters. Large differences in the high-temperature creep strength of CVD tungsten correlate with the fluorine impurity content with a transition in strength-ductility behavior observed at about 7 ppm F. (p. 212)

Tensile tests of T-111 doped with oxygen at 1000°C show that a level of 800 ppm O is sufficient to cause complete embrittlement even at test temperatures to 1300°C. Preliminary data suggest that a level of only 400 ppm O will cause complete embrittlement at doping temperatures of 825°C, a temperature which corresponds to conditions in the Pioneer thermoelectric generators. (p. 224)

Heat treatments above 1300°C ductilized T-111 containing up to 4000 ppm O through precipitation of noncoherent HfO_2 particles. (p. 224)

Wrapping T-111 with molybdenum foil and using zirconium getters under conditions similar to those in the Pioneer RTG were not very effective methods of reducing the rate of contamination; however, thin coatings of molybdenum were. (p. 229)

The molybdenum alloy TZM was also found to be embrittled by oxygen but, due to the lower rate of oxygen diffusion in molybdenum, longer times were required. (p. 232)

A Pt–30% Rh–10% W alloy was developed for cladding space isotopic power fuels. Comparing recrystallized materials, this alloy was stronger than the molybdenum alloy TZM at elevated temperatures. Sufficient material is being prepared to evaluate its fabricability and weldability. (p. 235)

CONTENTS

Page

HIGHLIGHTS iii

PART I. FAST REACTOR TECHNOLOGY

FUELS

1. DEVELOPMENT OF FBR OXIDE FUELS 3
Fabrication of $(U,Pu)O_2$ Fuels 3
Replacement Fuel for the F-1 Experiment 4
Fuel for GB-10 Capsule 6
Fuel for the ETR Instrumented Capsules 6
Irradiation Testing of $(U,Pu)O_2$ Fuels 7
Fast Flux Irradiation Tests 8
Uninstrumented Thermal Flux Irradiation Tests 12
ETR Instrumented Tests 15
Tests of Mechanical Interaction of Fuel and Cladding 17
Analysis of Fuel Element Performance 18
Analysis Data from SG-3 Thermal Performance Test 19
Analysis of Fuel—Cladding Chemical Interaction — A Statement of Approach 23
Fuel—Cladding Chemical Interactions 28
Grain Growth of $(U,Pu)O_2$ 32
Actinide Redistribution 34
Sensitivity Analysis of LMFBR Fuel Pin Performance . . . 35
2. ADVANCED FAST BREEDER REACTOR FUELS DEVELOPMENT 49
Irradiation Testing 49
Thermal Flux Tests 49
Fast Flux Tests 50
Synthesis, Fabrication, and Characterization of Advanced FBR Fuels 51
Characterization of $(U,Pu)N$ 51

ABSORBERS

3. DEVELOPMENT OF FBR NEUTRON-ABSORBER MATERIALS 53

Boron Carbide 53

Phase Studies in the Boron-Carbon System 53

Irradiation Testing of Boron Carbide Pellets in the EBR-II 57

Supplemental Evaluation of Powders from HEDL Experiment X 042 57

Performance Modeling of Boron Carbide Absorber Rods . . 58

Alternate Materials 70

Fabrication of Tantalum Borides 70

Microstructure of Irradiated Tantalum 71

Analysis of Self-Heating in Tantalum Irradiation Specimens 76

Helium Vents for Absorber Rods 79

CLADDINGS

4. MECHANICAL PROPERTIES OF ALLOYS IN REACTOR ENVIRONMENTS AND DEVELOPMENT OF FBR CLADDING AND STRUCTURAL ALLOYS 82

Examination of EBR-II Safety and Control Rod Thimbles 82

Some Effects of Composition and Microstructures on Radiation Damage in Stainless Steels 90

Annealed Materials 91

Cold Worked Materials 95

Postirradiation Mechanical Properties of Types 316 and Titanium-Modified 316 Stainless Steel 98

Precipitate-Free Ultra-Fine Grains, A New Approach to Heat Treatment 110

Effects of Heating and Cooling Rates on Recrystallization 112

Effects of Heating and Cooling Rates on Precipitation 112

Preliminary Results 113

5. FABRICATION DEVELOPMENT FOR FBR CLADDING 119

Studies of Defected Tubing 119

Production Speed Rotating Tube Scanner 119

Creep-Rupture Analysis of Type 316 Stainless Steel Tubing with Artificial Defects 119

FABRICATION DEVELOPMENT OF LMFBR COMPONENTS

6. COMPATIBILITY OF STEAM GENERATOR MATERIALS 124
Examination of ALCO/BLH Steam Generator 124
Disassembly Operations 124
Examination of Upper Tube Sheet 125
Examination of Lower Tube Sheet 129
Steam Corrosion of Advanced Steam Generator Materials 134
General Corrosion 134
Stress-Corrosion Cracking 136
7. JOINING OF STRUCTURAL MATERIALS 143
Austenitic Stainless Steels 143
Welding Development for FBR Stainless Steel Components . 143
Investigations of Mechanical Properties 144
Filler Metal Development for Pipe Welding 150
Nickel-Rich Alloys 151
Inconel 718 151
Incoloy 800 153
Ferritic Steels 156
Stabilized Grades 156
Low-Carbon Grades 157
8. NONDESTRUCTIVE TESTING DEVELOPMENT 160
NDT Development for Steam Generators 160
Radiography 162
Liquid Penetrants 162
Eddy Currents 163
Ultrasonics 163
Electromagnetic Inspection Methods (Eddy Currents) 164
Measurement of Liquid Level 164
Measurement of Cold Work in Stainless Steel 168
Ultrasonic Inspection Methods 169
Ultrasonic Frequency Analysis 169

Ultrasonic Imaging 171
Reference Notches 173
Penetrating Radiation Inspection Methods 173
Closed Circuit Television for Radiographic Evaluation 173
9. MECHANICAL PROPERTIES OF STRUCTURAL MATERIALS 175
Mechanical Properties of Type 304 Stainless Steel 175
Microstructural Characterization of Type 304 Stainless Steel Welds 183
Procurement of FFTF Vessel Weldment Test Specimens 186
Characterization of FFTF Vessel-Type Weldments 187
Mechanical Properties of 2-1/4% Cr—1% Mo Steel 193
Annealing Studies 194
Mechanical Properties 196
Welds 196
Base Metal 202

PART II. SPACE POWER TECHNOLOGY

10. DEVELOPMENT OF URANIUM MONONITRIDE 207
Fabrication of Uranium Mononitride 207
Irradiation Testing of Uranium Nitride 208
Capsule Fabrication 209
Operation of Capsules 209
11. TUNGSTEN METALLURGY 212
Fabrication Development for Advanced Cladding Materials . . . 212
Creep Properties of W and W Alloys 216
Creep Properties of CVD W 216
Creep Properties of W—3.8% ThO_2 219
Effect of Low Pressure Gases on the Creep Properties of Tungsten Alloys 222
12. PHYSICAL METALLURGY OF REFRACTORY ALLOYS 224
Effect of Oxygen Contamination on the Tensile Properties of T-111 224
Contamination Studies of T-111 in the Pioneer Heat Source Environment 227

Effect of Barriers on T-111 Contamination 229

Effect of Outgassing Graphite and Zirconium Gettering on Contamination of T-111 231

Effect of Oxygen Contamination on the Mechanical Properties of Molybdenum-Base Alloys 232

13. CLADDING MATERIALS FOR SPACE ISOTOPIC HEAT SOURCES 235

Development of Improved Alloys 235

Preparation of Pt-3010 Sheet 238

PART I. FAST REACTOR TECHNOLOGY

1. DEVELOPMENT OF FBR OXIDE FUELS

P. Patriarca A. L. Lotts F. J. Homan

The purpose of this program is to advance the technology of $(U,Pu)O_2$ as a fuel for the LMFBR. The oxide fuels studied in this program are derived from coprecipitation, mechanical blending, and sol-gel processes and are fabricated by cold pressing and sintering and Sphere-Pac. We emphasize determination of the properties and performance of oxide fuels derived from the sol-gel process and fabricated by Sphere-Pac techniques, but we also compare these fuels with those fabricated by other processes. The main objectives of the program are (1) to establish the performance characteristics and limitations of $(U,Pu)O_2$ fuel fabricated by the different processes, (2) to obtain a fundamental understanding of the mechanisms that are involved in the behavior of fuel elements under irradiation, (3) to develop fabrication techniques that provide both economy and a product with optimized performance, and (4) to develop analytical methods sufficiently accurate to optimize experimental design and to predict the response of fuel elements to LMFBR service conditions.

Fabrication of $(U,Pu)O_2$ Fuels

J. D. Sease R. A. Bradley

The objective of our $(U,Pu)O_2$ fabrication program is to develop processes by which mixed oxide fuel of controlled density and stoichiometry can be fabricated for irradiation tests. A large portion of this program has been the development of Sphere-Pac and sol-gel pellet fabrication techniques. During this report period we completed the pellet fabrication for the Gas-Cooled Fast Breeder Reactor (GCFBR) F-1 irradiation experiment replacement pins and began the fabrication of fuel for the GB-10 capsule.

We also heat treated and characterized the fuel for two instrumented capsules for in situ measurement of fission gas in the ETR.

Replacement Fuel for the F-1 Experiment

Eight fuel pin containing $(U,Pu)O_2$ pellets were fabricated previously for the GCFBR F-1 irradiation experiment in collaboration with Gulf General Atomic.[1] We have been requested to prepare the fuel for five additional pins that will be used in replacement capsules. The fuel requirements are summarized in Table 1.1. The mixed $(U,Pu)O_2$ powder for making these pellets was prepared by the sol-gel process described previously.[2] Sintering conditions which would yield the required pellet densities were established in a series of sintering tests.

The 88% dense solid pellets were made from calcined powder by pressing at 40,000 psi and sintering in Ar—8% H_2 at 1550°C for 14 hr. The 92% dense annular pellets were made from the same calcined powder after it had been ball-milled 5 hr. The pellets were pressed at 30,000 psi and sintered by heating to 1425°C in argon and then to 1550°C in Ar—8% H_2 for 15 hr. Argon was used in the initial stage of the sintering cycle because sintering tests showed that the ball-milled powder produced 95% dense pellets when sintered in a reducing atmosphere. The higher oxygen-to-metal ratio maintained by sintering in argon led to trapped porosity through enhanced grain growth, thus yielding pellets with the required density of 92% of theoretical. The densities and oxygen-to-metal ratios achieved are summarized in Table 1.1. An oxygen-to-metal ratio of 1.98 ± 0.01 was achieved during the sintering treatment by reduction in Ar—8% H_2 for the length of time calculated from the kinetic reduction model of

[1]T. N. Washburn, J. D. Sease, R. A. Bradley, E. J. Manthos, and M. K. Preston, LMFBR Fuel Cycle Studies Progr. Rept. May 1970, No. 15, ORNL-TM-3018, pp. 57—58.

[2]R. A. Bradley and J. D. Sease, GCR-TU Programs Semiannual Progr. Rept. for Period Ending September 30, 1970, ORNL-4637, p. 49.

Table 1.1 Densities and Oxygen-to-Metal Ratios of Pellets Fabricated for GCFBR F-1 Replacement Pins

Fuel Design Requirements[a]			Results		
Type[b]	Density[c] (% of theoretical)	Oxygen-to-Metal Ratio	Batch Number	Average Density (% of theoretical)	Oxygen-to-Metal Ratio
Annular	92.3 ± 1.0	1.98 ± 0.01	1	92.1	1.967
			2	92.2	1.969
			3	92.3	1.968
			4	91.8	1.967
			5	91.8	1.967
Annular	92.3 ± 1.0	1.94 ± 0.01	1	92.4	1.944
			2	93.1	1.948
			3	93.0	1.937
Solid	88.6 ± 1.0	1.98 ± 0.01	1	88.9	1.978
			2	87.2	1.975
			3	87.8	1.975
			4	87.9	1.972
			5	90.1	1.972

[a]Fuel composition: $(U_{0.85},Pu_{0.15})O_{2-x}$, 93% enriched U.

[b]All pellets have dished ends.

[c]Pellet densities required to yield fuel column smear density of 84.0 ± 1.0% of theoretical.

Lindemer and Bradley.[3] Pellets were heat treated in graphite boats in Ar–10% CO at 1550°C for 20 hr to obtain an oxygen-to-metal ratio of 1.94 ± 0.01.

We experienced considerable difficulty in determining the impurity content of the GCFBR F-1 pellets as well as pellets and microspheres for other irradiation experiments. Analysis by spark source mass spectroscopy showed all of the elements normally found in glassware (calcium, magnesium, sodium, boron, aluminum, and silicon) to be high—in some cases several thousand ppm. The problem was eliminated by dissolving the mixed oxide in aqua regia in Teflon containers. These pellets will be loaded into fuel pins fabricated at ORNL from hardware supplied by GGA. The weld development and qualification is complete and we will begin fuel pin fabrication in the near future.

Fuel for GB-10 Capsule

The fuel pin for the GB-10 capsule will contain 8.8 in. of nominally 87.5% dense, solid, dished-end pellets with an oxygen-to-metal ratio of 1.97. The smear density of the fuel pin is required to be 84.0 ± 1.0% of theoretical. The $(U_{0.88},Pu_{0.12})O_2$ powder, with the uranium containing 9% ^{235}U, was prepared by the sol-gel process.[2] The powder is presently being calcined.

We expect to fabricate these pellets in a manner similar to that used for the 88% dense pellets for the F-1 replacement pins.

Fuel for The ETR Instrumented Capsules

The fuel pins for two instrumented capsules (ORNL 43-125 and 43-126) for in situ measurement of fission gas release will each contain approximately 20 in. of mixed oxide fuel. One will contain $(U_{0.75},Pu_{0.25})O_{1.97}$ pellets fabricated by WADCO from mechanically mixed powders. The other will be loaded by the Sphere-Pac process with

---

[3]T. B. Lindemer and R. A. Bradley, "Kinetic Models for the Synthesis of $(U,Pu)O_{2-y}$ by Hydrogen-Reduction and Carbothermic Techniques," accepted for publication in Journal of Nuclear Material.

$(U_{0.73},Pu_{0.27})O_{1.97}$ coarse microspheres and UO_2 fine microspheres to provide a nominal fuel bed composition of $(U_{0.80},Pu_{0.20})O_{1.98}$. The smear density of both the Sphere-Pac and the pellet pin is to be 83.0 ± 1.0% of theoretical.

We heat treated both the pellets and microspheres to reduce sorbed gas and H_2O content to the specified limits. Analyses for H_2O content, sorbed gas, oxygen-to-metal ratio, carbon, and halides indicate that the fuel is within specification.

The hardware for the fuel pin has been fabricated and is ready for welding. Weld development and qualification is complete. We will begin fuel pin fabrication and loading in the near future.

Irradiation Testing of $(U,Pu)O_2$ Fuels

F. J. Homan T. N. Washburn

The performance characteristics of mixed $(U,Pu)O_2$ fuels are being evaluated in a variety of irradiation tests for potential application in an LMFBR. We are now concentrating on comparative tests of fuel fabricated as pellets or as microspheres loaded by the Sphere-Pac technique. The program includes thermal-flux experiments, which permit use of instrumented capsules and continuously controlled heat rates, and fast flux experiments, in which the fission rate distribution and radiation effects on the cladding are more typical of those for operating conditions anticipated in an LMFBR.

Fast Flux Irradiation Tests (A. R. Olsen)

The fast flux irradiation tests in the EBR-II are designed to approximate conditions to be encountered in a commercial-scale LMFBR. The objective of these tests is to establish the effects of fuel fabrication form (Sphere-Pac or pellet), void distribution, and stoichiometry on the swelling of the fuel, mechanical and chemical interactions of fuel and cladding, release of fission gas, and distribution of fission products in a $(U,Pu)O_2$ fuel operating at typical heat rates to design levels of burnup.

The five Series I encapsulated tests all contain Sphere-Pac fuels. Two of the capsules, S-1-A and S-1-E, were returned to ORNL after the initial period of irradiation in subassembly X050 which was discharged from the EBR-II at the end of run 42 on May 18, 1970. The other three capsules are continuing under irradiation in subassembly X119 with a scheduled incremental exposure of 5600 MWd of EBR-II operation. Subassembly X119 was installed in position 5F4 of the EBR-II grid on May 16, 1971. The subassembly was removed from the reactor after run 49d and not returned until the start of 50f. The subassembly was removed when it was found to be sticking during incidental handling. The cause of this binding was found to be a minor burr on the lower adaptor. The problem was corrected remotely. The subassembly was again removed at the start of EBR-II run 52 on September 20, 1971. This removal was caused by a reactivity limitation of the EBR-II loading. Two other experimental subassemblies of low priority were also removed at this time. At the time of the subassembly discharge the pins had been exposed for 2125 MWd or 38% of the planned incremental exposure. At the present time it is uncertain as to when this subassembly will be reinserted in the EBR-II lattice.

The postirradiation examination of pins S-1-A and S-1-E is continuing. Most of the examination is complete although some samples are currently being polished in a nonaqueous media to prepare them for electron microprobe analysis of fission product distribution. The burnup analyses are complete. The measured burnup from various sections from the two fuel pins is presented in Table 1.2. These values, as determined by three

Table 1.2

Burnup Analysis for Pin S-1-A

Section Identification	Axial Location Above Bottom of EBR-II Core (cm)	Burnup				
		EBR-II[a]	^{144}Ce	Actinide Isotopic	^{148}Nd	Measured Average
S-1-A-C	2.5	4.73	4.36	4.33	4.39	4.36
S-1-A-E	16.5	5.65	4.94	4.54	5.11	4.86
S-1-A-L	31.1	4.44	4.05	4.10	4.05	4.07
S-1-E-C	17.2	5.78	4.79	4.75	5.99	5.18
S-1-E-H	31.1	4.57	4.13	4.22	4.24	4.20

[a]Predicted value based on advertised fission rates for the EBR-II including depletion effects.

relatively independent measurements, agree quite well but the average of all three is from 8 to 14% below the burnup predicted by the advertised EBR-II fission rates. This difference is consistent with the findings of other experimenters in the EBR-II. The fluence seen by the cladding on these two pins has been determined by measuring the saturated activity of three monitor elements contained in the cladding: $^{58}Ni_{(n,p)}$ ^{58}Co, $^{54}Fe_{(n,p)}$ ^{54}Mn, and $^{59}Co_{(n,\gamma)}$ ^{60}Co. The peak total fluence measured by the nickel and iron reactions is within 10% of the anticipated 4.2×10^{22} neutrons/cm^2 ($E > 0.11$ MeV). In general the cobalt reaction indicates a higher fluence. However, the spectrum averaged cross section for the ^{59}Co, derived from spectrum averaged ENDF"B" data, is considered less reliable than the nickel and iron cross sections which are less affected by the flux in the intermediate and low energy levels. The statistical analysis of the cladding diameter measurements has been completed. This analysis indicates there is a greater uncertainty in the measured diameter changes for pin S-1-A with the type 304 stainless steel cladding than for the diameter changes measured on pin S-1-E with the type 316 stainless steel. However, this uncertainty does not change the previously reported conclusion[4] that the type 304 cladding shows a greater change than the type 316 cladding. The comparison is shown in Fig. 1.1.

The Series II tests are with unencapsulated pins in a 37-pin subassembly. Details of the testing program and the individual pin operating conditions are reported in the data package.[5] The Babcock and Wilcox Company fabricated 18 of the first 37 pins to be irradiated in subassembly X112 and 16 pins for replacement of pins removed at scheduled burnup levels. On July 1 we assumed responsibility for the entire irradiation program and postirradiation examination.

---

[4]A. R. Olsen, Fuels and Materials Development Program Quart. Progr. Rept. Dec. 31, 1970, ORNL-TM-3300, pp. 15–19.

[5]A. R. Olsen et al., Preirradiation Data for ORNL Series II and B & W Oxide Fuel Tests in EBR-II, ORNL-TM-3446 (in press).

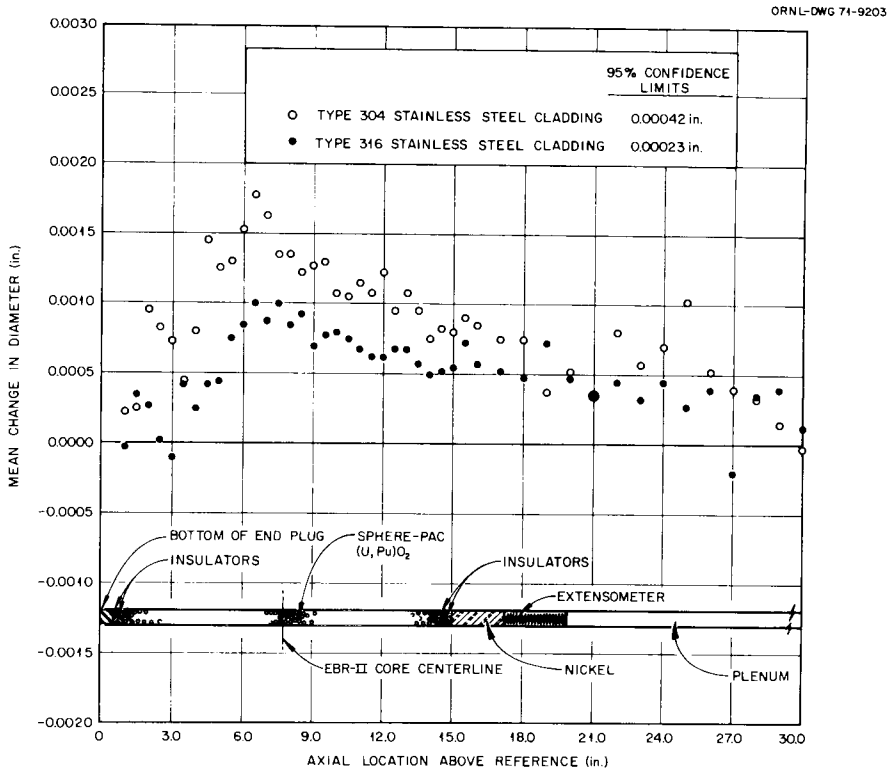

Fig. 1.1. Comparison of Diametral Changes for Pins Clad in Type 304 or 316 Stainless Steel.

The first incremental irradiation is being done in subassembly X112. Initially this subassembly was scheduled for an irradiation period of 16,000 MWd of EBR-II operation to achieve a peak pin average burnup of approximately 5.4% FIMA. However, because of some uncertainty in the amount of chemical interaction between the fuel and cladding at the cladding temperatures of 1200°F (650°C) in these tests, particularly with the coprecipitated fuels, and because of the current EBR-II restrictions on the plenum pressure in an oxide fueled test pin in this type of subassembly, the subassembly will be removed after 10,000 MWd of operation. The peak pin burnup at this time will be approximately 3.3% FIMA and the maximum plenum pressure will have reached the current 450 psia limit. We are currently working on a revised schedule for pin removal and examination. There are also tests in the EBR-II which are designed to investigate the effects of pin failures at higher plenum pressures so this current limitation may be modified.

At the start of run 49 subassembly X112 was inserted in EBR-II grid position 6B2 but it was moved to the requested higher flux position 6E3 before the start of run 50. As of September 21, 1971, the exposure has reached 3721 MWd of EBR-II operation or 37% of the planned incremental irradiation period.

Uninstrumented Thermal Flux Irradiation Tests (A. R. Olsen and D. R. Cuneo)

A series of uninstrumented capsules is being irradiated in the X-basket facilities of the ETR. Each capsule contains four test pins arranged in tandem. The initial objective of these tests was to investigate at extended burnup the effects of fabrication form on release of fission gas, migration of fission products, and swelling of the fuel. The capsules now being irradiated are to provide short-cooled irradiated fuel for LMFBR reprocessing studies. The current status of these tests is given in Table 1.3. The results of low and intermediate burnup level tests have been presented.[6,7]

During the past quarter the postirradiation examination of the pins from capsule 43-113 was initiated. The capsule was subjected to gamma scanning before a sample of the capsule gas was removed. After disassembly all four pins were radiographed in the ORR Neutron Radiography Facility.[8] No fission gas was detected in the capsule gas sample, indicating that none of the fuel pins failed. The gamma scans and the neutron radiographs both appear normal. There has been no significant change in fuel column length. All four pins show the development of a distinct central void although the void in the bottom pin, 43-113-1, appears to be only in the upper half of the fuel column where the flux and hence the linear heat rate was sufficiently high to produce this restructuring. Profilometry data indicate the peak diameter change on the highest heat rate pin was less than 0.001 in. or less than 0.4%.

---

[6]A. R. Olsen, C. M. Cox, and R. B. Fitts, Trans. Am. Nucl. Soc. 12, 605–606 (1969).

[7]A. R. Olsen, Trans. Am. Nucl. Soc. 13, 32–33 (1970).

[8]B. E. Foster, S. D. Snyder, V. A. DeCarlo, and R. W. McClung, Development and Operation of a High-Intensity, High-Resolution Neutron Radiography Facility, ORNL-4738 (in press).

Table 1.3 Noninstrumented Thermal Flux Tests of $(U,Pu)O_2$ Fuels

Experiment Number	Fuel		Number of Rods	Peak Burnup (% FIMA)[a]	Peak Linear Heat Rate (W/cm)	Peak Cladding Inner Surface Temperature (°C)	Status September 1971
	Form	Composition					
43-99	Sphere-Pac	$(^{235}U_{0.80},Pu_{0.20})O_{2.00}$	2	1.5[b]	1640[b]	1000	Examined
43-100	Sphere-Pac	$(^{235}U_{0.80},Pu_{0.20})O_{2.00}$	2	1.4[b]	1470[b]	900	Examined
43-103	Sphere-Pac Pellet	$UO_{2.02}$(20% ^{235}U) $UO_{2.00}$(20% ^{235}U)	3 1	5	690	530	Examined
43-112	Sphere-Pac	$(^{238}U_{0.85},Pu_{0.15})O_{1.97}$ $UO_{2.02}$(20% ^{235}U)	3 1	0.7	500	360	Examined
43-113	Sphere-Pac	$(^{238}U_{0.85},Pu_{0.15})O_{1.97}$ $UO_{2.02}$(20% ^{235}U)	3 1	10[c]	500[c]	380[c]	Being examined
43-115	Sphere-Pac	$(^{238}U_{0.85},Pu_{0.15})O_{1.97}$ $UO_{2.02}$(20% ^{235}U)	3 1	6.5	600	460	Examined
43-116	Sphere-Pac	$(^{238}U_{0.85},Pu_{0.15})O_{1.97}$	4	1.5[c]	600[c]	460[c]	Processed
43-117	FTR Pellets	$(^{238}U_{0.75},Pu_{0.25})O_{1.98}$	4	1.5[c]	430[c]	360[c]	Being examined
43-118	FTR Pellets	$(^{238}U_{0.75},Pu_{0.25})O_{1.98}$	4	8.0[c]	430[c]	360[c]	In-reactor ≈4.7% FIMA
43-119	FTR Pellets	$(^{238}U_{0.75},Pu_{0.25})O_{1.98}$	4	10.0[c]	430[c]	360[c]	In-reactor ≈4.5% FIMA
32-123	FTR Pellets	$(^{238}U_{0.75},Pu_{0.25})O_{1.98}$	4	4.0	350[c]	310[c]	In preparation

[a]FIMA is fissions per initial actinide metal atom.

[b]Rods failed in reactor from overpowering.

[c]These are target design values.

Statistical evaluation of this data is incomplete but the changes may be within the range of measurement errors indicating no significant mechanical interaction even at this high burnup level. The fission gas in the plenum of each pin was recovered and analyzed. Sections were removed for burnup analysis and metallographic examination. Some of the analytical results are available for burnup calculations and a preliminary evaluation based on mass spectrometric analysis for ^{148}Nd indicates a peak burnup in the UO_2 (20% ^{235}U) pin of 12% FIMA and in the peak (U—15% Pu)O_2 pin of 11% FIMA. Final burnup data should be available during the next report period. Transverse sections from the $(U_{0.85},Pu_{0.15})O_2$ pins have been examined metallographically in the as-polished condition. The fuel shows normal restructuring; there is no evidence of fuel-cladding chemical interaction. The only distinctive feature seen so far is a large number of pores, bubbles, or spherical voids in the essentially unrestructured fuel in the cooler radial regions adjacent to the cladding. Metallographic examination of these pins is continuing.

Capsules 43-117, 43-118, and 43-119 are the first capsules we have irradiated with mechanically mixed $(U,Pu)O_2$ pellet fuel. Only capsule 43-117 has completed its planned irradiation. Capsules 43-118 and 43-119 are continuing their irradiation to revised target burnup levels as indicated in Table 1.3. The irradiation schedule was altered to fit the planned usage of the hot cells where the reprocessing studies are done. Analytical data for the burnup analysis of the four pins from 43-117 are incomplete. When these are available they will be used to normalize the recently revised physics analysis of these pins so that ØRIGEN[9] calculations can be performed to provide fission product content predictions for comparison with the measured contents from the reprocessing studies. Metallographic sections from three of the pins are being polished for examination.

---

[9]M. J. Bell, ØRIGEN, The ORNL Isotope Generation and Depletion Code, ORNL-4628, in preparation.

ETR Instrumented Tests (A. R. Olsen and R. A. Buhl)

The ETR instrumented tests are designed to determine the performance of mixed oxide fuel under simulated LMFBR design operating conditions.

Series I consists of two capsules 43-120 and 43-121. Each capsule contains four fuel pins with two thermocouples at the fuel axial midplane of each pin. These tests are designed to investigate fuel swelling and fuel-cladding chemical interactions of Sphere-Pac and pelletized $(U,Pu)O_2$ fuels over a wide range of cladding temperatures up to a maximum of 650°C.

As of September 20, 1971, the Series I capsules have been irradiated approximately 260 effective full power days (EFPD) to a peak fuel burnup of 6% FIMA. The current peak inner cladding surface temperature has fallen to 520°C. A detailed history of the irradiation conditions for each pin has been plotted. Figures 1.2 and 1.3 show such histories for the highest heat rate pin in each of the capsules. Current plans are to relocate capsule 43-121 to a higher flux position during the next reactor shutdown. This move should increase the heat rate of the pins and bring the peak cladding inner surface temperature back up to approximately 650°C. Capsule 43-120 cannot be moved at this time because the step in flux would be too large and result in cladding temperatures in excess of the test limitations.

The Series II tests will consist of three instrumented capsules. These capsules will each contain a single fuel pin with a 20-in.-long fuel column. Each pin is instrumented with a pressure transducer, to measure gas pressure in the plenum region during irradiation, and nine thermocouples to measure cladding temperatures at selected axial locations along the fuel column and in the gas plenum region.

One capsule will contain FTR type pellets of the highest permissible density (94% of theoretical), the second will contain FTR pellets of the lowest permissible density (88% of theoretical), and the third will contain a packed bed of Sphere-Pac U-Fines[10] fuel. In the latter

---

[10] J. D. Sease, C. R. Reese, R. A. Bradley, and W. H. Pechin, "U-Fine Process," pp. 329–331 in Symposium on Sol-Gel Processes and Reactor Fuel Cycles, Gatlinburg, Tennessee, May 4–7, 1970, CONF-700502.

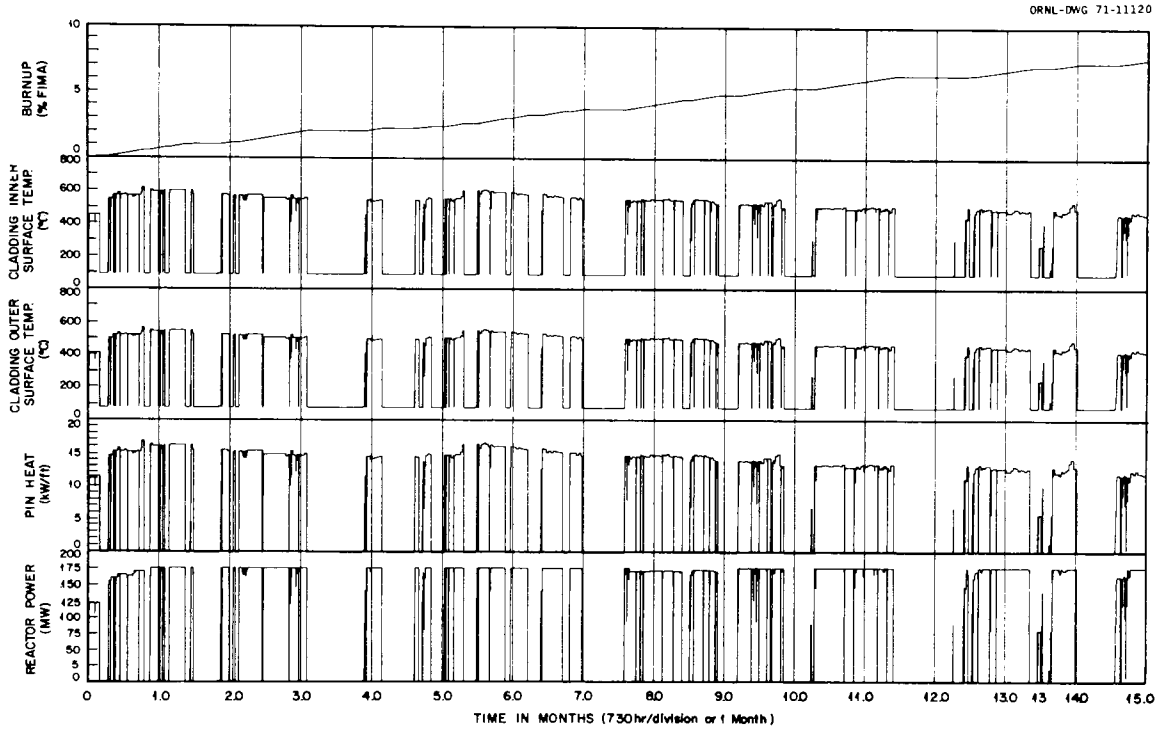

Fig. 1.2. Capsule ORNL-43-120, Fuel Pin 2.

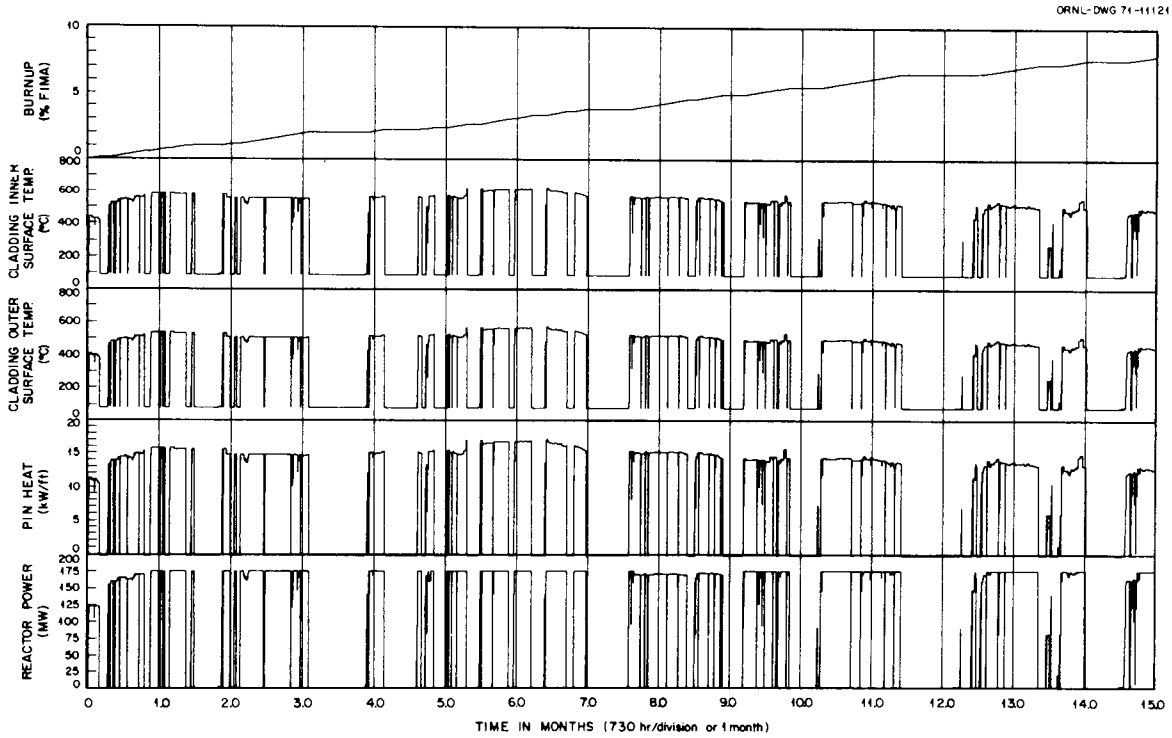

Fig. 1.3. Capsule ORNL-43-121, Fuel Pin 2.

fuel, all the plutonium is contained in the coarse fraction (∿400-μm diam) microspheres and a fine fraction (<44-μm diam) of depleted UO_2 is infiltrated into the coarse bed.

The two capsules containing the low density FTR pellets and the Sphere-Pac fuel are currently under construction. The status of the test pins and two capsules is reported on pages 3 through 7. The safety analysis for these capsules has been started with irradiation scheduled to start early in 1972.

Tests of Mechanical Interaction of Fuel and Cladding (B. Fleischer, R. L. Senn,[11] and R. B. Fitts)

The intent of our program is to measure in-reactor the axial extension of both the fuel column and cladding and also the fuel pin internal gas pressure during operation of prototypic LMFBR fuel pins under carefully controlled conditions. These include programmed power cycles and an occasional overpower cycle. The irradiation capsules are designed so that the fuel pin operates in the ORR Poolside irradiation facility at LMFBR prototypic power and temperature conditions. The irradiation tests will last one to two years and will give burnup levels of 5 to 9%.

As described previously,[12] the first in-reactor power cycling capsule (MINT-1) will contain a prototype Fast Test Reactor (FTR) fuel pin. The insertion date for MINT-1 has been delayed because of difficulties encountered during capsule assembly.

The thermocouples which penetrate the primary container through the bottom bulkhead were broken off at the bulkhead during bending. The breakage was attributed to a combination of bending stresses and to embrittlement resulting from braze metal used to seal the penetrations. To correct this a new assembly was made with provisions to avoid braze metal in the bend areas of the thermocouples. A jig was also incorporated to prevent stressing of the thermocouples at the braze joint during bending

---

[11] Reactor Division.

[12] R. B. Fitts, R. L. Senn, J. G. Morgan, and J. D. Jenkins, Fuels and Materials Development Program Quart. Progr. Rept. June 30, 1970, ORNL-4600, pp. 58–63.

operations. These changes solved the problem, and the capsule assembly has progressed to step 32 in the assembly (Spec. No. M-10571-RM-001-S). It is now estimated that the capsule will be completed in time for insertion into the ORR during either the November 16 or the December 5 shutdowns. A formal approval has been received from the Reactor Experiment Review Committee for operation of this capsule in the ORR.

During checkout of the solenoid used for calibration of the length measurement transducers it was found that the rotation cam was inoperative. The cause is unknown and corrective action is impossible. It is conceivable that the part will free itself during operation. Loss of rotation means we will have one, rather than two, fixed levels for calibration of the transducers. This downgrades our calibration system, but still allows us to check for signal drift. During this solenoid checkout the upper transducer was −8.87 V (volt) at the zero position, and the lower transducer was −8.77 V. At the high calibration point the upper unit was +4.79 V, and the lower unit was 5.50 V. Using the previously established coefficients of 31.16 mils/V for the upper unit and 29.90 mils/V for the lower unit, the distance to the calibration point was 425.7 mils and 426.6 mils, respectively. This very good agreement confirms the accuracy and stability of the coefficients measured during the earlier bench calibration tests. Comparison of the zero points with those measured in the bench tests indicates that the fuel column has compacted about 13 mils during assembly operations.

Analysis of Fuel Element Performance

F. J. Homan

The objectives of this work are a fundamental understanding of the behavior of LMFBR fuel elements and the development of analytical models to describe their performance and probability of their failure under various operating conditions. Special emphasis is given to modeling fuel-cladding mechanical interactions and to characterizing irradiated $(U,Pu)O_2$ fuels. This work is an integral part of the irradiation testing program, providing design methods and evaluation of the tests.

Analysis Data From SG-3 Thermal Performance Test (R. B. Fitts and F. L. Miller[13])

These irradiation tests are designed[14] to monitor the thermal performance of fuel pins as they operate in the Oak Ridge Research Reactor Poolside Facility. The capsule configuration and the relative location of the thermocouples in the two measuring planes (one plane at the axial centerline of each fuel pin) are shown in Fig. 1.4. The temperature of the fuel pin cladding and fuel center and the rates of heat generation are continuously recorded. These data are used to evaluate the thermal characteristics of the fuel and fuel pins and the effects of irradiation conditions upon the temperatures and structural changes within the operating fuels.

Data from the third capsule in this series, capsule SG-3 (Ref. 15,16), wherein Sphere-Pac[17] and pellet[16] fuel forms were compared, have indicated[18,19] a higher gap conductance and better thermal performance for the Sphere-Pac than for the pellet fuel. The difference between the fuels was small and therefore statistical analysis of the data is being implemented to assess the significance of these measured differences.

---

[13]Mathematics Division.

[14]R. B. Fitts and V. A. DeCarlo, Fuels and Materials Development Program Quart. Progr. Rept. June 30, 1968, ORNL-4330, pp. 20–23.

[15]R. B. Fitts, D. R. Cuneo, V. A. DeCarlo, and K. R. Thoms, Fuels and Materials Development Program Quart. Progr. Rept. September 30, 1969, ORNL-4480, pp. 26–27.

[16]R. A. Bradley and J. D. Sease, GCR-TU Programs Semiannual Progr. Rept. Sept. 30, 1970, ORNL-4637, pp. 6–8.

[17]F. G. Kitts, R. B. Fitts, and A. R. Olsen, "Sol-Gel Urania-Plutonia Microsphere Preparation and Fabrication into Fuel Rods," pp. 195–210 in Intern. Symp. Plutonium Fuel Technol., Scottsdale, Arizona, 1967, Nucl. Met. 13, American Institute of Mining, Metallurgical, and Petroleum Engineers, New York (1968).

[18]R. B. Fitts, E. L. Long, Jr., and J. R. Miller, Fuels and Materials Development Program Quart. Progr. Rept. December 31, 1970, ORNL-TM-3300, pp. 23–29.

[19]R. B. Fitts, Fuels and Materials Development Program Quart. Progr. Rept. June 30, 1971, ORNL-TM-3540, pp. 50–51.

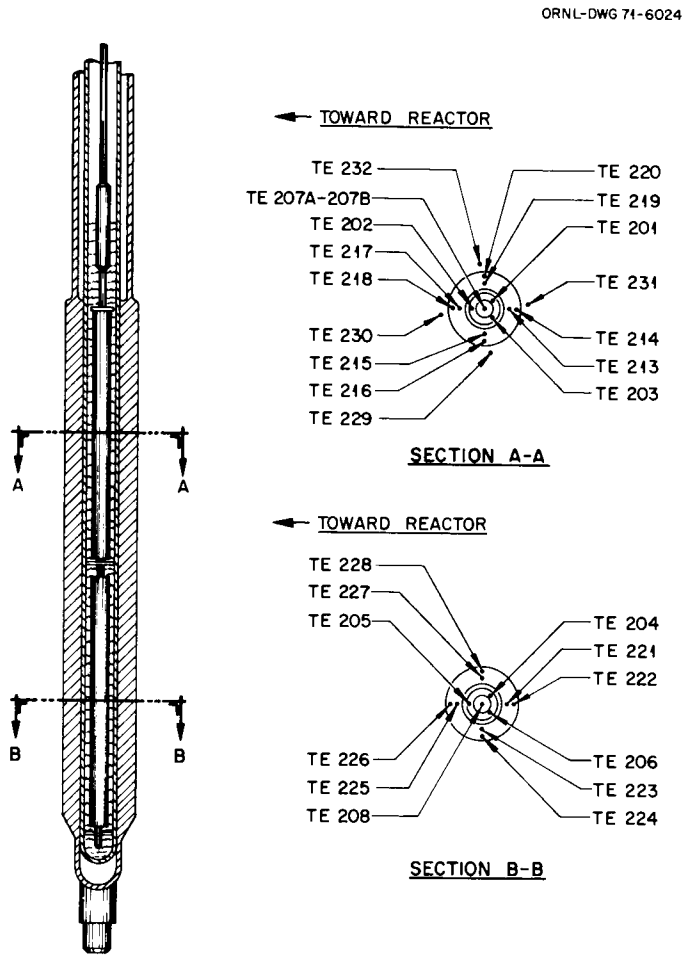

Fig. 1.4. SG Capsule Instrumentation.

The statistical analysis of the data from capsule SG-3 has employed about 7600 of the 45,000 sets of temperature measurements recorded during the test. This group of 7600 measurements represents data from each temperature hold during the operation of the test. The operating sequence is illustrated in terms of the Sphere-Pac fuel central temperature in Fig. 1.5. These 7600 sets of data were reduced for ease of manipulation to 261 sets by averaging all of the readings taken from a given thermocouple during any 3-min interval of operation. This transformation produced sets of data consisting of average temperatures recorded by each thermocouple. These sets of average temperatures generally exhibit standard deviations of less than 1% of the average value for any measured temperature.

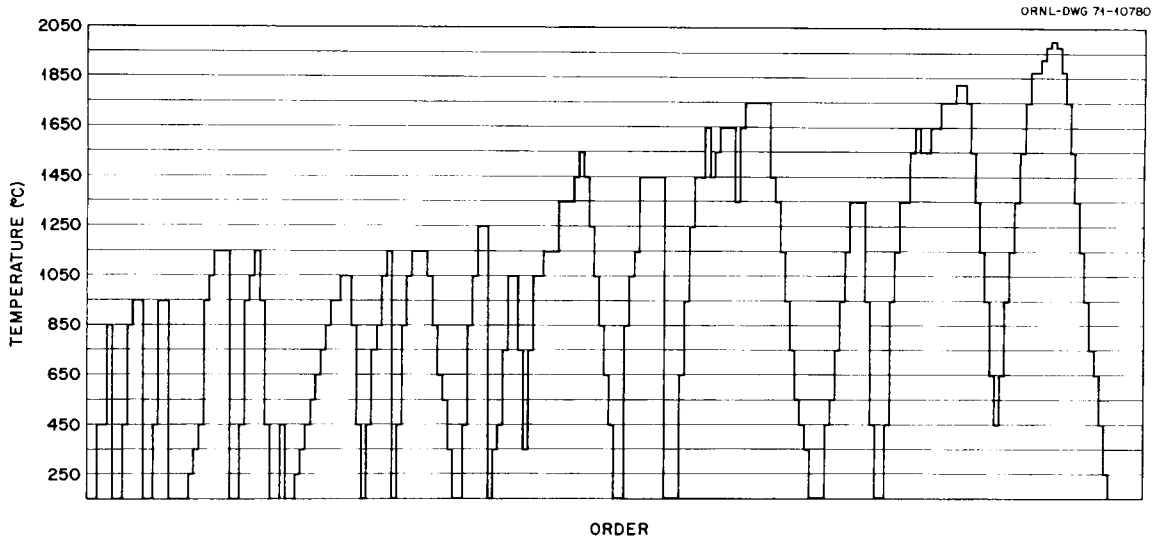

Fig. 1.5. Capsule SG-3 Operating Sequence.

The data from the Sphere-Pac fuel pin have been examined in some detail by analysis of the relationships between the measured fuel central temperature, the three measurements of cladding temperature, and the measurements of heat flow in four directions from the fuel pin. These analyses permitted the elimination of three sets of the data where there were obvious malfunctions of the recording system such as one temperature remaining constant while all of the others doubled, etc. The Sphere-Pac fuel central temperature and cladding temperature from the full group of 258 data sets are displayed in Fig. 1.6. The data fall close to the general relationship reported earlier for this fuel pin,[15] deviating at the high and low ends of the scale by about 10%.

A number of the data points in Fig. 1.6 appears to fall significantly above the bulk of the data and this was verified by the analysis displayed in Fig. 1.7. In this figure the difference (between the central temperature as calculated from a quadratic fit of the data in Fig. 1.6 and each measured temperature) is plotted on the ordinate as the residual and the data are arranged versus time (or chronological order) on the abscissa. The larger residuals correspond to shutdowns and startups, demonstrating that the general trend over the long period of experiment operation does not hold during periods of rapidly changing experiment power. During periods of slowly changing or constant power operation the fuel

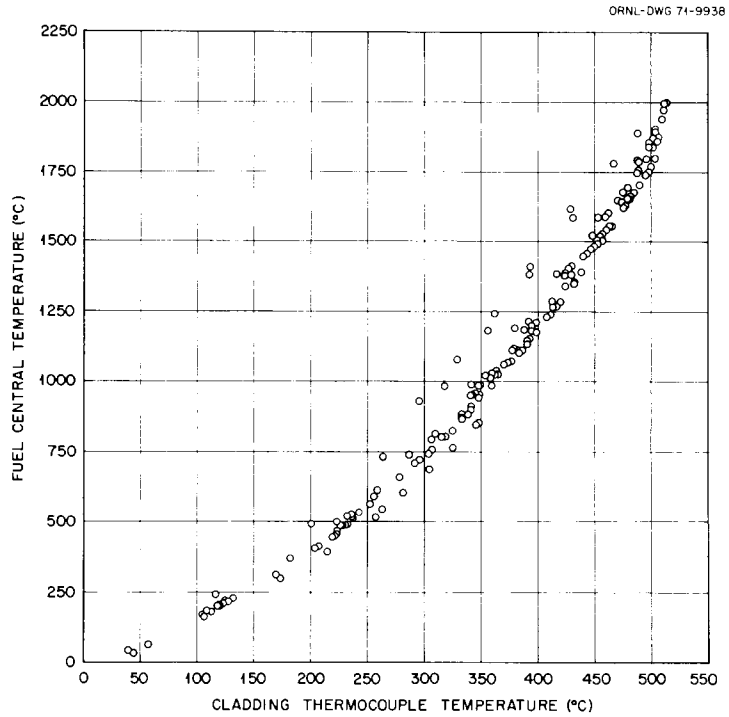

Fig. 1.6. Measured Temperatures in SG-3 Sphere-Pac Fuel Tests.

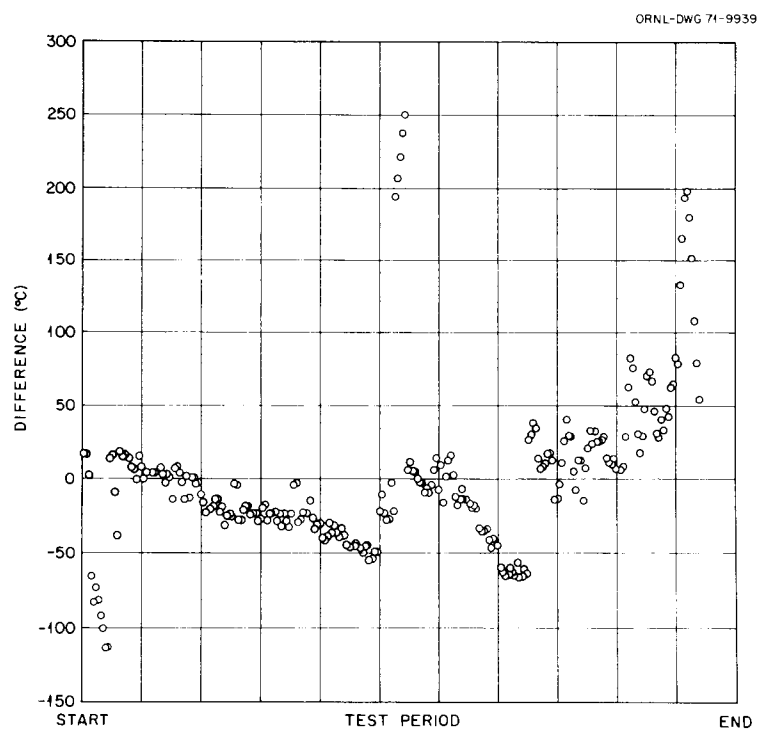

Fig. 1.7. Difference Between Measured Fuel Central Temperature and Those Calculated from Quadratic Fit of all Data.

central temperature showed a gradual decrease with time and during rapid (∿50°C/min) temperature changes the fuel pin thermal conductance was degraded.

Further analysis of the data has been carried out examining separately data from periods of slowly changing or constant power operation and data from the shutdown and startup periods. The shutdown and startup periods comprised 25 data sets. The remaining 233 sets were used to construct Fig. 1.8 where the Sphere-Pac fuel central temperature during "steady-state" operation is plotted against the average heat generation rate. These data have been further refined by elimination of the data collected during the midtest period from February 3 to March 8, 1970, when movement of adjacent experiments has been shown to cause changes in the pattern of heat flow from the experiment. The refined data are shown plotted in Fig. 1.9. Here the general relationship is the same as that in Fig. 1.8, but the variability in the data is significantly reduced. The least squares line fitted through this data is within 8°C of the tentative, hand drawn fit reported earlier.[18]

Analysis of the data from the pellet fuel pin is under way and the phenomena described above have also been observed in this pin. This analysis is just beginning but the plot of all of the data selected for this pin (191 sets) is shown in Fig. 1.10. The initial examination of this unrefined data shows that the least squares fit of this relationship for the pellet pin will yield temperatures about 10% above those for the Sphere-Pac pin at equivalent heat generation rates.

More detailed analysis of the data for the pellet fuel pin, including the separation of "steady-state" and "shutdown" data, is in progress. Further examination of the "shutdown" data from both fuel pins will also be undertaken.

Analysis of Fuel-Cladding Chemical Interaction — A Statement of Approach (J. M. Leitnaker, T. B. Lindemer, and F. J. Homan)

An oxide mechanism is the most likely postulate for chemical attack of cladding material on oxide fuel. This viewpoint is held by every

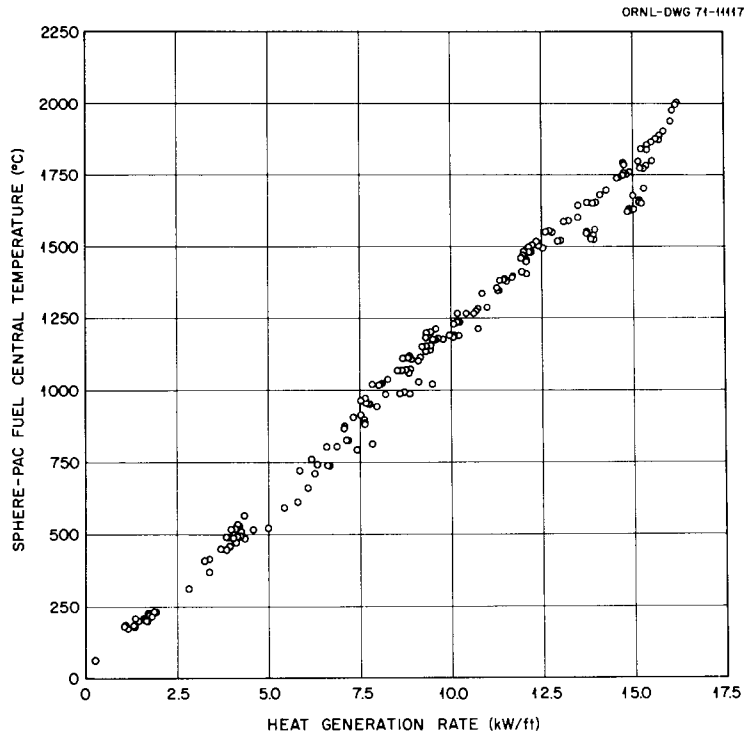

Fig. 1.8. Sphere-Pac Fuel Central Temperature in SG-3 as a Function of Heat Generation Rate. All steady-state data included.

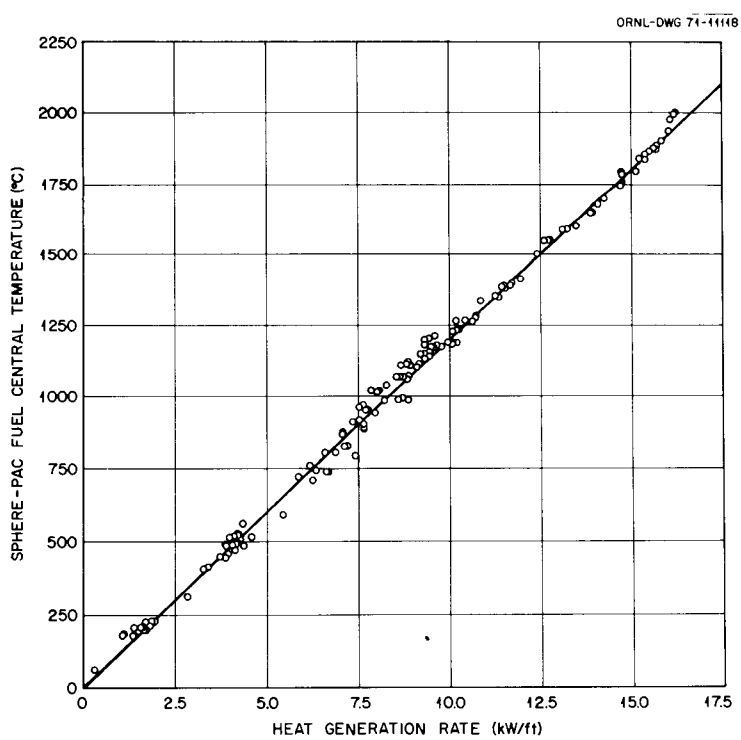

Fig. 1.9. Sphere-Pac Fuel Central Temperature in SG-3 as a Function of Measured Heat Generation Rate Refined Data.

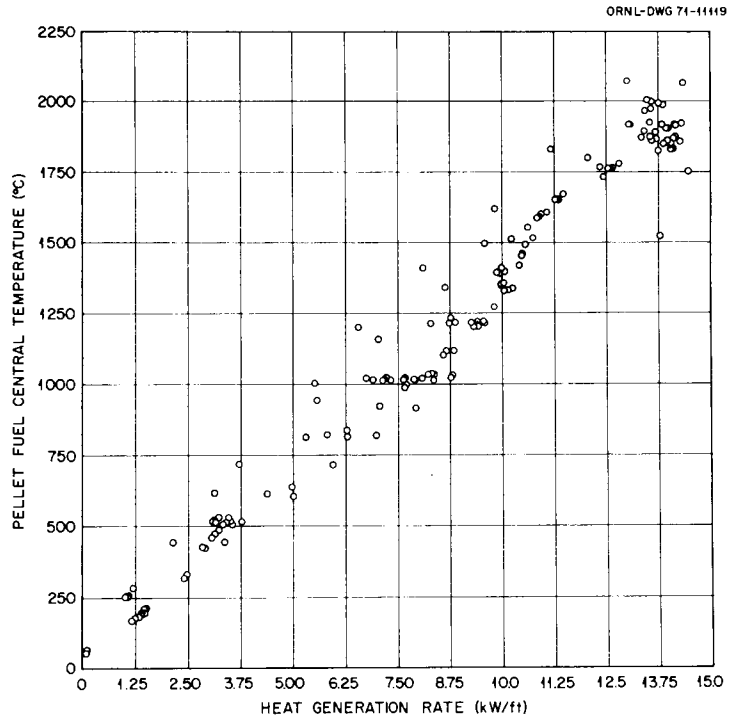

Fig. 1.10. Measured Pellet Fuel Central Temperature and Heat Generation Rates from Capsule SG-3. All data included.

major laboratory working on fuel irradiations. At present there seems no reason to spend any major effort looking for alternative explanations.

If our major assumption is granted, definition of the oxygen potential, μ_{O_2}, which is customarily given by

$$\mu_{O_2} = RT \ln P_{O_2} \tag{1.1}$$

is the most important single parameter to define at the fuel-clad interface or, perhaps more exactly, at the clad interior surface. If μ_{O_2} could be so defined, one could then investigate various mechanisms of attack in irradiated fuel elements.

A bulk diffusion mechanism exhibits its dependency on μ_{O_2} by a parabolic rate with time. This rate will be exponential with temperature, and the activation energy will be indicative of the mechanism. A grain boundary attack will exhibit behavior which obeys a different rate law. The activation energy will be lower. Here a difficulty arises in defining rate; maximum penetration might be a suitable one. The penetration then

might depend on a surface-limited reaction, if one can conceive of the end of a grain boundary acting as a surface. Or, a diffusion down a capillary tube, with possible depletion along the sides, may be the mechanism. Other mechanisms which may be imagined are liquid or gaseous diffusion transport, either of oxygen or an oxygen limiting material such as a chromate, ferrate, or the like.

The reason grain boundary attack occurs at all may be that the boundaries are sensitized by some other mechanism. That is, a "normal" piece of cladding may not undergo grain boundary attack, while a sensitized piece will. Mechanisms of sensitization might be temperature alone, fuel-cladding mechanical interaction, another chemical reaction, or something else altogether. Something as simple as internal scratching of the clad during loading may be responsible. In many, if not most, of the irradiation experiments the oxidation of the cladding is kinetically hindered. That is, it seems most likely in reviewing what is now known of the change in μ_{O_2} of fuel with burnup that oxygen attack of the clad, by whatever mechanism, <u>can</u> occur on thermodynamic grounds. This is not the only possibility. If the cladding either served as a sink for the oxygen or allowed diffusion through it at such a rate that the sodium coolant removed the oxygen at a sufficiently low potential, reaction might not occur on thermodynamic grounds. This last possibility seems unlikely.

Translating the above statements into experimental quantities which must be known or sought to elucidate reaction mechanisms, we have the following: First, one must know the oxygen potential "seen" by the clad. This number must be either measured or calculated from available thermodynamic data. However, there are so many possibilities of experimental variability in an irradiation experiment that direct measurement is much to be preferred. Such a measurement is possible.

Consider the reaction

$$Mo(s) + O_2(g) = MoO_2 \qquad (1.2)$$

for which the thermodynamic data are known. Molybdenum is a fission product which is seen in metallic inclusions in irradiated oxide fuel. Since the equilibrium constant, K, is given by

$$K = \frac{a_{MoO_2}}{a_{Mo} a_{O_2}} \quad , \tag{1.3}$$

the oxygen potential, μ_{O_2}, could be obtained by

$$\mu_{O_2} = RT \ln P_{O_2} = RT \ln a_{MoO_2} - RT \ln a_{Mo} - RT \ln K \quad . \tag{1.4}$$

Henry's law yields

$$a_{MoO_2} = k\ [MoO_2] \tag{1.5}$$

in which the bracketed quantity represents the concentration of MoO_2 in the oxide phase and k is the Henry law constant. A similar equation applies for the concentration of Mo, [Mo], in the fission product inclusion. Experimentally, [Mo] in the inclusions is nearly constant in a given fuel pin and varies only by a factor of 3 to 5 between various reported examinations. For our immediate purposes we can assume it is constant. Then

$$\mu_{O_2} = RT \ln [MoO_2] + \text{constant} \tag{1.6}$$

at any given temperature. One has only to relate $[MoO_2]$ at any given point to the rate of attack to have a relative measure of μ_{O_2}. Moreover, an absolute number is possible if one has the auxiliary thermodynamic data. Either the relative or absolute measurement is possible by measuring $[MoO_2]$ at various positions across the fuel pin.

The second important quantity is the temperature of the fuel and clad. The temperature of the inner cladding surface is the most important, for the rate of attack will be exponentially dependent on

this temperature while μ_{O_2} depends only on the first power of the temperature, as shown in Eq. (1.6).

Third, one must measure directly some kind of a reaction rate. For a uniform attack the easiest thing to measure is the depth of the reaction layer. For grain boundary attack the depth of penetration will be significant, as well as the attack inward at right angles to the boundary. For transport of clad into the fuel, a mass of transport must be obtained.

Fourth, information on the cladding itself must be obtained. The history of the clad may be important in stress corrosion, for example. Its composition may bear importantly on the mechanism and, in particular, possible inhomogeneities of structure brought about by fabrication.

A summarization of the approaches detailed above is now in order. We will attempt to correlate the available experimental irradiation results by considering both the chemical and kinetic behavior of the fuel-clad-coolant system. These two major areas are interrelated because the chemical behavior establishes the thermodynamic probability of and chemical gradients for fuel-clad interactions, and kinetic data based on observed failure rates often permit a deduction of the particular failure mechanism. Once the mechanism and chemistry are understood one may propose solutions for the minimization of the deleterious reactions.

Fuel-Cladding Chemical Interactions (J. M. Leitnaker)

We have begun a study of fuel-cladding chemical interactions in oxide fuel pins. The purpose of the study is twofold: (1) to describe the chemical interactions already observed in oxide pin irradiations in as quantitative a fashion as possible, and (2) to indicate the additional data necessary to permit reliable predictions of safe operating conditions and life for oxide fuel pins.

Such a study divides naturally into two areas: (1) failed, and (2) unfailed fuel pins. The failed pins are perhaps the most interesting for two reasons: (1) more complete examinations were performed, in general, on pins that failed; and hence, better descriptions of conditions are available, and (2) the failed pins represent a limiting condition for safe operation.

Our first analysis has been on General Electric pins B3B and B3C, as described in GEAP-13620 (June 1970). The remainder of this report deals with our analysis of these pins.

Our most significant conclusion is that the reaction data from pin B3C follow a simple rate law. If one measures the fraction of the cladding which has been attacked in GE Fig. 6-9 with a ruler and plots the log of this number versus 1/T (°K), a straight line is obtained. This plot is shown in our Fig. 1.11. The significance of this is made clear if one considers that a common rate equation is

$$\text{rate} = A\, e^{\frac{-E}{RT}} \tag{1.7}$$

or, taking the logarithm of both sides,

$$\ln\,(\text{rate}) = k - \frac{E}{R}\left(\frac{1}{T}\right) , \tag{1.8}$$

where k is ln (A), E is an "activation energy," R is the gas constant, and T is the temperature in °K.

The linear relationship shown indicates the overall reaction shown on the cladding in B3C is likely controlled by a single mechanism. Also indicated is a means whereby reasonable extrapolations to lower temperatures can be made. (We hasten to add that one not infrequently sees different controlling mechanisms at different temperatures. Extrapolation is only a first approximation.)

For comparison of these data with other pins, one must recognize that the oxygen potential, μ_{O_2} (= RT ln Po_2) is not known with certainty at the start or end of life. (We will return to this point subsequently.) Further, the attack plotted represents an integrated time rate. Thus, dividing by time would not necessarily yield a meaningful rate. Still, a useful approximation is obtained; with enough of these, firmer conclusions can be drawn. It is unfortunate that like data are not available for pin B3B.

Our second conclusion involves the mechanism of failure. In pin B3B, sodium-fuel reaction product was found in the failed region, while

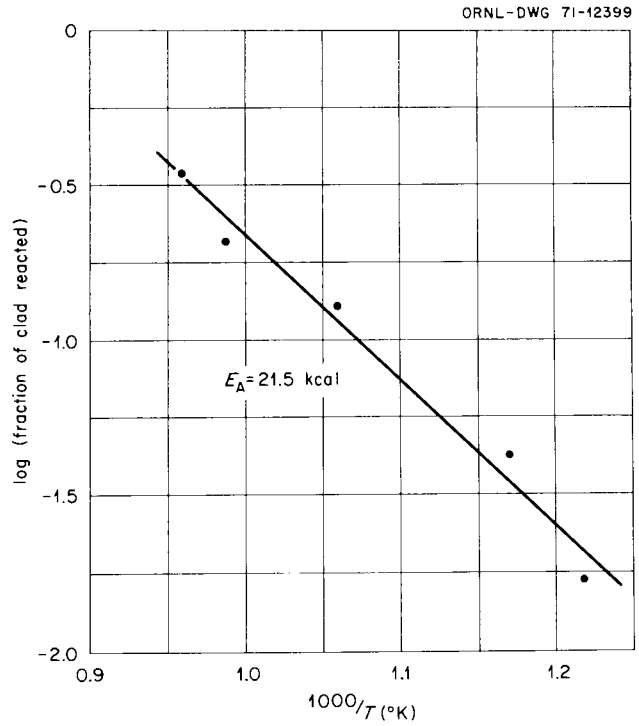

Fig. 1.11. Attack on Clad in B3C Pin (GEAP-13620).

this product was seen only outside the failed region in B3C area and substantial quantities of fuel were missing from the failed area. Further, metallic ingots and localized clad corrosion are seen to occur opposite radial cracks in the fuel. These observations provide a reasonable hypothesis for pin failure as follows: Once a fuel pellet cracks, the cladding is exposed to a hotter temperature near or at that point. As shown in our Fig. 1.11, corrosion rate is increased exponentially with temperature. With the increased corrosion rate the clad is weakened and a crack occurs. NaK diffuses into the pin, reacts with the fuel, and causes swelling and further cracking of the cladding. As diffusion of NaK continues in, at an increased rate now because of enlargement of the cracks, the fuel-NaK reaction product undergoes melting in contact with the excess NaK and diffuses out into the coolant chamber. Thus, we explain the difference between pins B3B and B3C in regard to the reaction product in B3B and the missing fuel in B3C. The postulate that melting of the fuel-NaK compound occurs may imply that at the extant oxygen potential the corrosion product is in equilibrium

with a liquid phase, rather than a second fuel-NaK compound. Phase diagram information would elucidate this point.

That the NaK is seen to react with the fuel allows some limits to be placed on both the oxygen potential and amount available for reaction in the pin. (Unfortunately, data on the NaK itself are not given. Hence, one cannot deduce where the oxygen came from.) Since a reaction did occur, the free energy, ΔG_T, for the reaction

$$\text{fuel} + \text{NaK} + O_2 = \text{compound} \tag{1.9}$$

must be negative. As a first approximation one should consider the more specific reaction

$$Na(\ell) + UO_2(s) + O_2(g) = NaUO_3(s), \tag{1.10}$$

for which data have been recently obtained through Ward Hubbard at Argonne National Laboratory. From the standard free energy we compute the equilibrium oxygen potential would be −146.5 kcal at 1000°K. Thus, this represents the lowest value possible for the oxygen potential and puts a first limit on our rate shown in Fig. 1.11. Since, however, an extensive reaction took place, we deduce μ_{O_2} was considerably higher than this. Although the photomicrographs shown in the GE report are not detailed enough, one could (from the original B3B pin) make a reasonable estimate as to the mass of reaction products. Also, if the oxygen content of the NaK were known, one could estimate the amount of oxygen which had come from the fuel. This information would permit a second estimate of the oxygen potential.

The failure mechanism postulated here leads to an interesting conclusion regarding sol-gel oxide microsphere fuels: These fuels should exhibit less attack at the same temperature or the same life service at a higher temperature (higher heat rating) compared to pellet fuels. Although the sol-gel microsphere fuel restructures in the center of the pin in a fashion similar to pelletized fuel, the fuel nearest the clad remains unrestructured. Hence, when the interior of the fuel cracks, the microspheres still maintain a protective barrier. We show in Fig. 1.12

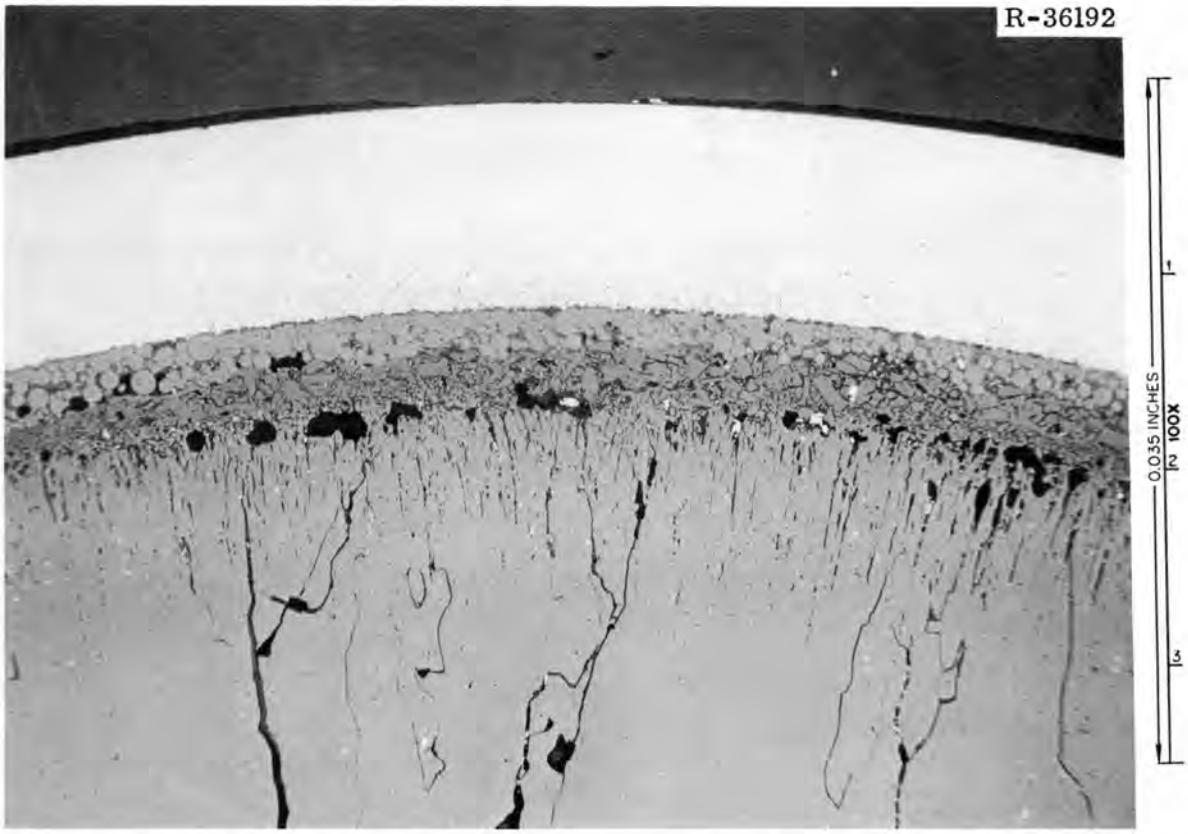

Fig. 1.12. Sphere-Pac $(U,Pu)O_2$ Irradiated in ETR to 2.8% FIMA at 50 kW/ft; Type 304 Stainless Steel Cladding at 1000°C. As-polished.

an example of such protection. If fuel cracks indeed initiate the localized corrosion as we have postulated, sol-gel fuel represents a significant advance in fuel technology for a previously unsuspected reason. Lower levels of attack on cladding by sol-gel microspheres compared to pelletized fuel have been observed at ORNL.[20]

Grain Growth of $(U,Pu)O_2$ (W. J. Lackey and R. A. Bradley)

Because of the influence that grain size and migration of grain boundaries is expected to have on release of fission gas, fuel swelling, and Nabarro-Herring creep of $(U,Pu)O_2$, we investigated the kinetics of in-reactor grain growth. The results, including kinetic equations, have

[20] R. B. Fitts, A. R. Olsen, C. M. Cox, and E. L. Long, Jr., Metals and Ceramics Div. Ann. Progr. Rept. June 30, 1971, ORNL-4770, p. 51.

been reported.[21,22] Briefly, the results showed in-reactor grain growth to be less temperature dependent than expected based on out-of-reactor grain growth of UO_2 and ThO_2. To determine if the lower temperature dependence was typical of the mixed oxide or was an irradiation effect, out-of-reactor grain growth kinetics of $(U,Pu)O_2$ have been investigated. The out-of-reactor data will also be of value in estimating the thermal treatment necessary to fabricate fuel of a specified grain size should it be required.

The out-of-reactor grain growth study was conducted using sol-gel $(U_{0.85},Pu_{0.15})O_{2.00}$ microspheres which were made by the same process used to make the fuel examined in the in-reactor study but from a different batch. The samples were heated isothermally in Ar—4% H_2 at 1200, 1356, and 1550°C for times up to 164 hr. The grain size is plotted as a function of annealing time in Fig. 1.13. Also shown in Fig. 1.13 for comparison are curves for 1356 and 1550°C which were calculated based on the in-reactor grain growth results. At 1356°C the in-reactor and out-of-reactor results are similar; at this temperature irradiation may have increased the rate of grain growth. At 1550°C comparison of the in-reactor and out-of-reactor results strongly indicated that grain growth was retarded by irradiation. This supports previous evidence[21] that above about 1300°C in-reactor grain growth was not as rapid as expected based on extrapolation of low-temperature data, perhaps as a result of the presence of fission gas bubbles or solid fission product inclusion at the higher temperatures.

Least squares analysis of the out-of-reactor data yielded the following equation:

$$D^2 - D_o^2 = 2.52 \times 10^{21}\ t \exp(-173{,}000/RT) \qquad (1.11)$$

---

[21] W. J. Lackey, Fuels and Materials Development Program Quart. Progr. Rept. September 30, 1970, ORNL-4630, pp. 47—54.

[22] W. J. Lackey, Fuels and Materials Development Program Quart. Progr. Rept. March 31, 1971, ORNL-TM-3416, pp. 33—38.

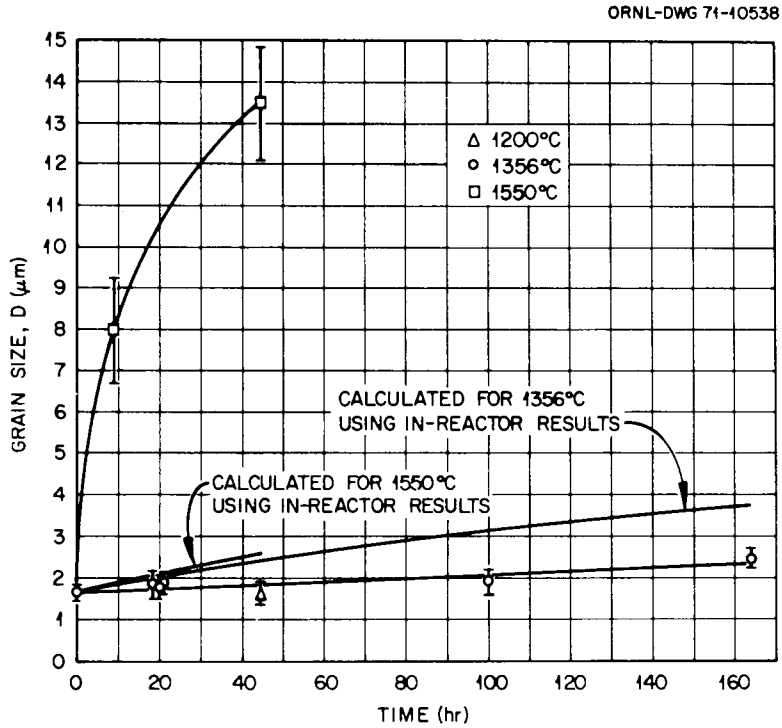

Fig. 1.13. Grain Size Versus Time for $(U_{0.85},Pu_{0.15})O_2$ Isothermally Annealed Out-of-Reactor.

where

D = final grain size, μm,

D_o = initial grain size, μm, and

t = time, hr.

The value for the activation energy (173 ± 25 kcal/mole at the 90% confidence level) is comparable to values observed out-of-reactor for UO_2 and ThO_2, but is considerably larger than the values of 29.2 and 5.96 observed for $(U,Pu)O_2$ in-reactor grain growth.[21] This demonstrates that data obtained from isothermal out-of-reactor tests cannot be used to predict in-reactor grain growth of $(U,Pu)O_2$.

Actinide Redistribution in Irradiated $(U,Pu)O_2$ (W. J. Lackey and F. J. Homan)

Our interest in actinide redistribution is that it is likely to significantly influence the thermal and compatibility behavior of LMFBR and GCBR fuel pins. We are also interested in oxygen redistribution

since it will influence fuel pin performance and also because actinide and oxygen movement are interrelated processes. Accordingly, we have developed a kinetic model[23] which predicts this redistribution.

The model is based on transport of fuel material down the temperature gradient by the evaporation-condensation mechanism. By knowing the initial plutonium-to-uranium ratio of a radial fuel increment and by calculating the quantity and plutonium-to-uranium ratio of the material transported into and out of the increment for a small time period, the resulting plutonium-to-uranium ratio of the fuel increment can be calculated. By performing such a calculation for each of 30 radial increments for each of a series of time periods, the plutonium-to-uranium radial profile is calculated as a function of time.

To date we have calculated the plutonium-to-uranium profile for only one fuel pin. A comparison of the predicted and experimentally measured profile is given in Fig. 1.14. Over the range for which experimental measurements are available the agreement is good. Although experimental data are not available for comparison over the remainder of the cross section, the shape of the predicted profile is reasonable and qualitatively very similar to those observed by other investigators.[24] Comparisons of measured and predicted plutonium-to-uranium profiles for fuel pins having different fabrication and irradiation conditions are necessary to determine the validity of the model, but these initial calculations are encouraging.

Sensitivity Analysis of LMFBR Fuel Pin Performance (F. J. Homan)

The sensitivity of predicted LMFBR fuel pin performance to uncertainty in fuel and cladding properties is being determined with the FMØDEL code. During this report period thermal expansion data for both fuel and cladding were analyzed and also thermal conductivity

---

[23] W. J. Lackey and F. J. Homan, LMFBR Fuel Cycle Studies Progr. Rept. June 1971, No. 28, ORNL-TM-3487, pp. 48–50.

[24] R. O. Meyer, D. R. O'Boyle, and R. Natesh, Trans. Am. Nucl. Soc. 14(1), 182–183 (1971).

ORNL-DWG 71-7964R1

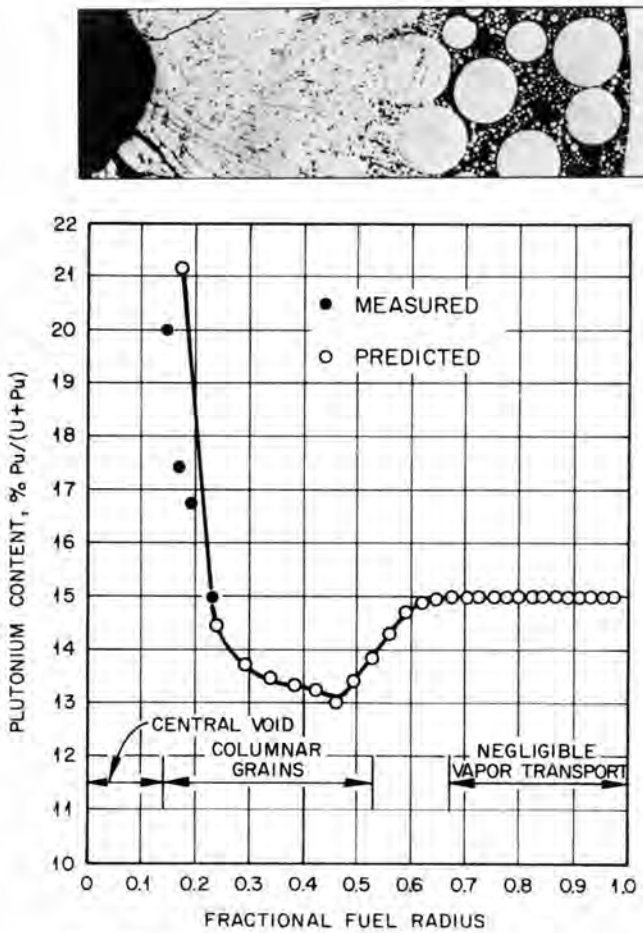

Fig. 1.14. Comparison of Measured and Predicted Radial Plutonium Distribution in $(U_{0.85},Pu_{0.15})O_{2.00}$ after Irradiation at 13.6 kW/ft to 0.7% FIMA.

data for $(U,Pu)O_2$ fuel material. The effects of uncertainty in these data upon the predicted performance of a typical LMFBR fuel pin were determined.

Fuel Thermal Expansion. - Examination of the available data for thermal expansion of mixed oxide fuel material leaves one somewhat confused. NUMEC investigators have shown that the coefficient of thermal expansion for mixed oxide systems generally increases with increasing plutonium content, and decreases with increasing oxygen-to-metal ratio. Polynominal expansions for the coefficient of thermal expansion for

several compositions studied by Roth and Halteman[25] are plotted in Fig. 1.15. Also plotted are the expression for thermal expansion currently used in the FMØDEL code, based on data for UO_2, and the expression used in the LIFE code.[26] Examination of these plots reveals that the thermal expansion is greater for the 5% Pu compound than for the 12.5% Pu compound (curves 5 and 6 of Fig. 1.15). Both compounds have about the same oxygen-to-metal ratio. This contradicts the observation of increasing thermal expansion with increasing plutonium content for mixed oxides. Two UO_2 samples were measured by Roth and Halteman with slightly different oxygen-to-metal ratios. Their thermal expansion characteristics were similar (see curves 3 and 4 of Fig. 1.15). However, two PuO_2 samples were measured, one prepared by oxalate precipitation and one prepared by hydroxide precipitation, and their thermal expansion characteristics were vastly different (see curves 8 and 9 of Fig. 1.15).

Since the oxygen-to-metal ratios of the samples studied by Roth and Halteman are so different, little can be concluded from the expansions given in Fig. 1.15. However, subsequent work by Roth et al.[27] suggests the following equation to describe the change in thermal expansion coefficient of $(U_{0.8},Pu_{0.2})O_2$ over the temperature range 0 to 1500°C.

$$\alpha = (125.9 - 57.3y) \times 10^{-6}\ °C^{-1} \tag{1.12}$$

where y is the oxygen-to-metal ratio. The suggested range of applicability of this equation is from oxygen-to-metal ratios from 1.930 to 2.020. According to Eq. (1.12) the expansion coefficient for stoichiometric $(U_{0.80},Pu_{0.20})O_2$ is about $11.3 \times 10^{-6}\ °C^{-1}$ and is decreasing with increasing oxygen-to-metal ratio. However, the expression shown in Fig. 1.15 for

---

[25] J. Roth and E. K. Halteman, Thermal Expansion of Coprecipitated $(U,Pu)O_2$ Powders by X-Ray Diffraction Techniques, NUMEC-2389-9 (October 1965).

[26] V. Z. Jankus and R. W. Weeks, LIFE-I, A FØRTRAN IV Computer Code for the Prediction of Fast-Reactor Fuel-Element Behavior, ANL-7736 (November 1970).

[27] J. Roth et al., Trans. Am. Nucl. Soc. 10(2), 457 (1967).

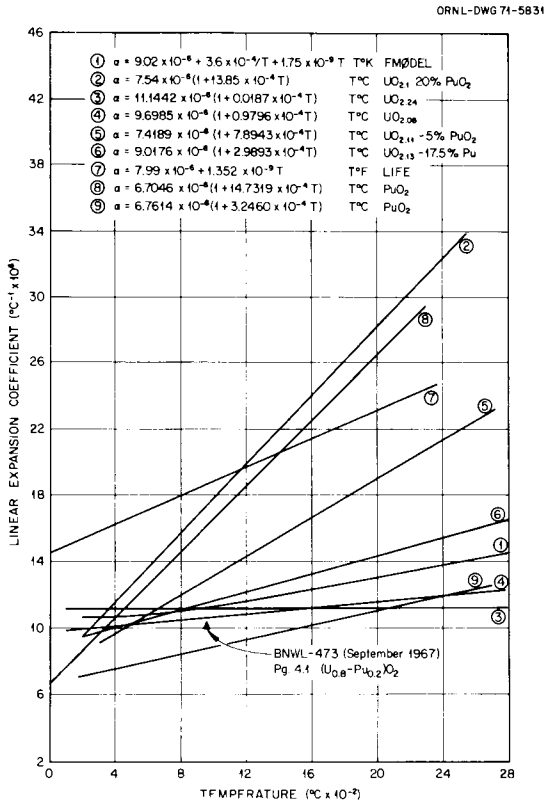

Fig. 1.15. Thermal Expansion Coefficient Versus Temperature for Mixed Oxide Fuels.

$(U_{0.80},Pu_{0.20})O_2$ with an oxygen-to-metal ratio of 2.1 is about 23×10^{-6} °C^{-1}. These two results are clearly contradictory.

The correct expression for thermal expansion coefficient versus temperature is not obvious from the data presented so far. However, using an equation of the form

$$\alpha = [8 + (B)(0.00107)\ T] \times 10^{-6}\ °C^{-1} \tag{1.13}$$

and varying B between 1.0 and 10.0 produces an envelope which includes most of the curves plotted in Fig. 1.15.

Cladding Thermal Expansion. - There is some variation in the reported thermal expansion data for type 316 stainless steel. Plots of thermal

expansion coefficient versus temperature from four different sources[28-31] are shown in Fig. 1.16. As was done with the fuel thermal expansion data, an envelope is formulated to include the curves plotted in Fig. 1.16. The equations for the top and bottom boundaries of the envelope are given in Fig. 1.16.

To test the sensitivity of predicted fuel pin performance to the uncertainty demonstrated for fuel and cladding thermal expansion properties, the FMØDEL code was run with assumed thermal expansion properties for fuel and cladding represented by the upper and lower boundaries of the envelopes shown in Figs. 1.15 and 1.16. When studying the effect of uncertainty in the fuel thermal expansion data, cladding thermal expansion values from the middle of the envelope shown in Fig. 1.16 were used. Fuel thermal expansion values from the middle of the envelope shown in Fig. 1.15 were used when the effect of the uncertainty in cladding thermal expansion data was being examined. The characteristics of the fuel pin assumed for the analysis are given in Ref. 32. The pin described there is 0.25 in. in diameter, contains 95% theoretically dense pellets, and has a small fuel-cladding gap. The assumed operating history includes a rise to normal power (16 kW/ft peak) over 10 hr, 100 hr of steady-state operation at normal power, a 10% overpower over a 1-hr period followed by 100 hr of operation in the overpower condition, and then a rapid return to normal power and steady-state operation thereafter.

---

[28] T. Lyman et al., eds., Metals Handbook, Vol. 1, Properties and Selection of Metals, 8th ed., p. 423, American Society for Metals, Novelty, Ohio (1961).

[29] Working Data, Carpenter Stainless and Heat Resisting Steels, Selection, Description, Fabrication, The Carpenter Steel Company, Reading, Pennsylvania (1962).

[30] I. B. Fieldhouse, J. C. Hedge, and J. I. Lang, Measurements of Thermal Properties, WADC-TR-58-274, Wright Air Development Center (1958).

[31] B. J. Seddon, Steels Data Manual, TRG Report-840, UKAEA Reactor Group (1965).

[32] F. J. Homan, LMFBR Fuel Cycle Studies Progr. Rept. April 1971, No. 26, ORNL-TM-3412, p. 73.

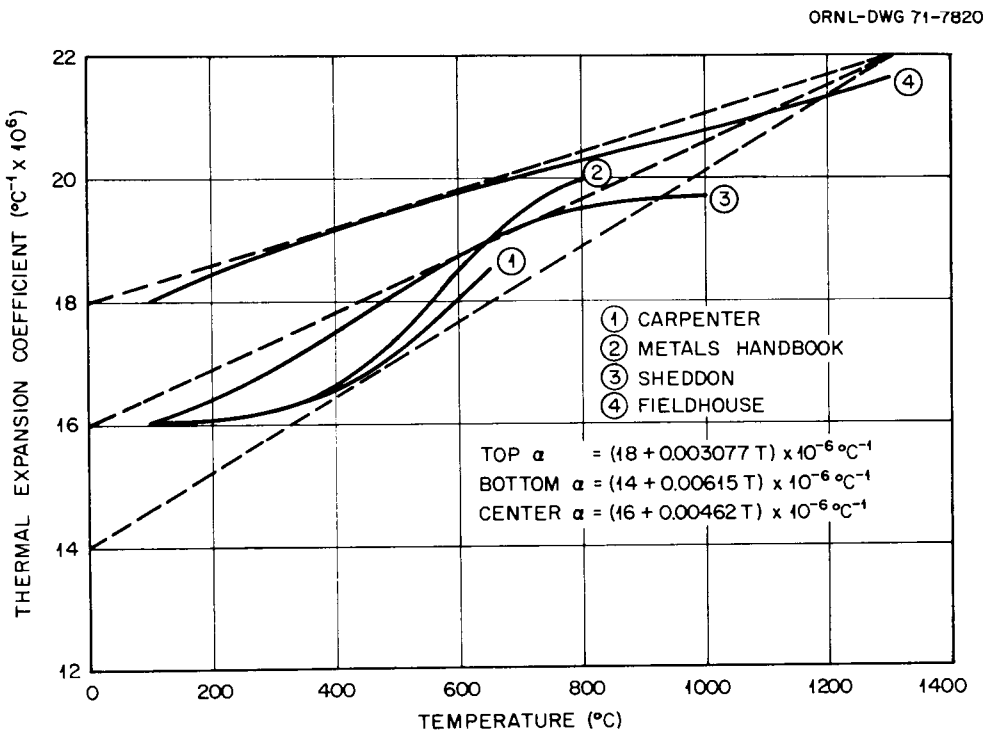

Fig. 1.16. Thermal Expansion Coefficient Versus Temperature for Type 316 Stainless Steel.

A comparison of the uncertainty envelopes for fuel and cladding thermal expansion data is shown in Fig. 1.17. Also shown is the predicted fuel-cladding mechanical interaction as a function of time using thermal expansion data from the top and bottom of each envelope. Comparing the shapes of the two sets of curves from the bottom of Fig. 1.17 it is easily seen that predicted performance of this pin is quite sensitive to uncertainty in the fuel thermal expansion data, but not sensitive to the uncertainty in the cladding data. The greatest sensitivity in the contact pressure versus time curve at the lower left of Fig. 1.17 occurs during the 10-hr initial startup. Figure 1.18 shows the predicted fuel-cladding contact pressure and plastic tangential strain at the cladding outer surface during this period. Several values for the slope [B in Eq. (1.13)] were considered. The indicated sensitivity of cladding plastic strain to the thermal expansion values assumed for the fuel demonstrates the need for additional characterization of this important physical property.

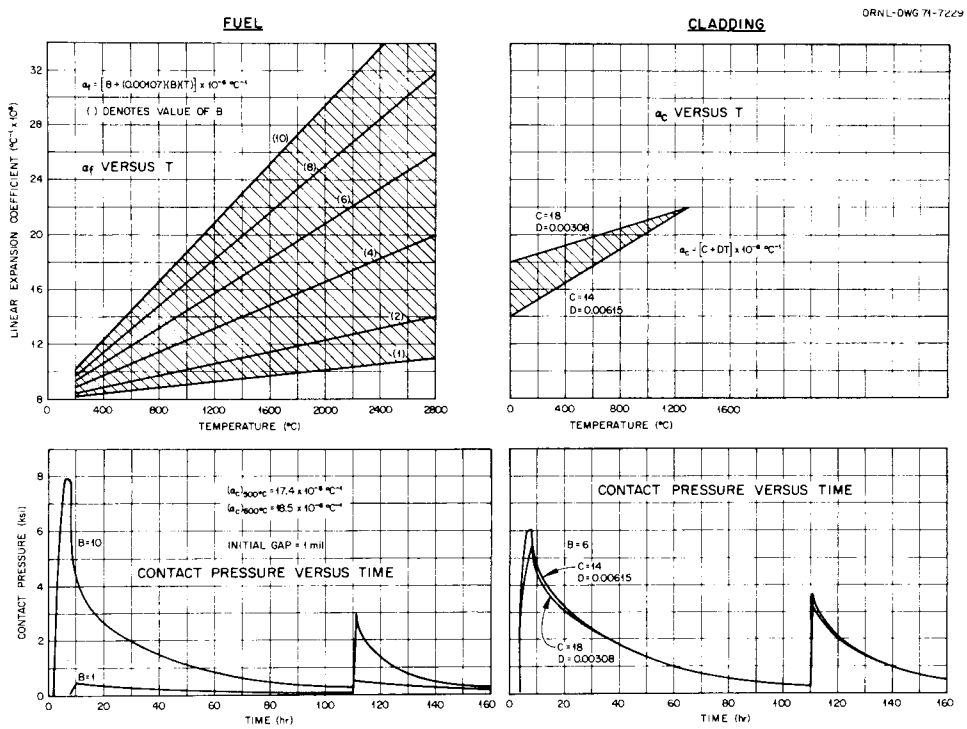

Fig. 1.17. Influence of Uncertainty in Fuel and Cladding Thermal Expansion Characteristics on Mechanical Interaction.

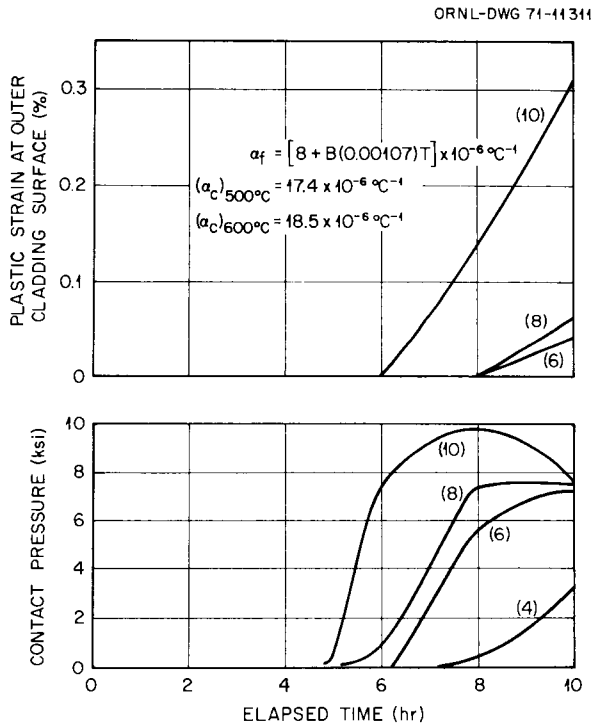

Fig. 1.18. Influence of Fuel Thermal Expansion on Fuel Pin Performance During Startup.

Fuel Thermal Conductivity. - Thermal conductivity of mixed oxide fuels is influenced by stoichiometry, density, temperature, burnup, plutonium content, and the shape and distribution of fabricated porosity. An excellent review of thermal conductivity data and other properties of mixed oxide fuels was recently compiled by Rubin.[33] Rubin shows a plot in his compilation of thermal conductivity measurements for $(U_{0.80},Pu_{0.20})O_x$ 95% of theoretical density, with values of x being 2.00, 1.982, and 1.93. If maximum scatter in the data is considered, the thermal conductivity has decreased 25% in going from stoichiometric to an oxygen-to-metal ratio of 1.93. If the curves fitting the data are considered, the drop is only 13%. Rubin's studies show that thermal conductivity decreases with any variation from the stoichiometric composition at temperatures below 1500°C because both oxygen vacancies and excess oxygen atoms cause scattering, increasing the number of phonon-phonon interactions. At higher temperatures (above 1700°C) the data for all three stoichiometries appear to merge. This is because the total number of thermal vacancies at high temperatures is so great that it swamps the difference in the number of vacancies that exist in the compounds of different stoichiometries at lower temperatures.

The effect of density and temperature on thermal conductivity of mixed oxide fuels is fairly well established based on the data of numerous General Electric investigators.[34] The GE equation for thermal conductivity as a function of temperature and porosity is given below.

$$K(T,P) = A + \frac{1}{T(B - CD)} \tag{1.14}$$

---

[33]B. F. Rubin, Summary of $(U,Pu)O_2$ Properties and Fabrication Methods, GEAP-13582 (November 1970).

[34]Baily et al., "Thermal Conductivity of Uranium-Plutonium Oxide Fuels," Intern. Symp. Plutonium Fuels Technology, Scottsdale, Arizona, Nucl. Met. 13, 293 (1967), (K. E. Horton, K. E. Macherey, and R. J. Allio, eds.) American Institute of Metallurgical Engineers, New York, 1968.

where

T = temperature, °C,

P = fractional porosity,

$D = 1. - P$, and

A, B, C = empirical constants.

Equation (1.14) is used in the FMØDEL code for $(U_{0.80},Pu_{0.20})O_{2.00}$ with values for the empirical constants 0.011, 0.4848, and 0.4465 for A, B, and C respectively. For stoichiometric UO_2 the value for A is 0.013. From the form of Eq. (1.14) it is clear that thermal conductivity decreases with increasing temperature and porosity.

Rubin references a series of GE experiments[35] in which the fuel center temperature changes with burnup were measured. The conclusion from these experiments was that the thermal conductivity of mixed oxide fuels decreases with burnup. However, the fact that the measured fuel centerline temperatures increased with burnup at constant heat rate may have been due to a decrease in the gap conductance in addition to or instead of a decrease in the fuel thermal conductivity. The GE investigators assumed that the gap conductance was independent of burnup which, as Cox has pointed out,[36] is not consistent with the gap conductance model incorporated in the FMØDEL code. It must be concluded that the effect of burnup on thermal conductivity is not adequately characterized at this time.

The influence of plutonium content on thermal conductivity is not well established at present either. Rubin's compilation points out that in some ceramic systems small additions of a second component may cause a rapid decrease in thermal conductivity (probably due to lattice strain and a reduction in the phonon mean free path). However there is experimental evidence, cited by Rubin, that $(U_{0.85},Pu_{0.15})O_2$ exhibits higher

[35] R. R. Asamoto et al., Center Temperature Measurements of Mixed Oxide Fuel Zero to 3,000 MWd/Te, GEAP-13603 (November 1970).

[36] C. M. Cox, LMFBR Fuel Cycle Studies Progr. Rept. August 1971, No. 30, ORNL-TM-3571, pp. 38–39.

thermal conductivity than UO_2 over some temperature ranges while samples of mixed oxide with plutonium contents between 3.6 and 5.5% Pu exhibited thermal conductivities below UO_2 at some temperatures and above UO_2 at other temperatures. Therefore it must be concluded that the effect of composition on thermal conductivity of mixed oxide systems needs additional characterization as well.

Perhaps the greatest influence on thermal conductivity is exhibited by the shape and distribution of porosity. Data published by Gibby and Weber[37] relating to the thermal conductivities of two batches of material with essentially the same porosity but different microstructures show the importance of pore shape and distribution. Sample 1 (using the same notation as Gibby and Weber) with a bulk density of 89% had porosity concentrated in randomly dispersed large and small spherical pores, with no localized inhomogeneities. Sample 2 with a density of 91.3% of theoretical had a microstructure containing dense arrays of fine microcracks. The grains were smaller than the grains in sample 1 and localized composition inhomogeneities were present. The two batches of fuel were adjusted to stoichiometric composition and the thermal conductivities measured by Gibby and Weber. Their results are shown in Fig. 1.19. Notice that the measured thermal conductivities of batch 2 are substantially lower than those measured for batch 1, even though batch 2 was slightly more dense.

Superimposed on the batch 1 data plotted in Fig. 1.19 are the thermal conductivities predicted using Eq. (1.14) for both 89 and 91.3% of theoretically dense material. Both of these curves fall within the scatter of data taken for batch 1. It is difficult to fit thermal conductivity data generated at a single porosity to an equation of the form of Eq. (1.14) where both temperature and porosity are variables. However, a regression analysis was performed on Gibby and Weber's data in conjunction with the ORNL analysis of the PNL-19 test.[38] In an effort to adequately treat the

[37] R. L. Gibby and E. T. Weber, WADCO Quart. Technical Rept., Vol. IV, October-November-December 1970, HEDL-TME-71-29 UC-25, Metals Ceramics and Materials, pp. 7-20 through 7-24.

[38] F. J. Homan, LMFBR Fuel Cycle Studies Progr. Rept. June 1971, No. 28, ORNL-TM-3487, pp. 42–48.

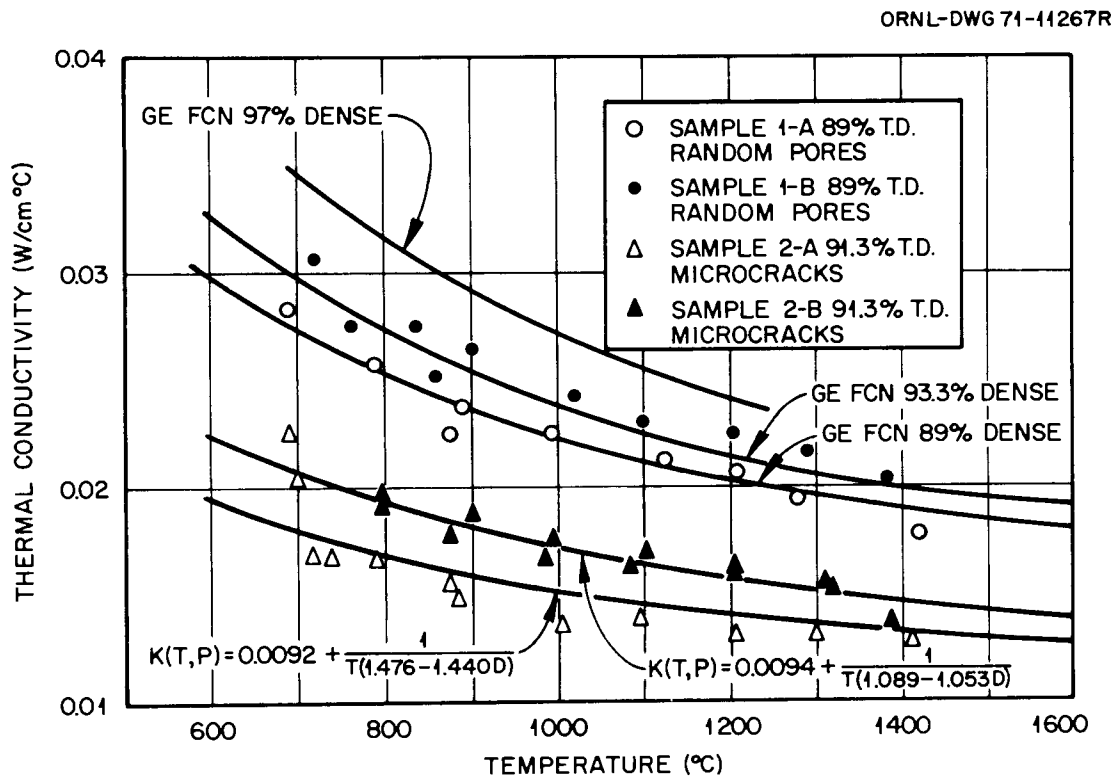

Fig. 1.19. Effects of Pore Morphology on Thermal Conductivity of UO_2–25% PuO_2 Pellets Sintered to ∿90% T.D.

porosity dependence it was assumed that the thermal conductivity of batch 2 material would approach the values predicted by Eq. (1.14) as the density of the material approached theoretical. Some "dummy" data points calculated from Eq. (1.14) for 100% dense material were included in the regression treatment. The equations generated are superimposed on the batch 2 data plotted in Fig. 1.19. The fit appears to be quite reasonable.

The large influence of the microstructure on the thermal conductivity measurements is shown by careful examination of Fig. 1.19. If the top of the scatterband for the batch 1 material thermal conductivity measurements is compared with the bottom of the scatterband for the batch 2 measurements, it can be shown that the microstructure of batch 2 has resulted in a 62.7% decrease in measured thermal conductivity at 1000°C. Similarly, if the plot thermal conductivity against temperature as calculated from Eq. (1.14) at 91.3% of theoretical density is compared with the two curves through the batch 2 data, the drop in thermal conductivity is 39.6 and 54.2% respectively. This shows the microstructure effect to far outweigh

the stoichiometry effect described earlier in this section. It is possible, of course, that the microstructure effect, and the stoichiometry effect could be additive, further decreasing the thermal conductivity of mixed oxide fuels.

To determine the influence of the decrease in thermal conductivity caused by microstructure on the predicted performance of an LMFBR fuel pin, an analysis was performed with the FMØDEL code similar to that presented earlier for the thermal expansion characteristics of both fuel and cladding. The results of the analysis for thermal conductivity are shown in Fig. 1.20. The predicted fuel-cladding contact pressure, fuel centerline temperature, and cladding plastic strain are plotted against time during the 10-hr startup of the typical LMFBR fuel pin. Three thermal conductivity functions are used, Eq. (1.14), and the two functions plotted through the batch 2 data in Fig. 1.19. The differences in predicted performance are striking. Fuel melting is predicted using the batch 2 thermal conductivity data, whereas melting was not predicted using the Eq. (1.14) thermal conductivity characteristics. Fuel-cladding contact pressures rose significantly in going from the batch 1 to batch 2 thermal conductivities and the cladding plastic strain increased by a factor of about 5. Fuel and cladding thermal expansion characteristics from the center of the data envelopes shown earlier were used in the analysis.

Uncertainty in the published data for $(U,Pu)O_2$ thermal expansion and thermal conductivity strongly influences the predicted performance of a typical LMFBR fuel pin with high fuel density and small fabricated diametral gap. The logical question at this point concerns the influence on predicted performance of the lowest thermal conductivity properties considered earlier used in conjunction with the highest thermal expansion characteristics. This case has been run with FMØDEL and the results are shown in Fig. 1.21. Shown for comparison are several other cases using thermal conductivity values calculated with Eq. (1.14). Curves 1, 2, and 3 represent curves through the top, center, and bottom respectively of the envelope of fuel thermal expansion data shown in Fig. 1.17. The relative positions of the predicted plastic strain versus time values for these three curves are about as expected. However, when the lower thermal

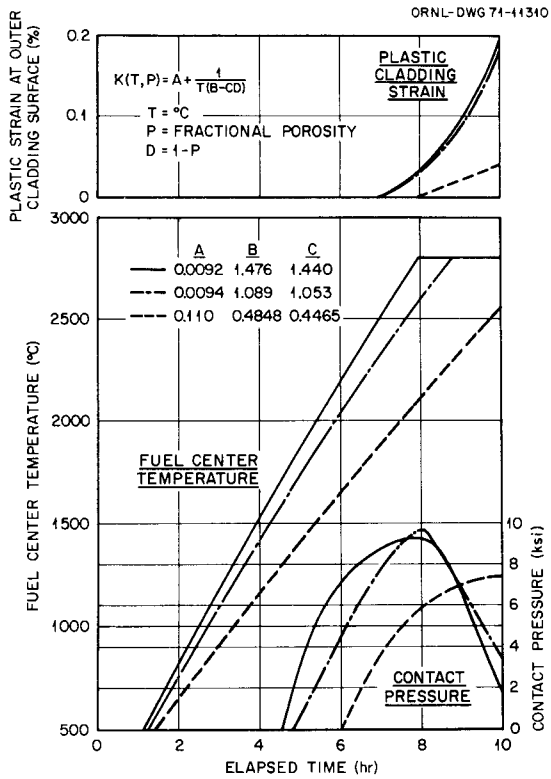

Fig. 1.20. Influence of Fuel Thermal Conductivity on Fuel Pin Performance During Startup.

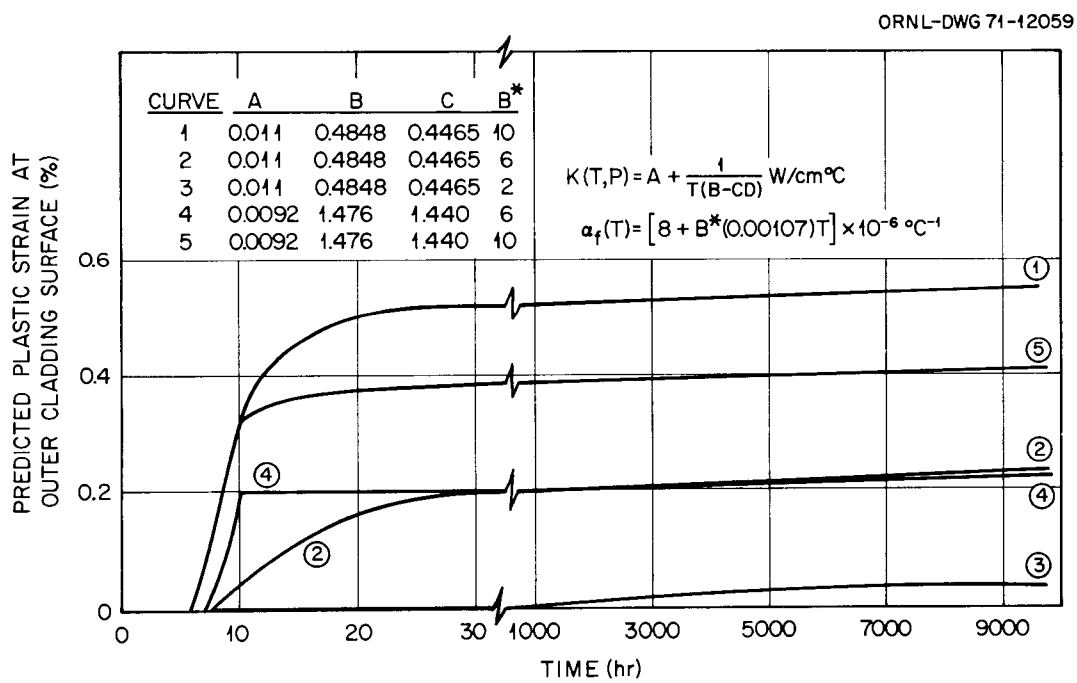

Fig. 1.21. Combined Influence of Fuel Thermal Expansion and Thermal Conductivity on Predicted Cladding Plastic Strain.

conductivity values are used (curves 4 and 5) the strain versus time function changes markedly. Comparing curves 2 and 4, it can be seen that the lower thermal conductivity values cause plastic strain to accumulate more rapidly during startup (because the fuel is hotter and therefore undergoes more thermal expansion) but the total amount of strain over the entire lifetime of the pin is less. This is due to the greater plasticity of the hotter fuel, with accompanying reduced capacity to strain the cladding. The same trend applies in the comparison between curves 1 and 5, although here the increased fuel plasticity (due to higher fuel temperatures brought about by lower themal conductivity at constant heat rate) during startup reduces the strain to the cladding during that portion of the operating history.

The results of this study have shown the usefulness of fuel performance models in analyzing data on materials properties of fuel and cladding. It appears that additional characterization is necessary on some basic physical properties before performance of LMFBR fuel pins can be predicted with confidence.

2. ADVANCED FAST BREEDER REACTOR FUELS DEVELOPMENT

J. L. Scott P. Patriarca

The goals of this program are to investigate the properties and behavior of those uranium- and plutonium-base ceramic fuels that we term conductors such as the mononitrides, carbonitrides, and monocarbides — and to compare their potential as liquid-metal fast breeder reactor (LMFBR) fuel with that of $(U,Pu)O_2$, which by comparison is an insulator. Since the thermal conductivity of the ceramic conductors is about ten times that of $(U,Pu)O_2$, one could theoretically operate a conductor at ten times the power density with the same central temperature. In practice, heat transfer limitations, thermal stresses in the cladding, and high rates of swelling at high temperatures limit the power density to about two or three times of $(U,Pu)O_2$ — still a challenging improvement. Additionally, the margins for transient overpower are much higher in the ceramic conductors than in $(U,Pu)O_2$.

In spite of the potential benefits of advanced LMFBR fuels, the level of effort is being reduced because of the budget crunch. For this reason this program is being phased out at ORNL and the work reported here represents an orderly phase out.

Other work on nitride fuels is reported in Chapter 10.

Irradiation Testing

T. N. Washburn

Thermal Flux Tests

Two noninstrumented capsules of four pins each are now being irradiated in the ETR. These "screening" tests are to determine the performance of high purity (U,Pu)N. The peak linear heat rating is 30 kW/ft and peak burnup will be about 5% FIMA. The fuel is cold-pressed pellets with densities from 86 to 91% of theoretical, and the fuel pins have a 0.010-in. radial gap between the fuel pellet and cladding, filled with NaK-19 to enhance heat transfer.

Capsules 43-N1 and 43-N2 were neutron radiographed at TREAT before insertion into the ETR. The reactor went to full power on December 9, 1970; as of September 1, 1971, the capsules have operated for 156 effective full-power days to a burnup of approximately 3.5% FIMA.

Fast Flux Tests (E. J. Manthos)

Fabrication of nine fuel pins and an archive pin containing (U,Pu)N, and two dummy sodium bond pins loaded with depleted UN pellets was completed. In addition two xenon tag dummies and two weld specimens required by EBR-II were fabricated.

The sodium was melted and bonded to the pellets ultrasonically in the nine fuel pins and two dummy depleted UN pins. A procedure developed earlier with depleted UN pellets in place of (U,Pu)N pellets was used. Eddy current inspections of the 11 pins (nine fuel and two dummy pins) after the sodium had solidified revealed that the two dummy pins were satisfactorily bonded; the nine fuel pins, however, showed numerous void indications larger than 1/16 in. in diameter. At present we do not know why there is a difference in the sodium bond quality between the two types [UN and (U,Pu)N] of pellets.

There are at least two visible differences between the two pellets. The depleted UN pellets have sharp square corners and square parallel ends because both the OD and ends of the pellets were ground. The (U,Pu)N pellets have rounded corners and ends that are not flat since only the OD of the pellets was ground. A few chips or pellet fragments were visible with x-ray radiography in the (U,Pu)N pins and only a very few or no chips were detected in the depleted UN pellets.

All nine of the fuel pins were cleaned with 600 grit abrasive paper and alcohol to remove the oxide film formed when the pins were heated during bonding. Each pin was then inspected to measure length, diameter, weight, and bow. Seven of the nine pins were shipped to Battelle Columbus Laboratory (BCL) for eddy current inspection at a temperature where the sodium is molten. If the sodium bond is still not satisfactory, BCL staff

will centrifuge each pin at an elevated temperature in an attempt to improve the bond. Depending on the condition of the pins after testing, they will either be returned to ORNL or shipped to EBR-II.

The remaining two fuel pins and the archive pins will be stored at ORNL. The archive pin contains all the remaining pellets plus representative pellets from each pellet batch or run. The two depleted UN sodium bond dummy pins will be disassembled at ORNL and the contained sodium will be analyzed for oxygen. Fabrication at ORNL of the fuel pins and associated dummy pins is complete unless the seven pins at BCL are returned for further cleaning and dimensional inspection.

Synthesis, Fabrication, and Characterization of Advanced FBR Fuels

V. J. Tennery

Our effort during this quarter has been directed toward developing a process that will permit the controlled conversion of all of our Pu-contaminated nitride scrap to oxide preparatory to shipping the material for recovery reprocessing and reducing our inventory to zero. This procedure must be completed before we can close down our inert atmosphere mixed-nitride facility. The process which presently looks most promising involves the oxidation of the nitride by subjecting it to either moist argon at temperatures of ~500°C or using a moist argon atmosphere containing carefully controlled levels of oxygen. Several samples of sintered (U,Pu)N have been oxidized using moist argon but pure UN does not readily oxidize in this atmosphere and it appears that some oxygen will have to be employed for this material.

Characterization of (U,Pu)N

V. J. Tennery

The lattice parameter measurements of the radiation self-damage in (U,Pu)N due to α-decay of the plutonium have been terminated. An analysis of the data obtained after approximately 400 days has been made and interpreted using the model of Rand, et al.[1]

[1] M. H. Rand, A. C. Fox, and R. S. Street, "Radiation Self Damage in Plutonium Compounds," Nature 195(8), pp. 567–568 (1962).

The observed damage in these materials is very similar to that reported by others for other refractory plutonium compounds. The data were fitted to the mathematical relation predicted by the model using non-linear least squares fitting procedures. The saturation damage value in PuN was $\Delta a/a_o = 2.23 \pm 0.05 \times 10^{-3}$. For $x \geq 0.6$ in $U_{1-x}Pu_xN$ the saturation damage was essentially independent on the plutonium content and $\Delta a/a \simeq 2.2 \times 10^{-3}$. For $x < 0.6$ the saturation damage decreased with decreasing plutonium content. The crystal volume saturated with defects by an α-disintegration was essentially constant for $0.6 \leq x \leq 1.0$ and was the volume encompassed by about 27×10^3 actinide atoms in the crystal. For $x < 0.6$ the number of actinide atoms in the defect saturated volume increased to about 70×10^3 in $(U_{0.81}Pu_{0.19})N$. At saturation the Frenkel defect density in these materials varied from 1 per 5 unit cells to 1 per 10 unit cells.

3. DEVELOPMENT OF FBR NEUTRON-ABSORBER MATERIALS

G. M. Adamson, Jr. W. R. Martin

The objective of our work is to characterize boron carbide sufficiently to provide measurable control parameters to properly evaluate fabrication techniques and the effects of irradiation. The irradiation studies will emphasize basic effects of materials variables in both thermal- and fast-reactor environments. A concurrent effort is to examine alternate absorber materials that are potentially better control materials for FBR service.

Boron Carbide

Phase Studies in the Boron-Carbon System (J. P. De Luca)

As part of our effort to manufacture, test, and evaluate boron carbide as a neutron absorber, we have undertaken a basic study of the binary boron-carbon system. This study is determining those portions of the boron-carbon phase system that will be useful in the overall AEC program. This study will help in the fabrication and characterization of boron carbide in several ways. By determining the true equilibrium binary system, one can determine at what level various impurities are important when considering various nuclear grade materials. This basic data will determine which boron-to-carbon ratios are expected to be stable, and also under what conditions these various ratios can be produced.

All of the available literature on phase work in the boron-carbon system has been reviewed. This information will be useful in many ways, one of which is the recognition of the various problems which other investigators have experienced that we must avoid.

Because impurities are of such great importance, "ultra pure" boron powders (−325 mesh) were purchased from three different vendors. The composition of the powders and the vendors are shown in Tables 3.1 and 3.2. All powders were reported by the commercial vendors to be 99.99 wt % B with respect to the heavy elements, but they did not furnish analyses.

Table 3.1. Chemical Analysis of Ultra Pure Powders

Sample Number	Vendor	Element, wt %		
		Carbon	Hydrogen	Oxygen
B-106-Boron	Research Organic/ Inorganic Chemical Corporation	1.41	0.13	0.21
C-5755-Boron	Atomergic Chemetals Company	0.106	0.048	0.51
UMC-Boron	United Mineral and Chemical Corporation	1.07	0.04	0.23
C-2459-Boron	Atomergic Chemetals Company	0.33	0.0005	> 1[a]
C-5536-Carbon	Atomergic Chemetals Company		0.0007	0.019

[a]Believed to be there, as H_2O analysis showed this sample to be 6.84 wt % H_2O.

The results of our chemical and spectrographic analyses are shown in Tables 3.1 and 3.2. Upon examining the three "test" samples, it was decided to purchase the starting material for these experiments from Atomergic Chemetals Company. Seventy grams of boron and 100 g of carbon were purchased. The analyses of these powders are shown as the last two samples, C-2459 and C-5536, in Tables 3.1 and 3.2. As can be seen from the tables, this boron powder, C-2459, has much more oxygen but is more pure with respect to the heavier elements. The reason for these large differences is not known, but an effort is presently being made to determine this large disparity.

An x-ray analysis showed that sample C-5755 was amorphous boron. An attempt was made to crystallize this powder into the thermodynamically stable beta-rhombohedral structure. A tungsten crucible was treated for 16 hr at about 1900°C under a 2-in. Hg pressure of argon to boride the crucible. This boriding process was followed by noting the increase in thickness of the crucible lid and walls. Boron powder C-5755 was placed in the crucible and heated for various times under a pressure of 2-in. Hg

Table 3.2. Spectrographic Analysis of Ultra Pure Boron Powder

Element	Content[a] of Samples, ppm by weight				
	B-106	C-5755	UMC	C-2459	C-5536
Ag	< 50	< 50	< 50	< 1	< 1
Al	1000	200	300	< 10	< 10
Ba	300	100	500	< 5	< 5
Be	< 10	< 10	< 10	< 1	< 1
Bi	< 100	< 100	< 100	< 1	< 1
Ca	1000	< 100	4000	2	< 2
Cd	< 300	< 300	< 300	< 30	< 30
Co	< 500	< 500	< 500	< 5	< 5
Cr	< 100	< 100	200	< 5	< 5
Cu	70	< 30	< 50	10	< 5
Fe	500	100	3000	< 5	< 5
K	< 100	< 100	< 100	< 5	< 5
Li	< 30	< 30	< 30	< 1	< 1
Mg	2000	< 50	3000	0.5	1
Mn	300	< 100	300	< 2	< 2
Mo	< 100	< 100	< 100	2	5
Na	< 100	< 100	< 100	< 1	< 1
Nb	< 300	< 300	< 300	< 30	< 30
Ni	300	< 200	300	< 5	< 5
Pb	< 200	< 200	< 200	< 5	< 5
Rb	< 100	< 100	< 100		
Sb	< 300	< 300	< 300	< 10	< 10
Si	2000	< 100	1000	2	1
Sn	< 100	< 100	< 100	< 5	< 5
Sr	< 100	< 100	< 100		
Ta	< 500	< 500	< 500	< 30	< 30
Ti	< 50	< 50	< 100	< 5	< 5
V	< 100	< 100	< 100	< 5	< 5
W	< 500	< 500	< 500		
Zr	< 200	< 200	< 200	< 10	< 10

[a]Semiquantitative, actual value should be within the range times 1/2 to 2 times.

of argon. Table 3.3 shows the results of these experiments. Conversion was accomplished, but the two extra lines, which resemble alpha-rhombohedral boron-type compounds (i.e., $B_{12}S$, $B_{13}O_2$, $B_{13}As_2$, etc.) were also present. To see if this was a characteristic of the powder, a second sample of boron powder, UMC, was treated at 1900°C in the same crucible and under the same conditions. The results were identical. Analyses are presently being performed to determine which impurity may give rise to these two "extra" lines.

Table 3.3. Results of Experiments to Convert Amorphous Boron Powder C-5755 to Beta-Rhombohedral Crystals

Temperature of Treatment (°C)	Time (hr)	X-Ray Results
As received		Amorphous
1200	4	No beta-rhombohedral lines; two unknown lines
1300	4	No beta-rhombohedral lines; two unknown lines
1400	4	Beta-rhombohedral lines; "extra" lines getting stronger
1500	4	Beta-rhombohedral lines; "extra" lines getting stronger
1600	4	Beta-rhombohedral lines getting quite sharp; "extra" lines also getting stronger
1700	4	Good crystallinity of beta-rhombohedral; "extra" lines remain

Also during this quarter, various items needed for future experiments were received. Both tantalum and TaB_2 crucibles were received. The tantalum crucible will be borided as were the tungsten crucibles noted above. These borided crucibles will in time be used for heating B_4C and mixtures of boron and carbon. The larger TaB_2 crucibles will be used to convert the amorphous boron to beta-rhombohedral boron. The pseudobinary phase diagrams between the diborides and B_4C and boron show a simple

eutectic, above 2000°C, with very limited solid solution. These crucibles should prove to be very compatible with boron and B_4C.

Also high-density B_4C mortars and pestles were received. These will be used to crush B_4C samples and also to mix boron and carbon samples. In every way that is reasonable, care is being taken to obtain and preserve pure B_4C samples.

Irradiation Testing of Boron Carbide Pellets in the EBR-II
(G. L. Copeland, R. G. Donnelly)

Test I. — Due to the low plant availability of the EBR-II during the past year, the burnup of the X 099 experiment will be much lower than previously anticipated by Nov. 4, 1971, when we had planned to remove it. The calculated burnup by Nov. 4, 1971, is 2.9% ^{10}B [6.0×10^{20} $(n,\alpha)/cm^3$] rather than the anticipated 4.5% ^{10}B [9.3×10^{20} $(n,\alpha)/cm^3$]. In view of this plus the planned change in the blanket of the EBR-II, we are now considering several alternatives for removing a part of the test and leaving some capsules in the reactor to attain additional burnup.

Test II. — We have approval-in-principle for insertion of a second test in EBR-II which comprises 11 capsules that fit into two Mark B-7A-type subassemblies. This test includes tantalum, tantalum alloys, and some tantalum borides in addition to boron carbide. Fabrication of the test is in progress. Its insertion will be coordinated with removal of X 099, so that no more than two ORNL subassemblies of neutron absorbers are in test at one time.

Supplemental Evaluation of Powders from HEDL Experiment X 042
(G. L. Copeland)

We have received about 5 g of boron carbide powder from each of the BC-2 and C-8 capsules that were irradiated by HEDL in the EBR-II experiment X 042. Capsules BC-2 and C-8 were Vi-Pac rods of boron carbide powder irradiated to 4.8% ^{10}B burnup [10×10^{20} $(n,\alpha)/cm^3$] and 3.7% ^{10}B burnup [7.7×10^{20} $(n,\alpha)/cm^3$], respectively, at estimated temperatures of 650 and 730°C, respectively.[1] Our evaluation will consist of

[1]A. L. Pitner, HEDL, personal communication.

measurement of residual helium by fusion with sodium carbonate and/or vacuum melting and examination of irradiation damage by transmission electron microscopy and x-ray diffraction both as irradiated and after heat treating at temperatures of 700 to 1900°C. These evaluations are currently in progress and should be completed during the next quarter.

Performance Modeling of Boron Carbide Absorber Rods (F. J. Homan)

Performance models have proved very useful in experimental programs to develop fuels for LMFBR application. Accordingly, we have begun a modeling effort in conjunction with our experimental program to develop absorber materials for LMFBR's. Since only a small fraction of the needed data are available for absorber materials, it was not clear initially what form the models should take. One possible route that could be used to develop a computer code for absorber-predicting performance would be to take an existing code for stainless steel-clad $(U,Pu)O_2$ fuel rods and replace the mixed oxide data with data for B_4C or some other absorber material. In situations where absorber data are not available, best estimates could be used, and the estimate replaced when better data are available. Another possible route for modeling absorber rods is to start from scratch after examining the available data and develop a modeling code that makes use of what is known about absorber materials and uses an empirical or parametric treatment in areas where suitable data are not available. We have chosen the second route. As with the oxide fuel models, we expect to replace empirical treatments when models founded on a sounder theoretical basis are available.

In order to determine what kind of physical phenomena would have to be considered for the absorber materials (i.e., restructuring, pellet cracking, grain growth, etc.) it was necessary to have some idea of the temperature ranges in which absorber rods would operate. The PRØFIL code[2] was used to make temperature calculations. To use PRØFIL, it is necessary that an expression for the absorber material thermal

[2]C. M. Cox and F. J. Homan, PRØFIL – A One-Dimensional FØRTRAN IV Program for Computing Steady-State Temperature Distributions in Cylindrical Ceramic Fuels, ORNL-TM-2443 (March 1969); ORNL-TM-2443, Addendum (August 1969).

conductivity in terms of temperature and porosity be known. The design equation for thermal conductivity of B_4C is

$$k(T,P) = 6.78 \exp(734/T)\rho^{1.5} , \tag{1}$$

where

$k(T,P)$ = Btu (hr ft °F)$^{-1}$,

T = °K, and

ρ = fractional density.

Unfortunately, this equation does not give good agreement with the experimental data in the temperature ranges of interest (above 500°C). This is shown in Fig. 3.1. Plotted are thermal conductivity data from the literature[3] covering a porosity range of 75 to 100% dense material. Also shown (solid curves) is the design equation for 100 and 80% dense material. It can be seen that the design equation yields thermal conductivity values that are too high at temperatures below about 1600°C for the 100% dense material and too low above this temperature. In addition, the data for 100% dense material appear to have a minimum thermal conductivity at about 1000°C, with thermal conductivities increasing with increasing temperature after this minimum. The form of Eq. (1) is such that the thermal conductivity calculated with the equation must always decrease with increasing temperature. Due to the demonstrated limitations of Eq. (1) it was decided to use an equation of the form given below to describe the thermal conductivity of B_4C.

$$k(T,P) = \left[\frac{1 - P}{1 + \beta P}\right][A + BT + CT^2 + DT^3 + ET^4] , \tag{2}$$

where

$k(T,P)$ = W cm^{-1} °C^{-1},

P = fractional porosity,

---

[3]Y. S. Touloukian et al., Thermal Conductivity of Nonmetallic Solids, Thermophysical Properties of Matter, Vol. 2, p. 574, IFI/Plenum, New York, 1970.

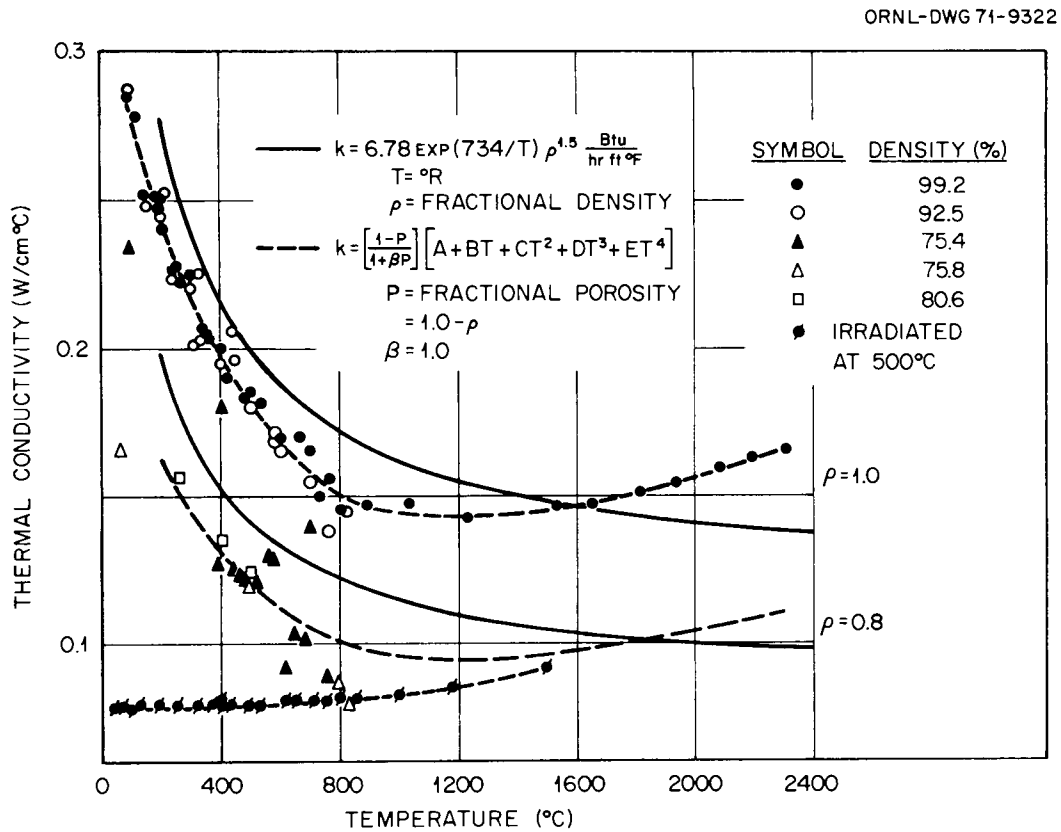

Fig. 3.1. Thermal Conductivity of B_4C.

T = °C,

A, B, C, D, E = empirical constants, and

β = constant (see ref. 3).

The constants appearing in Eq. (2) were evaluated from the data plotted in Fig. 3.1 (99.2% dense material) by standard regression techniques. The values are tabulated below:

Empirical Constant	Value
A	0.317
B	-0.436×10^{-3}
C	0.378×10^{-6}
D	-0.158×10^{-9}
E	0.238×10^{-13}

A fit of the data plotted in Fig. 3.1 using the above constants and a value of unity for β is also shown in Fig. 3.1. Inspection of the solid

and dashed curves indicates that the fit using Eq. (2) (dashed curves) is far superior to the fit obtained using Eq. (1) (solid curves). Also plotted in Fig. 3.1 are some thermal conductivity data for B_4C that had been previously irradiated at 500°C. These data will be discussed later. They were fit to Eq. (2), with the following empirical constants:

Empirical Constant	Value
A	0.457×10^{-1}
B	0.969×10^{-5}
C	-0.105×10^{-7}
D	0.100×10^{-10}
E	0.187×10^{-14}

In addition to the thermal conductivity function, the PRØFIL code requires the heat generation rate as a function of radial position. This was determined for B_4C by calculating the reaction rate as a function of pellet density and boron enrichment, and assuming a constant energy/reaction. The reaction rate was calculated from the following equations:

$$\dot{R} = N_{B_{10}} \sigma_c \phi \ , \tag{3}$$

where

$\dot{R}$ = reaction rate (cm^3/sec),

σ_c = absorption cross section (cm^2),

ϕ = neutron flux (neutrons cm^{-2} sec^{-1}), and

$N_{B_{10}}$ = atoms (B_{10}/cm^3);

$$N_{B_{10}} = X \, N_B \ , \tag{4}$$

where

X = fractional enrichment, and

N_B = boron atoms/cm^3;

$$N_B = 4 \, N_{B_4C} \ , \tag{5}$$

where

N_{B_4C} = B_4C molecules/cm^3;

$$N_{B_4C} = \frac{\rho N}{M} , \qquad (6)$$

where

ρ = density of B_4C (g/cm^3),

N = Avagadro's number (molecules/mole),

M = molecular weight (g/mole), and

$M = 4[X(10) + (1 - X)(11)] + 12$.

Using the values of σ_c and Φ for row 2 of the EBR-II core at the reactor midplane [1.15 b (ref. 4) and 3×10^{15} neutrons cm^{-2} sec^{-1} (ref. 5), respectively], and a value of 2.78 MeV/reaction[6] the temperature profiles plotted in Fig. 3.2 were generated. Several different pellet sizes were considered so that the results could be compared. The 0.98-cm-OD pellets represent a proposed FFTF design,[7] the 4.0-cm-OD pellets represent the vented control rods in the French Rapsodie-Fortissimo Reactor,[8] and the 1.91-cm-OD pellets (0.75 in.) represent an intermediate size between the small FFTF pellet and the large French pellet. The 800°C pellet surface temperature was chosen arbitrarily.

From Fig. 3.2 it can be seen that there is substantial variation in the pellet temperatures with enrichment and pellet size. The FFTF-type pellet does not reach high temperatures even at 90% enrichment, but the large French pellets at 90% enrichment can reach temperatures sufficiently high to cause restructuring, grain growth, and extreme plasticity in other ceramic systems.

The influence of enrichment on the temperature profile of a 1.91-cm-OD boron carbide pellet is shown in Fig. 3.3. Also shown is the influence of the lower thermal conductivity attributed to irradiated material (see Fig. 3.1) on the temperature profile.

---

[4]A. R. Olsen, personal communication, August 1971.

[5]J. H. Kittel, Guide for Irradiation Experiments in EBR-II, Rev. 4, Appendix C, Figs. C-3 and C-4, Argonne National Laboratory, Argonne, Illinois (February 1971).

[6]William J. Price, Nuclear Radiation Detection, p. 313, McGraw-Hill Book Company, New York, 1958.

[7]L. E. Strawbridge, Manager, Nuclear Design, FFTF Project Letter, FRP-294, Sept. 2, 1970.

[8]W. O. Harms, personal communication, September 1971.

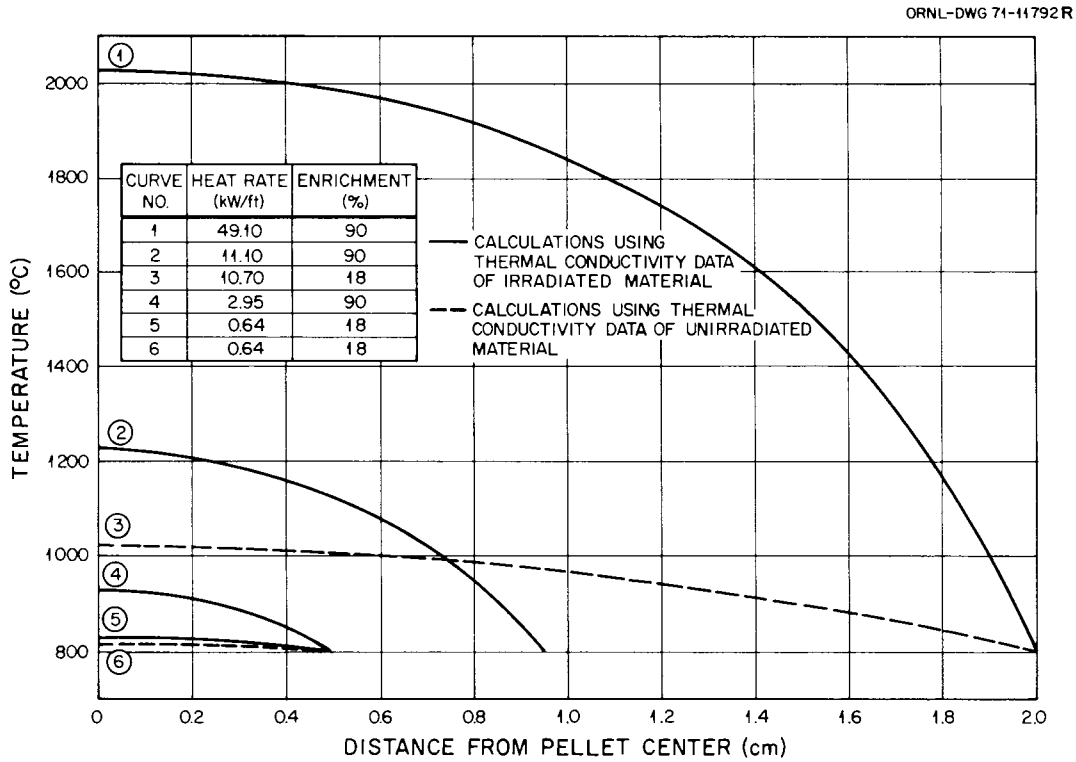

Fig. 3.2. Calculated B_4C Pellet Temperature for Different Pellet Sizes, Enrichments, and Thermal Conductivity Assumptions.

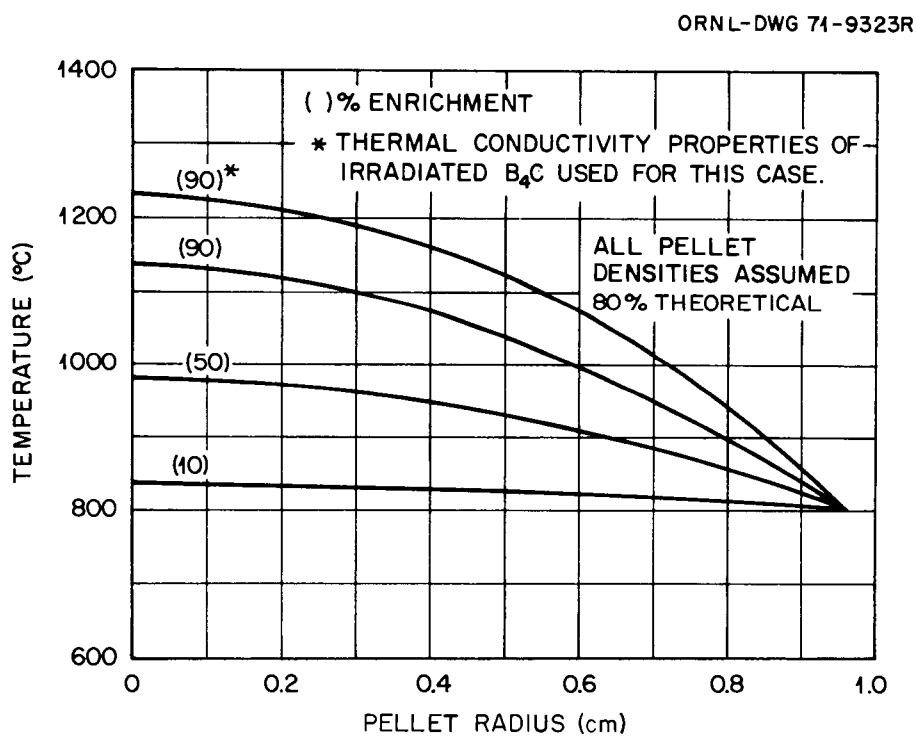

Fig. 3.3. Calculated B_4C Pellet Temperature Profiles for Different Enrichments.

Using the temperature profiles shown in Figs. 3.2 and 3.3, and standard finite difference techniques,[9] the thermal stresses were computed for the three pellets using different enrichments and thermal conductivities. For this analysis it is necessary to know the elastic modulus, Poisson's ratio, and the linear coefficient of thermal expansion as functions of temperature. Values for the elastic modulus and Poisson's ratio could only be found at room temperature [65.3×10^6 psi (ref. 10) and 0.21 (ref. 11), respectively]. These values were used in the calculation, which is equivalent to assuming that the elastic modulus and Poisson's ratio are not dependent upon temperature. Thermal expansion data from the literature[12] were fit to a polynomial expansion of the form

$$\alpha_{B_4C} = [A + BT + CT^2 + DT^3 + ET^4] \times 10^{-6}\ {}^\circ C^{-1} , \qquad (7)$$

where

$T = {}^\circ C$,

$A = 1.68$,

$B = 0.821 \times 10^{-2}$,

$C = -0.614 \times 10^{-5}$,

$D = 0.220 \times 10^{-8}$, and

$E = -0.292 \times 10^{-12}$.

Equation (7) and the thermal expansion data values are plotted in Fig. 3.4. Also plotted are rupture modulus data[9] for B_4C. The calculated elastic hoop stresses due to the temperature profiles shown in Figs. 3.2 and 3.3 are shown in Fig. 3.5. Notice that only in curve 1

---

[9]Richard L. Puthoff, A Digital Computer Program for Determining the Elastic-Plastic Deformation and Creep Strains in Cylindrical Rods, Tubes, and Vessels, NASA TM X-1723 (January 1969).

[10]W. Kermit Anderson and J. S. Theilacker, Neutron Absorber Materials for Reactor Control, p. 191, Naval Reactors, Division of Reactor Development, USAEC, 1962.

[11]T. W. Evans, The Effects of Irradiation on Boron Carbide (A Literature Review), BNWL-697, p. 3 (February 1968).

[12]J. C. Hedge, C. Kostenko, and J. I. Lang, Thermal Properties of Refractory Alloys, p. 9, ASD-TDR-63-597 (June 1963).

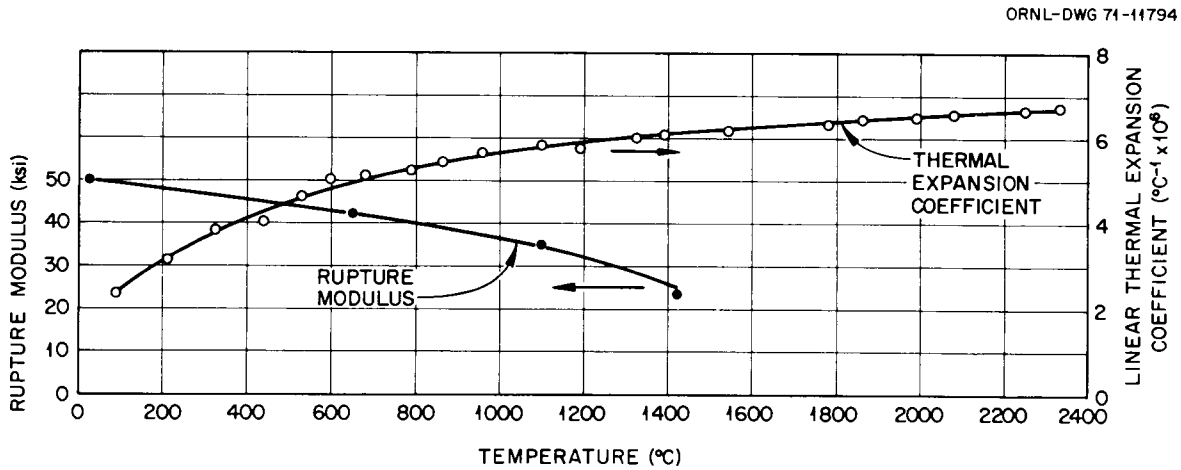

Fig. 3.4. Temperature Dependent Properties of B_4C.

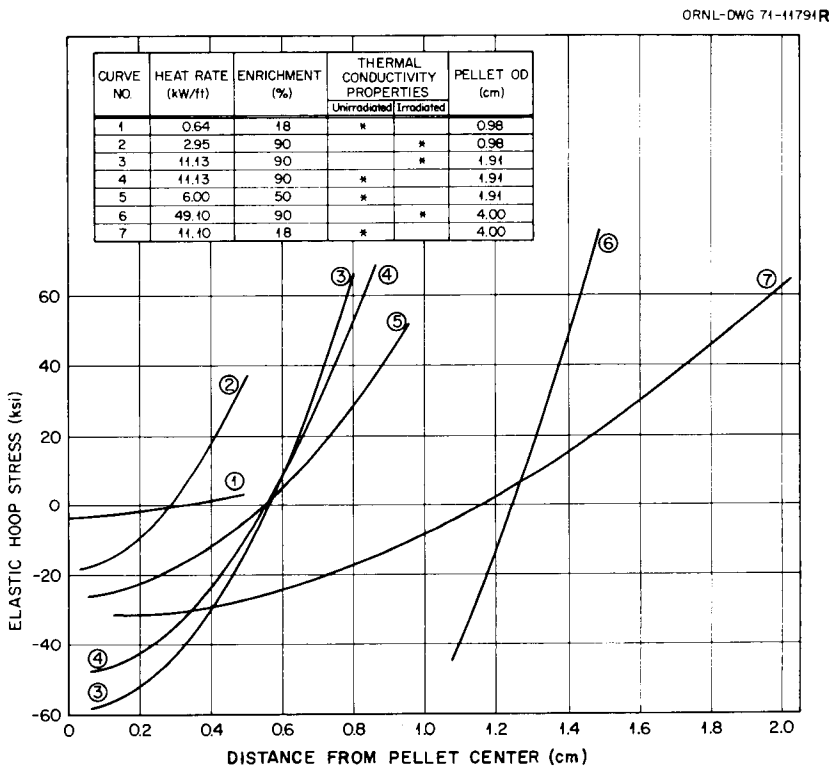

CURVE NO.	HEAT RATE (kW/ft)	ENRICHMENT (%)	THERMAL CONDUCTIVITY PROPERTIES Unirradiated	THERMAL CONDUCTIVITY PROPERTIES Irradiated	PELLET OD (cm)
1	0.64	18	*		0.98
2	2.95	90		*	0.98
3	11.13	90		*	1.91
4	11.13	90	*		1.91
5	6.00	50	*		1.91
6	49.10	90		*	4.00
7	11.10	18	*		4.00

Fig. 3.5. Calculated Elastic Stresses Due to Temperature Gradients in B_4C Pellets of Different Sizes and Enrichments Operating in Row 2 of EBR-II.

of Fig. 3.5 are calculated hoop stresses lower than rupture stresses shown in Fig. 3.4.

From this limited examination of the data published for boron carbide, several conclusions have been reached regarding the development of a performance model for absorber rods:

1. The present design equation for boron carbide thermal conductivity as a function of temperature and porosity is not adequate.

2. Pellet temperatures high enough to cause grain growth, restructuring, and plastic behavior may be reached in some absorber rod designs, but since we are mainly interested in FFTF absorber rods for the present, and since no experimental data to describe these phenomena have been found to date, they will not be included in the model.

3. Pellet cracking due to thermal stresses is very likely to occur, even in the FFTF design, and therefore must be considered in the model.

A computerized performance code for absorber rods containing boron carbide pellets clad in stainless steel tubes has been developed. The code is called ABSORB, and the characteristics of the code have been strongly influenced by our prior experience in modeling mixed oxide fuel pins, and on the nature and limitations of the data available on boron carbide. ABSORB does not contain a model for restructuring of the absorber pellets, but does contain a pellet cracking model. Pellet swelling due to accumulation of solid and gaseous reaction products (the reaction being neutron capture) is not well understood, and is therefore handled empirically in the code. An input number corresponding to the swelling rate expressed as percent $\Delta V/V$ per percent burnout (based on the initial number of boron atoms present) is required of the code user. The code is capable of calculating mechanical interaction between the pellets and cladding, but it is doubtful that this feature will see much use as current practice is to design absorber rods so that there will be no mechanical interaction.[13]

Due to low boron carbide operating temperatures calculated for the small diameter FFTF absorber rods and the planned lack of mechanical

---

[13]W. R. Martin, personal communication, August 1971.

interaction, the primary means of rod failure appears to be rupture due to buildup of helium gas pressure. The following calculation shows the importance of this aspect of the absorber rod performance:

$$\text{Burnout fraction} = \frac{\text{reactions}}{\text{initial B atom}}$$

$$= \frac{\left(\frac{\text{reactions}}{\text{cm}^3\ B_4C}\right)\left(\frac{\text{grams B}}{\text{mole } B_4C}\right)}{\left(\frac{\text{B atoms}}{\text{mole } B_4C}\right)\left(\frac{\text{grams B}}{\text{cm}^3\ B_4C}\right)} .$$

Using the FFTF design pellet[14] which is 90% dense

$$\frac{\text{grams B}}{\text{cm}^3} = (0.92)(2.52)(0.783) = 1.82 ,$$

where

0.92 = fractional density,

2.52 = theoretical density of natural B_4C (grams B_4C/cm^3),

0.783 = stoichiometry factor for natural B_4C (grams B/grams B_4C),

$$= \frac{4[0.18(10) + 0.82(11)]}{4[0.18(10) + 0.82(11)] + 12} = 0.783 .$$

$$\frac{\text{B atoms}}{\text{mole } B_4C} = \left(\frac{\text{B atoms}}{B_4C \text{ molecule}}\right)\left(\frac{B_4C \text{ molecules}}{\text{mole } B_4C}\right)$$

$$= (4)(6.023 \times 10^{23})$$

$$= 24.09 \times 10^{23}.$$

$$\frac{\text{grams B}}{\text{mole } B_4C} = \left(\frac{\text{grams } B_4C}{\text{mole } B_4C}\right)\left(\frac{\text{grams B}}{\text{gram } B_4C}\right)$$

$$= (55.28)(0.783)$$

$$= 43.3.$$

$$\text{Burnout fraction} = \frac{\left(\frac{\text{reactions}}{\text{cm}^3\ B_4C}\right)(43.3)}{(24.09 \times 10^{23})(1.82)}$$

$$= \left(\frac{\text{reactions}}{\text{cm}^3\ B_4C}\right)(0.988 \times 10^{-23}) . \qquad (8)$$

---

[14]L. E. Strawbridge, Manager, Nuclear Design, FFTF Project Letter, FRP-294, Sept. 2, 1970.

Again, using the FFTF design:

36 in. pellet stack

18 in. gas plenum filled with helium at 1 atm

0.395 in. cladding inner diameter

0.386 in. pellet outside diameter

the calculated initial gas volume is

$$V = \frac{\pi}{4}[(0.395^2 - 0.386^2)36 + (0.395^2)18] = 2.40 \text{ in.}^3$$
$$= 39.41 \text{ cm}^3.$$

The amount of helium in this space can be calculated from the ideal gas law at standard temperature and pressure:

$$PV = nRT$$
$$n = \frac{1(0.394)}{(8.206 \times 10^{-2})(298)} = 0.00161 \text{ mole} ,$$

where

$P = 1$ atm,

$V = 0.0394$ liter,

$R = 8.206 \times 10^{-2}$ liter-atm (mole °K)$^{-1}$, and

$T = 298$°K.

The volume of B_4C in this pin is

$$\frac{\pi(0.386^2)}{4} 36 = 4.21 \text{ in.}^3 = 69.04 \text{ cm}^3 ,$$

thus, at 1% average burnout, from Eq. (8)

$$\text{Reactions} = \frac{(0.01)(69.04)}{0.988 \times 10^{-23}} = 0.699 \times 10^{23} .$$

Assuming 1 He atom/reaction, this is equivalent to 0.116 mole of helium, which is 72 times the amount of helium initially present in the pin. If all of this gas were released from the pellets, the plenum pressure would increase nearly 3000 psi per percent burnout (assuming the average gas temperature to be about 500°C). Thus, it appears that the treatment of gas release is very important in predicting the fission gas buildup with time. The design equation for gas release is:

$$R = 0.3C \exp(-5050/T) \ , \tag{9}$$

where

R = fraction of helium released,

C = captures/cm^3 $B_4C \times 10^{-20}$, and

T = °K.

Gas pressure calculations for an FFTF-type absorber rod[14] operating under steady-state conditions in row 2 of EBR-II for 5000 hr are presented in Fig. 3.6. The ABSORB code was used to make these calculations, and Eq. (9) was used to describe gas release. The volume average fuel temperatures for the 18, 50, and 90% enriched boron carbide pellets, for which the gas pressure calculations shown in Fig. 3.6 were made, were 508, 534, and 570°C, respectively. Since there was no restructuring of the pellets, the operating temperatures did not change with time, and the fraction gas release calculated was a linear function of depletion, as predicted by Eq. (9) and shown in Fig. 3.6.

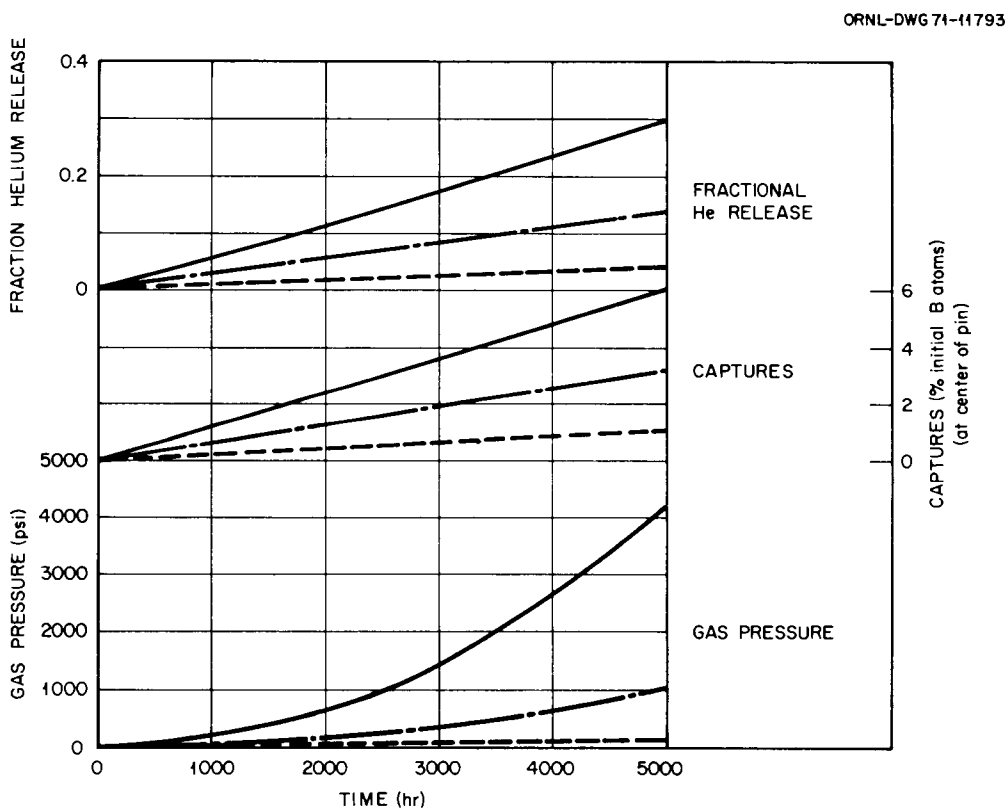

Fig. 3.6. Effect of ^{10}B Enrichment on the Buildup of Helium Gas Pressure in an FFTF Absorber Rod.

At this stage of absorber development, there is little data to evaluate with performance models. However, we are now ready with a modeling code when the data begins coming from experiments currently in progress.

Alternate Materials

Fabrication of Tantalum Borides (M. M. Martin, J. P. De Luca)

Various borides of tantalum are being studied for their application as neutron absorbers. Our objective is to determine the irradiation performance of Ta_2B ($Ta + Ta_3B_2$) and TaB_2 after an exposure of about 2.2×10^{22} neutrons/cm^2 (of energy greater than 0.1 MeV). We selected these compounds as promising alternate absorber materials for boron carbide – or tantalum control rods being considered for FBR's. Both tantalum borides are less dense than tantalum metal and possess more reactivity worth per unit volume. In fact, TaB_2 has 12% more worth per cubic centimeter than B_4C. Also, their total possible gas release is up to a factor of 2 less than that from boron carbide. However, they lack sufficient metallurgical characterization and irradiation experience to warrant consideration at this time. We plan to provide irradiation data to allow an evaluation of their performance in service.

The first draft of the Quality Assurance documents has been written for the fabrication of components to be used in the first irradiation.

We have decided to use the carbothermic reduction:

$$Ta_2O_5 + 2B_2O_3 + 11C = 2TaB_2 + 11CO$$

to produce the tantalum diboride to go into the reactor. The alternate reactions are direct synthesis from the elements, reduction of the metal oxide by boron, or reduction of the metal oxide by boron carbide with or without carbon. These methods all have disadvantages when considered with the fact that impurities, reproducibility, and cost are important.

This first lot of TaB_2 was prepared by the above reaction. The reaction was carried out at 1900°C in argon. The products were 95% TaB_2 and 5% TaC, by x-ray analysis. The production of TaC was a result of

loss of B_2O_3 by volatization during the reaction. The lattice parameter of TaC (fcc) was determined to be 4.460 Å, which is considerably larger than the 4.455 Å value reported for TaC having a tantalum-to-carbon ratio of 1. Thus, there is appreciable solubility of TaB_2 in TaC. The lattice parameters for TaB_2 (hexagonal) were found to be a_o = 3.085 Å and c_o = 3.245 Å. The a_o parameter is in close agreement with the ASTM quoted value; however, c_o is 0.02 Å smaller than the ASTM value. The significance of this is not apparent at this time.

An attempt was made to produce 100 g of Ta_3B_2 by carbothermic reduction. This reaction was carried out under conditions identical to those used to produce TaB_2. By weight, the reaction products gave the stoichiometric result; however, x-ray and chemical analyses have not been completed at this time.

Microstructure of Irradiated Tantalum (F. W. Wiffen)

Sheet specimens of unalloyed tantalum were irradiated in row 2 of the EBR-II at temperatures from 425 to 1000°C to fluences of 2.5 or 4.4×10^{22} neutrons/cm^2 (> 0.1 MeV). The specimens were 0.015 in. thick and had been recrystallized by annealing at 1100°C before irradiation. The specimens were thinned by remote techniques[15] and examined by transmission electron microscopy to characterize the irradiation-produced microstructure.

The microstructure in a sample irradiated to 2.5×10^{22} neutrons/cm^2 at 585°C was described previously.[16] Some of the data for that condition will be repeated here for completeness. Representative micrographs for the four irradiation temperatures are shown in Fig. 3.7. Void parameters for the specimens irradiated at the three higher temperatures are shown in Table 3.4.

---

[15]C.K.H. DuBose, T. L. Chandler, and C. Jones, Fuels and Materials Development Program Quart. Progr. Rept. Mar. 31, 1971, ORNL-TM-3416, pp. 95–102.

[16]F. W. Wiffen, Fuels and Materials Development Program Quart. Progr. Rept. Mar. 31, 1971, ORNL-TM-3416, pp. 102–103.

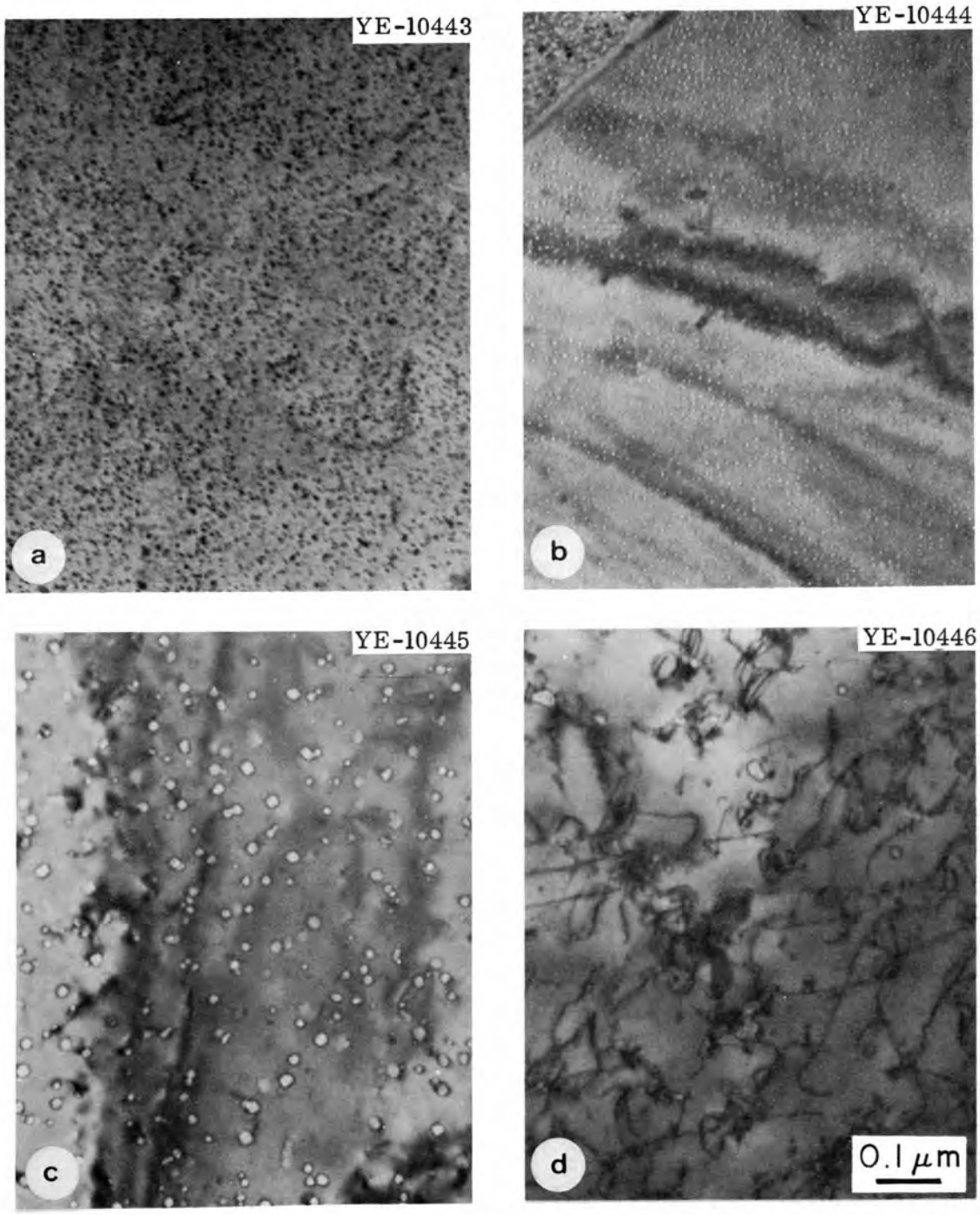

Fig. 3.7. Effect of Irradiation Temperature on the Microstructure of Neutron-Irradiated Tantalum. All {111} foil orientation. Irradiated at (a) 425°C, 2.5×10^{22} neutrons/cm^2 (> 0.1 MeV); (b) 585°C, 2.5×10^{22} neutrons/cm^2; (c) 790°C, 2.5×10^{22} neutrons/cm^2; and (d) 950 to 1050°C, 4.4×10^{22} neutrons/cm^2.

Table 3.4. Void Parameters for Neutron-Irradiated Tantalum

Irradiation Temperature (°C)	Fluence[a] (neutrons/cm^2)	Void Parameters		
		Concentration (voids/cm^3)	Average Diameter (Å)	Volume Fraction (%)
	$\times 10^{22}$	$\times 10^{15}$		
425	2.5	0		
585	2.5	190	61	2.4
790	2.5	6.1	117	0.65
950–1050	4.4	≤ 0.3[b]	130	≤ 0.03[b]

[a] $>$ 0.1 MeV.

[b] Void concentration locally variable. These are upper limits.

Irradiation at 425°C produced a microstructure [shown in Fig. 3.7(a)] containing primarily a very high density of small "black spots," approximately 2×10^{17} spots/cm^3, that could not be identified, but were likely dislocation loops. The diameter of these defects ranged from 20 to 100 Å, with few defects at the upper end of this range. There was no tendency for these loops to cluster, and no voids were identified in the sample. The damage was similar to that found at 450°C at one-eighth the present fluence.[17] A few dislocation segments were present in this sample. They were usually associated with "black spot" defect either attached or very close to them. The dislocation segments may be remnants of dislocations present before the irradiation began or may be a component of the damage.

Foils from this specimen often showed evidence of deformation in handling. This deformation occurred by dislocation channeling, and the moving dislocations swept the damage from the channels. An example of this channeling is shown in Fig. 3.8, where four channels can be seen.

[17] G. L. Kulcinski and B. Mastel, "Microstructure of High-Temperature Neutron-Irradiated Tantalum and Molybdenum," J. Appl. Phys. 41, 4752 (1970).

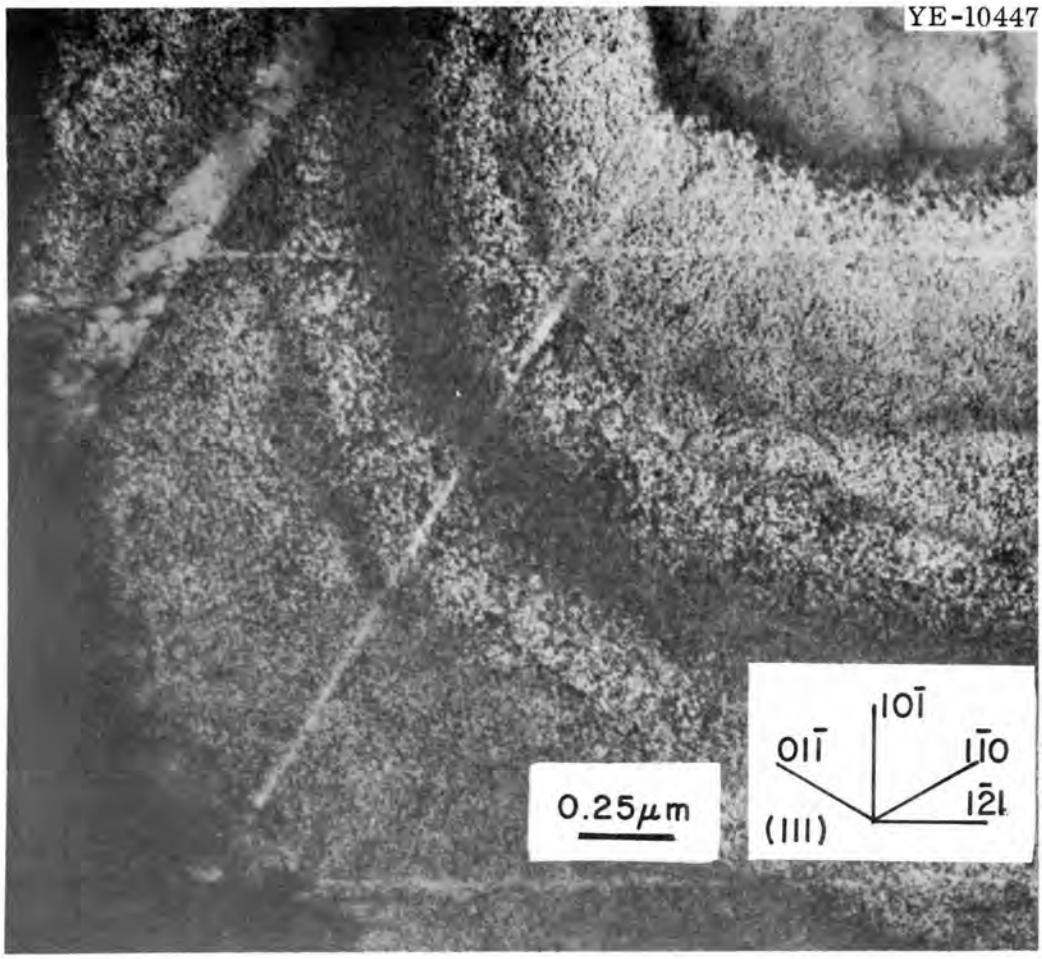

Fig. 3.8. Dislocation Channeling in Tantalum Irradiated at 425°C to 2.5×10^{22} neutrons/cm^2 (> 0.1 MeV). The foil orientation is {111} and the channel traces are in ⟨112⟩ direction. The channels have resulted from the passage of one dislocation with a/2⟨111⟩ Burgers' vector on each {110} slip plane in the channel.

Most of the channels were found to have ⟨112⟩ traces in {111} foils and are consistent with slip of a/2⟨111⟩ dislocations on {110} planes. This channeling behavior has been seen in several other irradiated body-centered cubic metals. Similar channeling was reported in bulk deformed, irradiated single-crystal niobium by Tucker et al.[18] Analysis of the offsets in Fig. 3.8 shows that the channels have been formed by the

[18]R. P. Tucker, M. S. Wechsler, and S. M. Ohr, "Dislocation Channeling in Neutron-Irradiated Niobium," J. Appl. Phys. 40, 400 (1969).

passage of approximately one a/2⟨111⟩ dislocation per {110} slip plane in the channel, the same result as found in niobium.[18] This channeling deformation was found only in the samples irradiated at 425°C and did not occur in samples irradiated at the higher temperatures that contained voids. This is further indirect proof that the damage at 425°C consists only of dislocation loops without an accompanying void population.

Samples irradiated at 585, 790, and 950 to 1050°C all contained voids. Typical microstructures are shown in Fig. 3.7(b) and 3.7(d) and the void parameters are given in Table 3.4. Table 3.4 shows that trends established in other metals are also seen in tantalum. Within the temperature range of void formation the void concentration decreased and the average void size increased with increasing temperature. Void-denuded zones adjacent to grain boundaries were quite narrow in these specimens, only a few hundred angstroms in width. These narrow denuded zones were usually bordered by zones with higher than average void concentrations. The data in Table 3.4 show that the temperature range for maximum swelling of irradiated tantalum falls somewhere between 450 and 750°C and suggest that the maximum will be in the range 500 to 650°C. These results also show that the lower temperature limit for void formation is between 450 and 550°C and suggest that the upper temperature limit, at the fluence reported here, is probably not very much above 1000°C. These limits on the "temperature window" in which voids form are in close agreement with the limits 500 to 1000°C for void formation calculated by the Bullough-Perrin model,[19] using an activation energy of self-diffusion of 4.78 eV and a vacancy migration energy of 1.25 eV.

The void ordering reported previously[20] for the 585°C irradiation temperature is shown in Fig. 3.9, with the voids overfocused and the orientation near a two-beam condition. The voids are partially ordered on a body-centered cubic superlattice, which is parallel to the body-centered cubic metal lattice and has a superlattice parameter of 205 Å.

---

[19]R. Bullough, UKAEA, Harwell, personal communication, June 1971.

[20]F. W. Wiffen, Fuels and Materials Development Program Quart. Progr. Rept. Mar. 31, 1971, ORNL-TM-3416, pp. 102–103.

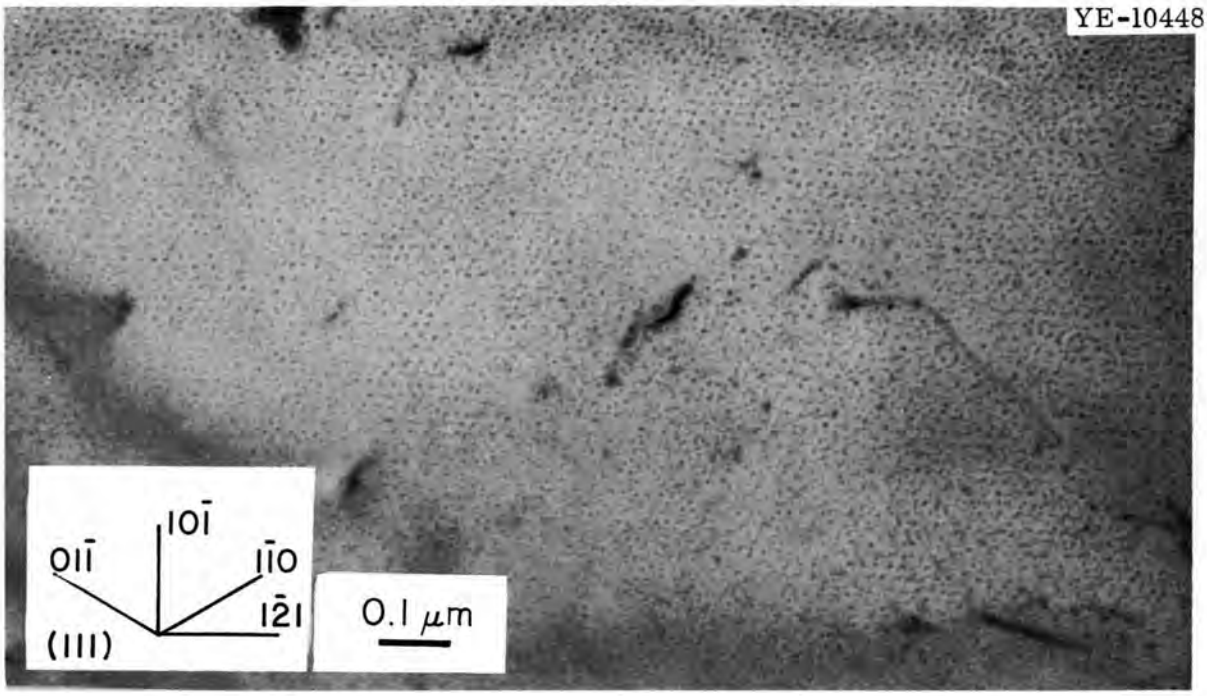

Fig. 3.9. Void Ordering in Tantalum Irradiated at 585°C to 2.5×10^{22} neutrons/cm^2 (> 0.1 MeV). The voids are imaged in an over-focused condition to improve visibility.

Comparison of the concentrations of superlattice points and of voids shows an occupancy of 80% of the superlattice points. The voids in the 790 and 1000°C specimens were not ordered, but they tended to be clustered in the specimen irradiated at 790°C.

The dislocation and loop structures in all samples were partially obscured by deformation during thinning and handling and have not yet been analyzed in detail.

Analysis of Self-Heating in Tantalum Irradiation Specimens (C. M. Cox, J. D. Jenkins,[21] M. J. Bell[22])

A series of calculations were performed to predict the self-heating of the tantalum specimens irradiated in row 7 of EBR-II. Spectrum-averaged cross sections were computed based on spectra from a Monte Carlo

[21]Reactor Division.

[22]Chemical Technology Division.

calculation by Edwards et al.[23] and by using the ENDF/B data. To emcompass the projected needs of the absorber materials program, we included both ^{181}Ta $\sigma(n,\gamma)$ (ENDF/B material 1035) and ^{10}B $\sigma(n,\alpha)$ (ENDF/B material 1009). The results are tabulated in Table 3.5 and represent

$$\bar{\sigma} = \int_0^\infty \sigma(E)\ \varphi(E)\ dE / \int_0^\infty \varphi(E) dE\ .$$

Depletion calculations were made for the tantalum specimens in row 7 using an activation cross section of 0.33 b for ^{181}Ta, a total neutron flux of 1.6×10^{15} neutrons cm^{-2} sec^{-1}, and a ^{181}Ta half-life of 115 days.

Comparative calculations were made with the ORIGEN code[24] to consider the interrelated chains involving Lu, Hf, Ta, and W isotopes. The effects of these cross chains on the photon and beta sources were quite negligible. We considered both a continuous irradiation history and the more likely intermittent operation of alternating between reactor power levels of 62.5 and 0 MW for periods of 30.74 and 8.11 days, respectively. The calculated activities were converted to power using an average energy release of 1.205 MeV/disintegration based on the compilation of Lederer et al.[25] These results are summarized in Fig. 3.10, which shows that internal heat source is sensitive to the power-time history. For comparison the saturation activity under these conditions is 47 curies/g, corresponding to a power output of 0.34 W/g. The total heat source is the sum of the internal heating, shown in Fig. 3.10, plus radiation heating in the reactor environment.

We also investigated the possibility that a significant fraction of the energy release might escape from the tantalum specimens, since about 90% of this energy is in the form of gamma radiation. Calculations

---

[23]W. E. Edwards, W. B. Henderson, and N. R. Baumgardt, Analysis of EBR-II Neutron Spectra by Monte Carlo and Discrete Ordinate Methods, GEMP-742 (December 1969).

[24]M. J. Bell, ORIGEN, The ORNL Isotope Generation and Depletion Code, ORNL-4628 (in preparation).

[25]C. M. Lederer, J. M. Hollander, and I. Perlman, Table of Isotopes, 6th ed., Wiley, New York, 1967.

Table 3.5. Neutron Capture Cross Sections for ^{181}Ta and ^{10}B in EBR-II

Row	Distance from Midplane (cm)	Activation Cross Section, b	
		^{181}Ta	^{10}B
2	0–5.71	0.261	1.15
2	5.71–11.43	0.268	1.18
2	11.43–17.14	0.278	1.24
2	17.14–27.69	0.394	1.62
2	27.69–39.13	0.566	2.22
2	39.13–50.56	0.676	2.57
2	50.56–61.98	0.729	2.78
7	0–5.71	0.326	1.38
7	5.71–11.43	0.333	1.42
7	11.43–17.14	0.350	1.49
7	17.14–27.69	0.479	1.87
7	27.69–39.13	0.601	2.29
7	39.13–50.56	0.657	2.47
7	50.56–61.98	0.807	2.97

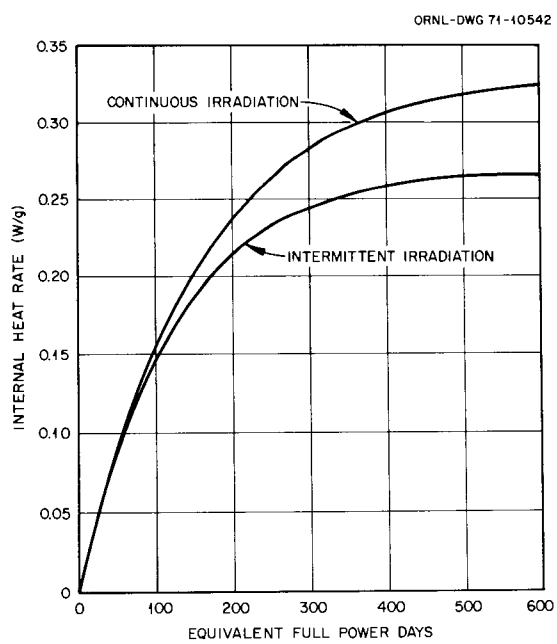

Fig. 3.10. Predicted Internal Heat Generation of Tantalum Specimens at Row 7 Midplane of EBR-II.

performed with the SDC code[26] for the gage length section (1/8 in. in diameter) of typical "buttonhead" specimens indicate that only about 10% of the gamma energy escapes. This code was a buildup factor approach and while more precise transport theory calculations could be made, they do not appear warranted.

Helium Vents for Absorber Rods

J. I. Federer

Boron absorber rods for the FTR consist of boron carbide pellets sealed in a stainless steel container. These rods are life limited due to the (n,α) reaction involving ^{10}B. The pressure of helium generated by the (n,α) reaction would eventually cause swelling of the stainless steel, forcing removal of the rods from the reactor before the ^{10}B has been used efficiently. A possible solution to this problem is the use of vents that allow the helium to escape from the rods into the reactor coolant. Therefore, we are studying the effects of thermal exposure, sodium corrosion, and neutron irradiation on the helium permeability of potential vent materials.

The first task is to install a vent experiment in an EBR-II, test 2 capsule. The objective of this experiment is to evaluate the effects of fast neutron irradiation and sodium exposure on the permeability of candidate vent materials. The experiment consists of 14 vents stacked in pin 0-19-B, Subassembly Beta. Seven of the vents will be exposed to sodium during irradiation, which will be conducted at a calculated temperature of 450°C for about one year. The vent materials to be investigated are types 304 and 316 stainless steel and molybdenum. The vents are porous disks of these materials fabricated by pressing and sintering powders. The disks will be metallurgically bonded to a holder to facilitate determination of helium leak rates before and after reactor exposure.

---

[26]E. D. Arnold and B. F. Maskewitz, SDC — A Shielding-Design Calculation Code for Fuel Handling Facilities, ORNL-3041 (March 1966).

The principal tasks required to attain the objectives of this experiment are: (1) fabrication of the vents; (2) design and construction of vent holders; (3) preirradiation testing of helium leak rates; (4) reactor exposure; and (5) postirradiation testing of helium leak rates.

We are presently finalizing the design of the vent holders. These are approximately 5/8-in.-diam by 3/8-in.-long cylinders of stainless steel or molybdenum into which the disks will be electron-beam welded. By connecting a source of helium to one side of the disk and a helium leak detector to the other, helium leak rates can be measured as a function of temperature and pressure. These measurements will be performed before and after, but not during, the irradiation test.

We have also begun fabricating stainless steel porous disks. Powder compacts measuring approximately 1/2 in. in diameter by 1/8 in. thick were prepared by cold pressing −400 mesh powder at 46 tsi. These were sintered at 1200°C in hydrogen for 0.5, 4, 8, and 16 hr. The disks were then connected to a helium leak detector by means of a rubber seal, and the helium leak rate was approximately determined at room temperature and 1-atm pressure difference across the disk.

A rough calculation of the helium leak rate required to prevent a pressure buildup in an FTR absorber rod is about 10^{-4} std cm^3/sec. The calculation assumed that the rod contained a 36-in.-high stack of 0.385-in.-diam boron carbide pellets of 90% theoretical density and that the burnup of ^{10}B was 10% per year. Table 3.6 shows that the density of disks prepared in this study increased and the helium leak rates decreased with increasing sintering time. The leak rates varied from 4.1×10^{-5} to 8×10^{-10} std cm^3/sec, the upper and lower limits of the leak detector. Disks having leak rates of about 10^{-6} std cm^3/sec, which were obtained by sintering for 8 hr, are expected to have leak rates of about the proper magnitude for FTR absorber rods when tested at about 500°C. We are presently fabricating additional disks for evaluation of leak rates and reproducibility.

Table 3.6. Characteristics of Stainless Steel Disks[a]

Stainless Steel Type	Sintering Time (hr)	Percent of Theoretical Density[b]	Helium Leak Rate[c] (std cm^3/sec)
304	0.5	89.7	$> 4.1 \times 10^{-5}$
316	0.5	88.0	$> 4.1 \times 10^{-5}$
304	4	87.2	$> 4.1 \times 10^{-5}$
304	4	89.1	$> 4.1 \times 10^{-5}$
316	4	90.1	$> 4.1 \times 10^{-5}$
316	4	91.0	$> 4.1 \times 10^{-5}$
304	8	89.3	$> 4.1 \times 10^{-5}$
304	8	90.5	5.3×10^{-6}
316	8	92.5	3.7×10^{-6}
316	8	92.5	6.1×10^{-7}
304	16	92.5	$< 8 \times 10^{-10}$
316	16	94.2	$< 8 \times 10^{-10}$

[a]Fabrication conditions: −400 mesh powder, cold pressed at 46 tsi, and sintered at 1200°C in hydrogen.

[b]Based upon a density of 7.85 g/cm^3.

[c]4.1×10^{-5} and 8×10^{-10} std cm^3/sec represent the upper and lower limits of measurement.

4. MECHANICAL PROPERTIES OF ALLOYS IN REACTOR ENVIRONMENTS AND DEVELOPMENT OF FBR CLADDING AND STRUCTURAL ALLOYS

J. R. Weir, Jr. and H. E. McCoy, Jr.

The main emphasis of this program is on austenitic stainless steels. Included in our work are types 304 and 316 stainless steel and Ti-modified types 304 and 316 stainless steel. Types 318, 19-9DL, and 12R72HV stainless steel have also been included in recent experiments inserted into the Experimental Breeder Reactor-II (EBR-II). The irradiation effects are determined by measurements of swelling and mechanical properties after irradiation. Experiments are run in three reactors: the EBR-II, the Oak Ridge Research Reactor (ORR), and the High-Flux Isotope Reactor (HFIR). Comparative results should reveal any effects of flux and reactor spectrum. Specimens of each material are irradiated in a variety of conditions so that the effects of irradiation temperature, fluence, and metallurgical condition can be evaluated.

Examination of EBR-II Safety and Control Rod Thimbles

E. E. Bloom, J. O. Stiegler, S. E. Dismuke

Density measurements and transmission electron microscopy examination of specimens of type 304 stainless steel from EBR-II control rod thimble 5A3 and safety rod thimble 3A1 are in progress. The Oak Ridge National Laboratory received flat 1 of the control rod thimble (including material 17.9 cm from centerline of reactor core) and flat 2 of the safety rod thimble (including material 10.6 cm from the centerline of reactor core). Specimens of 2, 3/4, and 1/2 in. lengths were cut from various positions along the flats. Mechanical property test specimens will be machined from the 2-in.-long specimens after density measurements are completed.

After cutting, the samples were cleaned by electropolishing and density measurements were made in water containing Kodak Photo-Flo 200 as a wetting agent. The reported densities are the average of five measurements on each sample. The neutron fluence values are calculated

using run 31F dosimetry data as determined from published curves.[1] The axial temperature distributions were assumed to be the same as for the 3D1 safety rod thimble that was examined previously. Both the neutron fluence and temperature distributions will be revised on receipt of additional information from the WADCO dosimetry center and EBR-II project.

Results of density measurements are presented in Tables 4.1 and 4.2 and the density changes as a function of axial position are shown in Figs. 4.1 and 4.2. In each case the density decrease was calculated using the density of the respective round robin samples. In the control rod thimble the maximum density decrease was 7.55% and occurred about 2 in. above the midplane. For the safety rod thimble the maximum change was 11.0% and occurred about 3 in. above the midplane.

Transmission electron microscopy has been completed on six of the specimens and the data combined with results obtained from previous examinations of components taken from EBR-II. Measurements of void concentration plotted in Fig. 4.3 on a linear scale now give a clear indication of saturation in the concentration of voids at 370°C at a level of about 1.5 to 2 $\times 10^{16}$ voids/cm^3. As saturation is approached the void size distribution changes form (Fig. 4.4). At fluences of 5×10^{22} neutrons/cm^2 and lower the mode of the distribution occurs in the smallest size interval (i.e., less than 100A) and the mean void size is very weakly dependent on fluence ($\bar{D} \propto (\phi t)^{0.15}$) (Ref. 2). At a fluence of 1×10^{23} neurtons/cm^2, where the concentration of voids is beginning to level off, the mode has shifted to a larger size interval and the mean void diameter is increasing at a faster rate. Surprisingly, the maximum void size, defined by the maximum diameter in the highest interval containing at least 1% of the void population, does not increase between 4.8×10^{21} and 1×10^{23} neutrons/cm^2.

Results from control rod thimble 5A3 are not included in Fig. 4.4 because they fall out of line with all the other components that have

---

[1] W. N. McElroy et al., EBR-II Dosimetry Test Data Analysis (Reactor Runs 31E and 31F), BNWL-1420 (1970).

[2] H. R. Brager et al., "Irradiation Produced Defects in Austenitic Stainless Steel," Met. Trans. 2, 1893 (1971).

Table 4.1 Results of Immersion Density Measurements on EBR-II Control Rod Thimble 5A3

Specimen	Specimen Length (in.)	Distance From Dimple[a] (in.)	Distance From Midplane[b] (in.)	Irradiation Temperature (°C)	Fluence,[c] (Neutrons/cm^2, > 0.1 MeV)	Density, (gm/cm^3)	Density Decrease (%)
					$\times 10^{22}$		
X13	0.5	-13.25	-12.05	370	3.3	7.8092	1.14
X12	2.0	-12.0	-10.80	370	4.0	7.8261	0.93
X11	0.75	-10.625	-9.43	370	4.8	7.7937	1.34
X9	2.0	-9.125	-7.93	370	5.7	7.7525	1.86
X6	2.0	-6.50	-5.30	377	7.5	7.6639	2.98
X5	0.5	-5.25	-4.05	383	8.1	7.5966	3.83
X4	2.0	-4.0	-2.80	387	8.8	7.5615	4.28
X3	0.5	-2.75	-1.55	393	9.2	7.4795	5.32
X2	2.0	-1.5	-0.30	400	9.4	7.4414	5.80
Dimple	0.75	0	+1.20	406	9.3	7.3530	6.92
Y2	0.5	0.75	1.95	411	9.0	7.3034	7.55
Y3	2.0	2.00	3.20	418	8.7	7.3401	7.08
Y4	0.5	3.25	4.45	420	8.0	7.3911	6.44
Y5	2.0	4.50	5.70	427	7.2	7.4960	5.11
Y6	0.5	5.75	6.95	429	6.4	7.6313	3.40
Y8	2.0	7.13	8.33	444	6.0	7.7139	2.35
Y9	0.5	8.38	9.58	455	5.7	7.7617	1.74
Y11	2.0	9.75	10.95	460	3.9	7.8087	1.15
Y12	0.5	11.00	12.20	462	3.3	7.8331	0.84
Y13	2.0	12.25	13.45	464	2.7	7.8544	0.57
Y14	2.0	14.25	15.45	465	2.1	7.8760	0.30
Round Robin	1.0	24.0	25.20	470	-	7.8995	0.00

[a]Distance from center of dimple to center of specimen. Negative numbers below, positive numbers above midplane.

[b]Assuming dimple to be 1.2 in. above midplane. Negative numbers below, positive numbers above midplane

[c]Calculated using total exposure of 36,785 MWd and a flux of 1.5×10^{15} neutrons·cm^{-2}·sec^{-1} (> 0.1 MeV) at 50 MW at r = 17.9 cm and Z = 0.

Table 4.2 Results of Immersion Density Measurements on EBR-II Safety Rod Thimble 3A1

Specimen	Specimen Length (in.)	Distance From Dimple[a] (in.)	Distance From Midplane[b] (in.)	Irradiation Temperature (°C)	Fluence,[c] (Neutrons/cm^2, >0.1 MeV)	Density, (gm/cm^3)	Density Decrease (%)
					$\times 10^{22}$		
B-22	0.5	-23.75	-22.55	370	0.92	7.9102	0.005
B-21	2.0	-22.50	-21.30	370	1.13	7.8887	0.24
B-20	0.5	-21.25	-20.05	370	1.41	7.8732	0.42
B-19	2.0	-20.00	-18.80	370	1.73	7.8696	0.47
B-18	0.5	-18.75	-17.55	370	2.1	7.8795	0.34
B-17	2.0	-17.50	-16.30	370	2.6	7.8690	0.47
B-16	0.5	-16.25	-15.05	370	3.3	7.8738	0.41
B-15	2.0	-15.00	-13.80	370	3.9	7.8503	0.71
B-14	0.5	-13.75	-12.55	370	4.7	7.8538	0.67
B-13	2.0	-12.50	-11.30	370	5.6	7.8251	1.03
B-12	0.5	-11.25	-10.05	370	6.6	7.8324	0.94
B-11	2.0	-10.00	-8.80	370	7.9	7.7818	1.58
B-10	0.5	-8.75	-7.55	372	9.2	7.7840	1.55
B-8	0.75	-7.93	-6.73	374	10.2	7.7219	2.3
B-7	0.5	-7.25	-6.05	375	10.9	7.7487	2.0
B-6	1.0	-6.50	-5.30	377	12.2	7.6981	2.6
B-5	0.5	-5.75	-4.55	380	13.2	7.6974	2.5
B-4	2.0	-4.50	-3.30	386	14.3	7.6000	3.9
B-3	0.5	-3.25	-2.05	392	14.7	7.4816	5.4
B-2	2.0	-2.00	-0.80	397	15.0	7.3410	7.2
B-1	0.5	-0.75	+0.45	403	15.0	7.2441	8.4
Dimple	0.75	-0.00	1.20	407	14.7	7.1509	9.6
A-1	0.5	+0.75	1.95	412	14.5	7.1050	10.1
A-2	2.0	2.00	3.20	420	13.7	7.0400	11.0
A-3	0.5	3.25	4.45	429	12.6	7.0522	10.8
A-4	2.0	4.50	5.70	436	11.3	7.2118	8.8

Table 4.2 (Continued)

Specimen	Specimen Length (in.)	Distance From Dimple[a] (in.)	Distance From Midplane[b] (in.)	Irradiation Temperature (oC)	Fluence[c] (Neutrons/cm^2, >0.1 MeV)	Density (gm/cm^3)	Density Decrease (%)
					$\times 10^{22}$		
A-5	0.5	5.75	6.95	444	9.8	7.4727	5.49
A-6	1.0	6.50	7.70	447	9.0	7.5877	4.07
A-7	0.5	7.25	8.45	450	8.1	7.6727	2.96
A-8	2.0	8.50	9.70	455	7.1	7.7262	2.28
A-9	0.5	9.75	10.95	459	5.7	7.7950	1.54
A-10	2.0	11.00	12.20	462	4.9	7.8124	1.19
A-12	2.0	13.50	14.70	465	3.4	7.8499	0.71
A-16	2.0	18.50	19.70	469	1.50	7.8862	0.26
A-18	2.0	21.00	22.20	470	0.98	7.8864	0.25
A-20	1.0	23.00	24.20	470	0.66	7.9020	0.05
Round Robin	1.0	24.00	25.20	470	0.56	7.964	0.00

[a]Distance from center of dimple to center of specimen. Negative numbers below and positive numbers above midplane.

[b]Assuming dimple to be 1.2 in. above midplane. Negative numbers below and positive numbers above midplane.

[c]Calculated using total exposure of 36,785 MWd and a flux of 1.5×10^{15} neutrons$\cdot$cm$^2\cdot$sec^{-1} (>0.1 MeV) at 50 MW at r = 17.9 cm and Z = 0.

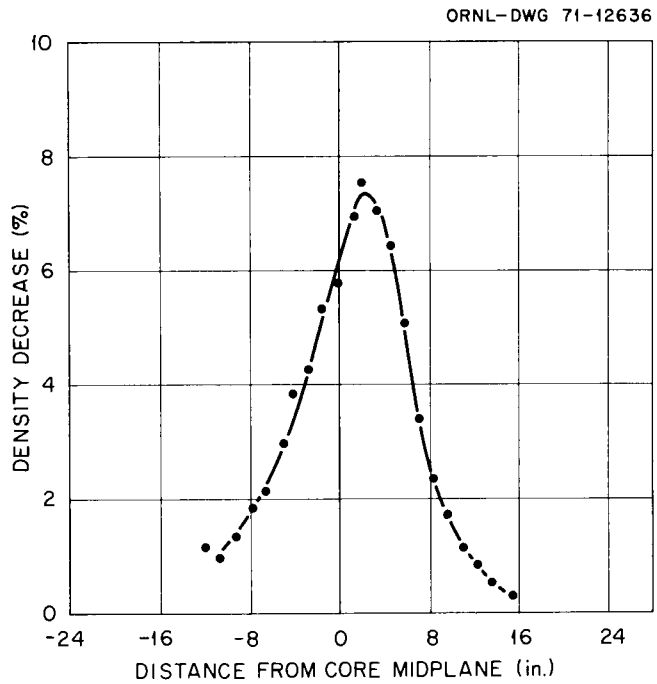

Fig. 4.1. Density Decrease as a Function of Position for EBR-II Safety Rod Thimble 5A3, Flat 2.

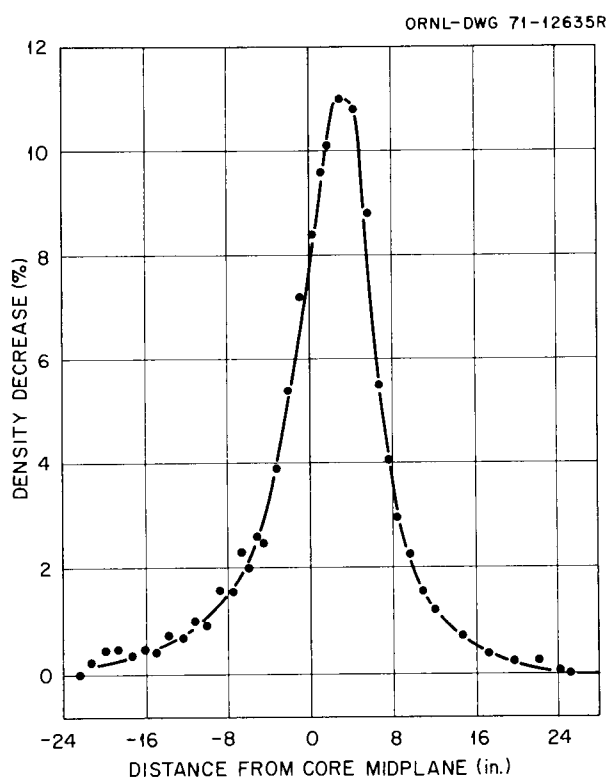

Fig. 4.2. Density Decrease as a Function of Position for EBR-II Safety Rod Thimble 3A1, Flat 2.

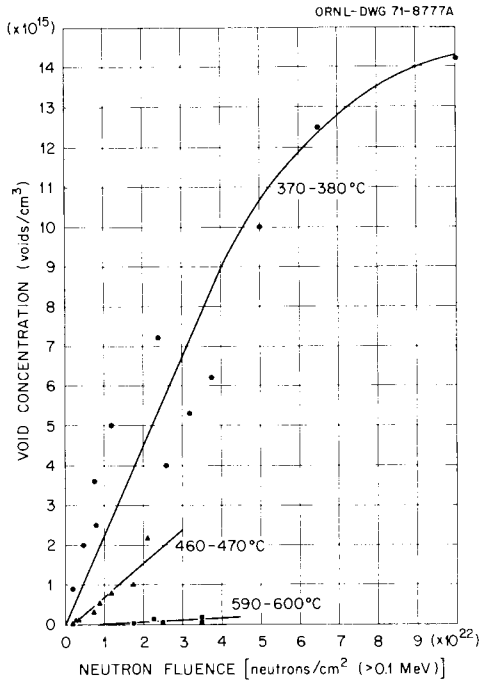

Fig. 4.3 Linear Plot of Void Concentration as a Function of Fast Neutron Fluence for Annealed Type 304 Stainless Steel.

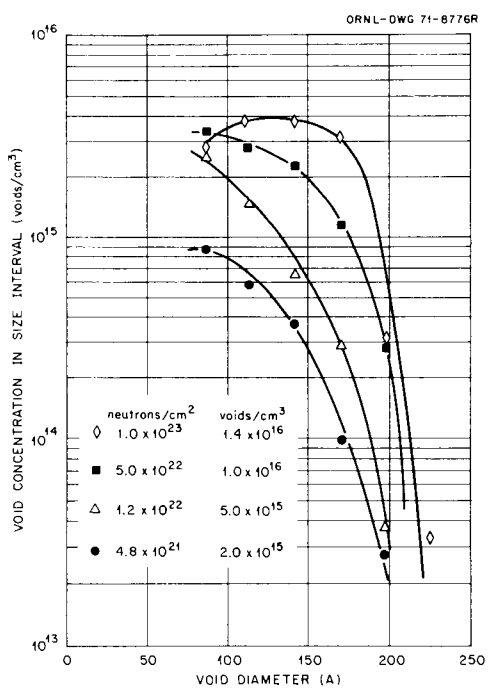

Fig. 4.4 Effect of Fluence on the Void Size Distribution Curve for Type 304 Stainless Steel Irradiated at 370–380°C.

been examined. This thimble was anomalous in that it swelled significantly more than expected by the empirical equations developed by Brager et al.[2] In the ORNL specimens the additional swelling resulted from excessive growth of the existing voids rather than by nucleation of additional ones. As a consequence, the maximum void size was well above the value of 210A found in the other specimens.

Not enough data are available at a temperature of 470°C to provide evidence of a saturation in the concentration of voids. Concentration values for specimens irradiated at 590°C in some experimental subassemblies are also plotted in Fig. 4.3. Although it is not obvious because of the scale required to display data from other temperatures on the graph, the void concentration has saturated at a value of about 2×10^{14} voids/cm^3 at a fluence of 3.5×10^{22} neutrons/cm^2. It appears that void nucleation will ultimately cease, but that the concentration and fluence at which saturation occurs are dependent on the irradiation temperature.

When the rate of nucleation of voids decreases, the rate of growth of the voids increases and swelling continues. Not enough data are available yet to determine whether the rate of swelling is changed when the void nucleation rate decreases.

In this work void sizes were determined by measuring the inner diameter of the dark ring delineating the void in micrographs taken in a slightly underfocused condition. Recently Ruhle[3] performed calculations that indicate that the outer diameter should be used. In addition, no corrections for finite foil thickness were applied. These are relatively constant systematic errors that will change the absolute values of the void diameters slightly, but should have little effect on relative values.

---

[3] Manfred Ruhle, "Transmission Electron Microscopy of Radiation-Induced Defects," International Conference on Radiation-Induced Voids in Metals, State University of New York, Albany, June 9–11, 1971 (to be published in the proceedings).

Some Effects of Composition and Microstructures on Radiation Damage in Stainless Steels

J. O. Stiegler, E. E. Bloom

Earlier studies have shown that the damage introduced in stainless steels by neutron irradiation at elevated temperatures is a very sensitive function of the composition[4,5] and microstructure.[6,7] Relatively small changes in these variables can produce large changes in the population of voids, dislocation loops and lines, and precipitate particles that form during irradiation. Since swelling and mechanical properties depend critically on the type, amount, and distribution of the defects that form, knowledge and understanding of the changes resulting from a given treatment are essential to defining the conditions that will produce the optimum structure for a particular reactor application.

EBR-II experimental subassembly X034A contained specimens of types 316 and titanium modified 316 (316 + 0.23% Ti) stainless steels in several annealed and cold worked conditions which can be compared with type 304 stainless steel irradiated in previous experiments. Here we report on the microstructural observations of specimens irradiated to a fluence of about 1.9×10^{22} neutrons/cm^2 (>0.1 MeV) at 450, 580 and about 700°C.

---

[4] T. Lauritzen, A. Withrop, and U. Wolff, "Swelling of Austenitic Stainless Steels Under Fast-Neutron Irradiation at Elevated Temperatures," Nucl. Eng. Des. 9, 244 (1970).

[5] E. E. Bloom and J. O. Stiegler, "A Comparison of Irradiation Induced Swelling and Void Formation in Two Austenitic Stainless Steels," J. Nucl. Mater. 35, 244 (1970).

[6] J. O. Stiegler and E. E. Bloom, "The Effect of Thermo Mechanical Treatments on Void Formation in Irradiated Stainless Steel," submitted to the Journal of Nuclear Materials for publication.

[7] J. L. Straalsund and H. R. Brager, paper presented at International Conference on Radiation Induced Voids in Metals, Albany, New York, June 9–11, 1971 (to be published in the proceedings).

Annealed Materials

The damage structures of the materials annealed and fully recrystallized before irradiation are qualitatively similar to those of type 304 stainless steel in the sense that they include voids, faulted dislocation loops for irradiation temperatures below about 550°C, and a loosely organized dislocation network at higher temperatures. Important differences exist in the numbers and sizes of these defects and in their variations with irradiation temperature.

Statistics describing the void populations in types 316, titanium modified 316, and 304 stainless steels are given in Table 4.3. The values for type 304 stainless steel were computed from the empirical equations developed by Brager et al.[2] At both 450 and 580°C void concentrations were over an order of magnitude lower in type 316 stainless steel than in type 304 stainless steel, but void sizes were larger in type 316 stainless steel. At 450°C the void concentration was so low in the type 316 that it swelled only about 10% as much as type 304, but at 580°C the larger void size in the type 316 overcame the reduced void concentration and the two swelled comparable amounts. At 450°C the titanium modified type 316 stainless steel exhibited void concentrations and swelling intermediate between the other two, but at 580°C it contained such a low concentration of voids ($\sim 10^{12}/cm^3$) that it swelled only a negligible amount.

It would appear from these limited observations that swelling in the three steels varies differently with temperature. The temperature of peak swelling seems to be higher in type 316 stainless steel than in type 304 and possibly lower in the titanium modified type 316 than in type 304. Alternatively, the results could be interpreted in terms of shifts in the threshold fluences for void formation as shown in Fig. 4.3. For example, the low void concentration in the titanium modified stainless steel at 580°C could arise because the threshold fluence for void formation in that material is at or near the fluence used in this study. At higher fluences the differences may not be as significant. This points out the necessity in screening studies to examine specimens irradiated at enough temperatures and fluences to understand threshold and temperature effects.

Table 4.3 Summary of Void Statistics

Stainless Steel Alloy Type	Condition	Irradiated Temperature (°C)	Fluence (Neutrons/cm², >0.1 MeV)	Void Concentration (cm⁻³)	Mean Void Diameter (A)	$\frac{\Delta V}{V_o}$ %
			$\times 10^{22}$			
316	Annealed	450	1.9	6.9×10^{13}	236	0.058
Ti-Modified 316	Annealed	450	1.9	6.8×10^{14}	172	0.20
304	Annealed	450	1.9	1.3×10^{15}	178	0.54
316	Annealed	580	1.9	10^{13}	666	0.21
Ti-Modified 316	Annealed	580	1.9	$\sim 10^{12}$	-	-
304	Annealed	580	1.9	1.7×10^{14}	258	0.26
316	20% cold work	450	1.9	0	0	0
316	10% cold work	580	1.9	0	0	0
316	20% cold work	580	2.7	(a)	(a)	(a)
Ti-Modified 316	10% cold work	580	1.9	0	0	0
316	Annealed	675/715	1.9	$\sim 7 \times 10^{12}$ [b]	200	-
316	20% cold work	675/715	2.3	0	0	0

[a] A very low concentration of non-homogeneously distributed voids were observed.

[b] Helium bubbles.

At 450°C all specimens contained faulted dislocation loops. Quantitative estimates of sizes and concentrations are in progress. The only unusual feature was large zones adjacent to grain boundaries denuded of voids but enhanced with loops in the titanium modified type 316 stainless steel.

At 580°C all specimens contained a dislocation structure although a few faulted loops were present in the titanium modified type 316 stainless steel as can be seen in Fig. 4.5. This specimen also showed a structure of small dislocation loops clustered about many of the dislocation lines.

At 450°C only fine scale precipitation of carbides occurred within the grains and grain boundaries were generally free of precipitates in all specimens. At 580°C both blocky and needle-like precipitate particles formed within the grains of the standard type 316 stainless steel (Fig. 4.6). Note that all voids are associated with these precipitates but that not all precipitates have voids attached. The blocky precipitates, which have been identified as $M_{23}C_6$, are present in a concentration of about $2 \times 10^{12}/cm^3$. The needle-like precipitates, which run in [001] directions, gave diffraction patterns that were inconsistent with any of the equilibrium phases formed in this system, viz $M_{23}C_6$, M_6C, MC, sigma, Laves, or chi. In some instances voids were located at the center of three mutually perpendicular needle-like precipitates giving an appearance of childrens' jacks. In a few instances several voids were found located along a single needle-like precipitate resembling a shish kebab. The needle-like precipitates were the most common form in this system and were present in a concentration of about $4 \times 10^{13}/cm^3$. Isolated precipitate particles were present in the grain boundaries of the standard type 316 stainless steel. The titanium modified steel was relatively free of precipitates. A few, isolated $M_{23}C_6$ particles were found on grain boundaries and within the grains.

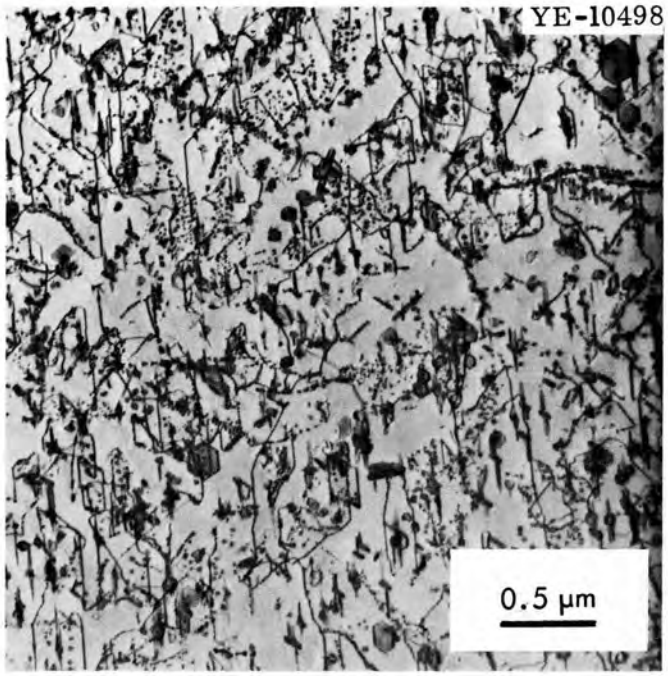

Fig. 4.5 Dislocation Structure in Titanium Modified Type 316 Stainless Steel Irradiated in EBR-II to a Fluence of 1.9×10^{22} neutrons/cm^2 (>0.1 MeV) at About 580°C.

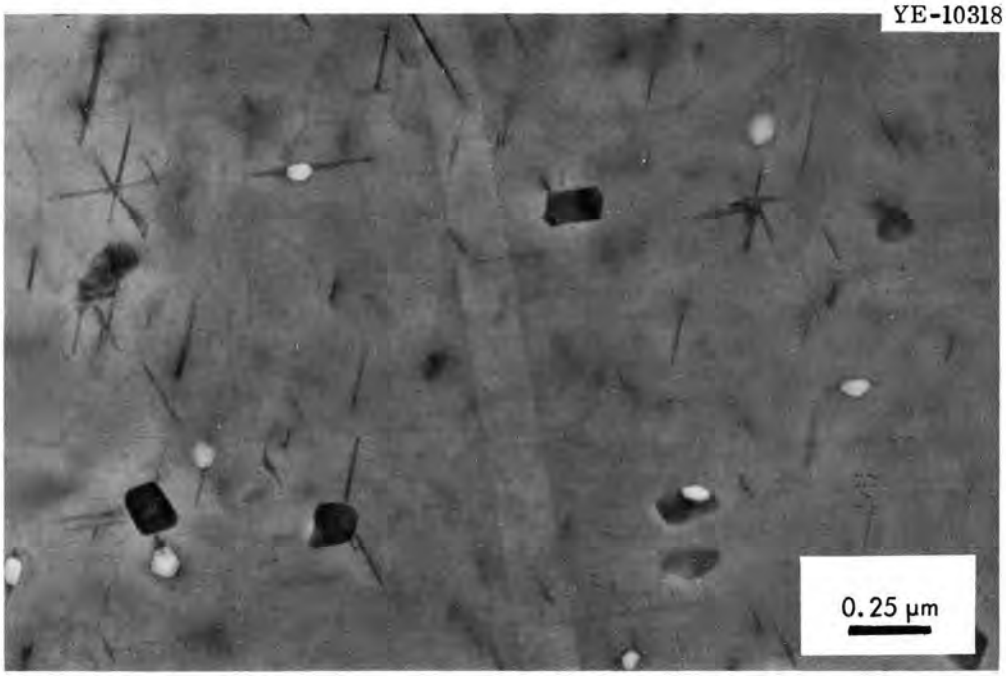

Fig. 4.6 Voids and Precipitate Structure in Type 316 Stainless Steel Irradiated in the Annealed Condition to a Fluence of 1.9×10^{22} neutrons/cm^2 (>0.1 MeV) at About 580°C.

Cold Worked Materials

Both void formation and precipitation reactions were altered by cold working stainless steels prior to irradiation. The changes appeared to be dependent on the temperature of irradiation and on the degree of deformation.

After a fluence of 1.9×10^{22} neutrons/cm^2 at 450°C, 20% cold working completely suppressed void formation. Little, if any, recovery was evident and no precipitation was obvious, although the microstructure was so complex that it would be difficult to resolve small precipitate particles.

At 580°C recovery, but not recrystallization, was obvious in type 316 stainless steel deformed both 10 and 20% prior to irradiation. No voids were visible in the specimen cold worked 10%. Discontinuous, blocky precipitates were present in all grain boundaries and continuous precipitation occurred on the stacking fault bands formed during deformation. Some $M_{23}C_6$ particles were also present but between and not on the stacking fault bands. In the specimens deformed 20% prior to irradiation more extensive recovery occurred and isolated patches of voids were found in some of the recovered regions between stacking fault bands (Fig. 4.7). Note that this specimen was irradiated to a slightly higher fluence than the others discussed in this section, 2.7×10^{22} neutrons/cm^2.

The titanium modified type 316 stainless steel deformed 10% prior to irradiation at 580°C also contained no voids. Some recovery occurred along with precipitation of massive, but isolated precipitates on all grain boundaries. Smaller, isolated precipitate particles were present on stacking fault bands and in recovered areas. All have been tentatively identified as $M_{23}C_6$.

During irradiation in the temperature range of 675 to 715°C, a small amount of recrystallization occurred in standard type 316 stainless steel cold worked 20%. The microstructure generally was composed of a recovered cell structure accompanied by σ phase precipitation (Fig. 4.8). Massive σ precipitates formed at grain boundaries and at interfaces between different textures of the cell structure within a single grain. Smaller σ precipitates were located on the cell walls. No voids or

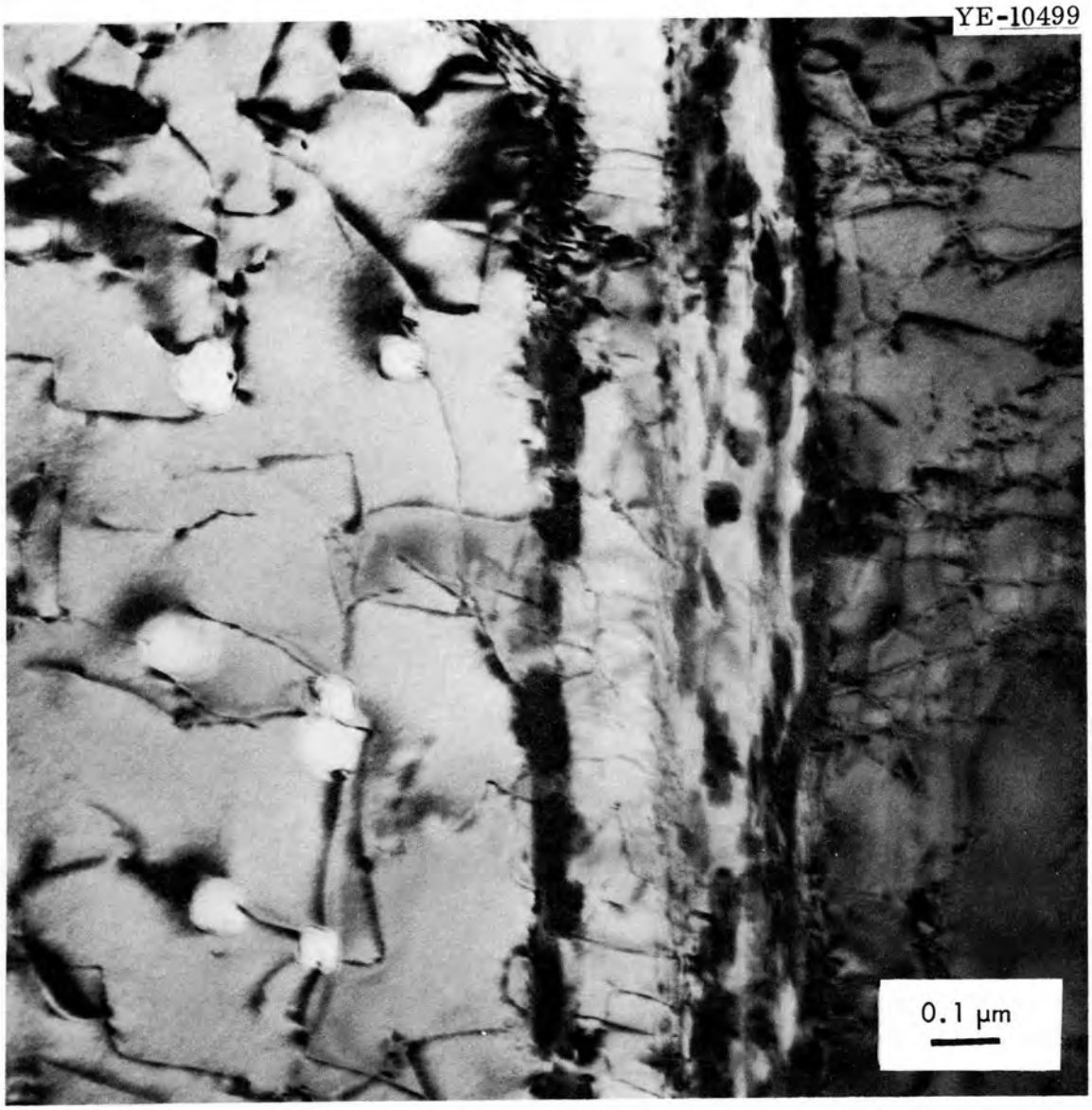

Fig. 4.7 Voids, Dislocation and Precipitates in Type 316 Stainless Steel Deformed 20% by Cold Working Prior to Irradiation at About 580°C to a Fluence of 2.7×10^{22} neutrons/cm^2 (>0.1 MeV).

Fig. 4.8 Recovered Structure and Sigma Phase Precipitates in Type 316 Stainless Steel Deformed 20% by Cold Working Prior to Irradiation at a Temperature in the Range 675–715 °C to a Fluence of 2.3×10^{22} neutrons/cm^2 (>0.1 MeV).

cavities of any sort were visible. Annealed material irradiated in this same temperature range contained small cavities 150 to 200 A in diameter in a concentration of slightly less than $10^{13}/cm^3$. Many, but not all, were attached to blocky $M_{23}C_6$ particles (Fig. 4.9). Because of their small size these cavities are believed to be equilibrium helium bubbles. In addition, all grain boundaries were covered by a continuous network of small, blocky precipitate particles. At slightly higher irradiation temperatures sigma phase also formed in annealed material primarily at triple grain junctions.

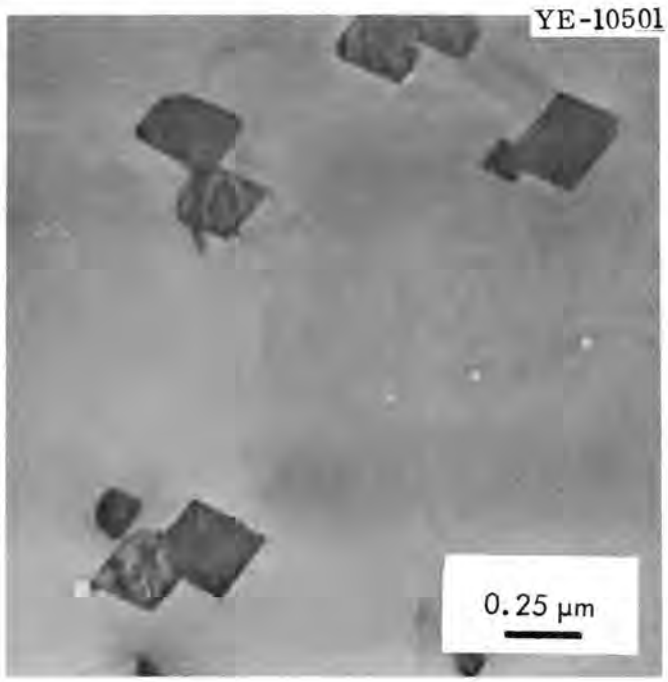

Fig. 4.9 Helium Bubbles and Precipitates in Type 316 Stainless Steel Irradiated in the Annealed Condition to a Fluence of 1.9×10^{22} Neutrons/cm^2 (>0.1 MeV) in the Temperature Range 675–715°C.

Postirradiation Mechanical Properties of Types 316 and Titanium-Modified 316 Stainless Steel

Figures 4.10 and 4.11 show the effects of fast neutron irradiation on the tensile properties of type 316 stainless steel when irradiated in the annealed and 20% cold worked conditions respectively. In the annealed condition, specimens irradiated and tested at 450°C exhibited an increase in yield stress over those unirradiated of approximately a

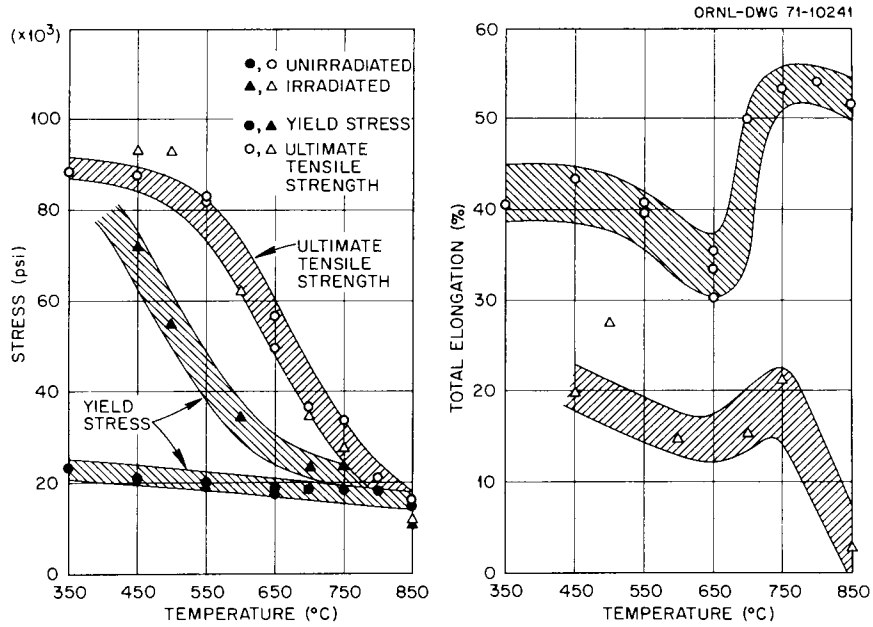

Fig. 4.10 Effect of Irradiation to Fluences in the Range 1.5–2.7 × 10^{22} Neutrons/cm^2 (>0.1 MeV) on the Tensile Properties of Annealed Type 316 Stainless Steel. Specimens were Irradiated and Tested at Approximately the Same Temperature.

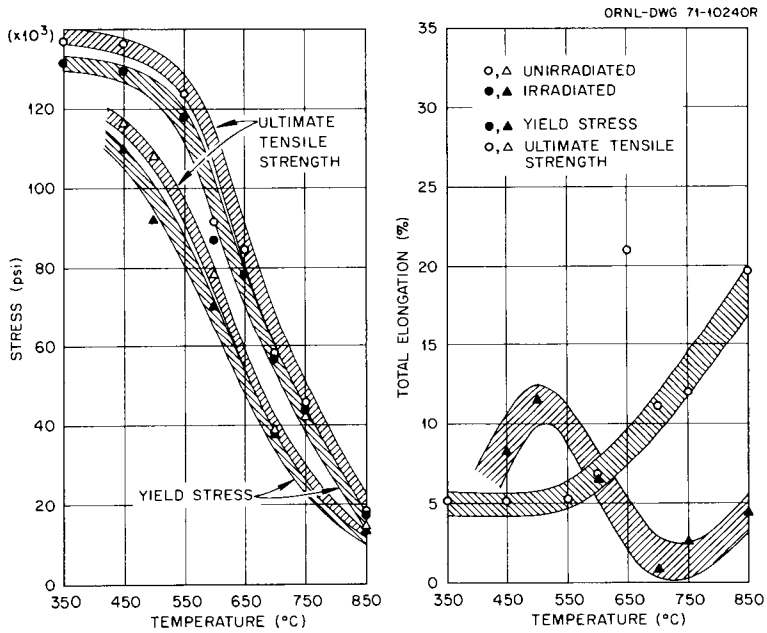

Fig. 4.11. Effect of Irradiation to Fluences in the Range 1.5–2.7 × 10^{22} Neutrons/cm^2 (>0.1 MeV) on the Tensile Properties of 20% Cold Worked Type 316 Stainless Steel. Specimens were Irradiated and Tested at Approximately the Same Temperature.

factor of 3.5. With increasing temperature the yield stress of the irradiated specimens decreased and became equal to that of unirradiated material at about 800°C. At the highest irradiation and test temperature (850°C), the yield stress of the irradiated specimen was lower than that of the unirradiated specimen by about 4000 psi. At the lower temperatures the ultimate tensile strength was increased slightly by irradiation while at the higher temperatures the values for the irradiated specimens were slightly lower than for unirradiated specimens. Irradiation caused a decrease in total elongation at all temperatures with the largest effect occurring at the highest temperature.

Irradiation of the 20% cold worked material caused a decrease of the yield stress and ultimate tensile strength when compared to the as-cold worked condition. This decrease was observed for irradiation temperatures as low as 450°C. The yield strengths of thermal control samples that had been 4000 hr at 450 and 550°C were nearly equal to those of the samples in the as-cold worked condition. Thus, irradiation may enhance recovery. Total elongation values reflect the fact that recovery has occurred i.e., the ductility of the specimens irradiated and tested at 450 and 500°C was higher than that of the specimens tested in the as-cold worked condition. At still higher temperatures (above 500°C) where transmutation produced helium became important, the ductility dropped below the unirradiated value. The apparent minimum in ductility at 700°C followed by higher values at 850°C may be a result of recrystallization.

Postirradiation creep-rupture properties are shown in Figs. 4.12, 4.13 and 4.14. Irradiation of annealed type 316 stainless steel resulted in reduced rupture life for all temperatures in the range of 550 to 750°C. The specimens were irradiated and tested near the same temperature. For these fast neutron fluences the reduction in rupture life was small at 550, 600, and 650°C but became larger at 700 and 750°C. No significant effect of irradiation on creep rate was found except at 750°C where the irradiated specimens exhibited creep rates about an order of magnitude higher than the annealed material. When irradiated in the 20% cold worked condition, an increase in rupture life and decrease in creep rate occurred at 550°C. At 600 and 650°C the rupture life was reduced

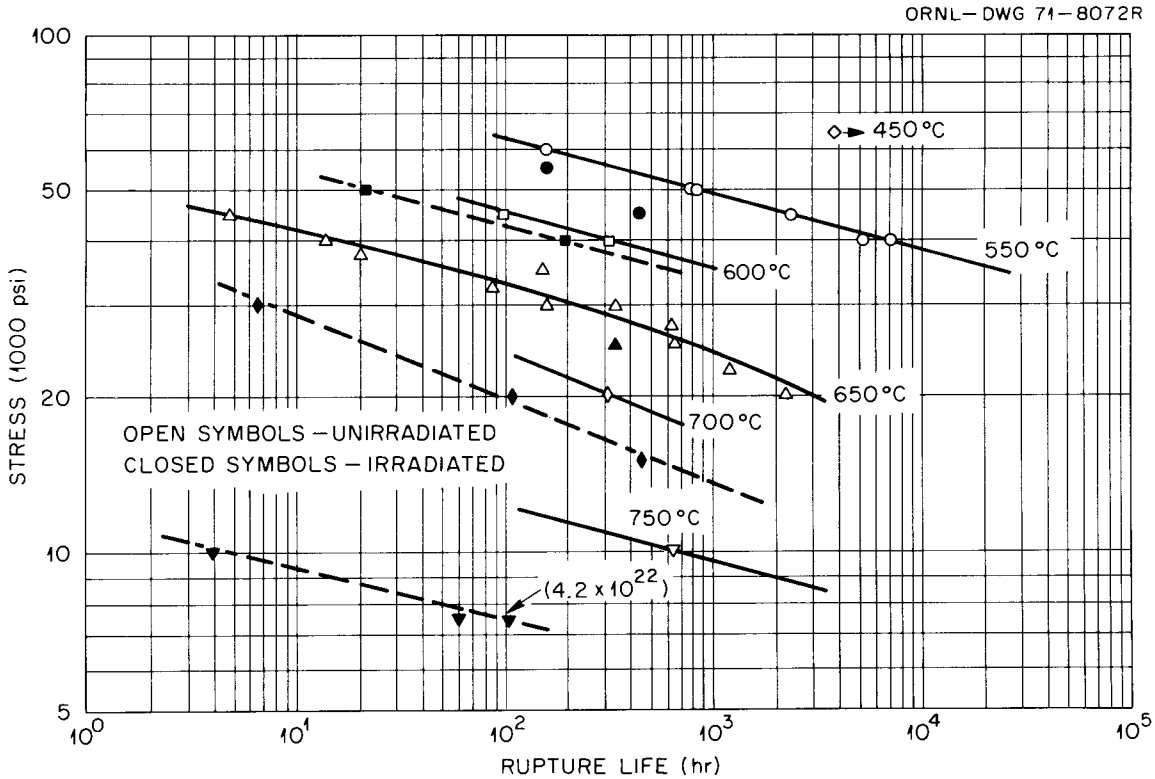

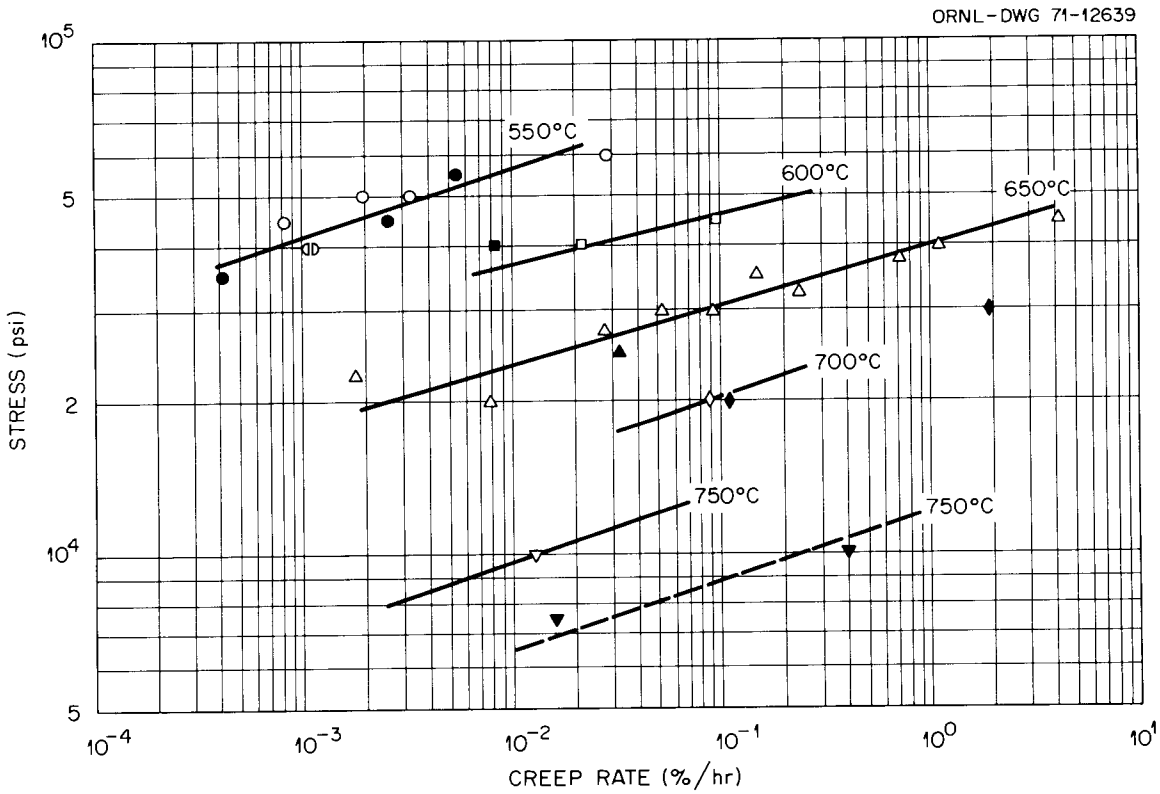

Fig. 4.12 Effect of Irradiation to Fluences in the Range 1.9 to 2.7 X 10^{22} Neutrons/cm^2 (>0.1 MeV) on the Creep Properties of Annealed Type 316 Stainless Steel. Specimens were irradiated within 30°C of the respective test temperatures.

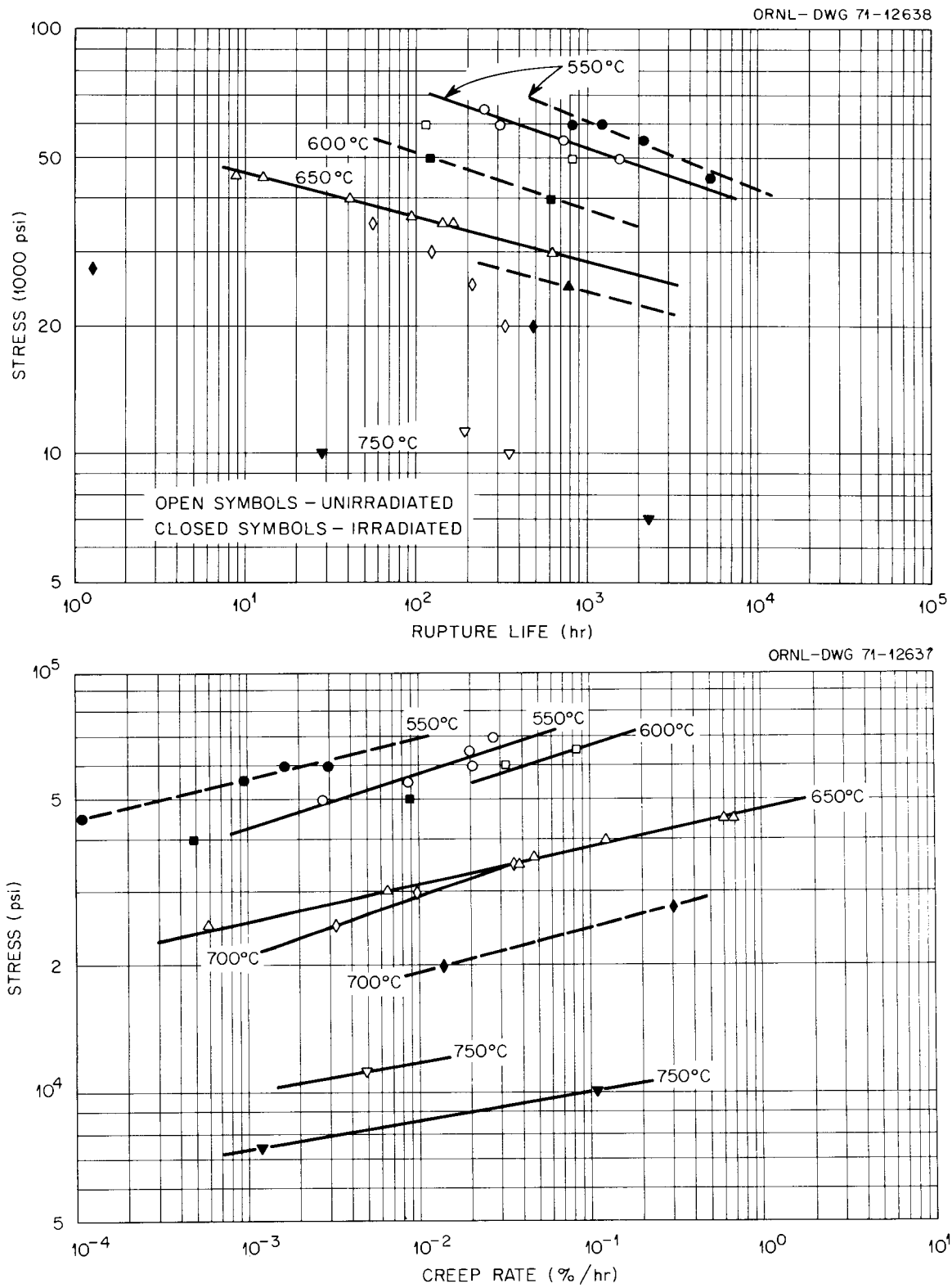

Fig. 4.13 Effect of Irradiation to Fluences in the Range 1.9 to 2.7×10^{22} Neutrons/cm^2 (>0.1 MeV) on the Creep Properties of 20% Cold Worked Type 316 Stainless Steel. Specimens were irradiated within 30°C of the respective test temperatures.

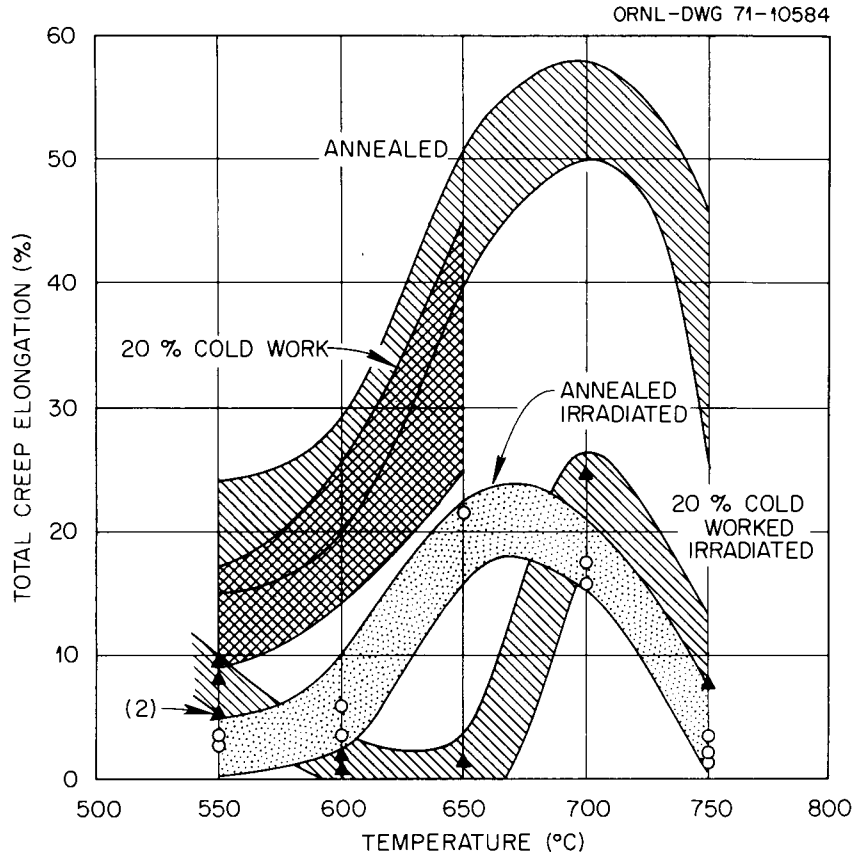

Fig. 4.14 Effect of Fast Neutron Irradiation on the Creep-Rupture Ductility of Type 316 Stainless Steel Irradiated in the Annealed and 20% Cold Worked Conditions to Fluences in the Range 1.5 to 2.7 × 10^{22} Neutrons/cm^2 (>0.1 MeV).

by a factor of 3 to 4 with no large change in minimum creep rate. At 700 and 750°C the rupture life was reduced and large increases in creep rate occurred.

Ductility, as measured by total elongation, is shown in Fig. 4.14. The scatterbands for the unirradiated specimens tested in the annealed and 20% cold worked conditions represent results for tests at 550, 600, 650, 700 and 750°C and tests having rupture lives in the range of 10 to 7000 hr. No correlation between creep elongation and stress (thus rupture life and creep rate) was apparent. For both the annealed and cold worked material the ductility was lowest at 550, then increased with temperature up to 700°C, and decreased at higher temperatures. The postirradiation creep-rupture ductility of both annealed and 20% cold worked specimens was reduced. The magnitude of this reduction was

strongly dependent on the irradiation temperature, but rather insensitive to stress, rupture life, and creep rate.

Examination of tested specimens using optical, transmission, and scanning microscopy is in progress. The microstructure of a specimen of standard type 316 stainless steel irradiated in the annealed condition at 580°C to 1.9×10^{22} neutrons/cm^2 (>0.1 MeV) is shown in Fig. 4.15. The blocky precipitates, present in a concentration of about 2×10^{12}/cm^3, have been identified as $M_{23}C_6$. About 4×10^{13}/cm^3 needle precipitates with their long direction parallel to the <001> direction of the lattice were also present. These precipitates have not been positively identified. The concentrations of voids, faulted dislocation loops, and dislocation lines were 1×10^{13} voids/cm^3, 1×10^{13} loops/cm^3, and 9×10^9 cm/cm^3. When tested at 550°C and 45,000 psi the specimen failed in about 500 hr after 3.6% total elongation compared with a rupture life

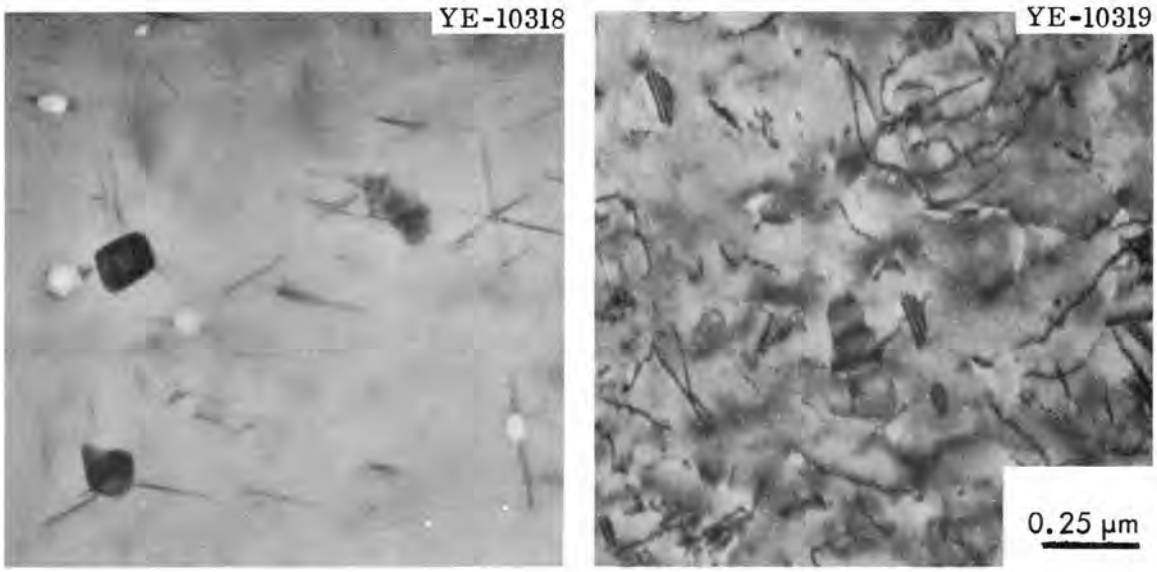

Fig. 4.15 Microstructures of Type 316 Stainless Steel Irradiated in the Annealed Condition at 580°C to 1.9×10^{22} Neutrons/cm^2 (>0.1 MeV).

of about 2500 hr and a total elongation of 17% for an unirradiated specimen. The fracture, shown in Fig. 4.16, was a mixture of inter- and intragranular. Numerous grain boundary cracks running normal to the applied load were present. Scanning microscopy revealed that a portion of the fracture had occurred in a completely intergranular fashion (Fig. 4.17a, while in other regions the fracture consisted of what appeared to be intergranular fracture areas surrounded by more ductile transgranular fracture areas (Fig. 4.17b). It appears that the failure is initiated by the formation of grain boundary cracks that propagate and eventually reduce the effective cross section of the specimen. The final separation occurs by the linking of these cracks at a high strain rate with considerable transgranular fracturing.

Fig. 4.16 As-polished Longitudinal Section of Fracture in Type 316 Stainless Steel Specimen Irradiated at 580°C to 1.9×10^{22} Neutrons/cm^2 and Tested at 550°C and 45,000 psi.

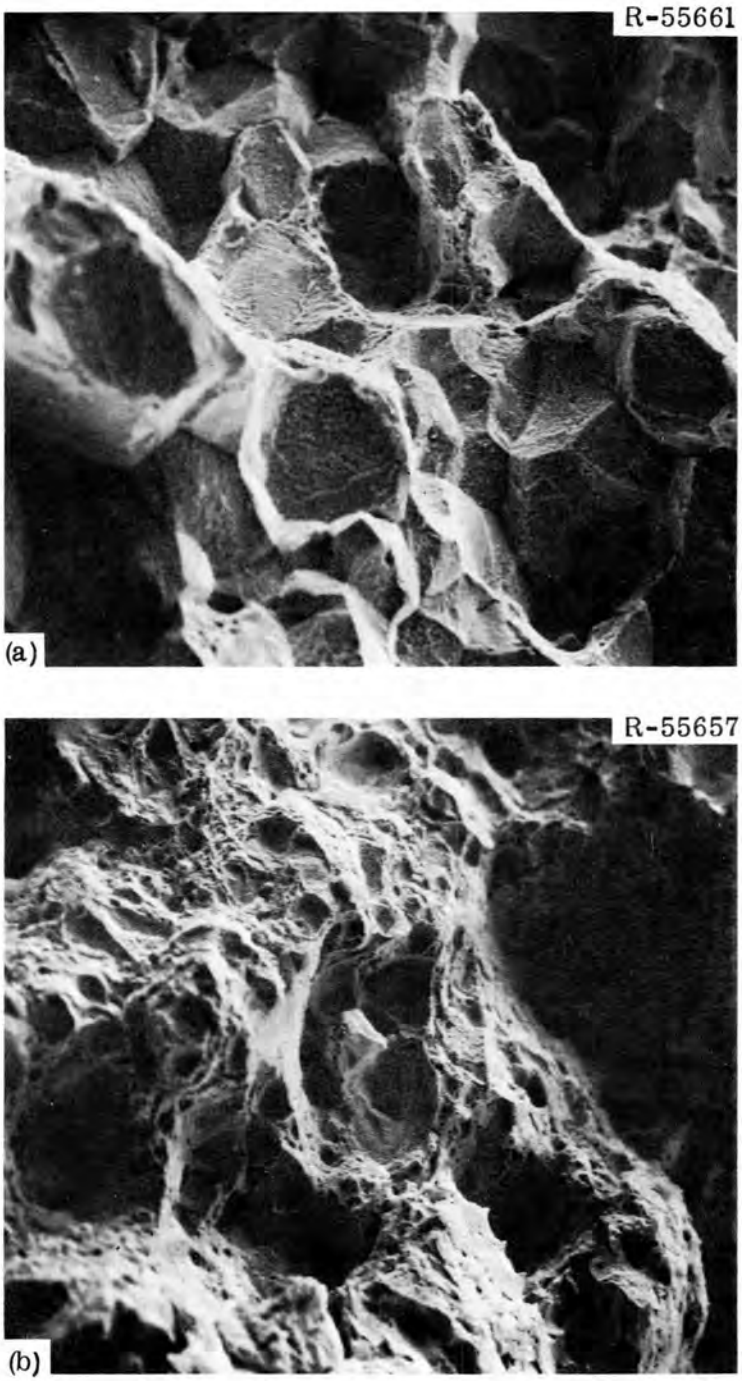

Fig. 4.17 Scanning Electron Micrographs of Fracture in Type 316 Stainless Steel Specimen Irradiated at 580°C to 1.9×10^{22} Neutrons/cm^2 and Tested at 550°C and 45,000 psi. a) area of intergranular fracture, b) area of inter- and transgranular fracture.

The microstructure of the tested gage section is shown in Fig. 4.18. Neither the void size nor concentration appeared to change significantly during test. The dislocation density had increased to 4×10^{10} cm/cm^3 and no faulted loops were found.

The behavior of type 316 stainless steel irradiated in the 20% cold work condition at 580°C to 2.7×10^{22} neutrons/cm^2 and then tested at 600°C and 40,000 psi stress is summarized in Fig. 4.19. During irradiation heavy precipitation occurred on the deformation bands that were produced during the cold working operation. Recovery of the cold worked structure had occurred in the regions between these bands. A heterogeneous distribution of voids, located primarily in the recovered regions, was present. The specimen failed at about 0.9% total elongation. The failure was almost entirely intergranular and only a few very narrow sharp grain boundary cracks were present near the fracture.

The results of tensile and creep-rupture tests on Ti-modified (0.23%) type 316 stainless steel irradiated in the annealed condition at temperatures in the range of 450 to 870°C to fluences up to 4.4×10^{22} neutrons/cm^2 are listed in Tables 4.4 and 4.5

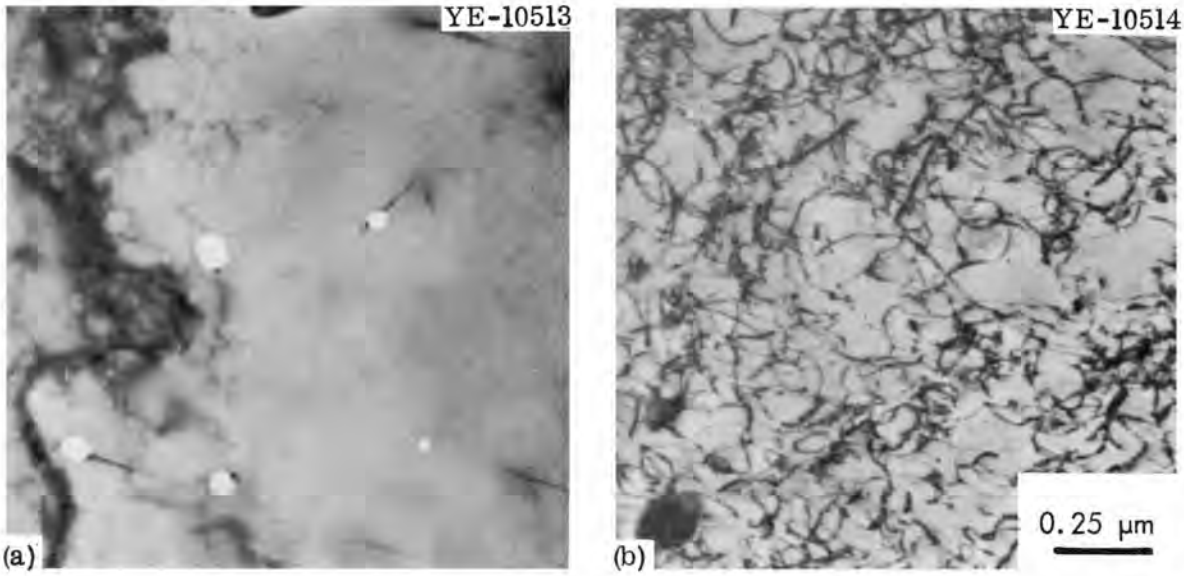

Fig. 4.18 Microstructures of Gage Section of Specimen Irradiated at 580°C to 1.9×10^{22} Neutrons/cm^2 (>0.1 MeV) and Tested at 550°C and 45,000 psi Stress. Diffraction conditions to show a) voids and b) dislocation

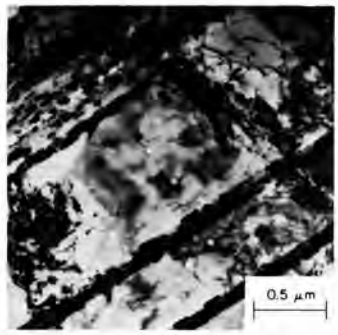

MICROSTRUCTURE OF SPECIMEN IRRADIATED AT 580°C TO 2.7 x 10^{22} neutrons/cm^2 (>0.1 MeV)

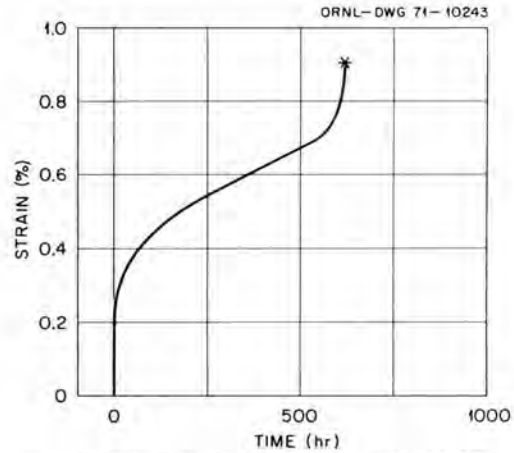

STRAIN-TIME CURVE FOR SPECIMEN TESTED AT 600°C AND 40,000 psi STRESS

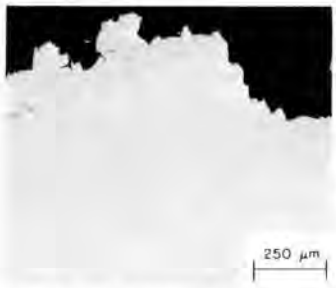

AS POLISHED SECTION OF FRACTURE

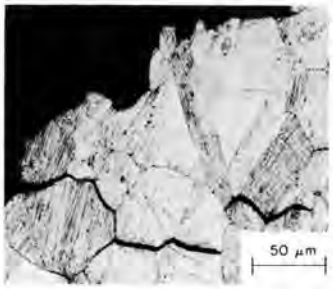

ETCHED SECTION OF FRACTURE

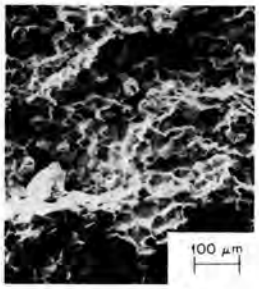

SEM MICROGRAPH

Fig. 4.19 Summary of the Postirradiation Creep Behavior of 20% Cold Worked Type 316 Stainless Steel.

Table 4.4 Postirradiation Tensile Properties of Ti-Modified Type 316 Stainless Steel [a]

Irradiation Temperature (°C)	Fluence (Neutrons/cm^2 >0.1 MeV)	Test Temperature (°C)	Yield Stress (psi)	Ultimate Tensile Stress (psi)	Total Elongation (%)	Reduction in Area (%)
	$\times 10^{22}$					
465	1.2	450	44,400	82,200	35.4	30.3
510	1.5	500	35,100	78,300	31.9	50.6
630	1.2	600	31,200	56,600	29.8	36.7

[a]Strain Rate 0.002 min^{-1}

Table 4.5 Postirradiation Creep-Rupture Properties of Ti-Modified Type 316 Stainless Steel

Irradiation Temperature (°C)	Fluence (Neutrons/cm², >0.1 MeV)	Test Temperature (°C)	Stress (psi)	Rupture Life (hr)	Creep Rate (%/hr)	Total Elongation (%)
	$\times 10^{22}$					
580	2.3	550	55,000	252.9	0.031	17.1
580	2.7	550	45,000	1930.0	0.0036	19.9
580	1.5	600	50,000	184.7	0.01	10.1
580	2.3	600	40,000	535.8	0.01	18.1
630	2.3	650	25,000	1590.3	0.01	28.2
870	4.4	750	7,500	>1250 [a]		>4.1
835	4.4	750	7,500	>335 [a]		>10.4

[a]Presently in test

At 450,500 and 600°C the yield and ultimate tensile strengths for the modified stainless steel were slightly lower than for standard type 316 stainless steel. (See Fig. 4.10) This appears to be a result of the lower concentration of voids and dislocations in the modified alloy for these fluence and temperature conditions. The total elongation was 10 to 15 percentage points higher for the modified alloy than for the standard steel. The rupture life of the modified steel appears to be slightly higher than standard type 316 stainless steel at 550, 600, and 650°C. On the basis of tests still in progress, the modified alloy appears to be significantly stronger at the higher irradiation and test temperature of 750°C. The total creep elongations for the modified steel were significantly higher (see Fig. 4.14) than those of the standard alloy. This was particularly true at 550°C where irradiation has its most pronounced effect on creep ductility.

Precipitate-Free Ultra-Fine Grains, A New Approach to Heat Treatment

D. Fahr

Great research efforts are being made to reduce the effect of irradiation-induced defects and formation of voids and bubbles on the postirradiation mechanical properties and the structural stability of stainless steels during irradiation. To increase strength, ductility, and corrosion resistance and to limit the amount of swelling, the microstructure is being changed by heat treatment or by modifying the composition of steels.

Very small compositional changes can cause drastic changes in the irradiation or void structure. Since interstitials migrate more rapidly than vacancies, they are more readily absorbed at sinks such as grain boundaries and dislocations, and an excess vacancy concentration develops and can ultimately lead to the formation of voids. An obvious way to counteract the formation of voids is to increase the density of sinks for vacancies and interstitials and effectively decrease the migration distance. This can be achieved by increasing the dislocation density, decreasing the grain size, or by finely-dispersed precipitates. Such precipitate particles are known to also act as nucleation and pinning sites for helium bubbles and prevent segregation of helium to grain boundaries. A fine grain size lowers the tendency to intercrystalline cracking in most materials in creep-rupture testing in the unirradiated condition. Since the thermal stability of a dislocation network or a microstructure characterized by small grains decreases with increasing amounts of cold work or decreasing grain size, there is an optimum range of these variables determined by their beneficial effects on void formation and their stability at elevated temperatures.

The composition of a steel can be changed directly by adding alloying elements or indirectly by allowing extensive precipitation to take place. The microstructure of a cold worked or small-grained steel can also be changed by recrystallization or grain growth. All this can be accomplished with heat treatments alone. Simultaneous working and heat

treating is known to increase strength and ductility in unirradiated steels; moreover, it permits precipitation to take place within the grains in steels where precipitates form preferrentially at grain boundaries during most traditional heat treatments. The practice of deliberately soaking steel after it has reached furnace temperature originated long ago when temperature control and measurement were far inferior to what is possible today. The recrystallization temperature is commonly defined as the temperature at which recrystallization can be completed within 1 hr. Such conditions lead to extensive precipitation, especially when grain refinement is achieved by several cold work and recrystallization cycles. While the final grain size can be measured, it is almost impossible to make any positive statement as to the ultimate composition of the matrix.

We have applied various thermo-mechanical treatments to standard type 316 stainless steel, 19-9DL, and Sandvik 12R72HV, and pre- and post-irradiation mechanical property data will be available soon. A widespread interest in the austenitic stainless steel, Sandvik 12R72HV, is mainly due to its excellent long-term creep strength at high temperatures. This high strength is caused by precipitation taking place during the creep process at temperatures between 650 and 750°C. The higher alloying content in this steel, as compared to that of type 316 stainless steel, reduces the diffusion rate of the alloying elements participating in the precipitation process to such an extent that deep strengths almost twice as high as in type 316 stainless steel can be attained around 700°C. The rate of growth and coalescence of the precipitate particles is also very low. To form the optimum precipitate during the creep process, the steel should be precipitate free at the outset. Thus a solution anneal has to precede the creep test or any intermediate plastic deformation at room temperature. For best results, Sandvik 12R72HV is usually solution annealed for 30 to 60 min at 1150°C. At this temperature, however, rapid grain growth occurs and the resulting grain size presents a serious problem in the fabrication of tubing from such a material. We have developed several heat treatments that utilize high heating and cooling rates to obtain small grains and a precipitate-free (supersaturated) microstructure.

Effects of Heating and Cooling Rates on Recrystallization

Independent of prior cold work, rapid heating through the critical A_{c1} to A_{c3} range and subsequent fast cooling after slightly exceeding the A_{c3} lead to small grain sizes in steels that undergo a gamma to alpha phase transformation on cooling.[8-10] Rapid heating can be accomplished by resistance[9], induction[10] or by immersing steel specimens in lead baths.[8] Rapid heating and cooling should lead to ultrafine grains (ASTM grain size No. $\geq$10) in steels that do not transform on quenching. At attainable high heating rates such as 900°C/sec there is little or no time for recovery. In some steels recovery can result in up to 70% softening without recrystallization.[11] Thus, no stored energy will be lost in recovery, and the driving force for recrystallization will be larger for a given amount of cold work than in a traditional recrystallization treatment involving slow heating. The higher driving force will result in a larger number of recrystallization nuclei and a smaller grain size. The recrystallization temperature will be higher at the higher heating rates. High cooling rates are also necessary to prevent grain growth.

Effects of Heating and Cooling Rates on Precipitation

Since diffusion is a time-dependent process, rapid heating makes precipitation almost impossible, especially when the temperature for accelerated recrystallization is so high that the driving force for precipitation (supersaturation) becomes almost zero. Diffusion along dislocations (pipe diffusion) is more rapid than lattice diffusion at temperatures below 0.5 T_m, and leads to nucleation and even growth of precipitates during the recovery process when traditional heat treatments are applied. During rapid heating and cooling there are at least three factors which suppress the precipitation process: a) high temperatures are reached very rapidly, effectively reducing the driving force

---

[8] R. W. Grange, Met. Trans. 2, 65–78 (1971).

[9] F. K. L'Vov, Metallov. Term Obrab. Met. 4, 8–14 (April 1959).

[10] M. N. Bodyako et al., Metallov. Term Obrab. Met. 1, 46–53 (1960).

[11] H. L. Crouch and J. D. Lubahn, Trans. AIME 215, 433 (1959).

(supersaturation) for precipitation; b) the dislocation density is lowered drastically within a very short time and removes potential nucleation sites and eliminates the contribution of dislocations to the diffusion rate of solutes at lower temperatures; and c) there is not enough time for long-range diffusion to occur.

Preliminary Results

Standard type 316 stainless steel samples were annealed for 1 hr at 1050°C (a higher temperature would be desirable) in argon and then rapidly cooled inside the furnace by pulling them onto a water cooled zone. This annealing was followed by 70% reduction in area by swaging at room temperature. Accelerated recrystallization was achieved by rapidly heating the specimen in a programmed resistance heating device up to pre-determined temperatures within 2 sec. A thermocouple was attached to the specimen and the power was cut off as soon as the desired temperature was reached. The specimen cooled rapidly since it was in contact with water-cooled copper electrodes. Figure 4.20 shows the microstructure of specimens rapidly heated under the above conditions to (a) 910°C, (b) 1000°C, and (c) 1070°C. At 910°C recrystallization was essentially complete. Grain growth had occurred in the specimen heated to 1000°C and even larger grains were found in the specimen heated to 1070°C. The number of annealing twins increased as grain growth progressed. The grains are remarkably "clean", and only a few particle-like features can be seen. These precipitates may be undissolved carbides or, more likely carbides that formed on cooling.

In contrast to the more or less precipitate-free microstructure obtained by rapid heating and cooling, Fig. 4.21 shows relatively coarse precipitates within the grains and formation of sigma-phase at grain boundaries and corners following the traditional recrystallization treatment of specimens with identical history. Annealing for 1 hr at 775°C is not sufficient for complete recrystallization (Fig. 4.21a), but recrystallization goes to completion during 1 hr at 800°C (Fig. 4.21b).

To obtain ultra-fine grains by the traditional approach, a cycle consisting of 40% reduction in area by swaging at room temperature followed by annealing for 1 hr at 760°C was repeated six times. The resulting microstructure was characterized by coarse precipitate

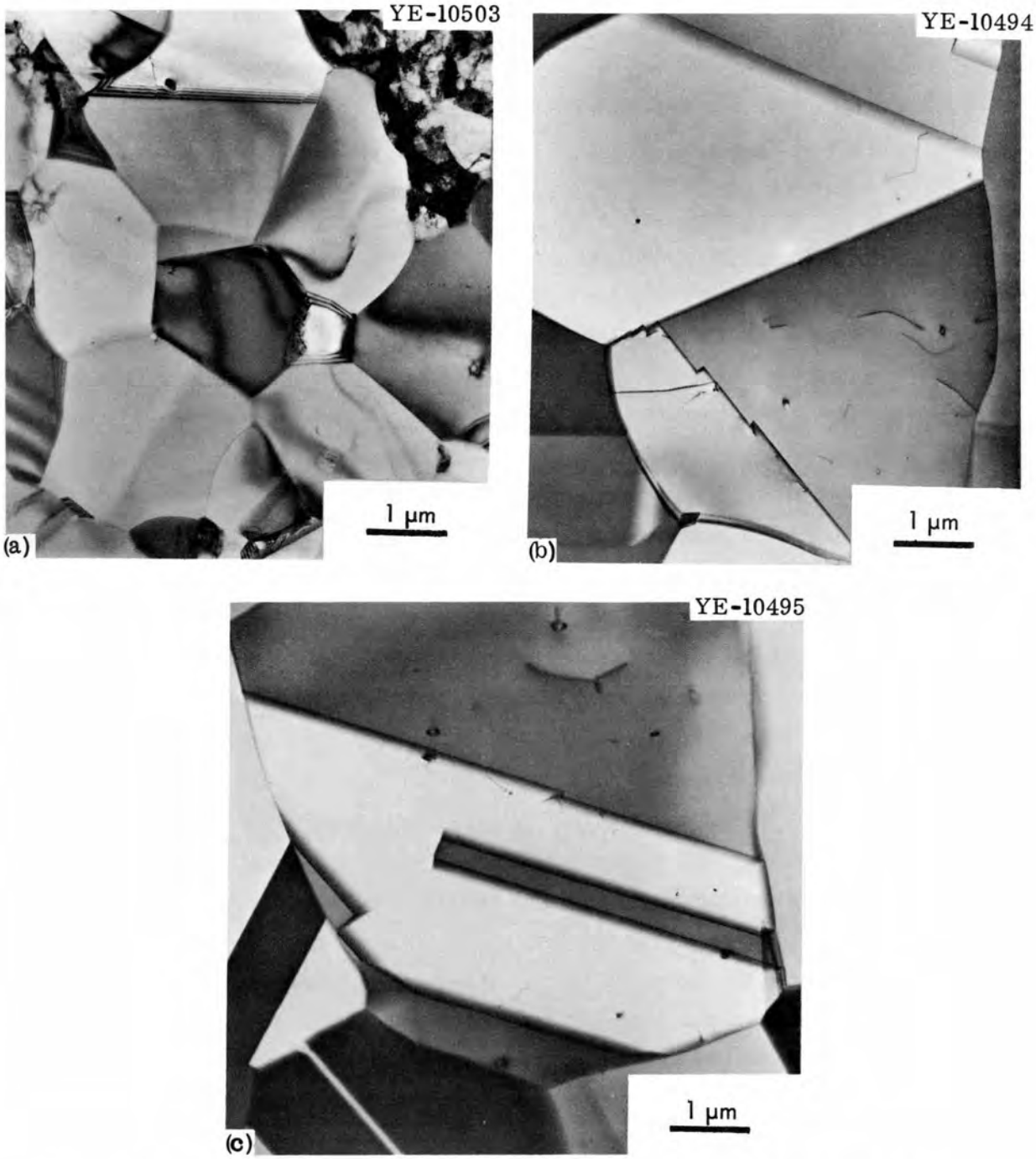

Fig. 4.20 Transmission Electron Micrographs of Type 316 Stainless after 70% Reduction in Area at Room Temperature Followed by Rapid Heating (within 2 sec) to a) 910°C, b) 1000°C, and c) 1070°C and Rapid Cooling.

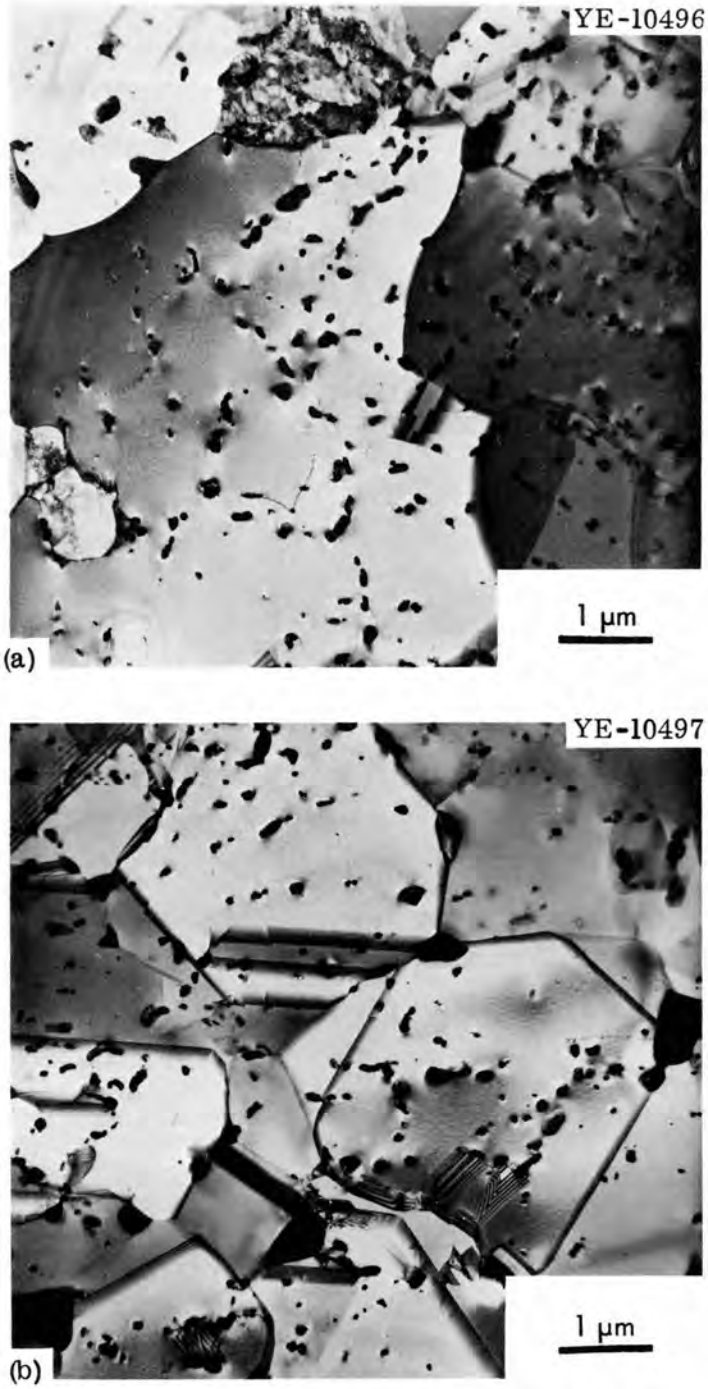

Fig. 4.21 Transmission Electron Micrographs of Type 316 Stainless Steel after 70% Reduction in Area at Room Temperature Followed by a Conventional Recrystallization Treatment of a) 1 hr at 775°C (~90% recrystallized), and b) 1 hr at 800°C (fully recrystallized).

particles and accumulations of sigma-phase (Fig. 4.22a). Figure 4.22b shows that a precipitate-free microstructure with similar ultra-fine grains can be obtained by the above rapid heating and cooling process. The difference in microstructure becomes even more obvious at higher magnifications (Figs. 4.23a and 4.23b).

Recent density measurements on ultra-fine-grain size standard type 316 stainless steel revealed an unexpectedly large volume change after irradiation at 515°C to 2.3×10^{22} neutrons/cm^2 (>0.1 MeV). (Ref. 12) The fine grain size was obtained by repeated cold-work and recrystallization cycles as described above, and the preirradiation microstructure is shown in Figs. 4.22a and 4.23a. Since extensive precipitation had taken place before the specimen was irradiated, the resulting change in the composition of the matrix may well have offset the expected benefits with respect to swelling to be derived from the smaller grain size. Since the void structure is very sensitive to compositional changes, the effects of changes in grain size on swelling can only be studied successfully when all other variables can be kept constant. This is possible with the suggested high speed recrystallization process. Some Russian studies [10, 13] reveal that the recrystallized grain size is much less dependent upon the amount of prior cold work when recrystallization takes place under rapid heating and cooling conditions than when the traditional approach is used. Thus, recrystallization by high speed heating may actually be easier to control.

---

[12] E. E. Bloom, ORNL, private communication.

[13] Ya. R. Rauzin, Metallovedenie i Obrabotka Metallov. 8, 14–17 (1958).

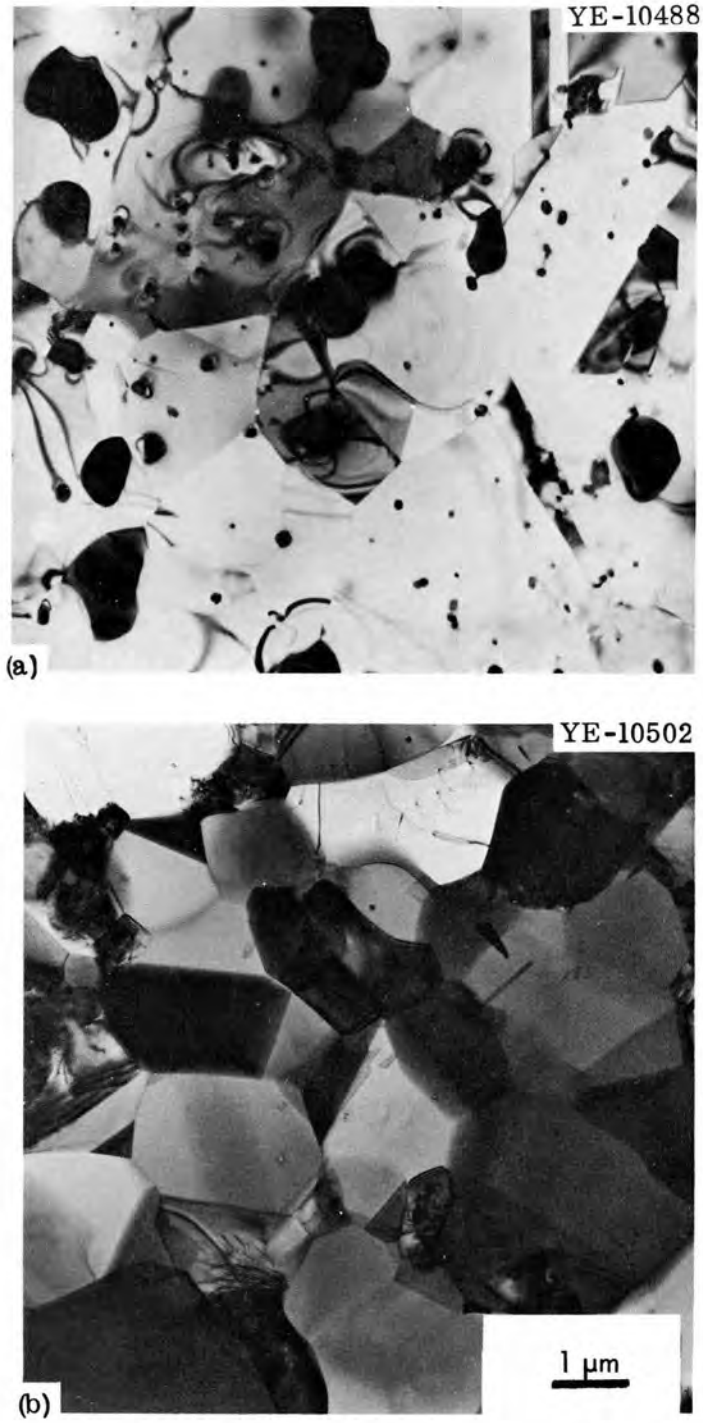

Fig. 4.22 Transmission Electron Micrographs of Ultra-Fine Grain Size of Type 316 Stainless Steel Obtained a) by 6 Cycles of 40% Reduction in Area at Room Temperature and Recrystallization by Annealing 1 hr at 760°C, and b) Through Rapid-Heating in 2 sec to 910°C and Rapid Cooling After 70% Reduction in Area at Room Temperature.

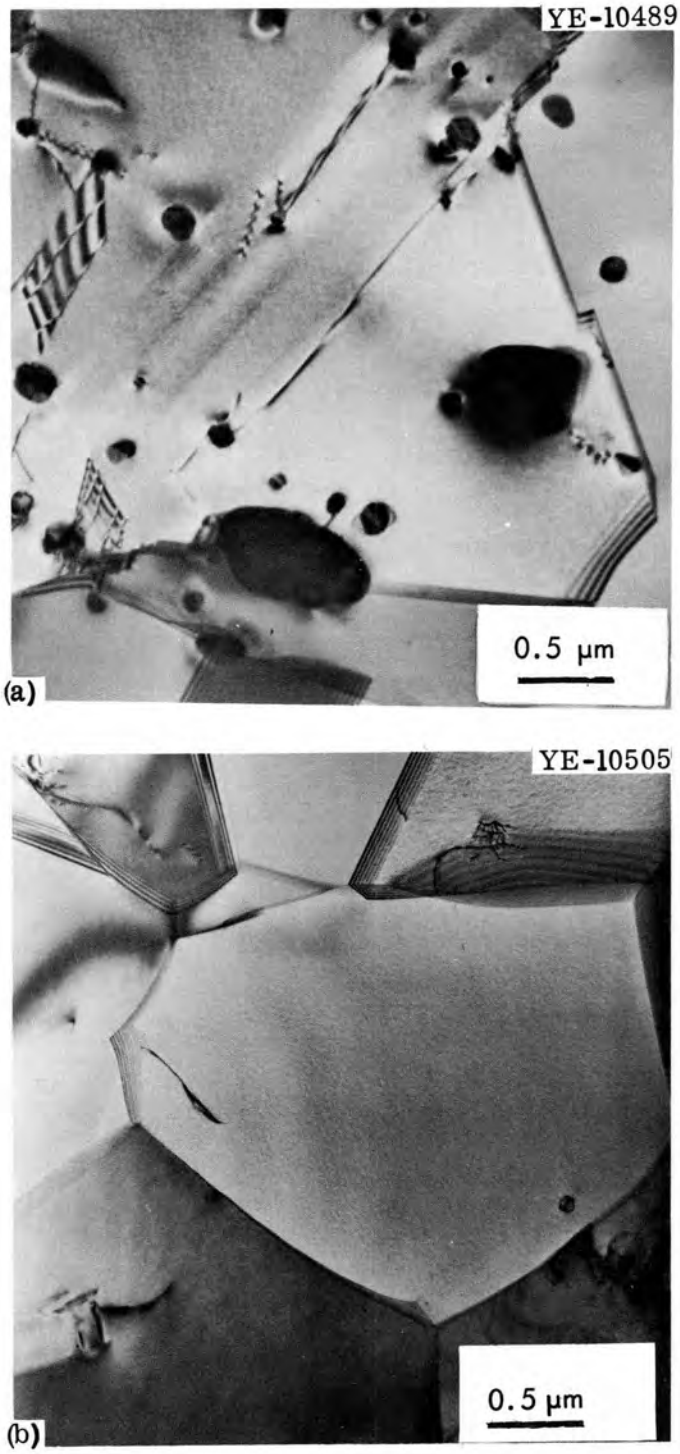

Fig. 4.23 Higher Magnification Transmission Electron Micrographs of the Specimens in the Previous Figure.

5. FABRICATION DEVELOPMENT FOR FBR CLADDING

G. M. Adamson, Jr. W. R. Martin

Our effort is currently directed toward a better evaluation of the effects of defects on the properties of unirradiated and irradiated type 316 stainless steel tubing.

Studies of Defected Tubing

Production Speed Rotating Tube Scanner (K. V. Cook, R. W. McClung)

The primary objective of the artificial defect study is to establish the effect of flaws of various sizes (simulated by electrodischarge-machined notches) on the mechanical properties of small diameter type 316 stainless steel tubing. Complete nondestructive testing of both end-product and upstream fabricated tubing is mandatory to select and document "defect free" tube sections for destructive testing.

Our time requirement to inspect the tubing has been greatly reduced by modifying our rotating tube scanner, purchased in the last year from an outside vendor, to allow stable and versatile manipulation of the inspection transducers and to allow quick changes of tube guide sizes. With this system we can perform two flaw detection tests (one for longitudinally oriented flaws and one for transverse oriented flaws) and a wall thickness test simultaneously as the tubing is "stuffed" through the scanner at any desired feed helix.

Creep-Rupture Analysis of Type 316 Stainless Steel Tubing with Artificial Defects (R. T. King, G. A. Reimann, K. V. Cook)

The results of an experimental investigation of the mechanical properties of type 316 stainless steel tubing containing artificial defects under creep-rupture conditions have been reported previously.[1] The data from this test program have been evaluated and a number of

[1]R. T. King, G. A. Reimann, and K. V. Cook, Fuels and Materials Development Program Quart. Progr. Rept. June 30, 1971, ORNL-TM-3540, p. 81.

existing theories dealing with the effects of cracks or flaws on the strength of similarly shaped bodies have been evaluated. A report covering this topic is in preparation and is summarized below.[2]

The effects of longitudinal electrodischarge-machined notches on the biaxial creep-rupture properties of 20% cold-worked type 316 stainless steel tubing at 650°C have been determined. The tubing was 0.635-cm-OD × 0.041-cm-wall thickness material similar to the proposed liquid-metal fast breeder reactor cladding material. Notch depths equal to about 10, 33, and 66% of the tube wall thickness and notch lengths of 0.076 and 0.635 cm were investigated. The effects of notches on the inner and outer tube walls were compared. The experimental results are summarized as follows:

1. All notched tubes failed at the notch (except for one specimen that failed at a weldment).

2. The rupture times were reduced by the presence of notches for stresses that caused rupture times between a few tenths of an hour and several hundred hours. A high density of intergranular cracks stands as evidence of accelerated straining under the notches. Rupture times generally decreased with increasing notch depth.

3. The effects of similar notches on the inner and outer surfaces were indistinguishable within the limits of experimental error.

4. Long notches generally had significantly greater effects than the short notches.

5. Because the strain rate of the bulk of the tube is unaffected by the presence of a notch some distance away, the nominal strain of the bulk of the tube at the time of failure is reduced by the notches in the same manner as the time to rupture.

The first type of theoretical analysis attempted was based on the observation that log-log plots of nominal hoop stress, $\sigma_{\theta,nom}$ vs time-to-rupture, were straight parallel lines for test time lasting up to several hundred hours. Thus, the ratio, K_{exp}, of stress required to

---

[2]R. T. King, K. V. Cook, and G. A. Reimann, "Behavior of Defective Stainless Steel Tubing During Biaxial Creep-Rupture Testing," in preparation.

fail an unnotched tube in a given time to the stress required to fail a notched tube in the same time was about constant, and it had the same general properties as a stress concentration factor. Calculated stress concentration factors for similar geometries[3,4] did not agree with our measured results, as shown in Fig. 5.1. No stress concentration factors, which account for the length of a finite root radius notch in a tube, were found.

Stress intensity functions were compared with our results, but similar discrepancies existed.[5,6] A numerically computed correction for finite notch length was arbitrarily used to modify the stress concentration factors, but again without producing satisfactory agreement. Arbitrarily normalizing the magnitude of stress intensity factors corrected for notch length to coincide with K_{exp} for short, shallow notches did not produce a set of functions that coincided with K_{exp}.

All of the techniques described above are based on elasticity theory and apply only to homogeneous, isotropic, elastic bodies. The shapes of the zones of plastically deformed material calculated to exist at the root of the notches[7–9] agree qualitatively with the heavily deformed zones in fractured notched tubes. The size of the region that is plastically deformed immediately upon loading has been calculated.[10,11]

---

[3]C. E. Inglis, "Stresses in a Plate Due to the Presence of Cracks and Sharp Corners," Trans. Inst. Naval Architects 40, 219 (1913).

[4]H. Neuber, Theory of Notch Stresses: Principles of Exact Calculations of Strength with Reference to Structural Form and Material, Springer-Verlag, Berlin, 1958, AEC-tr-4547.

[5]B. Gross and J. E. Srawley, "Stress Intensity Factors for Single Edge Notch Specimens in Bending or Combined Bending and Torsion by Boundary Collocation of a Stress Function," NASA Tech. Note D-2603 (1965).

[6]J. R. Rice and N. Levy, "The Past-Through Surface Crack in an Elastic Plate," NASA-NGL-40-002-08013 (September 1970).

[7]D. N. de G. Allen and R. Southwell, Phil. Trans. Roy. Soc. London, Ser. A 242, 379 (1950).

[8]L. Garr, E. H. Lee, and A. J. Wang, J. Appl. Mech. 23, 56 (1956).

[9]J. A. Hendrickson, D. S. Wood, and D. S. Clark, Trans. Am. Soc. Metals 50, 656 (1958).

[10]D. S. Dugdale, J. Mech. Phys. Solids 8, 100 (1960).

[11]G. R. Irwin, Appl. Mater. Res. 3(2), 71 (1964).

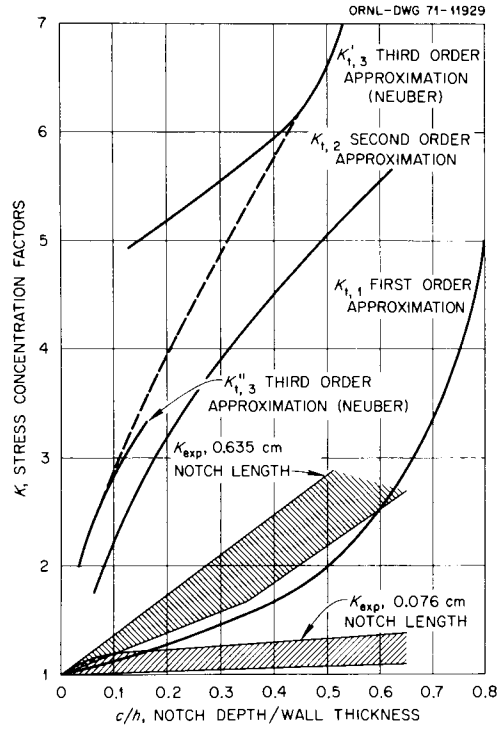

Fig. 5.1. Comparison of Observed Stress Ratio K_{exp} with Theoretical Stress Concentration Factors $K_{t,i}$.

These regions should not extend through the tube except for the longest, deepest notches investigated.

Empirical equations developed at Battelle to describe the deformation of large pressure pipes have also been tested.[12] One theory, which accounts for bending movements through a stress magnification factor, was found to be inapplicable. However, another formulation that used a flow-stress criterion was found to roughly describe the results of our experiments. However, the empirical nature of the relationships and their failure to account for creep processes make them less desirable than an approach based on time-dependent strain considerations.

A theory has been developed that predicts failure on the notched tubes when the strain at some point on the unnotched tube wall exceeds the average strain-to-rupture of control specimens. If most of the

[12]R. J. Siber, W. A. Maxey, A. R. Duffy, and T. J. Atterbury, Investigation of the Initiation and Extent of Ductile Pipe Rupture, BMI-1886 (1969).

plastic deformation occurs by steady-state, second-stage creep processes, then it is shown that in a given material, the ratio of stresses required to rupture an unnotched tube to that required to rupture a notched tube is a constant. The constants calculated from these assumptions agree within ±10% of the experimentally determined K_{exp} value. A rational is presented to explain why the values of the constant should vary with the properties of different materials and be sensitive to the load distribution immediately after the tubes are pressurized.

6. COMPATIBILITY OF STEAM GENERATOR MATERIALS

P. Patriarca J. R. Weir, Jr.

Examination of ALCO/BLH Steam Generator

G. M. Slaughter J. H. DeVan R. W. McClung
B. C. Leslie R. H. Jones[1]

We are examining the ALCO/BLH steam generator which failed while under test at the Liquid Metal Engineering Center (LMEC).[2,3] After installation at the Sodium Components Test Installation of the LMEC in 1965, the steam generator operated intermittently with sodium for 7600 hr and with steam for 4100 hr. A water leak on the feedwater chest was found in May 1970, and it was traced to an area of extensive cracking in the lower tube sheet. Extensive corrosion resulting from leakage of steam into sodium was also subsequently observed near the top tube sheet. In view of the vital role of steam generators in the LMFBR demonstration plant program and the well-documented fabrication and operational history of this unit, it is being examined to determine the mechanisms of failure and to study other metallurgical features of interest.

Disassembly Operations

The removal of the bottom tube sheet was discussed in a previous report.[3] Subsequently, short segments of the shell and liner were removed individually after they had been severed from the remaining portion with a Wachs air-driven saw. A 58-in.-long section containing the sodium outlet nozzle was the first such segment to be removed. Considerable difficulties were involved in this operation, particularly in cutting the weld attaching the liner to the nozzle. The additional segments ranged from 4 to 8 ft long.

---

[1]Member of the Plant and Equipment Division, ORNL.

[2]G. M. Slaughter, J. H. DeVan *et al.*, Fuels and Materials Development Program Quart. Prog. Rept., June 30, 1971, ORNL-TM-3540, pp. 97–98.

[3]G. M. Slaughter, J. H. DeVan *et al.*, Fuels and Materials Development Program Quart. Prog. Rept., March 31, 1971, ORNL-TM-3416, pp. 155–162.

The top tube sheet was removed from the tube bundle and shell by a band-sawing operation. The general appearance of the underside of the top tube sheet and the matching region of the tube bundle is shown in Fig. 6.1. Significant wall thinning is obvious on several tubes; also, the heavy deposits are concentrated in one quadrant.

Pie-sections were cut from both the top and bottom tube sheets, and extensive nondestructive and metallographic examinations on these sections have been conducted. The results of these detailed examinations follow.

Examination of Upper Tube Sheet

A pie-shaped section of the upper tube sheet was removed to permit a detailed examination of three leaking tubes contained within the section. The cut faces of this pie section disclosed a number of large cracks in the tube sheet, shown in Fig. 6.2. The cracks appear to have originated in the crevice region between the tube and tube holes, and closer inspection also reveals cracks running radially into the tubes from the same source.

Several tubes within the pie-shaped section were removed in the manner shown in Fig. 6.3. Note the reduction in wall thickness which occurs in the section of the tube leading away from the lower face of the tube sheet. As discussed previously,[3] this wall reduction was associated with a heavy concentration of sodium-steam reaction products near the underside of the lower tube sheet. The affected area was approximately 5 to 7 ft above the sodium level and, during normal operation, had been blanketed by argon. The stainless steel under these deposits was quite uniformly corroded, and in the case of the tubes shown in Fig. 6.2, the wall thickness was reduced by as much as 0.080 in. (approximately the thickness of the stainless steel portion of the tube). The extent of external corrosion of the tubes is much less within the header region than immediately below it. On the other hand, the occurrence of cracking appears confined totally to the tube sheet area.

Reaction products in the crevice between tube and tube hole also differ in composition from the heavy deposits formed in the gas space area below the header. The latter contained > 50% Na and were comprised of oxides of the type $Na_x(Fe,Cr,Ni)_y,O_2$. Diffraction patterns of products

Fig. 6.1. Underside of Top Tube Sheet and Matching Portion of Tube Bundle.

Fig. 6.2. Appearance of a Radial Surface of the Upper Header in Vicinity of Three Leaking Tubes. Cut was made parallel to the tube bundle axis using a band saw.

Fig. 6.3. Illustration of Cutting Method Used to Remove Tubes from the Section Shown in Fig. 1. Note reduction of tube wall as the tube exits from the header.

removed from the crevices agreed closely with standard patterns of Fe_3O_4, and chemical analyses of the products gave the following results:

Na - 2.3%	Mo - 0.1%
Fe - 46%	Mn - 0.8%
Ni - 4.5%	O_2 - 34%
Cr - 10.7%	CO_3- 3.3%

Although several of the tubes removed from this pie-shaped section exhibited radial cracks on their outside surface, in only three of the tubes did the cracks penetrate to the inside surface. In the other tubes, the cracks terminated on reaching the Inconel portion of the tubes. The metallographic appearance of one of the three leaking tubes (tube 52, row 3) is shown in Fig. 6.4. Note that the cracks are completely transgranular in the stainless steel portion of the tube and are completely intergranular in the Inconel part of the tube. The appearance of the cracks in the other two leaking tubes was generally similar, although in one of the tubes (tube 47, row 2), the cracks were considerably wider and

Fig. 6.4. Metallographic Appearance of Leaking Tube from Upper Header Region.

contained a greater volume of reaction product. This latter tube had failed nine months prior to shutdown of the steam generator. In order to permit further testing of the unit, the tube had been plugged to prevent water entry, and the widening of the cracks apparently occurred during the nine months subsequent operation.

Inspection of these failed tubes and of unfailed tubes from adjacent areas indicates that cracking is attributable to stress-corrosion conditions which were set up in the tube sheet crevice. In most cases, cracks stopped on reaching the Inconel portions of the tubes. However, in the few cases where cracks penetrated the Inconel, the cracks were again symptomatic of a stress-corrosion origin, indicating that Inconel, while much more resistant than stainless steel, was not totally immune to the corrosion environment.

There can be little doubt that the widespread cracking in the tube sheet and stainless steel portions of tubes in the upper header stemmed from the presence of steam and sodium in the tube-tube sheet crevices, which provided conditions conducive to caustic stress-corrosion cracking. However, the cause of the initial steam leak into the tube sheet crevice region remains in question. The following are all credible hypotheses:

1. The inner (Inconel) surfaces of the tubes within the header region were damaged by an expanding operation during fabrication. We have, in fact, seen evidence of galling of inside surfaces of the tubes over a length of one inch leading down from the steam side of the header.

Although the damage found so far appears superficial, if the Inconel cladding were compromised at some point in the unit, a strong case can be made that the stainless steel portion of the tube underneath would have failed by chloride stress-corrosion cracking from the water side.

2. Water left in the tube-tube hole crevices after hydrostatic testing of the unit led to caustic cracking of tubes from the outside-in. This hypothesis is impossible to assess because of the widespread caustic cracking that developed after the first tube leak.

Examination of Lower Tube Sheet

Several pie-shaped sections of the lower tube sheet have been cut. Sections were taken initially from the region of the tube sheet where radiographic examination had disclosed a high density of cracks and where cracks were visibly apparent on the outside surface of the steam generator. A typical cross section of a wedge-shaped slice from this area is pictured in Fig. 6.5. Like the upper tube sheet (Fig. 6.1), this section exhibits

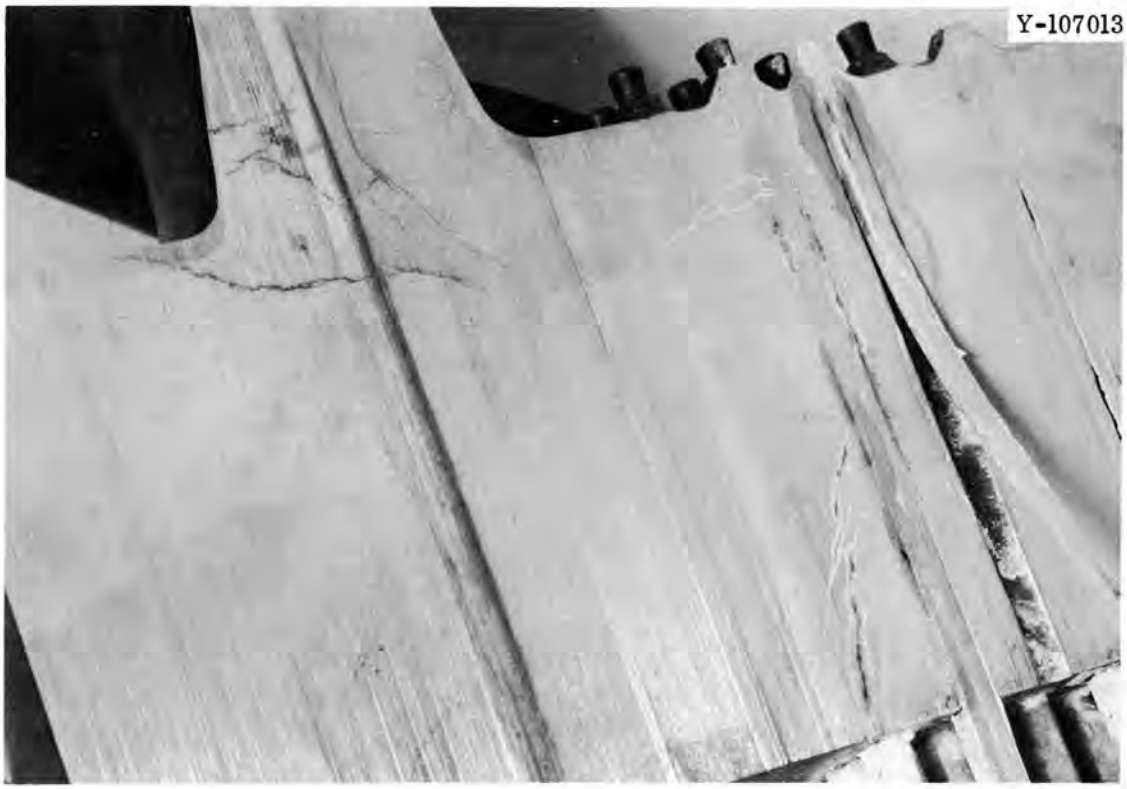

Fig. 6.5. Appearance of a Radial Surface in the Lower Header. Cut was made through an area where heavy cracking was apparent on the external surface of the header.

a number of cracks emanating from tube-to-tube hole crevices; however, cracking is much more widespread than in the upper tube sheet and encompasses virtually the entire cross section of the header from the second row of tubes outward. (Note, however, that there are no cracks between the second row of tubes and the central axis of the tube sheet.) Cutting of wedge-shaped sections was continued until we had enscribed the entire crack system in the header. The sector encompassing cracking was subtended by an angle of approximately 150°.

We are now mapping the crack system using a full-scale plastic mockup of the lower header in an attempt to discern the directional patterns and interfaces of the various crack systems. In this mapping operation, we are using the combined tools of ultrasonic inspection, visual(dye-penetrant) examination, and metallographic sectioning. We can classify at least four distinct crack systems based on the evidence gathered to date. Tubes in the outer two rows show a number of radial cracks from the outside-in which resemble the tube cracks found in the upper header. However, none of the cracks so far examined penetrate the Inconel portion of the tubes. We also see a heavy concentration of cracks within tubes in the vicinity of tube-to-header welds, as shown in Fig. 6.6. In some cases, these cracks have breached the weld fillet, as shown in Fig. 6.7.

A second crack system emanates into the tube sheet from tube-to-tube hole crevices. Note in Fig. 6.5 that one of these cracks appears to traverse the entire distance from the second row of tubes to the outer surface of the header, a distance of approximately 9 in. However, closer inspection indicates it is more probable that the crack was formed by two separate cracks which linked up somewhere inside the header. That is, we find a third system of cracks at the outer side (air) of the header (where it adjoins the water chest) which grew from the outside-in, as illustrated in Fig. 6.8.

The fourth system of cracks was formed because of a breach in the Inconel overlay which occurred where the water chest adjoins the header, as shown in Fig. 6.9. The likelihood of cracks in this area was presaged by a dye-penetrant examination of the overlay after test which disclosed flaws in the same area where we found cracking. The defect in the overlay,

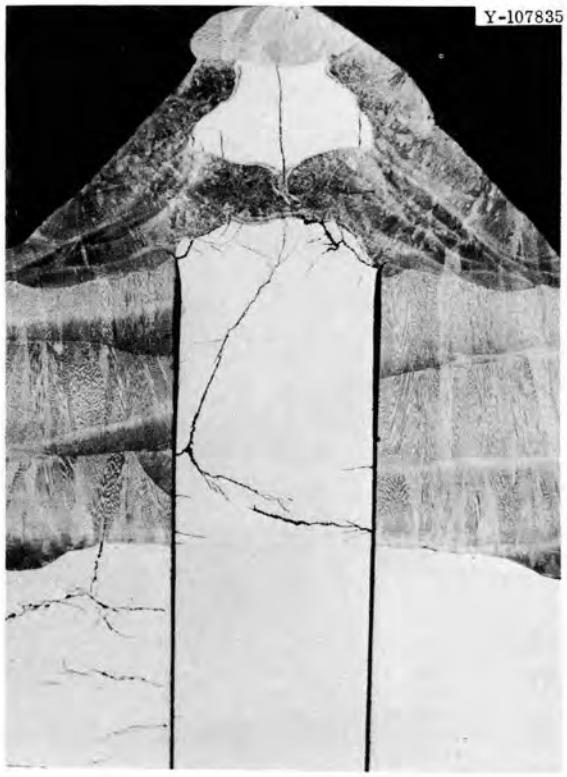

Fig. 6.6. Appearance of Crack System in Stainless Steel Portion of Tube at the Water Side of the Lower Header.

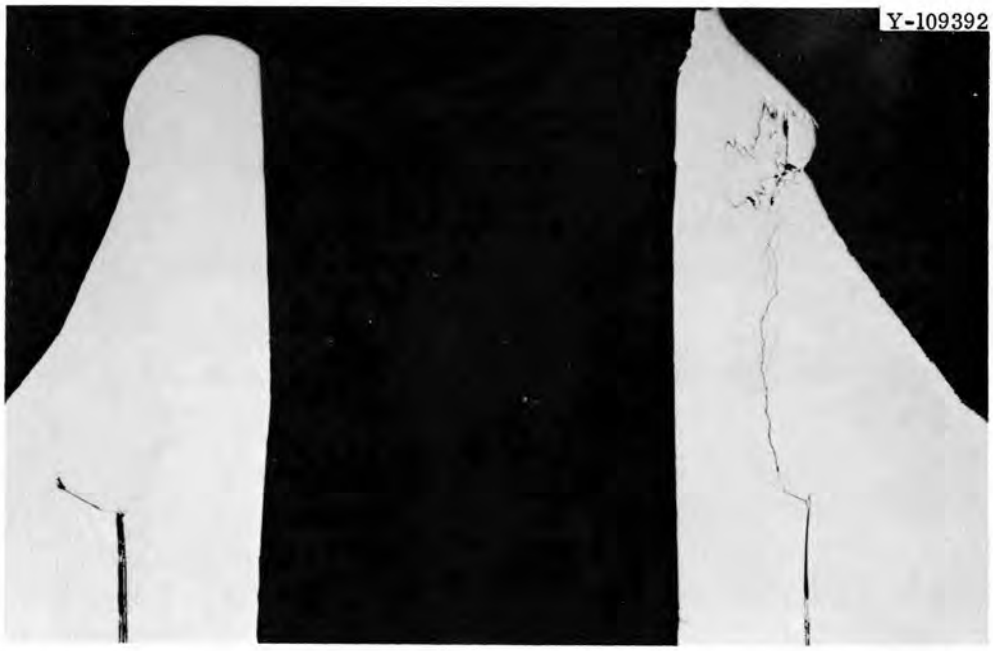

Fig. 6.7. Tube-to-Header Weld in Lower Header which Exhibits Cracks Leading from the Crevice to the Water-Exposed Surface.

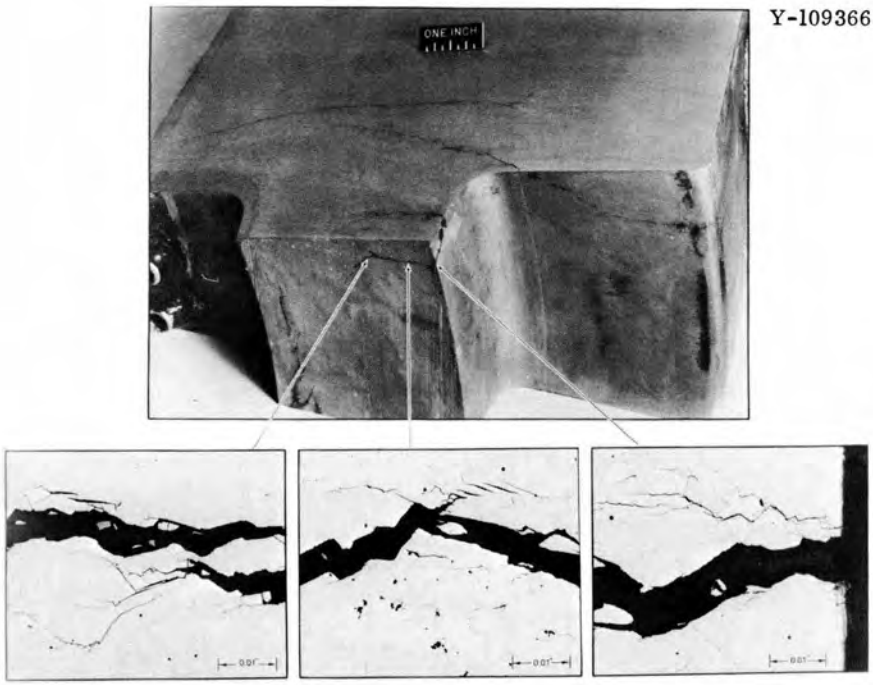

Fig. 6.8. Crack System Near Air Side of Lower Header which Had Apparently Grown from the Outside-In.

Fig. 6.9. Cracking of Stainless Steel in Corner of Lower Header where it Adjoins the Water Chest. Defects are apparent in the Inconel overlay.

apparent in Fig. 6.9, was found only after extensive serial sectioning, and there are relatively few penetrations of the Inconel in this area. As is apparent in Fig. 6.5, the Inconel overlay in other areas of the water chest exhibited a remarkable resistance to cracking despite extensive damage to the underlying stainless steel. We do not know whether the defects in the Inconel overlay may have existed prior to test (see below) or occurred because of cracking of the underlying stainless steel during test.

As with the upper header, we can conclude that most, if not all, of the cracking in the lower header is a product of caustic corrosion conditions set up by the reaction of steam and sodium. Again, however, we are left with the question of what started it. The same two hypotheses advanced for the upper header apply here also. To these we can add at least two others:

1. The flaws seen in the Inconel overlay on the water chest after test may have existed at the time the unit was fabricated. That they were not detected during pretest inspection of the unit could be blamed on smearing of the overlay surface when it was ground smooth. Operating conditions were such that chloride-induced stress-corrosion cracking of the stainless steel sections of the header could have resulted if such flaws were present. Cracking by this mechanism may have penetrated to the outside surface of the generator, where impurities in the insulation would have worsened the original problem. Or cracking may have led to a tube hole and to the initiation of more widespread caustic cracking.

2. It can be reasonably argued that conditions at the test site were conducive to halide stress-corrosion cracking at external surfaces of the lower header, either as a consequence of impurities in the insulation or airborne impurities.

We strongly discount the possibility that cracking of the lower header was caused by the steam leaks encountered in the upper header. There is no evidence whatever of any sodium-water oxidation products having been carried by the sodium to the lower header.

Steam Corrosion of Advanced Steam Generator Materials

G. M. Slaughter

The purpose of this program is to investigate the corrosion behavior of steam generator alloy weldments. Special emphasis is placed upon materials for LMFBR steam generator use and stress corrosion as the mode of failure.

The program currently includes two areas of investigation: (1) general corrosion (uniform scaling, including internal oxidation and localized attack at weld fusion lines) at 480 and 595°C (900 and 1100°F), and (2) stress corrosion cracking (induced by chloride or caustic as contaminants) in steam environments that include superheated conditions and cycling between the superheated and water-saturated states.

General Corrosion (J. P. Hammond)

The general corrosion loop[4] recently was shut down and refitted for conducting extended isothermal steam corrosion tests at 480 and 595°C on ferritic steels and other steam generator materials of interest for LMFBR use. All of the specimens in the similar- and dissimilar-metal welds that were investigated for advanced HTGR steam generators at 595 and 650°C (900 and 1200°F) were removed from the loop. Selected specimens from this group, many of which had total accumulated exposures of 26,000 hr, will be examined for any departures from anticipated linear corrosion.

New Test Specimens. — The test specimens of materials of interest for steam generators have been completed and will be installed shortly in the general corrosion loop for isothermal tests at 480 and 595°C. As in former general corrosion tests, the steam will be uncontaminated and taken from a superheater at the Bartow Plant of the Florida Power Corporation. The steam will flow past specimens at a velocity of about 5 fps at a pressure of 900 psi.

---

[4]J. P. Hammond *et al.*, "Corrosion of Advanced Steam Generator Alloy Weldments in 1100 and 1200°F (595 and 650°C) Steam," Paper 46 presented at the National Association of Corrosion Engineers 26th National Conference, March 2–6, 1970, Philadelphia, Pa.

The specimens are of the usual strip type (2 7/8 in. × 1/2 in. × 1/16 in. thick) and are listed below in two groups.

Group 1 - Specimens in this group were cut from weldments (normal to weld):

Materials	Surface Preparation
Incoloy 800 welded with Inconel 82	Ground
Inconel 600 welded with Inconel 82	Ground
Type 304 stainless steel welded with type 308 stainless steel	Ground
2 1/4 Cr—1 Mo steel welded with 2 1/2 Cr—1 Mo steel	Ground
Type 410 stainless steel welded with type 410 stainless steel	Ground

Group 2 - Specimens in this group were cut from unwelded strip:

Materials	Surface Preparation
Type 304 stainless steel	Ground and electropolished
Incoloy 800	Ground and electropolished
Inconel 600	Ground and electropolished
2 1/4 Cr—1 Mo steel	Ground and electropolished
2 1/4 Cr, Ni, Mo, Nb stabilized steel	Ground and electropolished
5 Cr steel	Ground
9 Cr—1 Mo steel	Ground and electropolished
9 Cr—2 Mo, V, Nb (stabilized) steel	Ground
Type 410 stainless steel	Ground and electropolished
12 Cr—1 Mo, Ni, W, V (stabilized)	Ground

Specimens from the first group were cut from 1/2-in.-thick-plate weldments prepared by the gas tungsten-arc process using 1/16-in.-wire filler metal and a 100° (included angle) welding groove. The hot-rolled plates were tested in the descaled-and-annealed condition and the specimens were tested in the as-welded condition but were given a 100-mesh belt grind. Additional weldments of ferritic materials will be added to this group subsequently.

Specimens from the second group were nonwelded strips taken from materials of two separate work histories. The type 304 stainless steel, Incoloy 800, and Inconel 600 specimens were cut from 1/16-in.-thick cold-rolled-and-annealed sheet stock. These will be examined in both the

100-mesh-ground and the electropolished (0.003 in. metal removed) condition. The remaining specimens of this group are of the various non-stabilized and stabilized ferritic steels. These materials are normally furnished in the tubular form only. Strip specimens in these were prepared by splitting and hot-flattening the tubular product and subsequently austenitizing, slow-cooling, and, finally, annealing just below the alloy's lower critical temperature. These specimens also were prepared in the 100-mesh ground and the electropolished condition to evaluate the effects of surface finish on corrosion.

The foregoing alloys will be investigated for general corrosion using the weight-loss and weight-gain methods of evaluation, making corrosion determinations after 2,000, 4,000, 6,000, 9,000, and 12,000 hr of exposure. In the instance of the ferritic materials, reliance will be placed predominantly on the weight-loss method of study as it is anticipated that corrosion products may not be completely retained during tests. The microstructures of scales will be examined after 6,000 and 12,000 hr and interpretive analyses will be made of the data at these times.

Stress-Corrosion Cracking (J. P. Hammond)

Loop Construction and Operation. — During the last reporting period, a sixth stress-corrosion run was conducted in the chloride-injection corrosion loop and is reported here. The design and details of operating this loop were given previously.[5] At the end of the fourth week of run 6, a steam leak was detected in the 1-in. tubing at the end of the second heater section, upstream of the first autoclave. The crack, about 3/4 in. long, was located in a very confined area between a weld made to join the heater tube to a U-bend fitting and another weld made to install a thermocouple insert. The crack appeared to have originated in the heat-affected zone of the insert weld and had all the external appearances of a stress-corrosion crack. The operating conditions of the prior runs made with this loop were given in the last report.[6] After partial removal of the

[5]J. P. Hammond, Fuels and Materials Development Program Quart. Progr. Rept., Sept. 30, 1970, ORNL-4630, pp. 280–287.

[6]J. P. Hammond, Fuels and Materials Development Program Quart. Progr. Rept., June 30, 1971, ORNL-TM-3540, pp. 90–94.

defect by filing, the crack was repaired in place with a coated-Inconel-type electrode. The repaired area was stress-relieved at 670°C (1240°F) for 30 hr.

While the repaired loop has performed without incident (12 weeks of operation), tubing and fittings required for making a replacement loop of the 9 Cr—1 Mo ferritic alloy were procured should the need arise to replace the damaged Incoloy 800 loop. The 9 Cr—1 Mo ferritic alloy was selected as the replacement material because of its good history of resisting chloride cracking and our desire to gain loop-operating experience with this type of constructional material. At some future date, it is anticipated that valuable information may be obtained by destructively analyzing these loops.

The Inconel 625 tubing required for constructing the caustic injection, steam-corrosion loop has been received, but the delivery date on the fittings is still some months away.

Work has been under way to develop statically stressed, stress corrosion specimens fabricated from commercial heat exchanger tubing in order to more closely simulate the materials systems involved in steam generators.

Results. — The results of the fifth stress-corrosion run, which consisted of cycling between 480 and 280°C (900 and 540°F) — 24 hr at 280°C saturation temperature three times per week — with 25 ppm NaCl and 50 ppm O, were given in the last report.[6] The sixth run consisted of cycling between 425 and 280°C (800 and 540°F) — 24 hr at 280°C three times per week— with 10 ppm NaCl and 20 ppm O. Besides lowering the level of contaminants for this run, the upper temperature was decreased by 55°C to reduce the extent of stress relaxation. The results of run 6 are given in Table 6.1. The test specimens incorporated in this run were made of three categories. The first consisted of strip specimens cut from similar-metal weldments prepared in 1/2-in.-plate material, furnished in the hot-rolled condition. These weldments incorporated type 304 stainless steel, Incoloy 800, and various high-nickel alloys as base metals. The second consisted of strip specimens cut from nonwelded, 1/16-in.-thick sheet in the same base metals. These sheet materials were originally in the cold-rolled-and-annealed condition. The third category consisted of

Table 6.1. Stress Corrosion Results on Steam Generator Materials Exposed to Steam Containing 10 ppm NaCl and 20 ppm O

Specimens were cycled between 425 and 280°C (800 and 540°C) — 24 hr 280°C saturation temperature three times per week.

Base Metal	Filler Metal	Surface Condition[a]	Number of Failures	Crack Time (week)	Crack Size (in.)	Crack Location[b]
Type 304 SS[c]	Type 308 SS	Ground	3 of 3	6	1/2	B&W
Type 304 SS	Type 308 SS	Process annealed	3 of 3	11	1/2	B&W
Type 304 SS	Type 308 SS	Pickled	3 of 3	3–10	1/2	B
Type 304 SS[d]	No weld	Ground	0 of 3			
Type 304 SS	No weld	Solution annealed	0 of 3			
Type 304 SS	No weld	Sensitized	0 of 3			
Type 304L SS[d]	No weld	Ground	0 of 3			
Type 304L SS	No weld	Solution annealed	1 of 3	8	1/8	
Type 304L SS	No weld	Sensitized	2 of 3	10	1/2	
Type 310 SS[d]	No weld	Ground	3 of 3	6–12	1/16–1/2	
Type 310 SS	No weld	Solution annealed	0 of 3			
Type 310 SS	No weld	Sensitized	0 of 3			
Type 316 SS[d]	No weld	Ground	1 of 3	6	1/2	
Type 316 SS	No weld	Solution annealed	1 of 3	6	1/8	
Type 316 SS	No weld	Sensitized	0 of 3			
Type 321 SS[d]	No weld	Ground	0 of 3			
Type 321 SS	No weld	Solution annealed	0 of 3			
Type 321 SS	No weld	Sensitized	0 of 3			
Type 347 SS[d]	No weld	Ground	1 of 3	8	3/16	
Type 347 SS	No weld	Solution annealed	0 of 3			
Type 347 SS	No weld	Sensitized	0 of 3			
18-18-2 SS[d,e]	18-18-2 SS	Process annealed	3 of 3	1–6	1/2	B
18-18-2 SS[c]	No weld	Ground	3 of 3	8	1/4–1/2	
18-18-2 SS	No weld	Process annealed	3 of 3	6–8	1/16–1/2	
Type 410 SS[c]	Type 410 SS	Ground	0 of 3			
Type 410 SS	Type 410 SS	Process annealed	0 of 3			
Type 410 SS	Type 410 SS	Pickled	0 of 3			

Table 6.1. (Continued)

Base Metal	Filler Metal	Surface Condition[a]	Number of Failures	Crack Time (week)	Crack Size (in.)	Crack Location[b]
Incoloy 800[c]	Inconel 82	Ground	3 of 3	6	1/16	B
Incoloy 800	Inconel 82	Process annealed	3 of 3	6–12	1/16–1/8	B
Incoloy 800	Inconel 82	Pickled	1 of 3	6	1/16	B
Incoloy 800[d]	No weld	Ground	0 of 3			
Incoloy 800	No weld	Process annealed	0 of 3			
Incoloy 800	No weld	Pickled	0 of 3			
Inconel 625[c]	Inconel 625	Ground	0 of 3			
Inconel 625	Inconel 625	Process annealed	0 of 3			
Inconel 625	Inconel 625	Pickled	0 of 3			
Inconel 625[d]	No weld	Ground	0 of 3			
Inconel 625	No weld	Process annealed	0 of 3			
Inconel 625	No weld	Pickled	0 of 3			
Inconel 600[c]	Inconel 82	Ground	2 of 3	5–12	1/16–1/8	B
Inconel 600	Inconel 82	Process annealed	0 of 3			
Inconel 600	Inconel 82	Pickled	0 of 3			
Inconel 600[d]	No weld	Ground	1 of 3	12	1/16	
Inconel 600	No weld	Process annealed	0 of 3			
Inconel 600	No weld	Pickled	0 of 3			
Inconel 601[d]	Inconel 601	Process annealed	0 of 3			

Table 6.1. (Continued)

Base Metal	Filler Metal	Surface Condition[a]	Number of Failures	Crack Time (week)	Crack Size (in.)	Crack Location[b]
Hastelloy X[c]	Hastelloy X	Ground	3 of 3	1–6	1/8–1/2	B&W
Hastelloy X	Hastelloy X	Process annealed	0 of 3			
Hastelloy X	Hastelloy X	Pickled	0 of 3			
Hastelloy X[c]	Hastelloy W	Ground	3 of 3	1–2	1/4–1/2	W
Hastelloy X	Hastelloy W	Process annealed	1 of 3	6	7/16	B&W
Hastelloy N[c]	Hastelloy N	Ground	2 of 2	11	1/2	W
Hastelloy N	Hastelloy N	Special anneal 1	0 of 2			
Hastelloy N[c]	No weld	Special anneal 2	2 of 2	1–2	1/2	
IN 102[c]	IN 102	Ground	3 of 3	2–5	1/2	B
IN 102	IN 102	Process annealed	3 of 3	5–12	1/8–1/4	B&W

[a]Ground = ground on a 100-mesh belt. Process annealed = ground and heated 10 min at 980°C except for ferritic materials which were ground and heated 10 min just below the lower critical temperature. Pickled = ground, process annealed, and pickled in solution recommended by supplier of alloy. Special anneal 1 = ground and heated 8 hr at 870°C. Special anneal 2 = ground and heated 1 hr at 1175°C.

[b]B = base metal and W = weld deposit.

[c]Weldment prepared from 1/2-in.-thick plates in hot-rolled, descaled, and annealed condition.

[d]Cold rolled and annealed sheet stock 1/16 in. thick.

[e]18 Cr–18 Ni–2 Si alloy furnished by U. S. Steel Corporation.

[f]Experimental 18 Cr–2 Mo alloy supplied by Republic Steel Corporation.

strip specimens cut from nonwelded, 1/16-in.-thick sheet in a variety of stainless steel alloys. These sheet materials were originally in the cold-rolled and solution-annealed condition. To determine the influence of surface preparation, the specimens of categories 1 and 2 were prepared in the three surface conditions: (1) 100-mesh ground, (2) ground and process annealed, and (3) ground, annealed, and pickled. The third category of specimens (various types of stainless steels) were prepared in the conditions: (1) ground, (2) ground and solution annealed, and (3) ground, solution annealed, and sensitized.

The results of the sixth run were like those of the previous one in several respects. Of the various surface preparations tested, the ground condition showed by far the highest susceptibility to cracking (see Table 1). The same similar-metal weldments prepared in 1/2-in.-plate material (category 1) that had cracked previously failed again. Weldment specimens in Inconel 625 and type 410 stainless steel joined with themselves did not crack in any surface condition, whereas type 304 stainless steel welded with type 308 stainless steel failed in all three conditions. Plate weldments of Hastelloy X, joined both with itself and Hastelloy W, showed substantial susceptibility to cracking as did Hastelloy N and IN 102 welded with themselves. Incoloy 800 welded with Inconel 82 showed some cracking in all three surface conditions, although the cracks were superficial and propagated slowly. Inconel 600 welded with Inconel 82 showed somewhat improved resistance to cracking; only two specimens showed small cracks and those were in the specimens tested in the ground condition.

The cracking in the foregoing weldment specimens generally was intergranular in nature and usually initiated in the heat-affected zone of the base metal on the root side of welds.

It will be noted in Table 6.1 that the base metals, when tested as nonwelded sheets (category 2 specimens), with minor exceptions, failed to exhibit any cracking. These base-metal alloys include type 304 stainless steel, Incoloy 800, and Inconel 600.

Finally, it should be noted that the various grades of stainless steel as sheet stock (category 3 specimens) showed surprisingly good resistance to cracking. An exception to this is the severe cracking

displayed by an experimental 18 Cr–2 Mo alloy supplied by the Republic Steel Corporation. Types 304L and 310 stainless steel displayed some tendency to crack.

The trend observed for alloys to fail when they are the base metals of weldments but to resist cracking when tested as sheet stock was unexpected, and tests are being planned (run 8) to explain these results. Nonwelded specimens will be tested in the 1/2-in.-plate materials that failed as weldments, and weldment specimens will be prepared in the sheet stock that resisted cracking in the nonwelded condition. It is suspected that microfissures, which sometimes formed at the edge of the weldment specimens alongside the root-pass protrusion during bending for mounting, may be an important factor. Such fissures would be expected to act as minute corrosion crevices as well as stress risers. Thus, specimens in the weldment materials that have the root-pass protrusion removed so as to eliminate edge microfissures will be included in these tests.

Stress-corrosion run No. 7, which is being conducted under the same operating parameters as run 6, is now under way. This test run primarily incorporates various advanced and commercial alloys supplied as sheet material by the International Nickel Company and the Cabot Corporation, together with all of the various ferritic materials of interest for LMFBR use.

After completing corrosion runs 7 and 8, which are to be conducted under the same test conditions as run 6 to permit comparisons between all of the materials under investigation, we plan to test at lower contamination levels. The types of alloys to be examined will be more restricted and an attempt will be made to determine the environmental conditions under which cracking begins.

7. JOINING OF STRUCTURAL MATERIALS

J. R. Weir G. M. Slaughter

Joining research and development is being carried out on a wide variety of structural materials of interest to the Liquid Metal Fast Breeder Reactor Project. The vessel, primary piping, and core support structure of the Fast Flux Test Facility (FFTF) are being made of austenitic stainless steel while steam generators for the demonstration plants will likely contain ferritic steels or Incoloy 800. Inconel 718, on the other hand, is being used or considered for such applications as the Power Burst Facility, the instrument tree for FFTF, and valves and bearing surface components for liquid metal service.

In view of the diversity of problems associated with those different classes of materials, the progress is reported under the general materials types (i.e., austenitic stainless steels, ferritic steels, and nickel-rich alloys).

AUSTENITIC STAINLESS STEELS

Welding Development for FBR Stainless Steel Components

G. M. Slaughter H. E. McCoy

We are evaluating the behavior of weldments in austenitic stainless steel at 370 to 750°C as a function of both welding process and the variables within a process for application to liquid-metal-cooled fast breeder reactor (LMFBR) vessels and components. The solidification substructure of the weld metal markedly influences the mechanical properties of a weldment at elevated temperature; since the size and type of substructure are significantly influenced by factors which the welder can control, our approach is to determine this link between welding variables, the solidification substructure which these variables produce, and the resultant mechanical properties. Also included in the studies are corrosion behavior, irradiation stability, and the effect of heat treatment on structure and properties.

In this report we have elected to present creep-rupture data in a form that differs from previous progress reports, a change intended to better serve the needs of designers.

Investigations of Mechanical Properties (R. G. Berggren, G. M. Goodwin)

Submerged-Arc Welds. — Creep-rupture tests on the six submerged-arc weldments, designated SA-2 through SA-7 (ref. 1), have now extended the data for all six welds to rupture times of about 1000 hr. Creep for these six welds in the "as-welded" condition are summarized in Table 7.1. This table, as well as Tables 7.2 and 7.3, presents stresses for a minimum strain rate (second-stage creep rate) of 10^{-6} hr^{-1}, stresses for rupture in 10^3 hr, 0.5% strain in 10^3 hr, and onset of third-stage creep (0.2% offset from linearity) in 10^3 hr, and fracture strain in 10^3 hr. The schedule of test parameters was designed primarily to provide ductility data for rupture lives of 1000 hr. The stresses for a minimum strain rate of 10^{-6} hr^{-1} and for the onset of third-stage creep in 10^3 hr were obtained by reviewing the original data. Due to the design of the test schedule these stress values often involved extrapolation of the available data. The tabulated values of stress for minimum strain rates of 10^{-6} hr^{-1} required extrapolations of one to two orders of magnitude in strain rate (i.e., the lowest recorded minimum strain rates were 10^{-5} to 10^{-4} hr^{-1}). The tabulated values of stress for 0.5% strain in 10^3 hr in the submerged-arc welds required extrapolations of more than one order of magnitude in time and in the shielded metal-arc welds required extrapolations only as indicated by footnotes. The tabulated values of stress for onset of third-stage creep in 10^3 hr required the extrapolations indicated by footnotes.

It is difficult to draw unambiguous conclusions from the results presented in Table 7.1 because of the scatter in the data and the extrapolations described above. Comparison of the results for welds SA-3, SA-4, and SA-5, where the only known variable is the energy input during

---

[1]R. G. Berggren and G. M. Goodwin, Fuels and Materials Development Program Quart. Progr. Rept. Mar. 31, 1971, ORNL-TM-3416, p. 118.

Table 7.1. Creep Properties of Submerged-Arc Welds: Type 308 Stainless Steel, As Welded

Weld No. SA-	Description	Stress for $\dot{\epsilon}_{min} = 10^{-6}$/hr (psi)	Stress (psi) in 1000 hr for			Rupture Strain at 10^3 hrs (%)	Reduction of Area at 10^3 hrs (%)
			Rupture	0.5% Strain	Start of Third Stage		
		Test Temperature: 650°C (1200°F)					
2	Arcos flux, medium heat input, sent to WADCO	8,000	12,800[a]	9,000[b]	11,600[a]	13[a]	< 10[a]
3	Arcos flux, low heat input	10,000	14,000	9,200[b]	13,000[a]	5	12
4	Arcos flux, medium heat input	8,000	13,200[a]	c	12,500[a]	8[a]	15[a]
5	Arcos flux, high heat input	7,600	13,800[a]	8,000[b]	13,000[a]	13[a]	28[a]
6	Hobart flux, medium heat input	8,400	15,000[a]	c	14,400[a]	11[a]	18[a]
7	Arcos flux, medium heat input, duplicate of NRL welds	c	13,500[a]	c	12,000[a]	9[a]	6[a]
		Test Temperature: 593°C (1100°F)					
2	Arcos flux, medium heat input, sent to WADCO	12,800	20,200	11,000[b]	18,000	13	c
3	Arcos flux, low heat input	14,400	22,400	14,000[b]	20,400	12	12
4	Arcos flux, medium heat input	12,600	20,400	9,400[b]	18,200[a]	12	15[a]
5	Arcos flux, high heat input	11,800	20,400	10,800[b]	19,000	10	20
6	Hobart flux, medium heat input	14,000	22,000	15,000[b]	20,000	11[a]	20[a]
7	Arcos flux, medium heat input, duplicate of NRL welds	11,800	19,600	11,000[b]	17,600[a]	18	46

[a]Extrapolated less than one order of magnitude in time.

[b]Extrapolated more than one order of magnitude in time.

[c]Not determinable from existing data.

Table 7.2. Creep Properties of Shielded Metal-Arc Welds: Type 308 Stainless Steel, As Welded — Test Temperature: 650°C (1200°F)

Weld No. F-	Description (coating)	Stress for $\dot{\varepsilon}_{min} = 10^{-8}$/hr (psi)	Stress (psi) in 1000 hr for			Rupture Strain at 10^3 hr (%)	Reduction of Area at 10^3 hr (%)
			Rupture	0.5% Strain	Start of Third Stage		
1	Lime (commercial)	12,200	14,600	10,600 [a]	14,400 [b]	1	3
2	Lime-titania (commercial)	17,600	17,400	17,000 [b]	17,000 [b]	< 3	< 7
3	Titania (commercial)	17,000	17,200	17,200 [b]	17,200 [b]	< 2	< 1
4	Lime-titania, low silicon	14,800	16,400	15,800 [b]	16,600 [b, c]	< 1	< 10
5	Lime-titania, high silicon	18,600	18,600	19,000 [b,c]	19,400 [b,c]	< 1	< 10
6	Lime-titania, low phosphorus	17,800	17,800	d	d	< 1	< 1
7	Lime-titania, high phosphorus	18,500	20,000	19,000	19,200	6	20
8	Lime-titania, low sulfur	17,400	16,800	17,000 [b,c]	17,200 [b,c]	< 1	< 5
9	Lime-titania, high sulfur	16,200	17,000	17,500 [b,c]	17,000 [b]	< 1	< 1
10	Lime-titania, low carbon	17,500	17,000	17,800 [b,c]	17,400 [b,c]	< 1	< 5
11	Lime-titania, high carbon	20,000	19,500	19,000	19,200	< 3	< 7
12	Lime-titania, medium boron	18,400	20,000	19,200	19,200	8	26
13	Lime-titania, high boron	18,600	20,400	19,400 [b]	19,800 [b]	8	29
14	Lime-titania, medium phosphorus	17,400	18,000	18,000	17,600	3	11
17	Lime, high boron, phosphorus, ferrotitanium	20,200	21,000	20,400	20,600	16	60
18	Lime, medium boron, high phosphorus ferrotitanium	19,200	20,600	20,200	20,600	14	40
21	Lime, high boron, phosphorus, ferrotitanium, 1/4 in. electrode	21,500	22,800	> 20,000	22,600	20	70

[a] Extrapolated more than one order of magnitude in time.

[b] Extrapolated less than one order of magnitude in time.

[c] Greater than stress to rupture in 1000 hr (extrapolation).

[d] Not determinable from existing data.

Table 7.3. Creep Properties of Heat Treated Type 308 Stainless Steel Welds — Test Temperature 650°C (1200°F)

Number	Heat Treatment[a]								Stress for $\dot{\epsilon}_{min} = 10^{-6}$/hr (psi)	Stress (psi) in 1000 hr for			Rupture Strain at 1000 hr (%)	Reduction of Area at 1000 hr (%)
	Annealing		Cooling Rate[b] (°F/hr)	Carbide Agglomeration		Cooling Rate[c] (°F/hr)	Aging[d]			Rupture	0.5% Strain	Start of Third Stage		
	Temperature (°F)	Time (hr)		Temperature (°F)	Time (hr)		Temperature (°F)	Time (hr)						
						Shielded Metal-Arc Weld F-21: Coating — lime, high boron, phosphorus, ferrotitanium								
1	No postweld heat treatment								21,500	22,000	21,000	22,600	20	70
3	1,950	2	150	1,472	10	400	Not aged		17,400	20,800	16,000[e]	20,800	29	74
4	1,950	2	150	1,472	10	400	1,200	100	15,600	20,000	f	19,800[g]	30	75
7	1,750	2	150	1,472	10	400	Not aged		18,500	20,900	17,000[e]	20,100	22	60
8	1,750	2	150	1,472	10	400	1,200	100	20,000	20,800	20,200	20,800	f	f
						Submerged-Arc Welds SA-9, SA-10, and SA-11: Arcos flux, medium heat input, 2-in. plate								
1	No postweld heat treatment								f	f	f	f	f	f
4	1,950	2	150	1,472	10	400	1,200	100	7,500	14,000	f	11,300[e]	32	45
6	1,950	2	150	1,472	10	100	1,200	100	7,500	13,500[e]	f	11,000[e]	21[e]	30[e]
8	1,750	2	150	1,472	10	400	1,200	100	7,500	13,500[e]	f	11,600[e]	10[e]	18[e]
10	1,750	2	150	1,472	10	100	1,200	100	7,500	12,300	f	11,000[e]	12	15

[a] R. G. Berggren and G. M. Goodwin, Fuels and Materials Development Program Quart. Progr. Rept. Mar. 31, 1971, ORNL-TM-3416, pp. 118–137.

[b] Cooling rate from annealing temperature to carbide agglomeration temperature (1472°F).

[c] Cooling rate from 1472 to 850°F, then water quenched.

[d] Cooling rate from 1200°F aging temperature was 100°F/hr to 850°F, then water quenched.

[e] Extrapolated more than one order of magnitude in time.

[f] Insufficient data.

[g] Extrapolated less than one order of magnitude in time.

welding, indicates that increasing the energy input lowers strength and increases ductility. Welds SA-2 and SA-4 should be similar except that different heats of plate and filler metal were used. As expected, there are only minor differences in strength and ductility between the two welds. Weld SA-7 was produced under full mechanical restraint but otherwise should be very similar to weld SA-2. The results for these two welds are not consistently different. It should be noted that the high reduction of area (46%) for weld SA-7 tested at 593°C is probably due to scatter in the data. Weld SA-6, made with the Hobart HS-300 flux, showed somewhat better strength and ductility properties than the other medium heat input welds made with another flux. Although there are apparent property differences between these submerged-arc welds, they are not as marked as for the shielded metal-arc welds discussed in the next section.

Shielded Metal-Arc Welds. — Our objective is to determine the effects of electrode coating on the shielded metal-arc (stick electrode) welding process. We are comparing the microstructures and elevated-temperature mechanical properties of 23 shielded metal-arc weldments made with type 308 stainless steel electrodes.[2] Six of these weldments were eliminated due to welding difficulties or other reasons. Included in the remaining 17 weldments are the three most popular electrode coatings produced by a commercial supplier: lime, titania, and lime-titania. The lime-titania is the most widely used, and we have been studying the effects of minor changes in C, Si, P, S, and B contents of the electrode coating and subsequent deposited weld metal (deposit composition is within the allowable type 308 stainless steel composition limits in all cases). We have now extended the data for all 17 welds to rupture times of about 1000 hr and in some cases to well over 1000 hr. Significant variations in creep strength and ductility were observed.

Table 7.2 summarizes the creep data for these 17 welds in the "as-welded" condition. Some data on the effects of postweld heat treatment

[2]N. C. Binkley, G. M. Goodwin, and D. G. Harman, Fuels and Materials Development Program Quart. Progr. Rept. Dec. 31, 1969, ORNL-4250, pp. 165–172.

are presented in the following section. The first series of controlled-chemistry weldments, welds F-4 through F-14, exhibited improved ductilities when either phosphorus (welds F-7 and F-14) or boron (welds F-12 and F-13) was increased. In addition, the creep strengths were somewhat increased. Based on results for welds F-4 through F-14, two additional weld compositions, welds F-17 and F-18, were studied. As may be noted in Table 7.2, these welds exhibited marked improvments in creep ductility and significant increases in creep strength. The final weldment in the present series, weld F-21, has exhibited a very significant improvement both in creep ductility and strength. A weld composition approximating weld F-21 was selected for the FFTF pressure vessel.

Effects of Heat Treatment. — Some results were reported previously[3] for commercially feasible heat treatments of both shielded metal-arc (weld F-21) and submerged-arc (welds SA-9, SA-10, and SA-11) weldments. A summary of the data now available on heat treatment of these welds is presented in Table 7.3. We do not yet have test data on welds SA-9, SA-10, or SA-11 for the "as-welded" condition. Heat treatment of the shielded metal-arc weld (F-21) resulted in slight increases in ductility and some loss of creep strength. Aging at 650°C for 100 hr had little or no effect on strength or ductility. Annealing at 955°C instead of 1065°C resulted in slightly higher strengths and slightly lower ductilities. However, annealing the submerged-arc weldment at 955°C instead of 1065°C resulted in both lower strengths and lower ductilities. The effect of cooling rate from the carbide agglomeration temperature (800°C) was slight with the better properties shown for the higher cooling rate.

In summary, the strengths of the improved shielded metal-arc weld, F-21, are markedly higher than for any of the other welds. The ductilities are higher than for any of the other welds in the "as-welded" condition and about the same as for any of the heat-treated welds.

---

[3]R. G. Berggren and G. M. Goodwin, Fuels and Materials Development Program Quart. Progr. Rept. Mar. 31, 1971, ORNL-TM-3416, pp. 118–137.

Filler Metal Development for Pipe Welding (Nancy C. Cole, G. M. Goodwin)

We are developing improved bare filler wires for welding stainless steel piping by the gas tungsten-arc process. The initial aim is to duplicate the deposit analysis produced by the special shielded metal-arc electrodes used in the production of the FFTF vessel. Since the amount of minor element recovered from wire to deposit is unknown, initial experiments must be conducted to optimize the composition of the filler wire itself. Then screening mechanical properties studies will be conducted to determine the degree of improvement afforded by the controlled minor element additions with the tungsten-arc process.

Production and Procurement of Experimental Filler Wire. — Small drop castings of type 308 stainless steel filler metals with the following deviation from the standard composition were made and fabricated into a sufficient amount of wire to yield a single test plate.

Heat Number	Composition	Heat Number	Composition
1	Remelted standard type 308 stainless steel filler wire	6	0.5% Ti
		7	1.0% Ti
2	0.007% B	8	0.007% B, 0.045% P
3	0.015% B	9	Pure stock; Si as low as possible
4	0.045% P	10	Pure stock; Si same as in heat 1
5	0.060% P		

We are also procuring an experimental batch of type 316 stainless steel-coated electrodes. The coating will be similar to that placed on the type 308 stainless steel-coated rod for the FFTF vessel application. Thus, we will be able to determine the feasibility of achieving the general strength and ductility improvements in the type 316 stainless steel composition that we did in the type 308 stainless steel composition.

Preparation of Weldment Specimens. — We are preparing weldment specimens in 1/2-in.-thick types 304 and 316 stainless steel plate to simulate piping welds made with both conventional and experimental filler metal compositions. Both the shielded metal-arc and gas tungsten-arc processes are represented.

Plate sections, 10 × 3 × 1/2 in. thick, are machined along their 10-in. length with a typical pipe-welding edge preparation (single "Vee" groove, 75° included angle, 1/16-in. root face) and welded in the flat (IG) position using welding parameters typical of pipe welds in the 1/2-in. wall thickness range.

All-weld-metal mechanical properties specimens will be machined from the test pieces and subjected to relatively short (< 1000 hr) screening-type creep-rupture tests at 650°C.

The status of the welds involved in the study is given in Table 7.4.

NICKEL-RICH ALLOYS

G. M. Slaughter

Inconel 718

D. A. Canonico P. Patriarca

We have been asked to assist Aerojet Nuclear Corporation in obtaining ASME Code approval for Inconel 718, an age-hardenable, nickel-chromium alloy. Our involvement included visits to corporations who are employing this alloy in the fabrication of high-strength components. We are concerned specifically with the effect of welding on the mechanical properties of the postheat-treated weldments. The prime concern lies in the attainable levels of ductility in the welds.

Currently, the Power Burst Facility (PBF) is being fabricated from Inconel 718. Bend ductility after welding was somewhat poorer than what was anticipated. We have discussed this problem with representatives of the Aerojet Nuclear Corporation. They feel that acceptable levels of bend ductility can be obtained, and they would prefer that we concentrate our efforts on the Code Case application.

We attended an ASME Meeting in New York in September and participated in discussions concerning those data needed for Code approval. Apparently, considerable data do exist for Inconel 718, and approval for the lower temperature (800°F and below) applications is readily obtainable. The major problem areas lie in the establishment of the weld bend ductilities for Section IX acceptance and strain fatigue data for several heats.

Table 7.4. Summary of Simulated Stainless Steel Pipe Welds in 1/2-in.-thick Plate

Weld Number	Process[a]	Base Plate (type stainless steel)	Wire/Electrode (type stainless steel)	Status as of 9/30/71
1	GTA	304	308 (standard)	Weld completed
2	GTA	304	308 (standard)	Weld completed
3	GTA	304	308 (remelted)	Wire available
4	GTA	304	308 (70 ppm B)	Wire available
5	GTA	304	308 (150 ppm B)	Wire available
6	GTA	304	308 (0.045% P)	Wire available
7	GTA	304	308 (0.06% P)	Wire available
8	GTA	304	308 (0.5% Ti)	Wire available
9	GTA	304	308 (1% Ti)	Wire available
10	GTA	304	308 (70 ppm B, 0.045% P)	Wire available
11	GTA	304	308 (0.0% Si)[b]	Wire available
12	GTA	304	308 (same percentage of Si as 3)[b]	Wire available
13	GTA	316	316 (standard)	Weld completed
14	GTA	316	316 (standard)	Weld completed
15–22	GTA	316	316 (standard)[c]	Wire to be ordered
23	SMA	304	308 (standard)	Electrodes on order
24	SMA	304	308 (standard)	Electrodes on order
25	SMA	304	308 (70 ppm B, 0.045% P)	Electrodes on order
26	SMA	316	316 (standard)	Electrodes on order
27	SMA	316	316 (standard)	Electrodes on order
28	SMA	316	16-8-2 (standard)	Electrodes on order
29	SMA	316	316 (70 ppm B, 0.045% P)	Electrodes on order

[a]GTA – gas tungsten-arc process; SMA – shielded metal-arc process.

[b]Start with pure melt stock, add other elements to obtain nominal composition.

[c]Same additions to standard type 316 stainless steel as in 3–10 above.

A program has been written and costed for doing the work necessary for approval of Inconel 718 for higher temperature applications. Here, extensive elevated-temperature data must be obtained.

Incoloy 800

D. A. Canonico

We are conducting a metallographic study at magnifications of 20 to 200× the as-welded qualification welds made with the previously discussed experimental alloys of a basic Incoloy 800 composition. This study is concerned with the presence of fissures in the weld metal. Our observations of those alloys that contain only titanium and aluminum (in addition to the Fe-Ni-Cr) have shown that titanium is most effective for avoiding fissuring. The range of aluminum and titanium is 0.15 to 0.60%. Those alloys that contain 0.38% Ti and less showed evidence of microfissuring. Those with 0 to 0.15% Ti were rated severe, whereas those with 0.38% Ti are rated slight. Only the alloy with 0.60% Ti (and 0.60% Al) contained no discernible fissures.

Table 7.5 synopsizes the results of this study. It can be seen that the alloy that contains little titanium was severely fissured, and the results indicate that a modest titanium content is needed to avoid weld-metal fissuring. Further, the presence of aluminum appears to be somewhat beneficial, but it will not avoid fissuring in its own right.

The investigation of the microstructures also included the commercial filler metals for joining Incoloy 800. This facet of the program included Inconel 82T, the currently recommended filler metal for joining Incoloy 800 and a candidate filler metal under development by Huntington Alloy Product Division of the International Nickel Company. The analyses of these alloys were previously reported.[4] The Inconel 82T alloy (and the experimental commercial alloy) do not contain fissures. The fissures

---

[4]D. A. Canonico, "Weldability of Incoloy 800," Fuels and Materials Development Program Quart. Progr. Rept. Mar. 31, 1971, ORNL-TM-3416, p. 224.

Table 7.5. Effect of Aluminum and Titanium on Cracking Tendency of Experimental Incoloy 800 Weld Metal

Alloy Identification	Nominal Weight Percent		Metallographic Observations
	Al	Ti	
175	0.15	0.15	Severe fissuring
176	0.38	0.38	Few fissures
177	0.60	0.60	No fissures
143	0.38	0.15	Moderate-to-severe fissures
144	0.38	0.60	Slight tendency
145	0.15	0.38	Few fissures
146	0.60	0.38	Few fissures
208		0.38	Few fissures
209	0.38		Severe fissuring

that are observed in the experimental weld metal are intergranular. Further, the experimental weld metal structure is composed of large columnar grains, whereas the fissure-free welds do not contain clearly delineable grain boundaries. This microstructural difference can be seen in Fig. 7.1.

A study of the fusion line shows the difference in the behavior of the solidification mode of the commercial and experimental alloys. The epitaxial growth of the heat-affected zone grains is short ranged in the Inconel 82T alloy, whereas it continues unhindered into the experimental weld metal. The gross difference in fissuring behavior between the experimental and commercial filler metals is believed to be due in part to these microstructural differences.

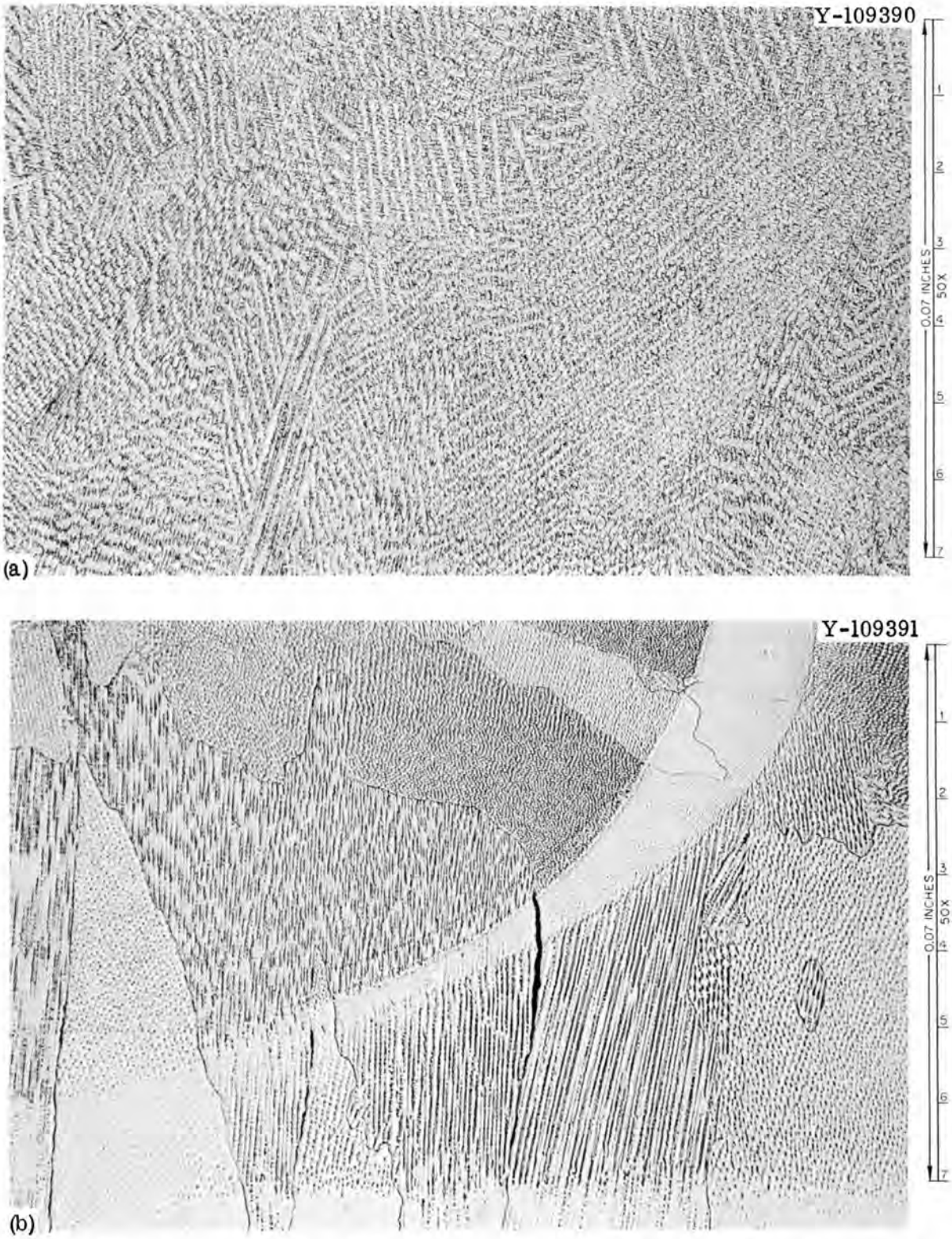

Fig. 7.1. Metallographic Differences Between Weld Metals Deposited from Commercial Filler Metals and Experimental Incoloy 800 Filler Metal. Note fissure in large columnar grains in the experimental alloy. (a) Alloy Inconel 82T. (b) Experimental alloy.

FERRITIC STEELS

G. M. Slaughter

Stabilized Grades

D. A. Canonico

The investigation of the stabilized ferritic steels has concentrated on the niobium-stabilized 2 1/4 Cr—1 Mo—1/2 Ni low-alloy grade. The effort is directed toward the determination of the basic weldability of this alloy. Our studies have shown that it is prone to hot cracking when welded under highly restrained conditions. The cracks can be back-filled with an Fe_2Nb-δ iron eutectic thereby eliminating the actual cracks.

The current studies are involved in determining the mechanical properties of "sound welds." We have prepared ASME qualification welds of both 1/4- and 1/2-in.-thick plates of niobium-stabilized steel from two heats obtained from Sandvik Steel. The heat numbers and their chemical composition are shown in Table 7.6. Filler metal has been prepared from material from each heat.

Table 7.6. Chemical Composition of Niobium-Stabilized Steel Plate Used in this Study

Heat Number	Composition, %								
	C	Si	Mn	P	S	Cr	Ni	Mo	Nb
4-03150	0.09	0.27	0.48	0.017	0.004	2.36	0.60	0.97	0.98
4-50543	0.08	0.35	0.46	0.011	0.005	2.18	0.54	0.94	1.08

Fully restrained qualification welds have been made using the gas tungsten-arc (GTA) welding process. No preheat was used for the first series. These welds have successfully passed radiography and root- and face-bend tests (1/4-in.-thick plate) and side-bend tests (1/2-in.-thick plate) where the radius of curvature was two times the thickness. They are metallographically sound and are being tensile tested at room temperature and 1050°F.

The weldments, although sound, have their prior austenite grain boundaries distinctly outlined with what is believed to be the Fe_2Nb-δ iron eutectic. Charpy V-notch specimens are being prepared to determine the effect of this structure on the toughness of these weldments.

We have initiated tubular weld studies on 20-mm-diam tube with 2-mm wall. Our aim is to weld these tubes with one pass using parameters similar to those being employed commercially. These welds are being made in simple butt joints with and without inserts and with beveled end-preparations.

Low-Carbon Grades

D. A. Canonico

The study of the low-carbon 2 1/4 Cr–1 Mo steels is directed toward the assessment of the effect of carbon content on the mechanical properties of weldments. These properties will serve as a guide in the selection of the optimum carbon level to be used in the fabrication of steam generators for demonstration plants.

Welds have been made with identical parameters to those previously[5] reported. These were made in 1/2-in.-thick plates that had been normalized at 930°C for 1 hr and tempered at 705°C for 1 hr. These weldments were sectioned to provide transverse specimens for the mechanical property studies.

Hardness traverses, through the weld metal, heat-affected zone, and base metal, were conducted on weldments of all three carbon levels. These data are presented for the as-welded and welded-and-stress relieved conditions in Table 7.7. In the as-welded condition, it is evident that the base metal is the softest zone regardless of carbon content. This is also true for welds made with the medium (0.035%) and high (0.11%) carbon materials after a 705°C postweld heat treatment. (No postweld heat treatment data are available for the low-carbon welds since there was not sufficient material to conduct a study.)

---

[5]D. A. Canonico and H. E. McCoy, Fuels and Materials Development Program Quart. Progr. Rept. Mar. 31, 1971, ORNL-TM-3416, pp. 143–146.

Table 7.7. Results of Hardness Traverses on Welds with Varying Carbon Contents

Weld Designation	Carbon Content (%)	Diamond Pyramid Hardness Number				
		Heat-Affected Zone		Weld Metal		Base Metal
		Last Pass	Early Pass	Last Pass	Early Pass	
2A	0.003					
As welded		166/239	165/177	242/266	152/180	129/135
Stress relieved						
2B	0.035					
As welded		163/225	180/210	291/307	205/275	127/145
Stress relieved		135/176	126/142	203/211	164/196	115/117
2C	0.11					
As welded		238/264	234/312	361/394	256/361	177/194
Stress relieved		205/228	190/218	223/234	199/228	180/192

We have prepared tubular weld specimens with various joint configurations and are currently developing parameters for welding 2 1/4 Cr—1 Mo steel tubes (ASTM A213 T-22) with varying diameters and wall thicknesses. Our efforts are concentrated on making single pass welds in as heavy a walled tube as possible. Where necessary, a multipass technique is being employed.

The mechanical properties studies are somewhat handicapped by a tubular-type specimen. Therefore, we have developed a simulated bore-side tube weld that can be made on flat plate. Configurations representing the tube sheet and tube have been prepared. Figure 7.2 illustrates this specimen and the suggested weld sequence to provide the simulated overlap region of a tubular weld. We are currently developing the parameters for welding the simulated bore-side weld.

ORNL-DWG 71-9023

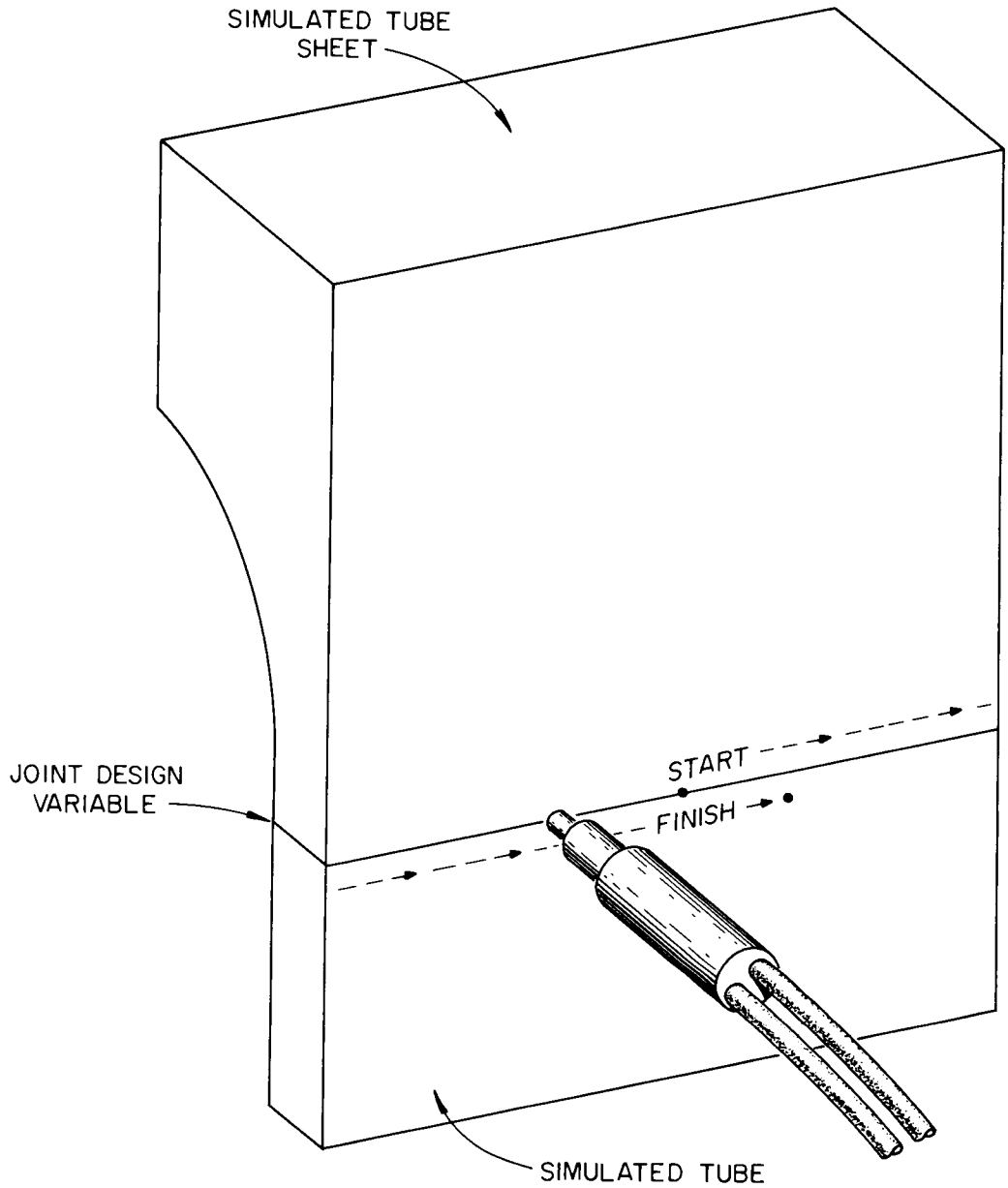

Fig. 7.2. Welding Study, Specimen Configuration to Simulate Bore-Side Welds.

8. NONDESTRUCTIVE TESTING DEVELOPMENT

W. O. Harms R. W. McClung

This program is designed to develop new and improved methods of examining LMFBR materials and components. Among the methods being studied are electromagnetic induction, ultrasonics and penetrating radiation. Special emphasis is being given to developing techniques for inspection problems related to the steam generator.

NDT Development for Steam Generators

R. W. McClung

We began a development program to solve specific problems of nondestructive testing of steam generators for LMFBR. Discussions with appropriate personnel of reactor contractors and steam generator fabricators assisted in the definition of the most important problem areas. Unanimous concurrence established the inspection of bore-side tube-to-tube sheet joints as being the area most needing investigation. Among other recognized problems are the post-operation examination of steam generator tubing for wall thinning and integrity, and inspection of end-closure weldment on the "scabbard" tube in the bayonet tube design. Emphasis in this report is on the planned program to develop techniques to inspect the tube-to-tube sheet joints. Several techniques including radiography, liquid penetrants, eddy currents and ultrasonics are being considered and will be studied. Typical test specimens for the development program are shown in Fig. 8.1. The configuration on the left represents a section of tube sheet (on the bottom) welded to a section of tubing. All examination techniques for this joint will be performed from the bore of the tube with access from the face of the tube sheet. The specimen on the right represents the tube-to-tube sheet joint as if the cylindrical specimen had been split longitudinally and flattened. The simulated tube sheet is at the bottom and the tube section is at the top. By proper design of the flat weld specimen, the welding parameters can accurately simulate the condition to be encountered in the cylindrical

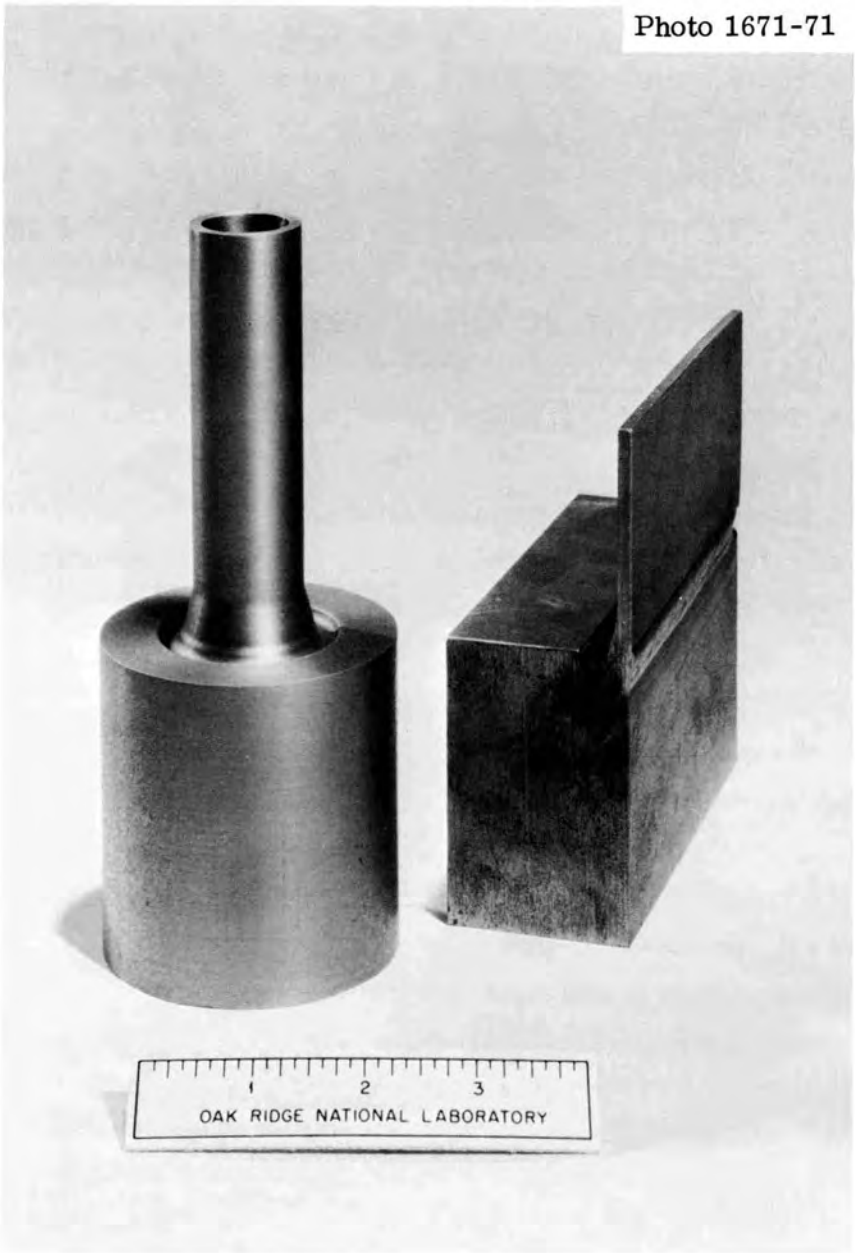

Fig. 8.1. Simulated Tube-to-Tube Sheet Joints for LMFBR Steam Generator.

shape. For much of the NDT development the flat specimen offers simpler, more economical approaches for establishing the basic test parameters.

Radiography

An x-ray tube with a 3/8-in. diam rod anode[1] has been developed and built on a limited commercial basis to inspect circumferential welds in tubing. Steel sections as thick as approximately 1/8 in. have been examined with this device that operates at energies up to 75 kvp. Some difficulties have been reported in maintaining proper focus of the electron beam, particularly in steel sections with stray magnetic fields. A similar unit with x-ray energies up to 100 kv and with a smaller focal spot (0.1 mm rather than 0.25 mm) is reported to have been developed in Holland and used by Roentgen Technische Dienst, Rotterdam. Additional information about each of these units will be obtained.

As an alternate, radioisotopic sources should be considered. Our inquiries disclosed two potential candidates, ^{109}Cd and Ytterbium. The other isotopes considered had an improper energy or too short a half life. The more promising (and more expensive; e.g., $40,000 per curie) appeared to be cyclotron-grade Cd with an energy of 87 keV and a 1.3 year half life. Ytterbium, although significantly less expensive (approximately $1500 per curie), has an average energy between 150–200 keV and a 30-day half life. The potential for useful radiography using radioisotopes will depend, in part, on the special design details of the tube-to-tube sheet joint including the choice of material, thickness of the weld, and diameter of the tubing.

For both the x-ray and isotopic inspection, work is needed to establish ultimate sensitivity, realistic reference standards and improved methods for application of the radiographic film.

Liquid Penetrants

Another accepted and beneficial examination technique is the use of liquid penetrants to detect surface discontinuities. In previous work on

[1]D. E. Elliott, "An Insertion X-ray Generator and Its Application," Los Alamos Scientific Laboratory, unpublished report, July 15, 1965.

tubing, we developed preliminary techniques for the examination of the inner surface of the tube with fluorescent penetrants using a black light borescope. Needed work in this area includes development of prototype hardware for penetrant application and removal, and borescope examination and post-cleaning. Coupling of the borescope to a closed-circuit television camera will allow more viewing and recording on video tape.

Eddy Currents

Although not widely used in the past for examination of weldments, the potential for high-speed examination with real-time, qualitative, recorded data makes eddy-current techniques a strong candidate for study. A high probability of success is predicted because of (1) previous work in developing phase-sensitive eddy-current instruments that are relatively insensitive to variations in coil-to-specimen spacing, and (2) development of mathematical models to optimize coil design and other test parameters for optimum results. The preliminary work will be on the flat weld specimens with existing instrumentation and simple scanners. This will provide experimental confidence and guidelines for performing the more difficult development within the bore of the tubular weldment.

Ultrasonics

Ultrasonic methods also offer a strong potential for the examination of tube-to-tube sheet weldments. As with eddy currents, there is a strong potential for real-time quantitative data from the examination. The first work is being conducted on a flat weld specimen to determine optimum test parameters; ultrasonic frequency size, type and number of transducers, optimum angles of incidence, effect of surface irregularities, et al. As with eddy currents, the ground work will be established on the flat specimens before developing the more expensive probes for the tubular configuration.

Electromagnetic Inspection Methods (Eddy Currents)

C. V. Dodd, W. A. Simpson, Jr., C. C. Lu,[2] W. E. Deeds,[3] and C. C. Cheng[4]

We continued research and development of electromagnetic inspection methods on both theoretical and experimental bases. We have continued to study the measurement of thickness of single layers as well as thickness of one material clad on another using the phase-sensitive eddy-current instrument. We have determined the optimum coil design for various cases of thickness measurement to give minimum lift-off effects. We are varying the coil dimensions (primarily the minimum lift-off and the coil length) to give the minimum lift-off effect at the same value of $\omega\mu\sigma\bar{r}^2$ as the maximum sensitivity. For the case of cladding thickness measurements, there is an optimum value of coil radius ($\bar{r}$) and of the dimensionless product $\omega\mu\sigma\bar{r}^2$ for maximum sensitivity which in turn depends on the ratio of the conductivities of the two materials. Figure 8.2 shows how the coil length for minimum lift-off effect varies as the ratio of conductivities for various values of minimum lift-off.

We are calculating the optimum parameters to use for detecting defects on the opposite side of a plate from the probe. These calculations are being verified by measurements. In addition, since the calculations are for small, regular-shaped defects, we are experimentally determining the shape and orientation factors for larger crack-shaped defects.

Measurement of Liquid Level

The computer-based studies of electromagnetic induction and the mathematical models that have been developed have applicability beyond the field of nondestructive testing. For example, a small project for the development of a liquid-level monitor using electromagnetic induction techniques is

---

[2]Mathematics Division.

[3]Consultant from the University of Tennessee.

[4]Consultant, Knoxville, Tennessee.

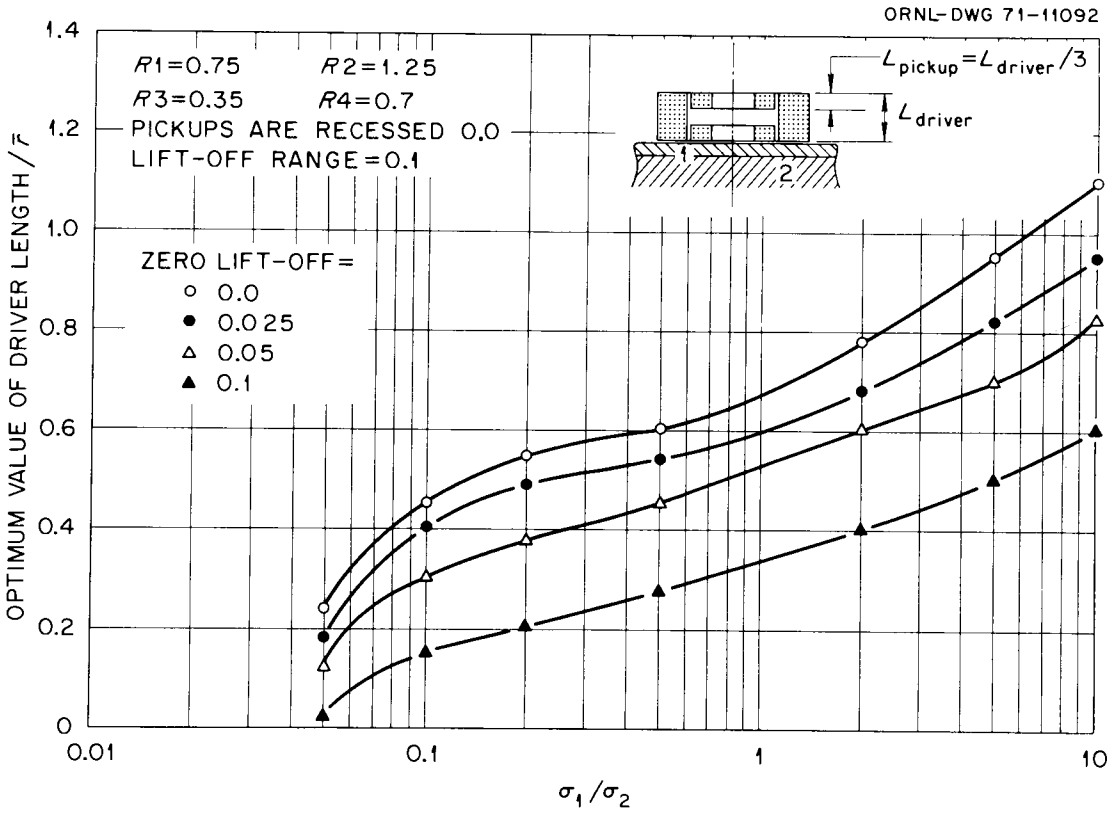

Fig. 8.2. Coil Length for Minimum Lift-Off Error vs Ratio of Conductivities for Various Zero Lift-Offs.

being supported by the Chemical Technology Division. The problem is to measure at elevated temperatures the relative level of liquid bismuth (a poor electrical conductor) surrounding the electromagnetic probe that is encased in a molybdenum tube (a good electrical conductor). The measurement of the low conductivity medium surrounding the high conductivity tube is much more difficult than if the circumstances were reversed (e.g., with liquid sodium surrounding stainless steel).

The study of liquid level measurement of bismuth has been divided into two parts: (1) analytical calculations to determine optimum conditions for maximum sensitivity to a level change and minimum drift due to temperature, and (2) instrumentation modification and application at room temperature to confirm the results.

Preliminary calculations were performed using a two-conductor model consisting of a bifilar coil inside a molybdenum tube, with either liquid bismuth or air on the outside of the tube. These calculations showed how the magnitude and phase of the signal in the secondary coil varied as tube

size, tube wall thickness, and operating frequency were changed. We determined that we should get adequate phase shift in the sinusoidal electromagnetic signal (approx 11° phase shift from no bismuth to all bismuth) using a 0.030-in.-thick molybdenum tube with a diameter of 0.785 in. Using a more accurate three-conductor calculation, which included the effects of the outer molybdenum container, we then determined that the phase shift could be measured at any frequency between 20 KHz and 34 KHz with approximately the same sensitivity. The maximum change in magnitude of the secondary voltage was about 30% at a frequency of 8 to 12 KHz.

Once maximum sensitivity had been achieved, we began to minimize the drifts produced by the large temperature variation from 600°C to 700°C. This caused a calculated thermal expansion of the molybdenum tube of approx 0.05%. The phase shift due to this expansion was calculated to be less than 0.01°. The calculated change in resistivity for the bismuth is from 145.7 to 151.3 $\mu\Omega$ cm and for the molybdenum is 17.7 to 21.0 $\mu\Omega$ cm. While this change in properties with temperature produces a considerable phase shift over most of the frequency range, as shown in Fig. 8.3, we discovered that there was a minimum change of about 0.1° at 25.2 KHz for no bismuth and 30.2 KHz for all bismuth. We therefore reasoned that at 27.7 KHz there would probably be a minimum for the level detector being half full of bismuth.

Another big variation is in the dc resistance of the primary and secondary coils, which change from 69.4 to 79.2 ohms over the 600°C to 700°C temperature range. However, by matching the impedance of the primary circuit and the secondary circuit with the cable capacitance, we were able to essentially eliminate (less than 0.001°C) the effects due to the coil dc resistance. We also determined that changes in the operating frequency, the amplitude of the driving signal, the output impedance of the primary signal, the input impedance of the secondary signal and the cable capacitance of 1% will change the phase less than 0.01%.

Experimental measurements were performed at room temperature to verify the calculations. These measurements were made using the actual coil in the actual molybdenum container. One-inch-thick annular Inconel disks were stacked on the probe to simulate increases in the liquid level. We attempted to use the original instrumentation cable, but variations in phase with slight

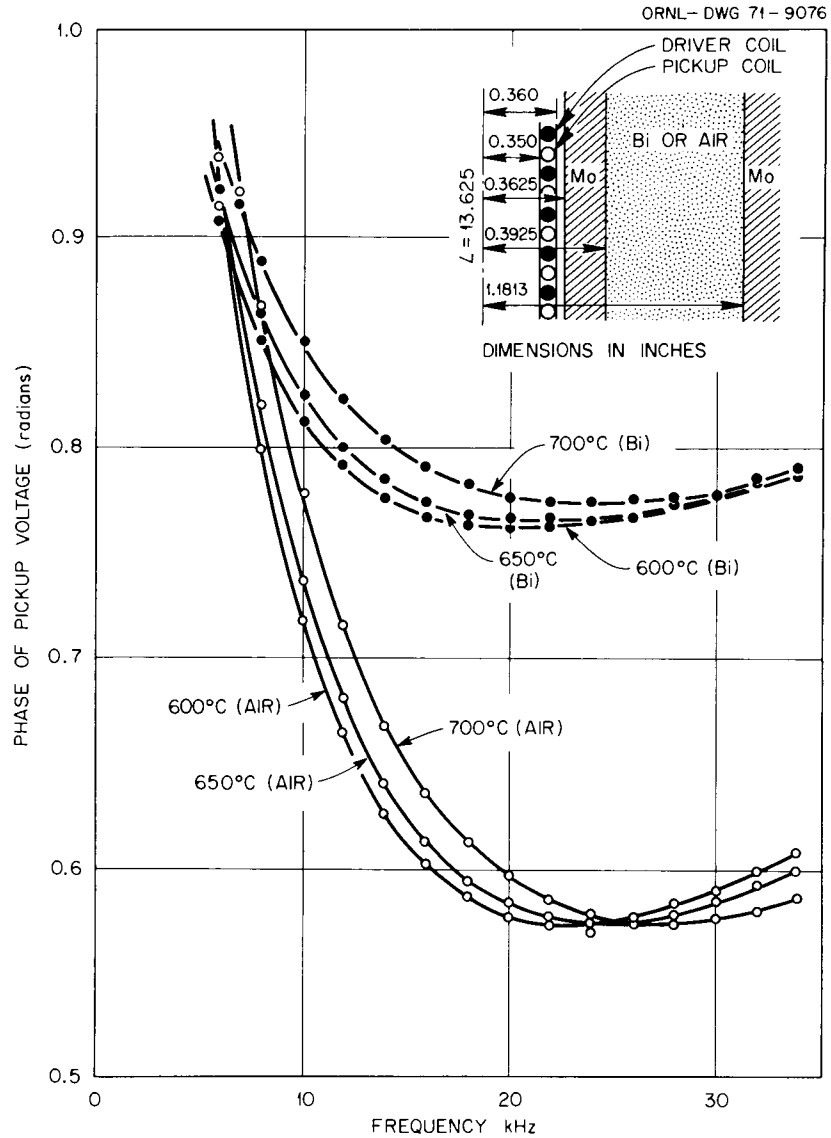

Fig. 8.3. Phase Shift With and Without Bismuth vs Operating Frequency for Various Operating Temperatures.

flexing and shorting made it totally unusable. As a substitute we used two single conductor shielded cables and recommended that a high temperature version of this type cable be used in the actual tests. Measurements of phase shift with Inconel level were made at 10 KHz and 20 KHz. The measured results at 10 KHz were linear and repeatable to within 0.01°. The sensitivity was 0.6° per inch, compared to the calculated value of 0.525°/in. These produce a linear sensitivity to changes in the bismuth level of approx 0.015 in. The sensitivity of 20 KHz was considerably less, 0.3° per inch,

due to the high conductivity of molybdenum at room temperature. The measured results were as repeatable but not quite as linear as those at 10 KHz. The addition of an outer container made of ferromagnetic steel decreased the sensitivity 0.02° per inch at 10 KHz at room temperature although this would be considerably increased at 650°C. There was a ± 0.015° random noise in the measurements at both 10 KHz and 20 KHz, due to the wide frequency response of both the driving and receiving amplifiers. This noise can be easily eliminated by limiting the bandpass of either amplifier.

Measurement of Cold Work in Stainless Steel

We are continuing our investigations into the feasibility of using a low frequency eddy-current bridge for measuring the changes in magnetic permeability produced in type 316 stainless steel tubing by various degrees of cold working. The bridge and its associated electronics were designed to provide an inspection speed of 200 ft per minute.

We have completed the computer analysis, design, construction and testing of a new type of coil system utilizing two driver coils and two pickup coils. This configuration isolates the recording equipment from dc drifts in the bridge portion of the instrument and provides greatly improved temperature stability. The final coil configuration had a calculated total error of 2.3% for the worst combination of error terms. Our initial measurements on the 0.230-in. diam tubing for which the coils were designed yielded values which were very near those predicted by our computer programs.

Along with Argonne National Laboratory and WADCO, we are engaged in a "Round-Robin" program for measuring cold work in 0.230-in. diam 316 stainless steel tubing fabricated by five different vendors. The program consists in distributing to each of the three labs a set of standards and three sets of unknowns. We have presently received the standards and two of the three sets of unknowns and have completed measurements on all of them. The indicated statistical error within a given vendor is about ± 0.25% cold work (± one standard deviation). However, our results indicate that while we can obtain good correlation between instrument reading and cold work within

a given vendor, the large variation among vendors makes a single calibration curve impossible. It thus appears that, as expected, it will be necessary to recalibrate (establish end points for a calibration curve) for different vendors and fabrication histories of the tubing (and perhaps even for different heats). Otherwise, if a single universal calibration is demanded, very careful control and standardization of the chemical composition and fabrication history will be required.

Ultrasonic Inspection Methods

H. L. Whaley, K. V. Cook and Laszlo Adler[3]

Ultrasonic Frequency Analysis

We continued our basic studies of frequency effects in ultrasonic testing by means of spectral analysis. We are employing a special electronic system developed for these studies to learn more about the effects of frequency on conventional ultrasonic techniques and to develop new test techniques based upon principles derived from these studies.

We are studying the spectral variations in broad-banded ultrasonic pulses as a function of the acoustical discontinuity with which they have interacted. Such a study will lead to improvements in the characterization of hidden flaws in materials and components by ultrasonic inspection.

We continued to investigate the advantages and problems of using a two-transducer technique for characterization of reflectors by ultrasonic spectral analysis. We used circular reflectors of three diameters (0.125 in., 0.250 in., and 0.500 in.) and irregularly-shaped reflectors with dimensions in the same range. Data was taken first with the angle of the reflector lying in a plane perpendicular to the face of the receiver and including the center of the reflector (designated "one-angle" case) and then with the angle of the reflector outside this plane ("two-angle" case). In both cases, the data agreed well with theory when the reflector was inclined away from the receiver (orientation A in Fig. 8.4) and poorly when the reflector was inclined toward the receiver (orientation B in Fig. 8.4). The reason for this inconsistency has not yet been determined. Certain assumptions made to simplify the mathematical analysis may have to be reconsidered in view of this problem.

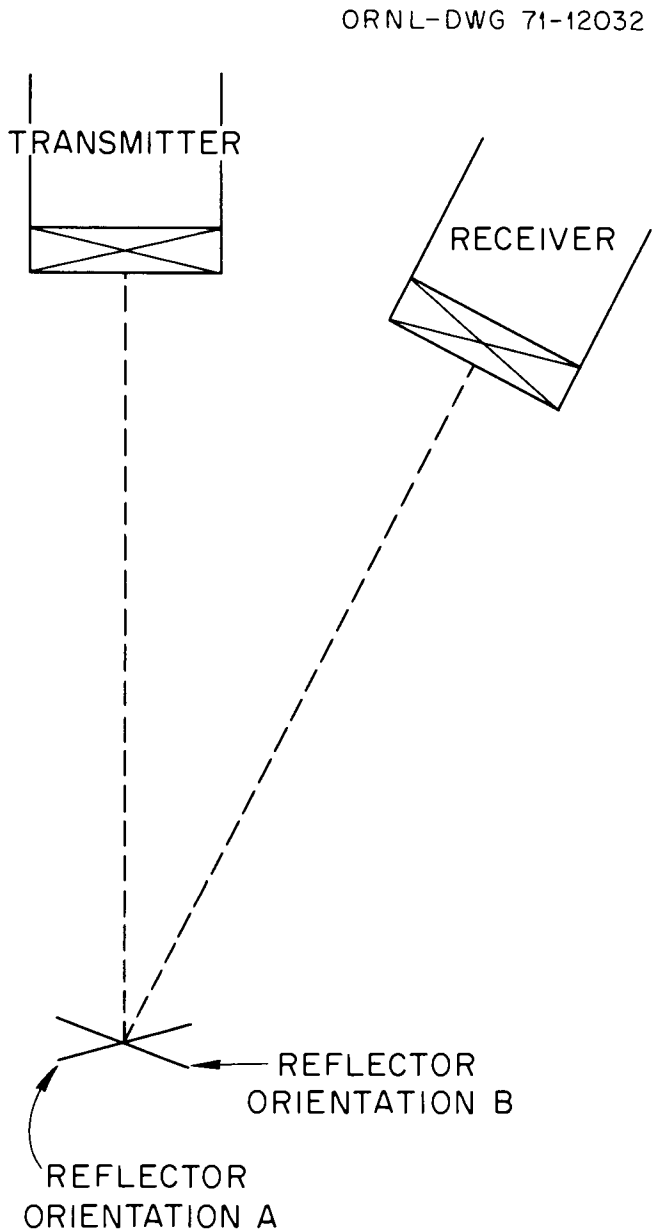

Fig. 8.4. Relative Positions of the Transmitter, Receiver, and Reflector for the Two Transducer Method of Spectral Analysis.

Additional mechanical apparatus has been added to the tank so that spectral analysis may be performed on ultrasonic pulses reflected from discontinuities in rod, pipe, and tubing. This will allow us to investigate another class of component geometries of importance to the LMFBR.

Ultrasonic Imaging

Optical techniques are useful to gain an understanding of ultrasonic interactions difficult to analyze by conventional methods employing purely electronic equipment. Schlieren techniques image the sound field itself, while Bragg diffraction and volume holography display any acoustical discontinuity with which the ultrasound field has interacted. We are interested in all such techniques and have developed a flexible optical system for various studies. The basic system is a mirror schlieren system with both continuous and pulsed light sources, a 6-in.-diam field of view and a television display. We have added a video tape system for data recording.

We improved the ability of the schlieren system to effectively image ultrasound at high frequencies (15–25 MHz). We discovered that at these frequencies, the light may be diffracted at angles so large that it cannot be captured by the television camera lens. The angle to which the light is diffracted is directly proportional to the frequency of the ultrasound. Since the oscillator frequency is set by observing the image of the ultrasound beam and adjusting for maximum brightness, the tendency was to tune to a lower frequency which would admit more diffracted light to the camera while being below the resonant frequency of the transducer. Thus the result was a weak image of the ultrasonic beam. By properly adjusting the vertical orientation of the second (focusing) parabolic mirror (formerly fixed) it is now possible to achieve maximum response beyond 25 MHz while retaining the full field of view of the system. The beam from a small continuous laser may also be directed through the ultrasound field to determine the frequency at which maximum response is achieved. A second rf oscillator has been obtained and necessary alterations made to employ it as a continous wave source to power the ultrasonic transducer. This oscillator will provide very high power for some specialized applications.

We continued our study of the detection of defects in welds using the schlieren imaging technique. The samples are butt-welded, 1-in.-thick aluminum and stainless steel plates containing areas that were intentionally poorly welded to produce porosity, inclusions, incomplete fusion and incomplete penetration.

The stainless steel weld samples were inspected in the improved optics room described in an earlier report.[5] Initial results were found to be biased because of surface irregularities of the weld. Therefore, the weld crowns were removed, and the plates were surface-ground to provide flat, parallel surfaces for the inspection. Transducers of various frequencies were tried, and best results were obtained at about 2 MHz. Three basic transducer orientations with respect to the sample were investigated, two of which proved useful, and in some cases, yielded complementary information. In the first method, the ultrasonic beam was at perpendicular incidence to the plate, and observation was made of the reflection from the back surface as well as the pulse transmitted through the sample and emerging from the back side. The second method used a small angle of incidence which generated a refracted longitudinal wave inclined at about 30° from normal to the surface. The pulse transmitted through the plate was observed in this method. The third method used larger angles of incidence so that a shear wave beam at various angles from 30° to 70° could be employed. However, this method was unsuccessful due to the very weak pulses emerging from the sample. With the first two methods, reference holes drilled into the weld areas were detected in all samples except the weld intended to have excessive porosity; other anomalous areas were also located which were believed to be the intentional defects in the welds. Data was recorded on video tape, but interpretation is difficult. Information obtained from the schlieren test will now be used in tests performed on these samples in an automatic-scan facility using purely electronic (no optics) instruments with plan-view recording capabilities for more simplicity in interpretation.

---

[5]H. L. Whaley, K. V. Cook, and Laszlo Adler, Fuels and Materials Development Program Quart. Progr. Rept. June 30, 1971, ORNL-TM-3540, p. 138.

Reference Notches

We are continuing our work with electrodischarge machining to generate realistic and reproducible reference discontinuities and appropriate reference curves.

We designed and fabricated a base plate assembly that allows the precision alignment of flat plate material on which various sizes and shapes of simulated flaws can be machined. Quick removal and accurate replacement is possible. We also designed and fabricated a mechanism which attaches to this base plate and allows a faster method of cutting shim stock tools.

Our research has shown that oil flow and shim vibration are two primary variables for reliable and reproducible ED machining because molten metal must be continuously removed (related to oil flow) and because a volume of material is being removed (related to shim vibration). For deeper notches which are very narrow (i.e., 0.020-in. deep x 0.004-in. wide), oil flow through a hypodermic needle accurately placed for each cut and tool restraint are keys to reproducibility.

Penetrating Radiation Inspection Methods

B. E. Foster S. D. Snyder

Closed Circuit Television for Radiographic Evaluation

We are continuing our development of a closed circuit television system[6] for use as a rapid densitometer for interpreting radiographs. A series of tests are being conducted to determine the settings of the sensitivity controls on the sampling unit and x-y recorder for best response when using an optical magnification of approx 2.5X and to determine the maximum span (film density change per chart div) of the system as well as effects of magnification on span and contrast.

---

[6]B. E. Foster and S. D. Snyder, Metals and Ceramics Div. Annu. Progr. Rept. June 30, 1971, ORNL-4770, pp. 138–139.

From the test data thus far, it appears that we achieve optimum system response with the sensitivity controls on the sampling unit and x-y recorder set at 10 mv/cm and 80 mv/cm, respectively or vice versa. (A film density change from 0.4 to 0.6 will produce approx 4 cm deflection of the recorder at these settings.) However, the ac response of the system is much better when the sampling unit is set at 10 mv/cm than at a setting of 80 mv/cm. We also found that when the optical magnification is increased, there is some reduction in the maximum span and contrast of the system.

9. MECHANICAL PROPERTIES OF STRUCTURAL MATERIALS

J. R. Weir, Jr. and H. E. McCoy, Jr.

The use of structural materials in nuclear reactors at progressively higher temperatures requires that we improve design methods to insure dependable and safe operation of such systems. The improved design methods involve the procurement of mechanical property data under various possible service conditions and that analytical methods be developed for using these materials properties to design complex structures. ORNL is currently active in both of these areas, but the present report will be concerned only with the mechanical properties information.

Although many of the methods that will be developed will be universally applicable for high temperature design, the current work is concerned primarily with LMFBR's. The materials being studied include types 304 and 316 stainless steel, types 304 and 316 stainless steel weldments prepared by different welding processes, and base metal and weldments of Cr—Mo— steels of various compositions.

Mechanical Properties of Type 304 Stainless Steel

R. W. Swindeman and R. D. Waddell

Mechanical property tests, including tensile, creep, relaxation, and strain-cycling are being performed on type 304 stainless steel over the temperature range of interest to the LMFBR program. Emphasis is being placed on deformation behavior, rather than rupture studies, since the scarcity of deformation data has been a handicap in the updating of design codes for nuclear vessels and piping systems. Of special interest to us are the influences of chemistry and thermo-mechanical history on subsequent mechanical behavior. We expect that as many as twenty heats of type 304 stainless steel will be involved in our studies.

At the present time we are working with four heats of type 304 stainless steel plate. They are listed in Table 9.1 along with vendor certification data.

Table 9.1 Vendor Chemistry and Mechanical Property Data for Four Heats of Type 304 Stainless Steel Plate

	Heat Number			
	9T2796	8043813	600414-1A	300380-1A
Size (thickness, in.)	1	1	2-3/8	2-3/8
Source	USS	Republic	Carlson	Carlson
Chemistry, %				
Carbon	0.048	0.062	0.061	0.058
Manganese	1.22	1.79	1.48	1.60
Phosphorous	0.028	0.036	0.016	0.016
Sulfur	0.015	0.007	0.014	0.011
Silicon	0.48	0.50	0.64	0.55
Chromium	18.6	18.24	18.88	18.68
Nickel	9.7	9.10	9.56	8.44
Mechanical Properties				
0.2% Yield Stress (ksi)	43.9*	36.3	37	40
Ultimate Tensile Stress (ksi)	81.4	80.8	82	86.5
Elongation (%)	55	66	57	55
Reduction in Area (%)	67	-	69	68

*1/2% Total strain.

The yield and tensile strengths of these four heats are shown in Fig. 9.1 and compared to the minimum expected values. The tensile yield appears to be significantly influenced by the re-annealing treatment and data for all four heats cluster near or below the minimum expected for type 304 stainless steel. We know, of course, that most stainless steel product forms are delivered by the mill to the user with some degree of cold work. Generally this is a result of flattening or straightening operations. The yield strength would naturally reflect this cold work. Never-the-less it is expected that re-annealed material should also exceed the minimum strength. The low yield stresses that we obtained are surprising and we are attempting to find the reason.

Creep and stress-rupture data for heats 8043813 and 9T2796 are summarized in Tables 9.2 and 9.3. At high stresses, heat 8043813 exhibits remarkably good creep and rupture resistance while heat 9T2796 is relatively weak. A series of creep tests at 649°C are shown in Fig.9.2 for heat 8043813. These curves are almost entirely composed of the primary stage of creep. We find that neither the parabolic nor the exponential strain-time law provides a good fit to these curves. Modified exponential or hyperbolic forms look promising, however. For example, in Fig. 9.3 we have used several equations in which the argument is taken to a power. These curves show better fits than the simple parabolic and exponential forms.

Creep data for heat 9T2796 at 593°C have been obtained to times approaching 4000 hr, but trends are not sufficiently developed to permit meaningful analysis. The creep curves are shown in Fig. 9.4.

A stress of 35,000 psi at 593°C has been chosen as the initial testing condition for the study of the effect of chemistry and thermomechanical history on creep rupture. This corresponds to the average 100 hr rupture strength expected for type 304 stainless steel.

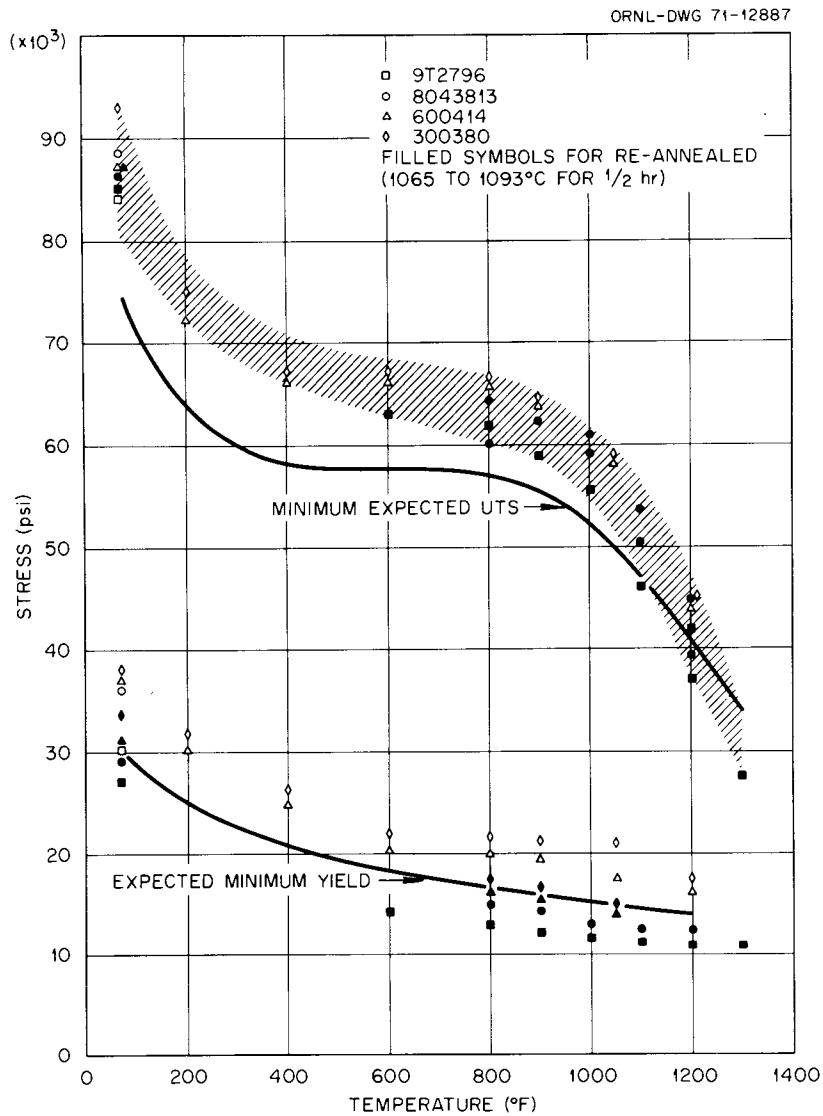

Fig. 9.1 Yield and Tensile Strength Data for Four Heats of Type 304 Stainless Steel Plate. Tested at strain rates between 0.005 and 0.05 min^{-1}. The minimum expected values come from draft of ASME Code Case 1331, Revision 5.

Table 9.2 Summary of Constant Load Creep Data for Heat 8043813
[Re-Annealed 982-1066°C (1800-1950°F)]

Specimen Number	Temperature °C, (°F)	Stress (ksi)	Plastic Strain (%)	Minimum Creep Rate (%/hr)	Zero Time Intercept[a] (%)	Life (hr)[b]	Elongation (%)
P12	538(1000)	50	22	0.021	0	348R	43.2
P13	538(1000)	45	17	0.005	0	837R	26.5
P7	593(1100)	40	12	0.31	2.3	55R	41.3
P6	593(1100)	35	10	0.0375	2.8	287R	33
P8	593(1100)	33	8	0.00975	4	723R	30.8
P18	593(1100)	32	8.5	0.0033	0.9	1570R	25
P9	593(1100)	30	-	0.0015	2.5	3184R	19.1
P4	649(1200)	28	4.5	0.76	2	35R	54.6
P1	649(1200)	25	5.5	0.177	1.6	104R	37.6
P2	649(1200)	22	3	0.013	3	577R	25.2
P3	649(1200)	20	2.5	0.004	1.9	1642R	22.5
P5	649(1200)	17	1.5	≤0.00022	1.65	5033D	4.3
P15	649(1200)	15	0.55	≤0.00006	≥0.75	2003D	1.4
P16	649(1200)	12.5	<0.1	≤0.00002	≥0.55	2010D	~0.6
P17	649(1200)	10	nil	≤0.00001	≥0.38	2003D	0.38
P32	649(1200)	8	nil	≤0.00001	≥0.15	2009D	0.15

[a]Zero time intercept does not include initial elastic and plastic strain.
[b]R = Rupture; D = Discontinued.

Table 9.3 Summary of Constant Load Creep Data for Heat 9T2796
[Re-Annealed at 1093°C (2000°F)]

Specimen Number	Temperature °C, (°F)	Stress (ksi)	Plastic Strain (%)	Minimum Creep Rate (%/hr)	Zero Time Intercept[a] (%)	Life (hr)[b]	Elongation (%)
RP6	538(1000)	45	18.6	~0.03	~0	60R	28.6[c]
RP8	538(1000)	40	14.3	0.021	~0	163R	19.3
RP9	538(1000)	35	11	0.004	~0.3	595R	14.5
RP24	538(1000)	30	8.3	≤0.00064	≥0.5	1171D	9.5
RP26	538(1000)	20	3.3	≤0.00003	-	4000I	0.35
RP31	538(1000)	10	<0.05	<0.00001	-	3000I	0.05
RP4	593(1100)	35	11.7	0.34	~0.2	26R	26.7
RP5	593(1100)	30	8.3	0.046	0.85	111R	15.8
RP7	593(1100	25	5.8	0.011	0.7	440R	15.8
RP54	593(1100)	25	5.5	0.011	0.6	402D	11
RP32	593(1100)	22.5	4.6	0.0035	0.6	878R	11
RP23	593(1100)	20	3.3	≤0.00085	≥0.45	1000D	5.3[e]
RP58	593(1100)	20	2.8	≤0.001	≥1.2	2000I	6.2
RP40	593(1100)	17.5	2.8	≤0.00025	≥1.0	3000I	4.6
RP25	593(1100)	15	1.6	≤0.00033	≥0.2	1006D	2.5
RP62	593(1100)	12.5	0.65	≤0.0001	≥0.3	3000I	1.2
RP28	593(1100)	10	0.16	≤0.00005	-	3500I	0.46
RP1	649(1200)	25	5.5	0.46	0.95	28R	25.5
RP2	649(1200)	20	3.3	0.087	0.6	111R	25.3
RP3	649(1200)	15	1.35	0.015	0.3	730R	21.3
RP61	649(1200)	12.5	0.76	≤0.005	≥0.2	260D	2.26
RP22	649(1200)	10	0.06	≤0.0009	≥0.3	1002D	1.26

Table 9.3 (Continued)

Specimen Number	Temperature °C, (°F)	Stress (ksi)	Plastic Strain (%)	Minimum Creep Rate (%/hr)	Zero Time Intercept[a] (%)	Life (hr)[b]	Elongation (%)
RP27	704(1300)	15	1.8	0.33	0.4	47R	22.8
RP29	704(1300)	10	0.18	≤0.038	≥0.1	75D	3.2
RP30	760(1400)	10	0.25	0.43	0.3	46R	26.2
RP41	760(1400)	7.5	nil	≤0.105	≥0.08	20D	2.2
RP59	815(1500	5	nil	≤0.03	≥2	167D	6.9

[a]Zero time intercept does not include initial elastic and plastic strain.
[b]R = Rupture; D = Discontinued; I = In test
[c]Includes 1.6% plastic strain at 20 hr
[d]Includes 0.05% plastic strain at 570 hr
[e]Includes 0.66% plastic strain at 47 hr
[f]Includes 0.27% plastic strain at 700 hr
[g]Includes 0.08% plastic strain at 2200 hr

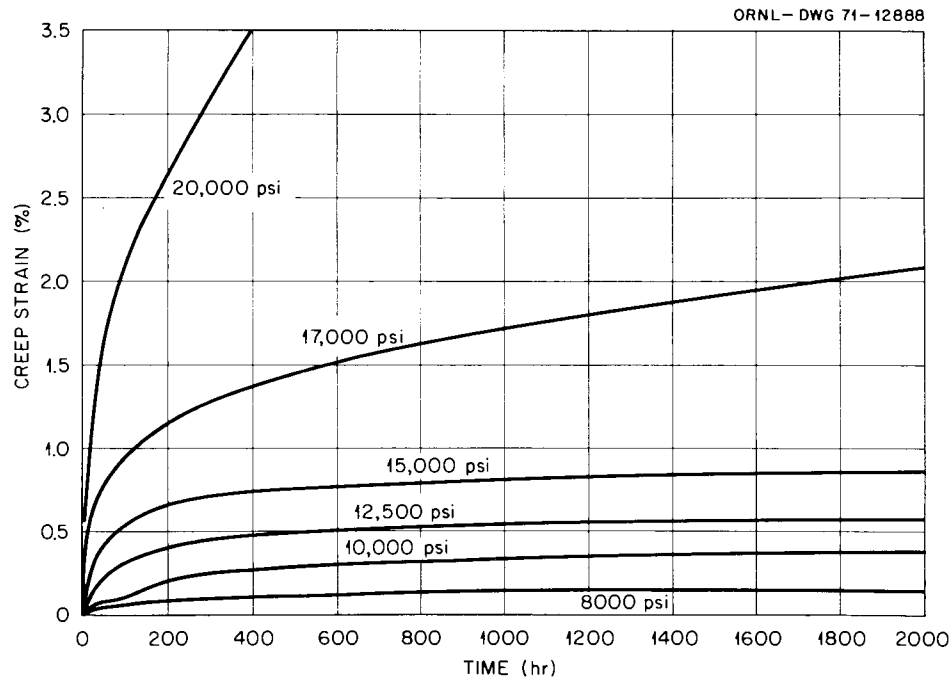

Fig. 9.2 Creep Curves for Heat 8043813 at 649°C (1200°F) Specimens Re-Annealed at 982 - 1066°C (1800 - 1950°F).

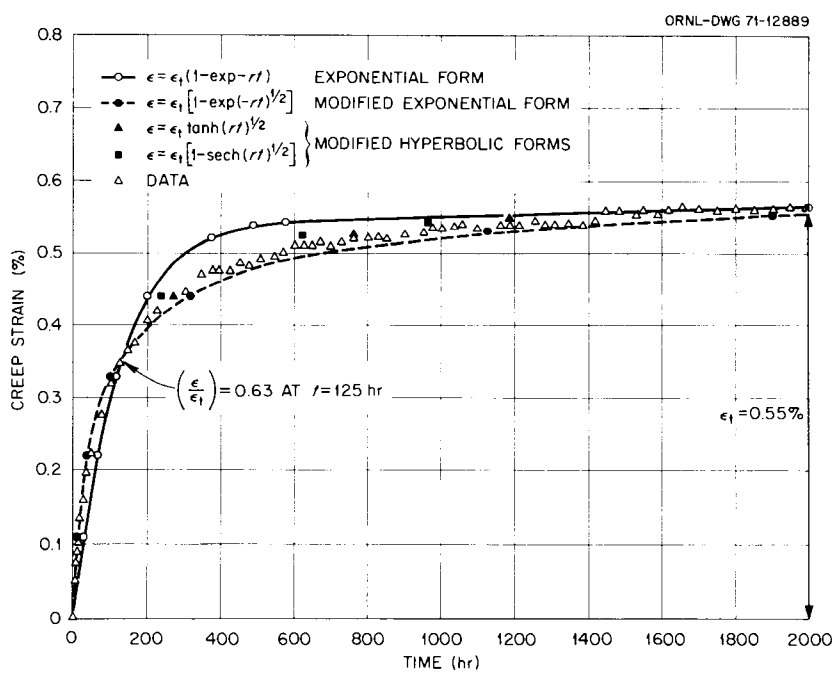

Fig. 9.3 Comparison of Several Strain-Time Expressions for Primary with Data at 12,500 psi and 649°C (1200°F).

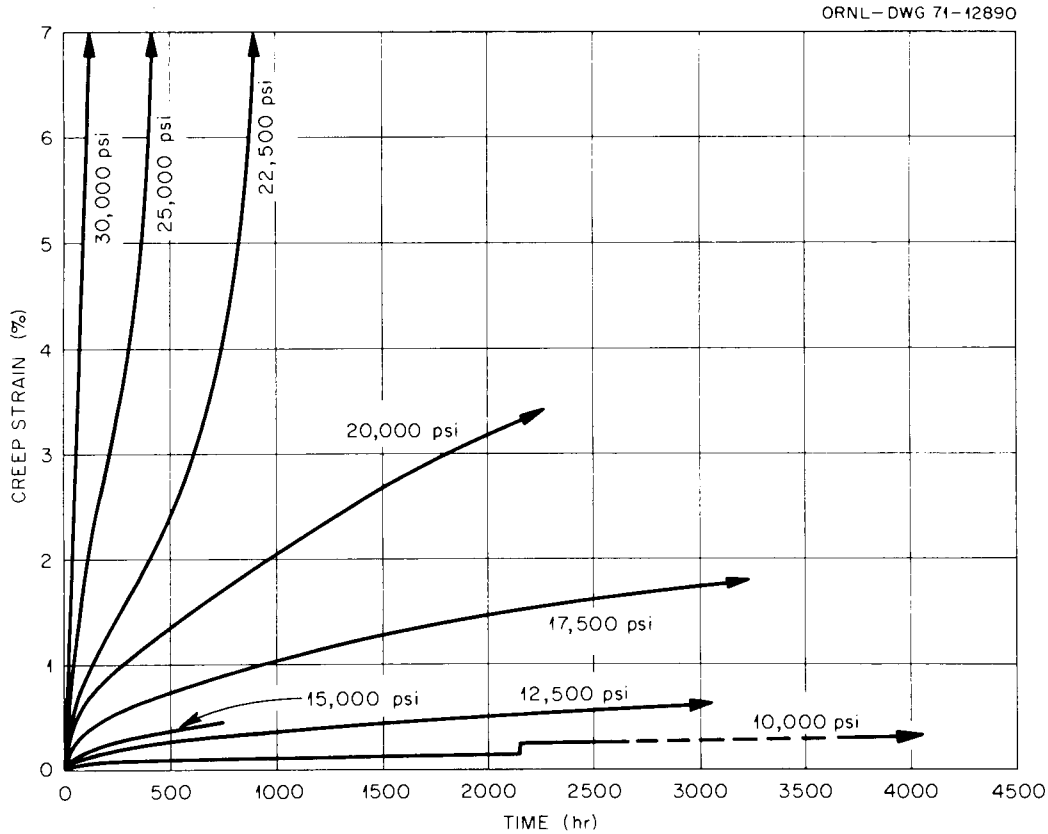

Fig. 9.4 Creep Curves for Heat 9T2796 at 593°C (1100°F) Specimens Re-Annealed at 1093°C (2000°F).

Microstructural Characterization of Type 304 Stainless Steel Welds

R. E. Gehlbach

We are initiating a program to study the microstructural changes which occur in type 308 stainless steel weld metal during exposure to elevated temperatures. Optical metallographic studies carried out previously have indicated that the ferrite present in the weld metal transforms to sigma or carbides depending on the time and temperature of exposure. Changes in mechanical properties, notably ductility, occur in elevated temperature creep tests which indicate that these transformations may play a major role in determining properties. The phases that form during elevated temperature exposure are quite small and optical studies do not give the information required to relate microstructural changes with properties.

This study will be directed at characterizing the microstructures of the welds to determine the reasons for the observed embrittlement at service temperatures. The techniques that we expect to use include transmission electron microscopy, scanning electron microscopy, optical microscopy, electron and x-ray diffraction from precipitates, extraction replication, and microprobe analysis. Coordinated use of these tools will enable us to characterize the microstructure, identify precipitates with respect to type and composition, and overcome the inherent problem of heterogeniety.

We have made some preliminary transmission electron microscopy observations on several creep specimens from a shielded metal arc weld made with standard lime-coated electrodes (F1). The specimen histories are given in Table 9.4. The microstructure of the as-welded condition consists of ferrite in austenite with spherical particles (probably carbides) distributed randomly throughout the weld metal as shown in Fig. 9.5. The austenite contains a very high density of tangled dislocations. During exposure at 650°C, many of the dislocations anneal out although it is likely that some extremely fine precipitation occurs on the dislocations and effectively pins them. The creep specimen tested at 28,000 psi contains a relatively well-defined substructure with the

Table 9.4 Mechanical Properties of Creep-Rupture Specimens

Rupture Life (hr)	Stress (psi)	Reduction in Area[a] (%)
7	28,000	47.2
82	20,000	25.3
1315	14,000	1.5

[a]Fractures occurred in the weld metal.

Fig. 9.5 Transmission Electron Micrograph of Straight Lime-Coated Type 308 Stainless Steel in As-Welded Condition. Note the fine cell structure present in the austenite, the small primary particles, and the well defined ferrite particles. 10,000X.

dislocations arranging themselves into cell walls. This cell structure is on the order of 0.8 μm. The cell structure is much less pronounced in the specimen which failed in 82 hr after a much lower strain. Observations of the substructure in the specimen that failed after 1315 hr are too limited to make any correlations at this time.

The most obvious difference in the microstructures of the sample as-welded to those tested at 650°C is the formation of $M_{23}C_6$ carbides along the edges of the ferrite. This effect is more pronounced in the test specimen that failed after 82 hr than in that which lasted 7 hr. Figure 9.6 shows the formation of these carbides around the ferrite in the 82 hr test specimen. The spherical particles are present in all specimens examined to date. Sufficient tests have not been run to date to determine whether sigma phase is present or absent after exposure at 650°C.

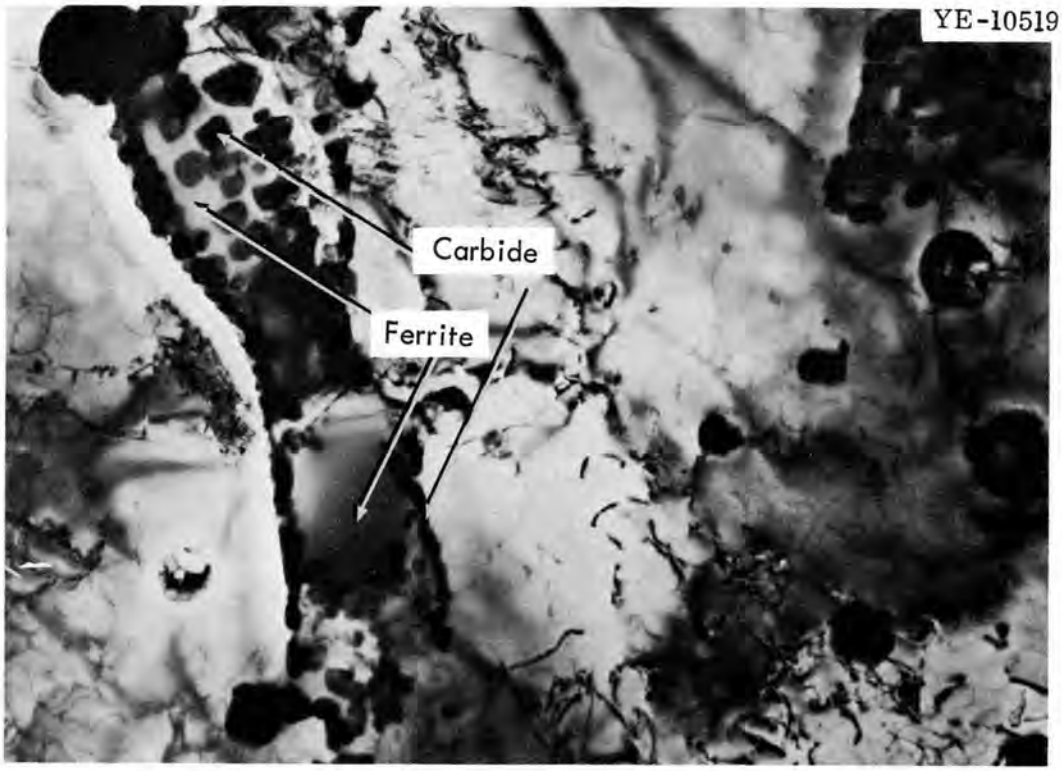

Fig. 9.6 Transmission Electron Micrograph of Straight Lime-Coated Type 308 Stainless Steel Weld Creep Tested at 650°C and 20,000 psi. The sample ruptured in 82 hr with 25.3% reduction in area. Note the formation of $M_{23}C_6$ carbides in and around the ferrite. 25,000X.

We are in the process of extracting precipitates by electrolytic dissolution of the welds to identify the phases. X-ray diffraction and electron microprobe techniques will be employed to determine types and compositions of precipitates.

We are sectioning a plate (Combustion Engineering Lot HBEA) which was welded with FFTF electrodes to be used for an aging program. A weld made with FFTF electrodes having a standard coating will be examined similarly for microstructural comparison with that made with the actual FFTF electrodes.

Procurement of FFTF Vessel Weldment Test Specimens

G. M. Goodwin

Arrangements have been made with Combustion Engineering, Inc., Chattanooga, Tennessee, to provide approximately 43 linear feet of weld

test pieces for incorporation into programs at ORNL and several other installations.

Plate material for the weld test pieces was procured from G. O. Carlson, Inc., from two of the five heats of plate represented in the FFTF vessel, heats 300380 and 600414. Approximately 18 ft^2 of heat 300380 and 24 ft^2 of heat 600414 were obtained, all in the form of 2-3/8 in.-thick plate. The plates were sectioned into pieces approximately 8 in. long × 6 in. wide × 2-3/8 in.-thick and coded to identify position in the original plates.

The 8-in. length of each of the pieces was machined to the FFTF vessel weld joint geometry, that is, a double-U groove with a 15° included angle, 1/2-in. root radius, and 1/4 in. root face. Electrodes from four of the six production batches used in the vessel to date are being used to weld the test pieces, with welding conditions (i.e., current, voltage, travel speed, etc) maintained identical to those used on the FFTF vessel. A small fraction of the total number of test pieces will be produced with a standard E308-15 electrode for use as control specimens. The shielded metal arc welding process is being used. As of this date, approximately one-third of the total number of test pieces have been completed, and the remainder is scheduled for delivery by January 1972.

Characterization of FFTF Vessel-Type Weldments

R. T. King and R. E. Gehlbach

A program is in progress to evaluate the mechanical properties of weldments similar to those used to fabricate the FFTF vessel with the emphasis on obtaining design data. To aid in interpreting the results, the as-welded microstructure of the weld and its stability under conditions similar to service conditions are also being studied. The mechanical properties design data include tensile, creep-rupture, fatigue, and stress relaxation results for tests performed at temperatures which span the anticipated vessel operating temperature range insofar as is practical. The procurement of materials for this task and the fabrication of the test weldments was described in the previous section by Goodwin.

We shall describe the results of preliminary evaluations of the microstructure and hardness of a type 308 stainless steel test weldment, CE-1, from Combustion Engineering batch HBEA weld metal. The chemical composition of the core wire is given in Table 9.5; the flux coating contained controlled impurities which had previously been shown to produce properties superior to those of weldments made with standard coated electrodes.[1] The base metal was 2-3/8-in.-thick sections of Carlson Heat 600414-1A type 304 stainless steel; the heat is one of several being used in the fabrication of the FFTF vessel. Vendor's chemical analysis of the heat is given in Table 9.5.

[1] G. M. Goodwin et al., Fuels and Materials Development Program Quart. Progr. Rept. June 30, 1971, ORNL-TM-3540, pp. 82–89.

Table 9.5 Chemical Composition of Type 308 Stainless Steel Weld Wire and Type 304 Stainless Steel Weld Plate

Element	Weld Wire[a]	Weld[b] Base Plate
Cr	19.70	18.88
Ni	9.61	9.56
Mn	1.83	1.48
Si	0.56	0.64
C	0.064	0.061
S	0.005	0.014
P	0.040	0.016
Mo	0.07	0.016
Co	0.03	
Cu	0.04	
Cb + Ta	<0.01	
N	0.030	
B	0.007	
Ti	0.06	
Fe + other	67.94	69.35

[a] Type 308 stainless steel weld wire is Combustion Engineering Lot HBEA
[b] Type 304 stainless steel weld plate is Carlson Heat 600414-1A

A complete cross section of the weld was mounted for metallographic examination and hardness measurements. The macro-etched weld is shown in Fig. 9.7. Individual passes in the weldment are easily distinguished. Subsequent polishing and electrolytic etching in a 10% oxalic acid solution produced a surface suitable for examination at higher magnification. In Fig. 9.7, the grain size of the base metal appears quite coarse, and this observation was confirmed on the repolished and etched specimen from which the ASTM grain size was estimated to be 2 or 3. (The mean grain diameter was 0.007 to 0.005 in.) Several types of precipitates suspected to be carbides were observed in the base metal (Fig. 9.8). The larger inclusions had been elongated in the plane parallel to the plate surface during their fabrication. These primary inclusions will be identified by electron microprobe analysis or x-ray diffraction. The weld metal contains ferrite and inclusions as shown in Fig. 9.9. Quantitative determination of the ferrite content and identification of other phases are in progress.

Two hardness test traverses were made using a Vickers microhardness machine. One traverse began just beneath the center of the top weld surface shown in Fig. 9.7 and extended vertically to a point 1.2 in. (3.05 cm) beneath the surface. These hardness numbers are plotted versus distance beneath the weld surface in Fig. 9.10, and they clearly show that the room temperature hardness of the weldment increases with increasing distance from the weld surface. No gross microstructural variations were found which could account for this observation. The locations of interpass boundaries are shown on the graph of Fig. 9.10, but no consistent variation in hardness across individual passes can be identified. A second traverse was made with similar inter-indentation distances along a line parallel to the top surface of the weld, beginning at the weld centerline. These results are plotted in Fig. 9.11, and the location of the fusion line is shown on the graph. The hardness of the weld metal at this depth does not appear to vary systematically with distance from the centerline and has an average value of DPH 191.8 for 11 readings (standard deviation = 7.6). On the other hand, the base metal hardness decreases with increasing distance from

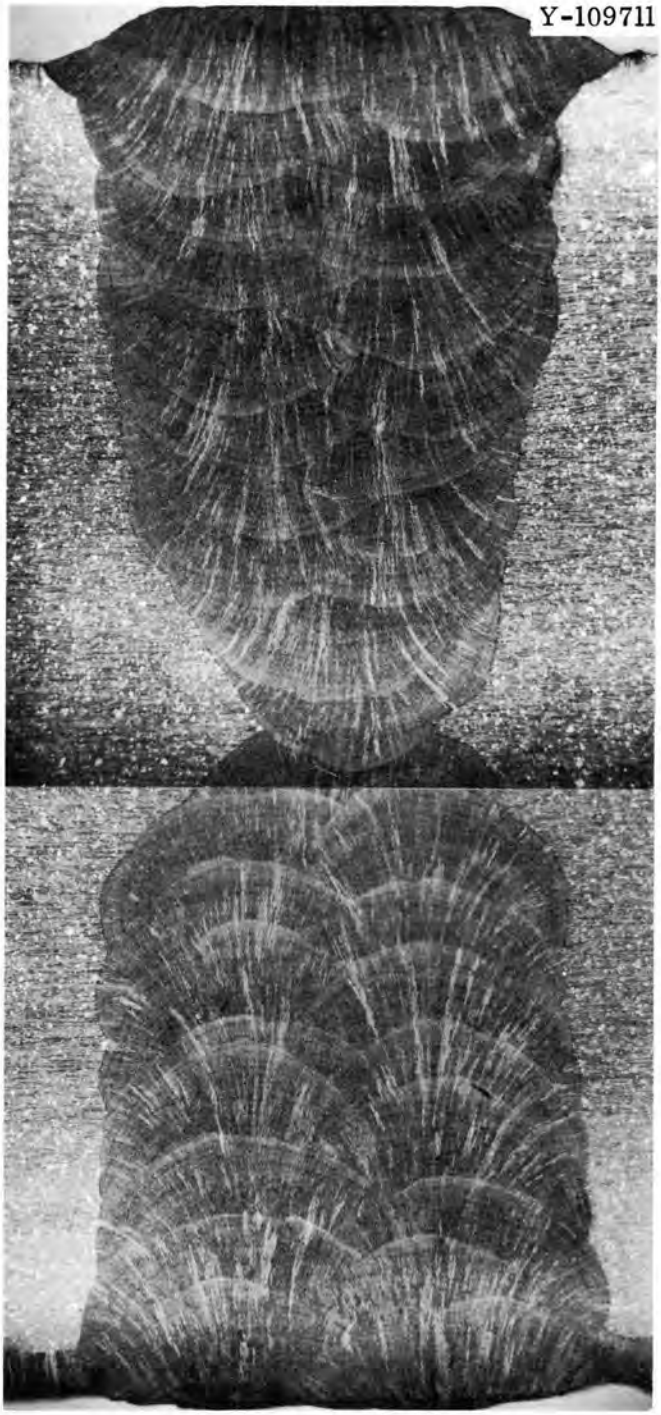

Fig. 9.7 Type 308 Stainless Steel Weldment CE-1 After Macroetching.

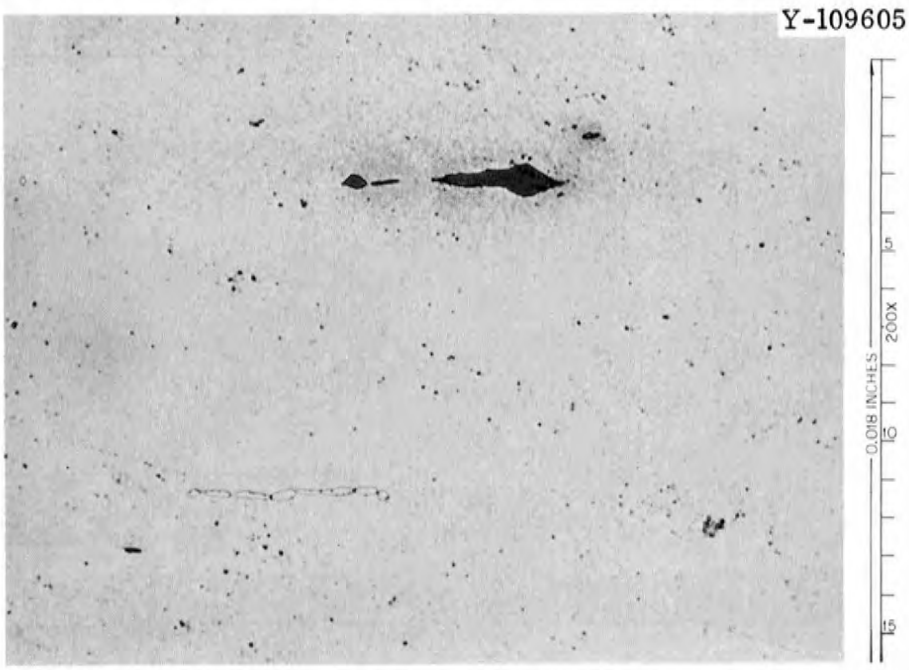

Fig. 9.8 Typical Microstructure of Type 304 Stainless Steel Base Metal (heat 600414-1A). Electro-etched in oxalic acid.

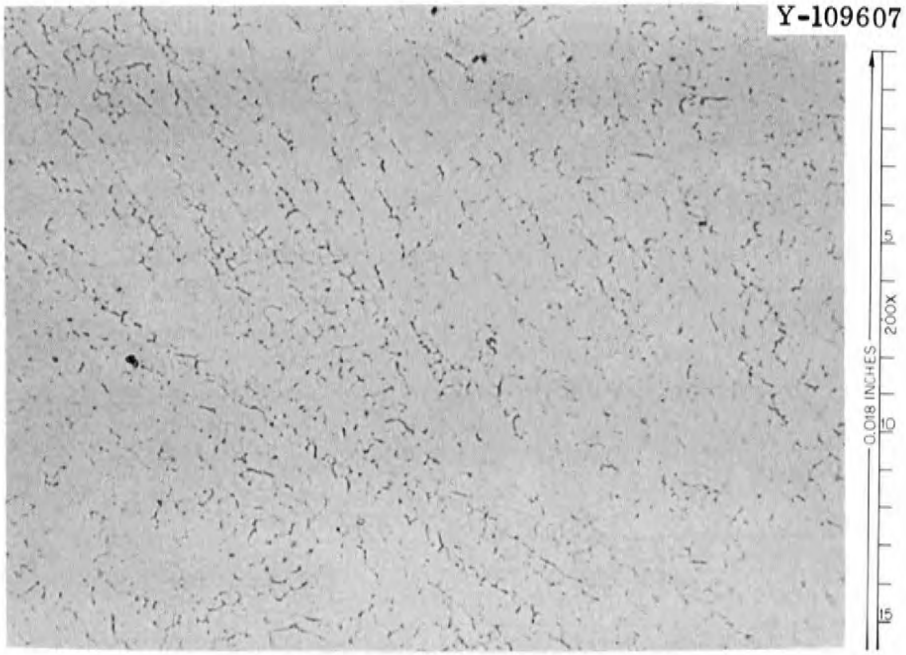

Fig. 9.9 Microstructure of Type 308 Stainless Steel Test Weldment CE-1 Showing Ferrite and Inclusions. Electro-etched in oxalic acid.

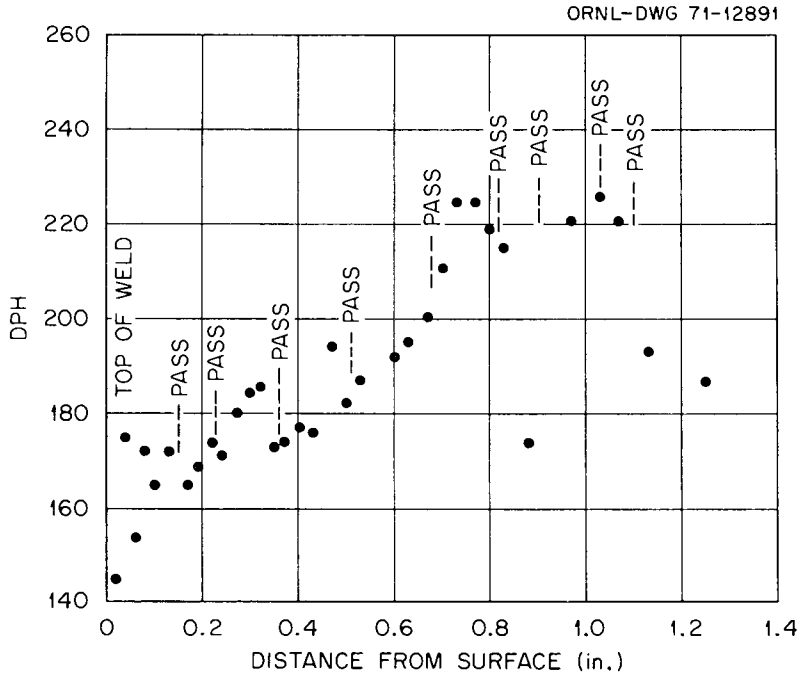

Fig. 9.10 Hardness Profile Through Weld Metal From Top Surface to Near the Center of the Test Weldment.

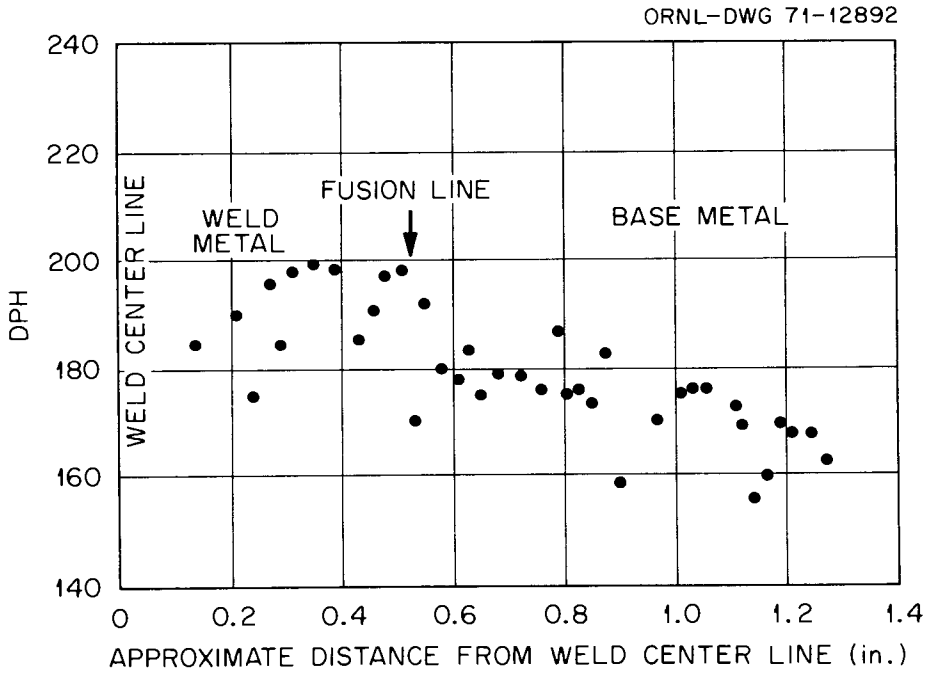

Fig. 9.11 Hardness Profile Through Weld Metal, Fusion Line, and Adjoining Base Metal.

the fusion line and has an average hardness of DPH 173.5 for 27 readings (standard deviation = 9.0). These results do not indicate the presence of a heat-affected zone in the base metal in which the properties are grossly altered.

These initial observations will be supplemented with similar investigations of cross-sections from different locations in the test welds. If consistent variations in properties with location in the weldment continue to be observed, we will conclude that the location and orientation of other types of mechanical properties specimens may be an important variable in determining properties and must be factored into the test program. Since these results are to be used for design and safety calculations, it is extremely important that all such important variables and their effects be identified and characterized as well as possible.

Mechanical Properties of 2-1/4% Cr—1% Mo Steel

R. L. Klueh and H. E. McCoy

Three 300 lb heats of 2-1/4% Cr—1% Mo steel with 0.003, 0.035, and 0.110% C were prepared by the Bureau of Mines by the consummable vacuum melting process, and fabricated into 1 in. plate, 3/4-in. OD tubing, and 7/8-in.-diam rod.[2] The plate was rolled to 1/2-in. thickness and welds were made by the Welding and Brazing Laboratory using filler wire from the same heats. Small tensile specimens of all weld metal and transverse weldments have been machined from the welded plate. The tubing has been joined and will be tube burst tested. Tensile specimens have been made from the 7/8-in.-diam rod, and tests are in progress to evaluate the mechanical properties of the base metal. A 1-in.-thick plate of standard Croloy was procured from Babcock and Wilcox, upgraded to meet RDT standards, and will later be factored into the test program.

---

[2] D. A. Canonico and H. E. McCoy, Fuels and Materials Development Program Quart. Progr. Rept. Mar. 31, 1971, ORNL-TM-3416, pp. 143—146.

Annealing Studies

The tempering characteristics of the three modified carbon steels were studied. Two specimens (from each heat) of the 7/8-in. rod - one 7/8-in.-long and one 1/8-in.-long - were annealed for 1 hr at 982°C(1800°F), 927°C(1700°F), 871°C(1600°F), and 815°C(1500°F) and then air cooled; two specimens (from each heat) were also water quenched from 927°C. After annealing, each of the specimens was quartered, and one quarter from each was annealed at 593°C(1100°F), 649°C(1200°F), and 704°C(1300°F) and the hardness measured after 1, 3, 10 and 100 hr.

Table 9.6 gives the average hardnesses after the initial heat treatment; hardness transverses showed hardness differences only near the surface. In general, the hardness of the 0.003 and 0.035% C steel did not differ greatly from one another, while the hardness of the 0.11% C steel was significantly greater. The hardness of the 0.11% C steel was relatively unchanged when air cooled from above 871°C. For the two low-carbon Croloys, however, no such upper plateau was reached. The

Table 9.6 Hardness of 2-1/4% Cr—1% Mo Steel After Annealing 1 hr and Air Cooling

Annealing Temperature, °C(°F)	Carbon Content, wt, %	Hardness (DPH)	
		7/8 in.-long	1/8 in.-long
982(1800)	0.003	205	240
	0.035	166	243
	0.110	317	351
927(1700)	0.003	115	156
	0.035	135	165
	0.110	304	328
871(1600)	0.003	106	115
	0.035	128	160
	0.110	295	330
815(1500)	0.003	108	115
	0.035	131	144
	0.110	221	252

hardness of these two steels was highest for the specimens annealed at 982°C, thendropped to a lower hardness plateau when annealed at the three lower temperatures.

The highest hardnesses were attained in the specimens water quenched from 927°C; hardnesses for the 1/8 in. specimens were 230, 299, and 412 (DPH) for the 0.003, 0.35, and 0.11% C, respectively, with little differences between the 1/8 in.- and 7/8 in.-long specimens. The as quenched hardness of the 0.11% C steel was in good agreement with the water quenched hardness reported for standard Croloy[3] (ASTM A–387, Grade D).

The specimens that were air-cooled from 927°C were examined metallographically. The steel with 0.003% C contained very few austenite decomposition products (pearlite and bainite), the steel with 0.035% C contained 10 to 20% decomposition products, and the steel with 0.11% C was almost entirely bainite.

The final hardness of the tempered steels depended upon the initial heat treatment (initial hardness), carbon content, and tempering time. Tempered hardnesses decreased with increasing temperature, decreasing carbon content, and increasing time. After the 100 hr temper, the hardnesses paralleled the initial hardnesses in that the hardness plateaus with initial annealing temperatures were again observed, but at lower hardness levels.

Though the hardness decreased with time, the decrease was not always continuous, but instead, went through an initial hardness peak. Two types of peaks were observed: 1) a peak that appeared during the first hour of tempering and reached a hardness greater than the hardness before tempering; or 2) a small peak that followed an initial softening. The first type of peak appeared only in specimens tempered at 593°C, indicating that at the higher temperatures the reaction causing the peak was complete in less than an hour. Since all the specimens were carried through the 100 hr temper, it was not possible to correlate the hardness peaks with microstructural changes.

---

[3] E. H. Kottcamp, D. A. Canonico, and R. D. Stout, Welding J. (N.Y.) 41, 350-s–354-s (1962).

Mechanical Properties

Welds

The tensile properties of all weld metal specimens at room temperature and 565°C are given in Table 9.7. The following observations seem important:

1. The yield and tensile stresses increase with increasing carbon content.

2. The yield and tensile stresses are decreased at both test temperatures by tempering for 1 hr at 704°C. The largest effect is in the high carbon alloy.

3. There is very little effect of strain rate on the strength and ductility parameters at 565°C.

4. The uniform strain values range from 3 to 12% and the total strains are from 8 to 20% with little systematic variation; reductions in area are quite large, indicating low uniform elongation, but high local strains at the fracture.

The tensile properties of transverse weld specimens are given in Table 9.8. Before welding, the plates were annealed for 1 hr at 925°C and air cooled. Specimens were machined so that they were oriented transverse to the weld and contained base metal, weld metal, and heat affected zone. The strength increases with increasing carbon content and decreases with tempering. Although the strength values are all below those for the weld metal (Table 9.7), there is little difference in the ductility parameters. The fracture strains are somewhat improved by tempering.

In Fig. 9.12, the tensile properties for our welds are compared with those reported by Smith[4] for standard 2-1/4% Cr—1% Mo steel, and the tensile and yield strengths of welds (reported by Smith) are higher than those of tempered base metal. The all-weld metal specimens from the heats with variable carbon have strengths above those for the standard base metal and fall in or above the scatterbands reported by

---

[4] G. V. Smith, "An Evaluation of the Elevated Temperature Tensile and Creep-Rupture Properties of 2 1/4% Cr—1% Mo Steel," to be published.

Table 9.7 Tensile Properties of All-Weld-Metal of Variable Carbon 2-1/4% Cr–1% Mo

Carbon Content,%	Postweld Anneal*	Test Temperature, °C	Strain Rate %/min	Yield Stress, psi	Ultimate Tensile Stress, psi	Fracture Stress, psi	Uniform Strain,%	Total Strain,%	Reduction in Area,%
0.003	A	25	5	88,500	101,400	47,900	7.8	14.4	79.5
	B	25	5	60,200	74,000	30,600	11.6	20.1	88.7
	A	565	5	53,800	56,700	22,900	3.4	12.1	80.5
	A	565	0.2	57,800	61,000	32,000	2.8	8.8	69.4
	B	565	5	46,300	50,100	15,700	4.2	15.9	86.3
0.035	A	25	5	82,000	104,500	53,200	8.9	15.7	80.4
	B	25	5	72,200	86,100	42,600	10.2	18.6	81.2
	A	565	5	68,800	92,400	55,400	11.8	17.8	69.7
	A	565	0.2	74,600	90,700	62,300	7.5	12.6	52.5
	B	565	5	55,000	57,500	20,600	2.9	13.1	87.5
0.11	A	25	5	135,200	157,600	90,200	9.0	14.5	72.0
	B	25	5	90,700	101,600	46,000	8.8	15.7	84.0
	A	565	5	102,500	118,400	77,000	7.9	13.1	60.8
	A	565	0.2	101.500	116,900	106,500	6.4	7.7	13.1
	B	565	5	66,000	68,600	22,400	2.8	13.9	85.0

*A - None

B - 1 hr at 704°C(1300°F)

Table 9.8 Transverse Weld Specimens from Variable Carbon 2-1/4% Cr—1% Mo Steel

Carbon Content,%	Postweld Anneal*	Test Temperature, °C	Strain Rate %/min	Yield Stress, psi	Ultimate Tensile Stress, psi	Fracture Stress, psi	Uniform Strain,%	Total Strain,%	Reduction in Area,%
0.003	A	25	5	38,600	54,100	21,400	9.9	15.5	71.0
	B	25	5	32,300	55,200	24,900	12.9	21.4	71.7
	A	565	5	31,300	44,200	17,300	4.8	13.5	67.4
	B	565	5	20,500	44,300	2,500	8.1	16.8	79.8
0.035	A	25	5	47,100	61,100	28,900	7.3	16.0	81.8
	B	25	5	41,300	60,200	28,600	8.9	19.0	82.0
	A	565	5	34,100	46,200	15,600	4.7	15.9	85.7
	B	565	5	22,400	42,900	14,000	6.7	17.1	87.5
0.11	A	25	5	68,300	88,100	44,400	7.2	15.2	79.0
	B	25	5	58,100	82,600	42,500	6.1	14.6	76.9
	A	565	5	57,600	58,600	19,400	1.0	11.9	82.7
	B	565	5	41,800	53,200	17,200	3.6	14.7	86.4

*A - None

B - 1 hr at 704°C(1300°F)

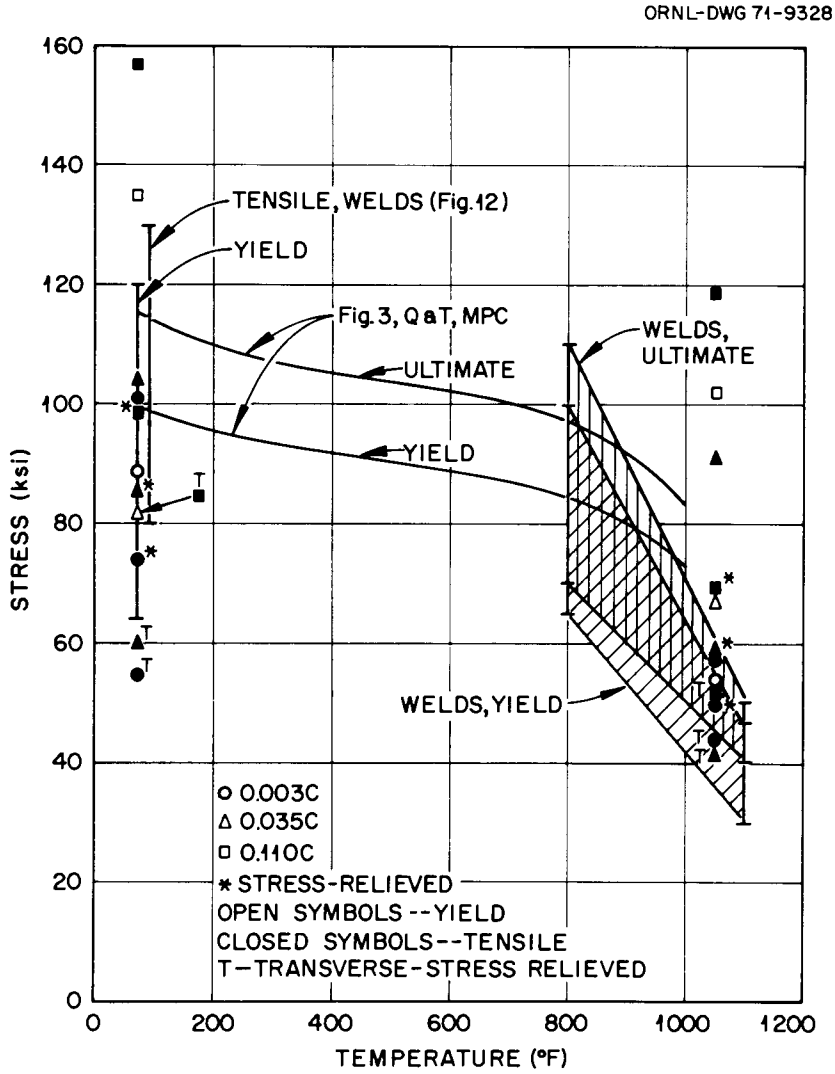

Fig. 9.12. Tensile Properties of Croloy (2 1/4% Cr—1% Mo). (Ref. G. V. Smith, "An Evaluation of the Elevated Temperature Tensile and Creep-Rupture Properties of 2 1/4% Cr—1% Mo Steel," to be published.)

Smith for welds. With the exception of the 0.11% C alloy, the tensile stresses of the transverse weld specimens fall below those for the base metal.

In Fig. 9.13, the fracture strains of our all-weld metal specimens are compared with those reported by Smith for tempered welds. The fracture strains are generally lower for all the modified carbon alloys, while the reductions in area are as good or better than those reported by Smith.

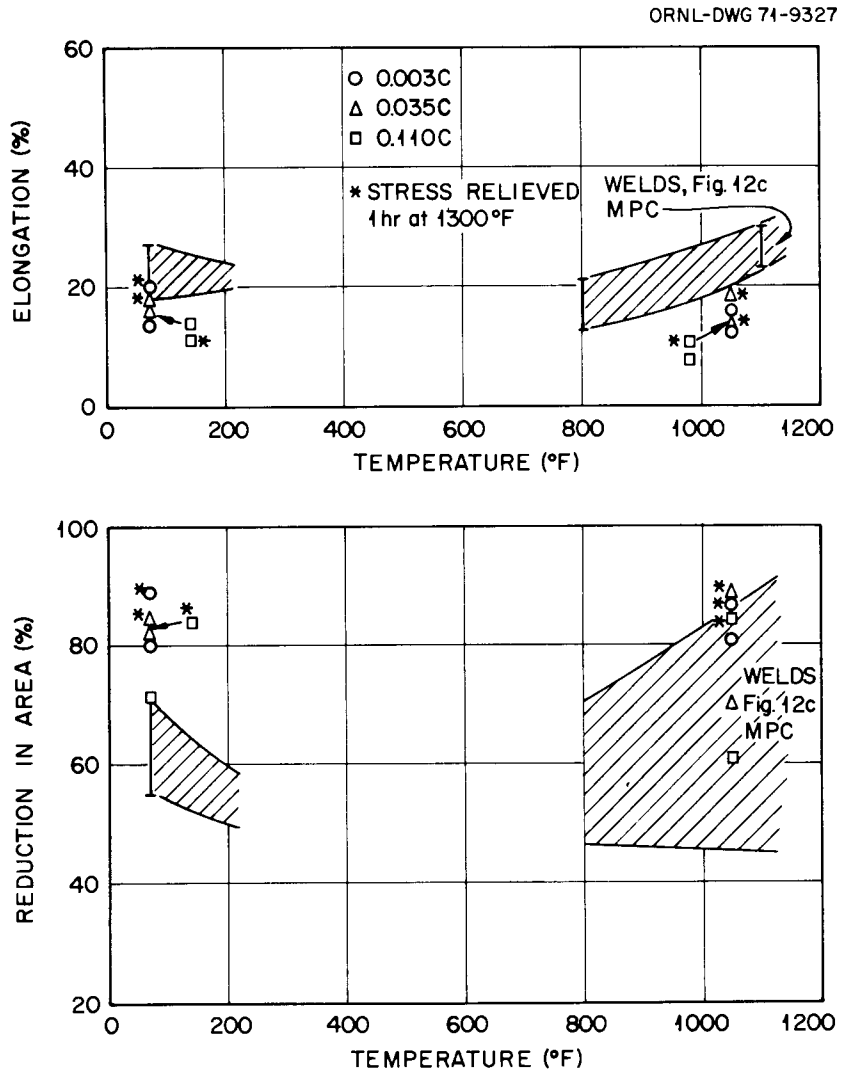

Fig. 9.13. Ductilities of All-Weld-Metal Specimens 2 1/4% Cr—1% Mo Steel (Ref. G. V. Smith, "An Evaluation of the Elevated Temperature Tensile and Creep-Rupture Properties of 2 1/4% Cr—1% Mo Steel," to be published.)

We have determined the creep-rupture properties of several of the transverse weld specimens at 565°C (Table 9.9); in Fig. 9.14 the results are plotted and compared with Smith's data on standard 2-1/4% Cr—1% Mo base metal at 635°C and weld metal at 565°C. The rupture life of the transverse weld samples is shorter than that of Smith's base metal and weld metal. These limited data also indicate that the rupture lives of the two lower carbon alloys are quite similar and less than the 0.11% C alloy. There seems to be little effect of tempering. In all

Table 9.9 Creep Properties of 2-1/4% Cr–1% Mo Transverse Welds at 565°C(1050°F)

Carbon Content, %	Stress, psi	Rupture Life, hr	Strain, %	Reduction in Area, %
0.003	30,000[a]	16.4	17.2	89.6
	20,000	51.1	24.2	81.0
	15,000	150.9	26.4	94.1
0.035	30,000[a]	11.7	17.0	83.1
	25,000	13.6	23.5	83.8
	20,000	46.8	32.8	92.4
	15,000	362.5		80.9
	12,000[b]	670.0		
0.110	30,000[a]	35.0	21.6	85.7
	25,000	75.4	27.9	87.7
	20,000	591.9	23.8	81.8
	25,000	105.8	18.5	83.7
	15,000[b]	1092.0		

[a]Tested as welded. All other specimens were tempered for 1 hr at 704°C(1300°F).

[b]Test in progress.

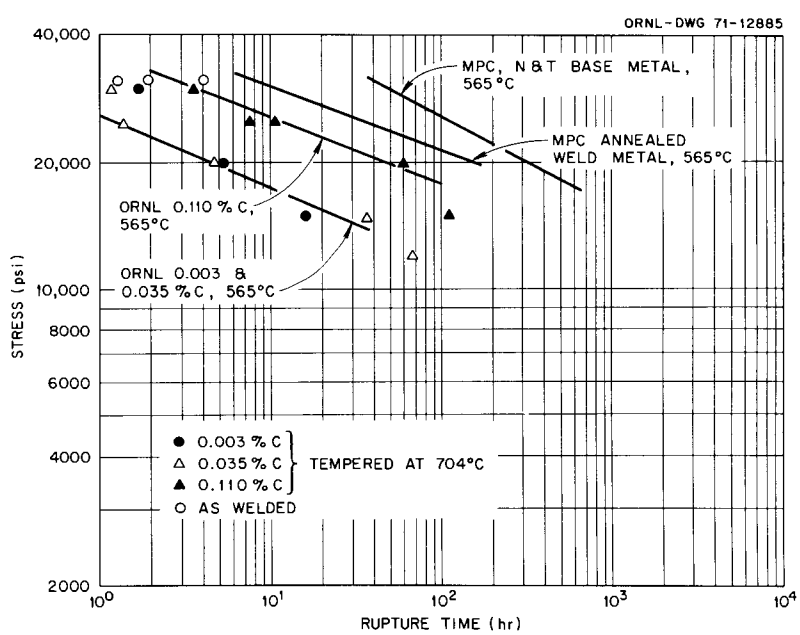

Fig. 9.14 The Creep-Rupture Properties of Transverse Weld Specimens of 2-1/4% Cr–1% Mo Steels with Varying Carbon Contents at 565°C. Results compiled by Smith on Standard Croloy weld metal and bar stock are also shown.

cases the ductility is good with fracture strains on the order of 20% and reductions in area of 80%.

The failures of all the transverse weld specimens occurred near one end of the specimen, and consistently occurred in the base metal and close enough to the fusion line that the properties may have been affected by heating during welding. Measurements made along the tested sample showed that the deformation was confined to a region about 0.4 in. long. Similar calculations on the samples crept at 30,000 psi, gave deformed zone lengths of 0.44, 0.40, and 0.39 in. for the three carbon levels.

We are also determining the creep properties of all-weld metal specimens at 565°C. To date, only a low carbon test at 20,000 psi is complete. Failure occurred after 182 hr with 35.5% strain and 82.5% reduction in area. Tests for the 0.035 and 0.11% C steels at 20,000 psi are in progress and have completed 407 and 760 hr, respectively, indicating rupture times that will exceed those of the transverse welds under similar conditions (Fig. 9.14).

Base Metal

The mechanical properties of the base metal are being determined on 6 in. specimens machined from the 7/8 in.-diam rod; the specimens have a 2.5 in. gage length and are 0.250 in. in diameter. The results of completed tests at 565°C are given in Table 9.10. The stress-rupture curves for the three carbon levels are compared with Smith's compilation in Fig. 9.15.

The limited data indicate that the creep-rupture life of the base metal at a given stress level increases with carbon content. The ductility of all materials was good, with fracture strains of about 20% and reductions in area greater than 80%. There appears to be a ductility variation with carbon with the medium carbon material showing the largest fracture strain and reduction in area.

Table 9.10 Creep Properties of 2-1/4% Cr–1% Mo Base Metal at 565°C(1050°F)

Carbon Content, %	Stress, psi	Rupture Life, hr	Strain, %	Reduction in Area, %
0.003	25,000	5.6	28.7	87.3
	20,000	48.7	26.0	90.3
	20,000	59.6	25.3	91.2
0.035	25,000	10.1	53.9	90.3
	20,000	424.1	42.2	89.2
0.11	25,000	435.9	30.1	71.2
	20,000	1115.0[a]		

[a]Test in progress.

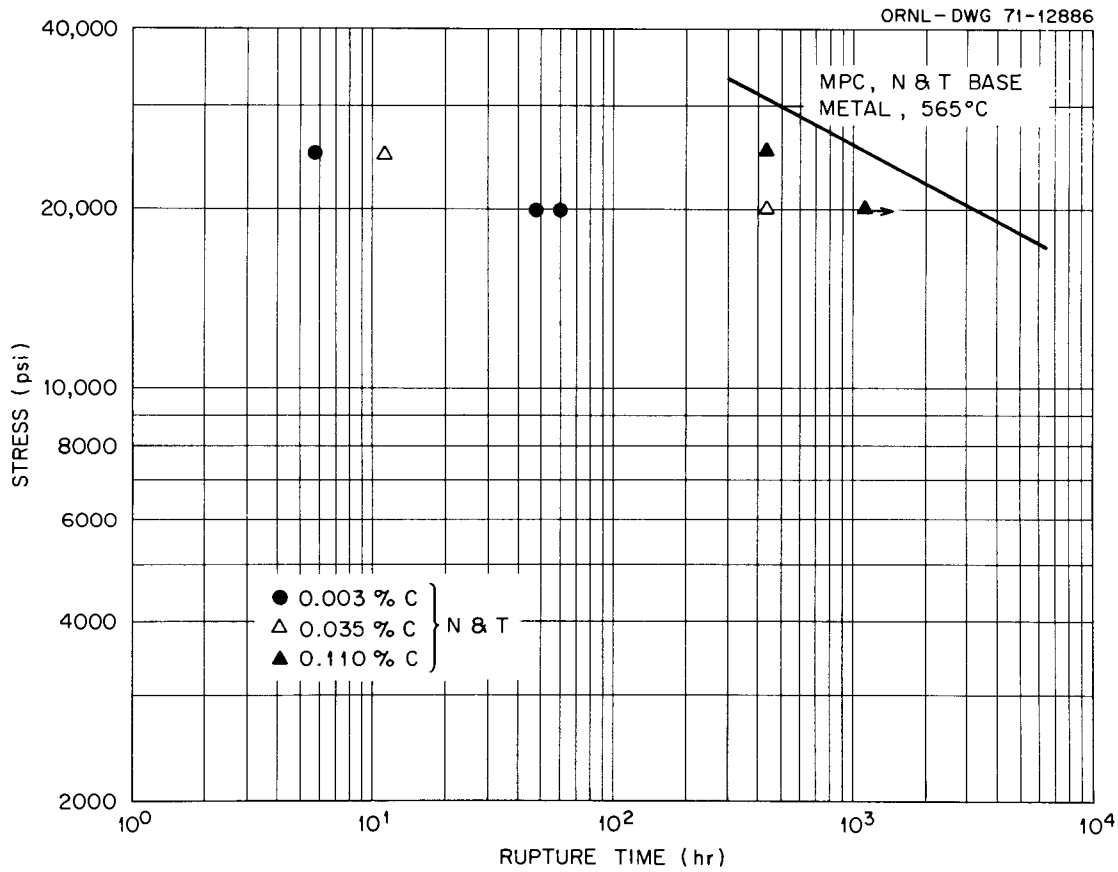

Fig. 9.15 The Creep-Rupture Properties of 2-1/4% Cr–1% Mo Steels with Varying Carbon Contents at 565°C. Results compiled by Smith on standard Croloy bar stock are also shown.

PART II. SPACE POWER TECHNOLOGY

10. DEVELOPMENT OF URANIUM MONONITRIDE FUELS

J. L. Scott P. Patriarca

Uranium mononitride is of interest as a fuel material for space-nuclear reactors because of its high thermal conductivity, high melting point of 2800°C, and good irradiation stability. Because space reactors reject heat by radiation, fuel pin cladding temperatures of interest are 1000°C or greater. The objective of our program is to establish the rate of swelling and fission-gas release of UN irradiated in refractory metal cladding at surface temperatures above 1000°C. The program also includes development of fabrication of very high-purity UN, because impurities such as carbon or oxygen may adversely affect performance.

Fabrication of Uranium Mononitride

V. J. Tennery R. A. Potter

We are presently conducting development work on UN for NASA-Lewis Research Center.[1] The development of a dimensionally stable coarse-grained porous microstructure in UN is of interest for application in a space reactor. We are attempting to do this by coarsening our fine uranium nitride powders by heat treating them prior to fabrication. The effect of calcining fine uranium nitride powders at various temperatures from 1100–1400°C for varying times is to decrease the specific surface area of the powder while affecting the particle size distribution very little. The specific surface area of a powder was decreased from 1.2 to 0.17 m^2/g by heat treating it at 1400°C for 3 hr while the median particle size increased from 2.4 to 4.2 μm. The fabricating and sintering properties of these powders are now being evaluated. Various fabricated and sintered shapes of high purity UN, such as annular cylinders and slabs, are being delivered to NLRC.

---

[1]NLRC contract C-54560-B.

Irradiation Testing of Uranium Nitride

T. N. Washburn

The objective of the ORNL program for irradiation testing of uranium mononitride (UN) is to obtain basic information on fuel swelling, fission-gas release, and compatibility with cladding materials at fuel temperatures from 1000 to 1500°C, cladding outside surface temperatures of 900 to 1400°C, and linear heat ratings of 5 to 10 kW/ft. Detailed descriptions of our capsule design[2] and previous test results[3,4,5] have been reported.

Three new irradiation test capsules were fabricated: one (UN-5) sponsored by the AEC and two (UN-4 and UN-6) by NASA. Capsules UN-4 and UN-5 contain two types of UN pellets — solid 85%-dense cylinders and annular 95%-dense cylinders. The inner diameter of the annular pellets was sized such that both types of pellets provided the same fuel smear density. The six fuel pins in these two capsules have T-111 (Ta–8% W–2% Hf) cladding. Capsule UN-6 contains UO_2 pellets with T-111 cladding on one fuel pin and Nb–1% Zr on two. Capsule UN-6 serves to investigate the backup or derated design being considered for advanced space reactors. The control cladding temperature of each capsule test is 1000°C, with the UO_2 fuel central temperature restricted to 1550°C. Thus, the UO_2 fuel will operate at 6.5 kW/ft maxima, while the UN will operate at 9 to 10 kW/ft.

---

[2]V. A. DeCarlo, F. R. McQuilkin, R. L. Senn, K. R. Thoms, and S. C. Weaver, Design of a Capsule for Irradiation Testing of Uranium Nitride Fuel, ORNL-TM-2363 (February 1969).

[3]T. N. Washburn, D. R. Cuneo, and E. L. Long, Jr., "Irradiation Performance of Uranium Nitride at 1500°C," Amer. Ceram. Soc. Bull. 50, 427 (1971).

[4]T. N. Washburn, K. R. Thoms, S. C. Weaver, D. R. Cuneo, and E. L. Long, Jr., "Examination of UN-Fueled Pins Irradiated at 1400°C Cladding Temperature," Trans. Amer. Nucl. Soc. 13, 101 (1970).

[5]S. C. Weaver, K. R. Thoms, and V. A. DeCarlo, "Irradiation Testing of UN in ORR," Trans. Amer. Nucl. Soc. 12, 547 (1969).

Capsule Fabrication (E. J. Manthos)

Thermal simulation fuel pins which will be tested out-of-reactor at the same temperature as the pins in UN-4, -5, and -6 were fabricated. A total of eight pins was fabricated as shown in Table 10.1. These pins are identical in design to the pins in the irradiation capsules and were fabricated in the same manner. In the case of the UN-6 pins, they were fabricated at the same time.

Because the fabrication of capsules UN-4, -5, and -6 is now complete, all remaining fuel pellets will be assembled into a sealed stainless steel archive pin and stored. Control specimens of cladding, tungsten liners, end plug stock, etc., are identified and stored in the Irradiation Capsule Fabrication Laboratory.

Operation of Capsules (B. Fleischer, K. R. Thoms, T. N. Washburn)

UN-4. — This capsule was installed in the ORR on February 9, 1971, and has been operating 4390 hr above 800°C cladding temperature as of September 21, 1971.

The capsule is presently being controlled by maintaining the middle fuel element at a heat rating of 10.2 kW/ft. Control was keyed to this level in July when the thermocouples on this element continued to show a downward drift. To avoid overheating we chose to operate conservatively until reliability of the thermocouples could be determined. Our efforts to date have not revealed any obvious fault with the thermocouples. All thermocouples on the fuel elements in the capsule have shown this drift throughout the test life. Thermocouples on UN-5 which are from the same batch and operating about the same temperature have not shown this drift. The amount of drift has been greatest at the bottom pin which is at the highest temperature and the drift is smallest in the top pin which is at the lowest temperature. To investigate the possibility of physical

Table 10.1. Summary of Thermal Simulation Fuel Pins for Capsules UN-4, -5, and -6

Capsule Designation	Fuel Pin		Fuel Pellets				
	Number	Material	Material	Density (%)	Enrichment (% ^{235}U)	Solid or Annular	Batch and Stack No.
UN-4, -5	2	T-111	UN	85	20	Solid	532-4
UN-4, -5	3	T-111	UN	85	20	Solid	532-5
UN-4, -5	7	T-111	UN	85	11	Solid	B4-1
UN-4, -5	8	T-111	UN	95	11	Annular	534-3
UN-4, -5	9	T-111	UN	95	11	Annular	534-4
UN-6	TS-16	Nb-1% Zr	UO_2	95	10	Annular	10-2
UN-6	TS-17	T-111	UO_2	95	10	Annular	10-4
UN-6	TS-18	Nb-1% Zr	UO_2	95	8	Annular	8-2

changes in the capsule such as reductions of the gap, we plan to examine the capsule by neutron radiograpny early in October. We will continue to operate the capsule conservatively until an explanation of the thermocouple behavior has been obtained.

UN-5. — This capsule, which was installed in the reactor March 1, 1971, has operated 3930 hr above 800°C cladding temperature as of September 21, 1971. The operation continues to be completely satisfactory.

UN-6. — This capsule was installed in the reactor August 3, 1971, and has operated 950 hr above 800°C cladding temperature as of September 21, 1971.

This capsule is presently being controlled by maintaining 900°C as the maximum cladding temperature on any fuel element. This necessitates shifting control from one element to another as a function of core burnup during a reactor cycle. This method of operation was chosen to avoid overheating of the fuel which is not to exceed 1600°C. The cladding temperatures are, therefore, running 100–150°C lower than anticipated. To achieve the desired 1000°C cladding temperature on the middle element would require overheating of the fuel in all elements. We are presently investigating the possibility of introducing less conductive (compared to helium) gases in one or both of the two annuli and, therefore, reduce the power level necessary for 1000°C operation.

During the early part of operation of this capsule we investigated cladding thermocouple behavior using a high speed recorder to determine if perturbations similar to those found in UN-4 and UN-5 were present.[6] The results were negative, therefore, confirming the benefit of reducing the allowable misfit between the NaK capsule and primary container to eliminate these perturbations caused by capsule flexing due to non-symmetrical thermal stresses. The close fitting of the capsule components and efforts to obtain better centering, however, did not eliminate the disparity between predicted and measured cladding temperatures.

---

[6]B. Fleischer and K. R. Thoms, Fuels and Materials Development Program Quart. Progr. Rept. June 30, 1971, ORNL-TM-3540, p. 123.

11. TUNGSTEN METALLURGY

A. C. Schaffhauser

The objective of this program is to provide the base technology on W materials for advanced space power applications. We are developing fabrication processes for W alloys based on chemical vapor deposition (CVD) and high-temperature extrusion techniques. Since a primary criteria for use of W materials for fuel cladding is based on the creep properties, we are conducting extensive long-time tests at the temperatures of interest and determining the mechanisms that control creep behavior. The effects of decomposition products from a reactor fuel on creep properties is being determined. We are also evaluating the effects of high-temperature fast-neutron irradiation damage on the structure and physical properties of W alloys.

Fabrication Development for Advanced Cladding Materials

A. C. Schaffhauser R. E. McDonald

Previously we have developed CVD techniques for the fabrication of high purity W and W-Re alloys.[1,2,3] The creep properties of these materials are currently being evaluated and further CVD studies will be based on these results.

---

[1] J. I. Federer, Fuels and Materials Development Program Quart. Progr. Rept. September 30, 1970, ORNL-4630, p. 207.

[2] J. I. Federer and A. C. Schaffhauser, "Chemical Vapor Deposition and Characterization of Tungsten-Rhenium Alloys," pp. 74–81 in IEEE Conference Record of 1970 Thermionic Conversion Specialist Conference, October 26–29, 1970, IEEE, New York, 1970.

[3] J. I. Federer, Metals and Ceramics Division Ann. Progr. Rept. for period ending June 30, 1971, ORNL-4770, p. 115.

A high-temperature floating-mandrel extrusion process has also been developed for fabrication of 3/4 to 1 1/2-in. diam W and W–25% Re tubing from powder-metallurgy and arc-melted billets.[4] The process is shown schematically in Fig. 11.1. Using this technology, we are now developing the parameters for extrusion of bar and tubing of the high strength W–5% Re and W–2% ThO_2 alloys. The extrusion conditions for fabricating tubing of these materials and representative solid bar extrusions is given in Table 11.1. All extrusions were performed on our high-speed 1250-ton press using 4-in. diam billets.

---

[4]R. E. McDonald and G. A. Reimann, Floating-Mandrel Extrusion of Tungsten and Tungsten-Alloy Tubing, ORNL-4210, February 1968.

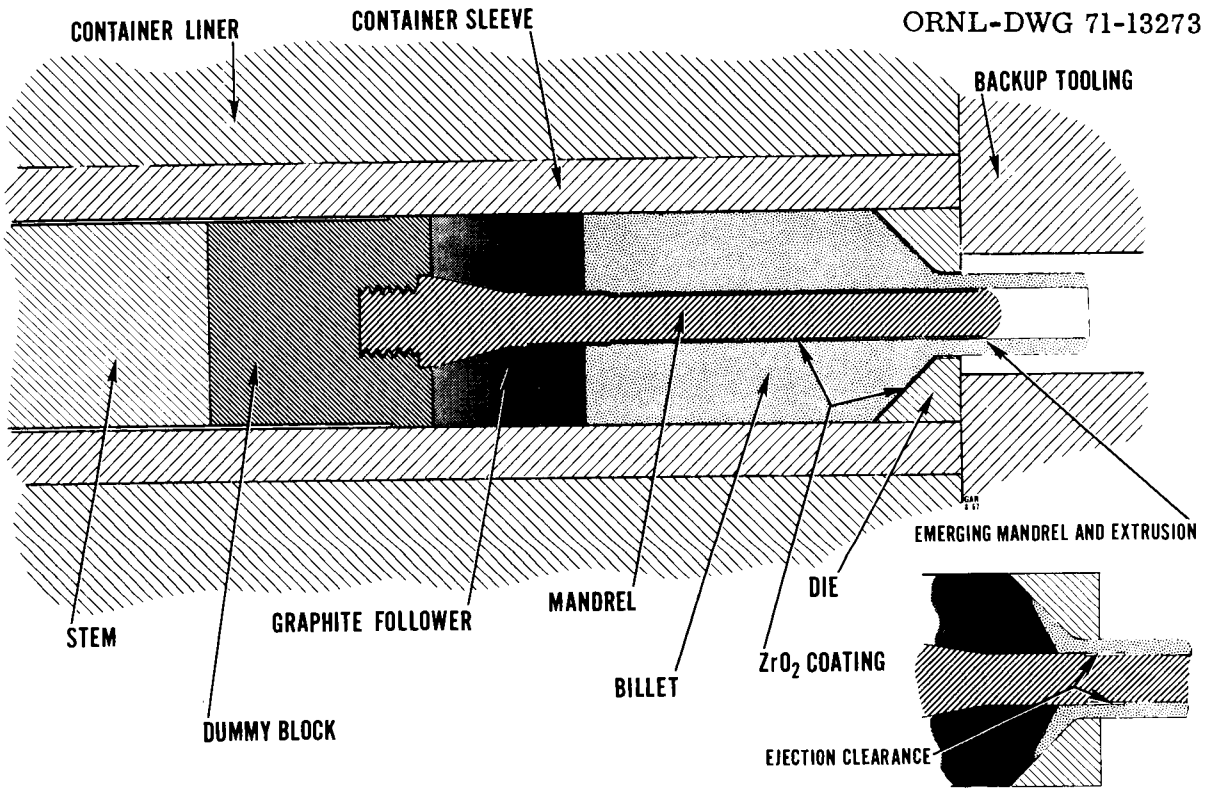

Fig. 11.1. Schematic of Floating-Mandrel Extrusion Technique.

Table 11.1. Extrusions of High Strength W Alloys

Material	Extrusion No.	Type of Extrusion	Temperature (°C)	Extrusion Ratio	Dimension of Alloy[a] O.D., in.	I.D., in.
W–5% Re	945	Solid, duplex	1850	6.2	1.250	
W–5% Re	1156	Tubeshell, duplex[b]	1850	7.0	0.875	0.750
W–2% ThO_2	1175	Tubeshell, duplex[c]	1750	6.8	0.940	0.58–0.62
W–2% ThO_2	1176	Tubeshell, duplex[c]	1750	11.2	1.250	1.0
W–2% ThO_2	1180	Solid	1700	7.3	1.500	
W–2% ThO_2	1182	Solid	1800	7.3	1.500	
W–2% ThO_2	1184	Solid	1850	8.7	1.375	
W–2% ThO_2	1188	Solid	1850	10.5	1.250	

[a]For duplex extrusion, dimension after removing TZM core.

[b]Floating-mandrel extrusion.

[c]Deformable TZM core used.

An arc-melted W–5% Re ingot, procurred from Wah Chang Corporation,[5] was first extruded to 1.25-in. O.D. bar at 1850°C. Tube blanks machined from this bar were then enclosed in a Mo alloy (TZM) can and successfully extruded to 0.875-in. O.D., 0.750-in. I.D. tubing at 1850°C. The microstructure of the extruded tubing was recrystallized to a uniform equiaxed grain structure as seen in Fig. 11.2(a).

Tubing of W–2% ThO_2 from Thermo Electron Corporation (TECO)[6] was extruded in duplex billets using both floating-mandrel and deformable-core techniques. The first extrusion using a deformable TZM core produced a

[5]Wah Chang Albany, Albany, Oregon.

[6]Thermo Electron Corporation, Metals Division, Woburn, Massachusetts.

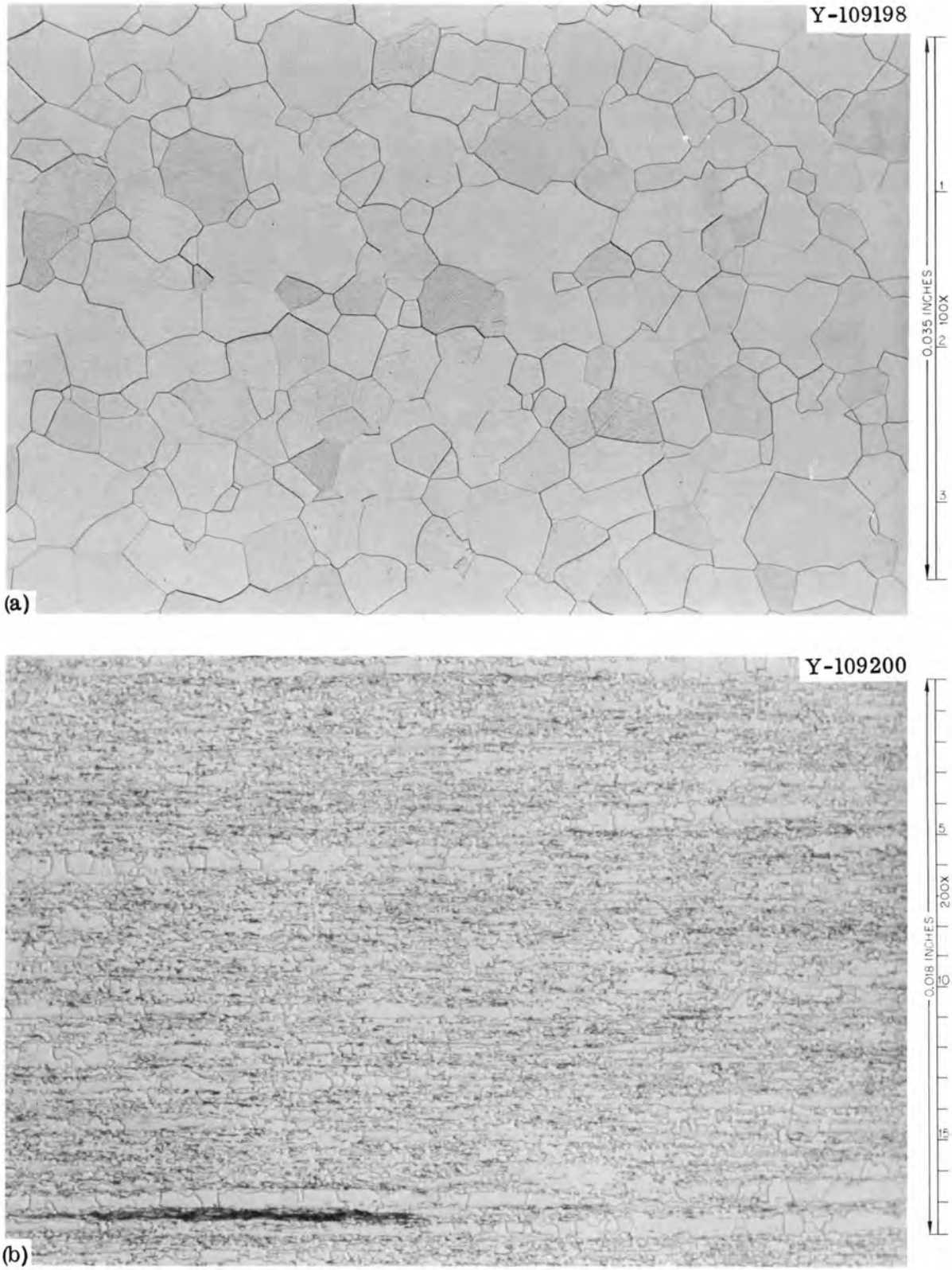

Fig. 11.2. Microstructures of Extruded W-Alloy Tubing. (a) W–5% Re annealed 1 hr at 2000°C, (b) W–2% ThO_2 annealed 1 hr at 2000°C.

heavy-wall tube with a variable I.D. due to nonuniform deformation of the core. The second extrusion using the floating-mandrel process with a ZrO_2 coated tool steel mandrel resulted in a thin wall tube with excellent I.D. dimensions and surfaces. This material is suitable for fabricating an internally fueled thermionic emitter with a welded bottom. Both these extrusions at 1750°C produced a warm worked grain structure with elongated grains. The microstructure of the second extrusion after recrystallization 1 hr at 2000°C is shown in Fig. 11.2(b). The fine grain size and dispersion of ThO_2 particles is evident.

Data for the extrusion of solid bars of W–2% ThO_2 is also given in Table 11.1. The larger diameter bars have been machined by TECO for externally fueled thermionic fuel elements. The smaller diameter bars are suitable for machining to closed end internally fueled emitters.

Creep Properties of W and W Alloys

H. E. McCoy

Creep Properties of CVD W

The creep properties of several lots of CVD W have been determined in vacuum at elevated temperatures. The test materials have generally been sheet from 0.040 to 0.060 in. thick that has been deposited from WF_6 on a molybdenum sheet mandrel. Small sheet specimens have been EDM machined and the surfaces and edges lapped to remove flaws and irregularities. One lot of material (GGA-1) received from Gulf General Atomic is a duplex material having layers deposited from fluoride and chloride gases.

The test results obtained to date are summarized in Table 11.2. The stress rupture properties at 1650°C are shown in Fig. 11.3 with the various lots identified. The limited data on each lot made it difficult to pick up trends with much confidence. The duplex material from Gulf General Atomic[7] (GGA-1) had an exceptional rupture life at 5000 psi although the rupture life at 7000 psi was not high.

---

[7]Gulf General Atomics, San Diego, California.

Table 11.2. Creep Properties of CVD Tungsten

Lot No.	Temperature (°C)	Stress, (psi)	Rupture Life (hrs)	Min. Creep Rate (%/hr)	Fracture Strain (%)	Fluorine Content (ppm)
WF-1	1650	10,000	6.5	0.18	1.7	17
WF-1	1650	5,000	172.0	0.015	1.5	
WF-1	1650	3,500	740.1	0.005	30.9	
WF-1	1650	3,500	89.8[a]		1.7[a]	
WF-1	1400	7,000	956[a]		1.7[a]	
WF-2	1650	10,000	7.3	0.20	6.3	9
WF-2	1650	5,000	270.8	0.0093	3.1	
WF-2	1400	7,000	1723.2	0.0005	1.4	
WF-5	1650	5,000	126.1	0.075	18.9	6
WF-6	2200	1,000	156.5	0.075	62.4	7
WF-6	2200	700	235.7	0.077	27.2	
WF-6	2200	300	2016[b]	0.001	2.5[b]	
WF-6	1650	10,000	1.0	8.6	45.6	
WF-6	1650	5,000	108.8	0.16	28.8	
WF-6	1650	3,000	743.5[b]	0.0054	4.5[b]	
WF-6	1650	2,250	1407.4[b]	0.0011		
WF-6	1400	15,000	0.55	20.4	23.0	
WF-6	1400	7,000	134.8	0.031	13.0	
WF-9	2200	800	255.3	0.048	66.7	7
WF-9	1650	5,000	77.6	0.31	46.4	
WF-9	1650	5,000	3.8[b]	0.22	1.6[b]	
WF-9	1650	3,500	206.8	0.015	11.9	
WF-55	1650	5,000	379.6	0.0046	3.5	15
WF-55	1400	7,000	1004[a]		2.1[a]	
GGA-1	1650	7,000	6.1	0.86	5.9	6
GGA-1	1650	5,000	1686.7	0.015	51.1	

[a]Test in progress; time and strain to date is listed.

[b]Discontinued before rupture; time and strain at end of test is listed.

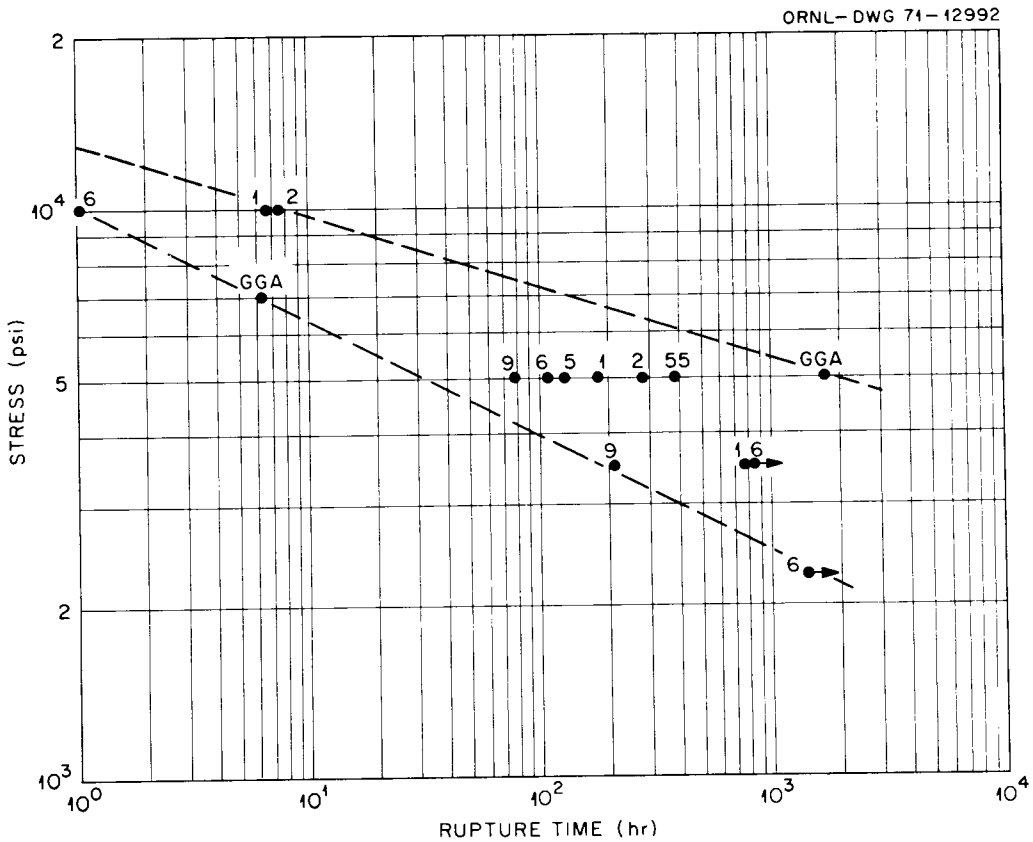

Fig. 11.3. Stress-Rupture Properties of Several Lots of CVD Tungsten at 1650°C. The numbers refer to the lot numbers in Table 11.1.

The creep rates of these materials (Fig. 11.4) seem to show systematic variations. A "minimum strength" curve is made up by lots 5, 6, 9, and the duplex material. Note that these materials have high fracture strains, generally 20 to 50%, and their fluorine contents are 5 ppm, 7 ppm, 7 ppm, and 6 ppm, respectively. Lots 1, 2, and 55 are stronger and have lower creep rates. These heats have fluorine contents of 17 ppm, 9 ppm, and 15 ppm, respectively. The fracture strains of 1.5 to 6% are much lower than those of the materials that comprise the "minimum strength" curve. There are three data points on lot 1 and these indicate that the creep rate approaches the "minimum curve" at low stress levels. However, the lowest stress point for this lot that is quite close to the minimum curve also has a high fracture strain Table 11.2).

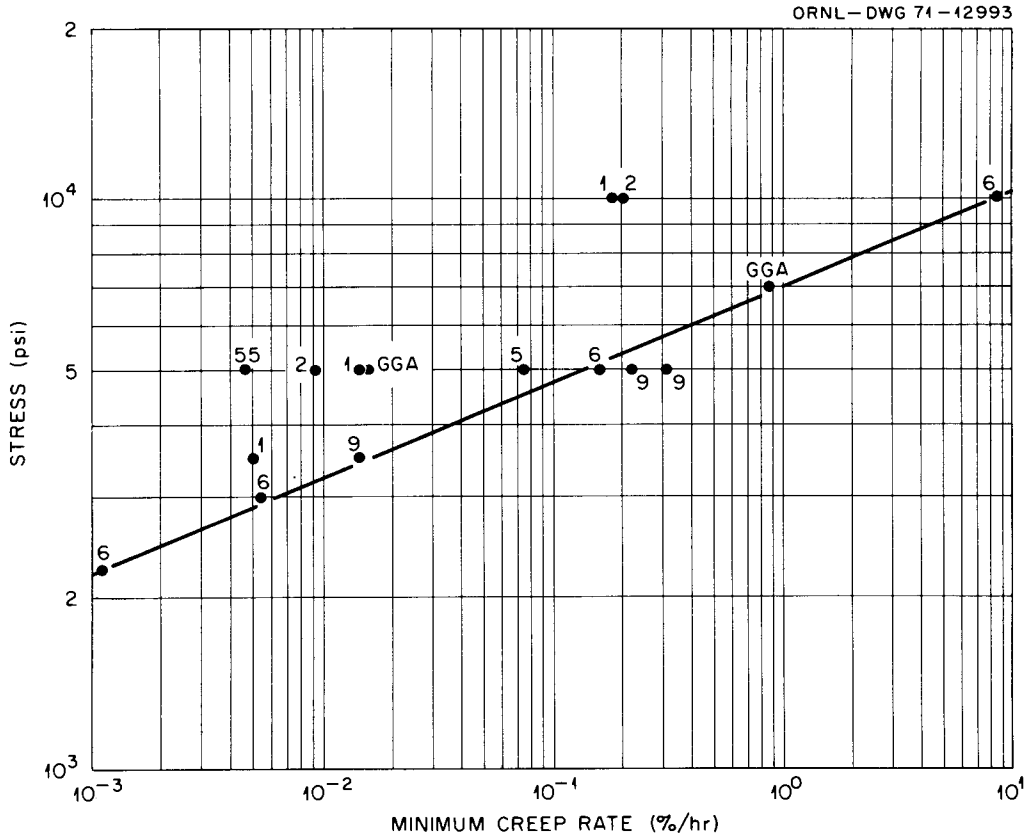

Fig. 11.4. Creep Properties of CVD Tungsten at 1650°C. The numbers refer to the lot numbers in Table 11.1.

Thus, at this time it appears that there are systematic variations in the creep strength from lot to lot. The materials with low creep strength have good fracture strains and those with better creep strength have lower fracture strains. This transition in behavior seems to occur at fluorine levels above 7 ppm. However, other characteristics of the microstructure may be changing in addition to the fluorine content. This will be studied further by electron microscopy.

Creep Properties of W–3.8% ThO_2

The creep-rupture properties of W–3.8% ThO_2 have been determined under several conditions. The 1/4 in. diam material was prepared by the Westinghouse Electric Corporation[8] and had been cold worked 91%. Creep

[8]Westinghouse Electric Corporation, Lamp Division, Bloomfield, N.J.

specimens having a gage section 1 in. x 1/8 in. diam were prepared and tested in vacuum in the as-received condition. The test results are listed in Table 11.3.

Table 11.3. Creep Properties of W–3.8% ThO_2

Temperature (°C)	Stress (psi)	Rupture Life (hrs)	Min. Creep Rate, (%/hr)	Fracture Strain, (%)
2200	5,000	18.4	1.2	28.0
2000	10,000	3.1	3.2	7.5
2000	5,000	34.1	0.47	18.1
1650	30,000	0.1		12.5
1650	15,000	72.3	0.13	11.8
1650	10,000	56.7	0.087	9.0
1650	8,000	477.8[a]		About 18.0[a]
1400	40,000	0.3	4.7	12.5

[a]Test in progress; time and strain to date as listed.

The stress-rupture properties are shown in Fig. 11.5. Presently, the limited number of data points at a given temperature makes it impossible to draw complete stress-rupture curves. Two curves are also shown in Fig. 11.5 for W–2% ThO_2 (Ref. 9). The time to rupture at a given stress is not appreciably different for the two materials at 1650°C for rupture times up 100 hr. For longer rupture times the W–2% ThO_2 shows a deviation from linearity, but the W–3.8% ThO_2 shows a deviation from linearity, but the W–3.8% ThO_2 does not appear to have this break. At 2200°C the rupture life of the W–3.8% ThO_2 is about a factor of 100 higher than that of W–2% ThO_2. However, the heat of W–3.8% ThO_2 that we are studying has shorter rupture lives than those reported by

[9]H. E. McCoy, Creep-Rupture Properties of Tungsten and Tungsten-Base Alloys, ORNL-3992 (1966).

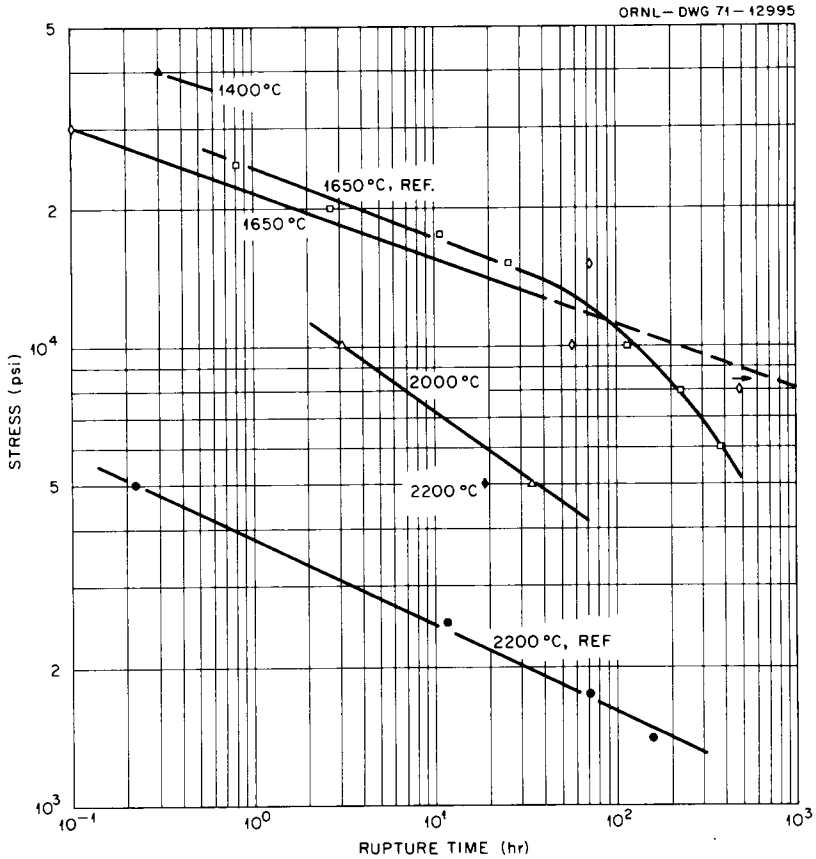

Fig. 11.5. Comparison of Stress-Rupture Properties of W–3.8% ThO_2 with referenced W–2% ThO_2 Properties. Ref: H. E. McCoy, Creep-Rupture Properties of Tungsten and Tungsten-Base Alloys, ORNL-3992 (1966).

Westinghouse for a similar heat which had 1 hr and 10 hr rupture stresses of 12,500 and 9500 psi, respectively.[10]

The minimum creep rates are shown in Fig. 11.6 for this heat and compared with those for W–2% ThO_2. At 1650°C the strengths of the two materials are quite similar. At 2200°C the allowable stress for the W–2% ThO_2 is significantly lower than that for the W–3.8% ThO_2 material. The fracture strains at all temperatures were good with the minimum being a value of 7.5% at 2000°C.

---

[10]H. G. Sell, W. R. Morcom, and G. W. King, Development of Dispersion Strengthened Tungsten Base Alloys, Technical Report AFML-TR-65-407, Part II (1966).

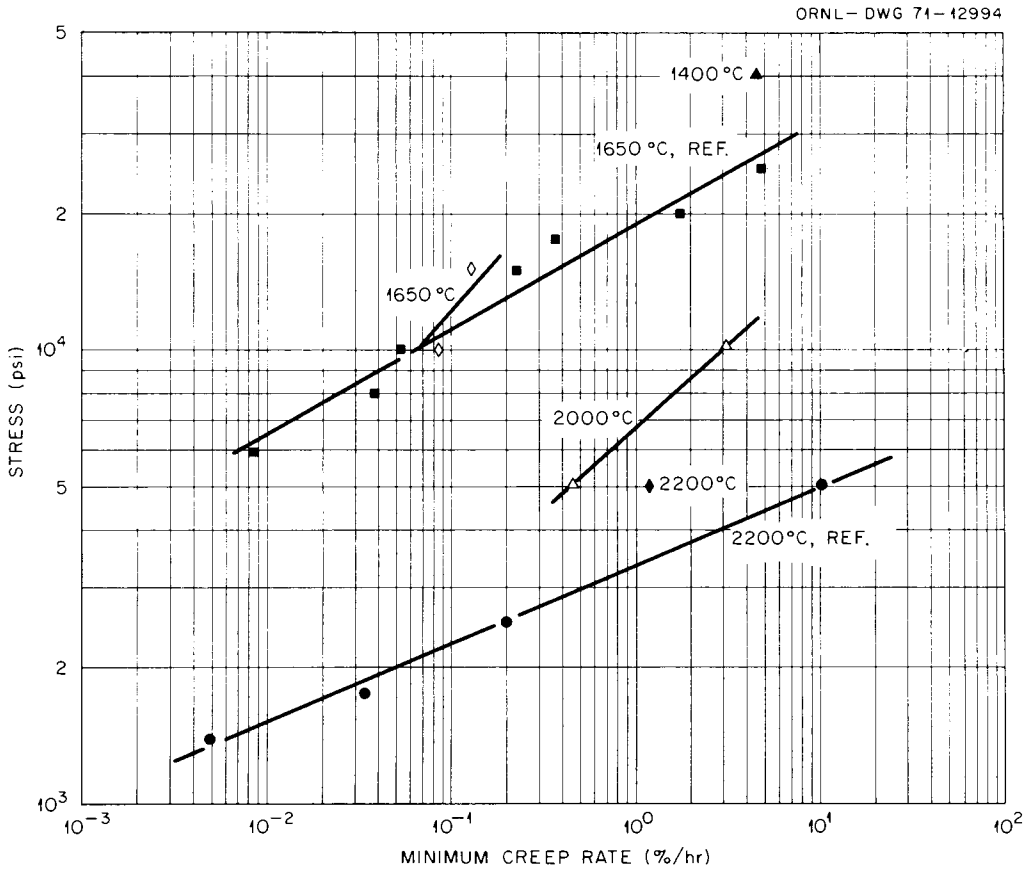

Fig. 11.6. Comparison of Creep Properties of W-3.8%.ThO_2 with referenced W-2% ThO_2 properties. Ref: H. E. McCoy, Creep-Rupture Properties of Tungsten and Tungsten-Base Alloys, ORNL-3992 (1966).

Effect of Low Pressure Gases on the Creep Properties of Tungsten Alloys

H. Inouye

The creep properties of 0.040-in. diam tungsten wire are being measured in low-pressure CH_4 to simulate the effect of its carburization by UC at thermionic temperatures. A series of creep tests run at 1800°C and a stress of 2000 psi has shown that the rupture ductility and rupture life progressively decreases as the CH_4 pressure increased from about 3×10^{-6} to 3×10^{-5} torr.[11] Preliminary results at 1650°C and a stress

[11] H. Inouye, Metals and Ceramics Division Annual Prog. Rept. for Period Enging June 30, 1971, ORNL-4770, p. 118.

of 2000 psi shows that carburization strengthens tungsten relative to the vacuum test. A comparison of the results at 1650 and 1800°C in Fig. 11.7 show a reversal in the effect of carburization between 1650 and 1800°C. Post-test x-ray analyses of the specimens exposed to CH_4 show the presence of W_2C on the specimen surface tested at 1650°C, but not on the specimen tested at 1800°C. As the 1650°C creep curve shows, about 0.20% negative creep was observed for the first 25 hrs of test. Chemical analyses of the carburized specimens in Fig. 11.7 had carbon contents of only 14 and 11 ppm at 1800°C and 1650°C, respectively compared to an as-received carbon content of 6 ppm.

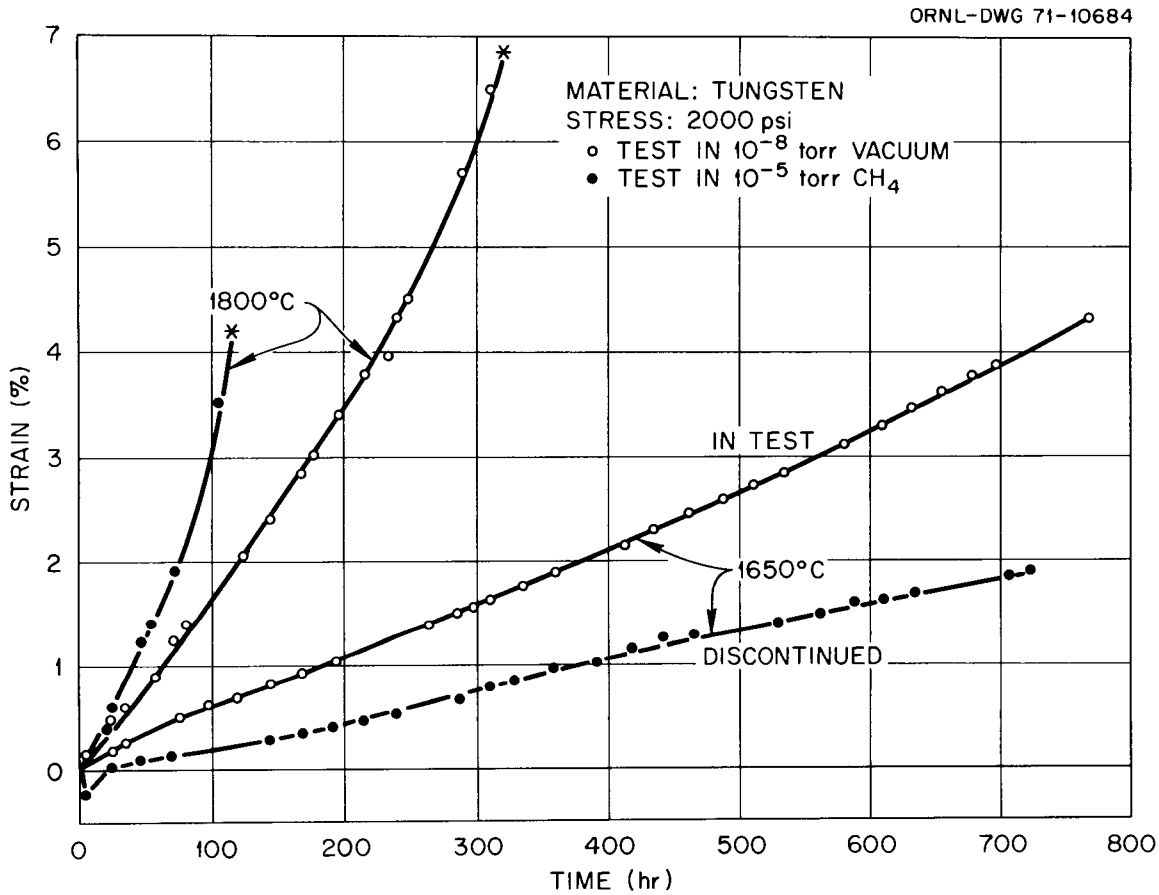

Fig. 11.7. Effect of Low-Pressure CH_4 on Creep of Tungsten at Elevated Temperatures.

12. PHYSICAL METALLURGY OF REFRACTORY ALLOYS

R. G. Donnelly P. Patriarca

The purpose of this program is to provide a base technology evaluation of high-temperature materials for use in space applications of radioisotope thermoelectric generators (RTG's). Emphasis is presently on tantalum and molybdenum alloys used as containment materials for $^{238}PuO_2$.

Effect of Oxygen Contamination on the Tensile Properties of T-111

C. T. Liu

The objective of this study is to provide information on the embrittlement of T-111 applicable to radioisotope thermoelectric generator uses. T-111 specimens 20 mils thick were doped with controlled amounts of oxygen in a dynamic system at oxygen pressure of 1 to 2 $\times 10^{-5}$ torr at 1000°C. The contaminated specimens were then tested in tension in two different conditions; one set of doped specimens was heat treated 15 min at 1700°C to simulate reentry heating, while another set was tested in the as-doped condition. The results are presented in Figs. 12.1 and 12.2 as a function of oxygen content at four test temperatures. For the specimens heat treated after doping, Fig. 12.1 indicates that:

1. Tensile strength increases slightly and elongation decreases moderately with oxygen level up to 3000 ppm.

2. Beyond 3000 ppm the strength increases and ductility decreases sharply with oxygen contamination. The increase of tensile strength is more pronounced at low temperatures. Lattice parameter measurements of the T-111 also show sharp increases at about this oxygen level. Calculations show that this oxygen level corresponds to that required to tie up the hafnium in T-111 as HfO_2. Thus, the tensile properties above 3000 ppm are apparently due to the oxygen solid solution.

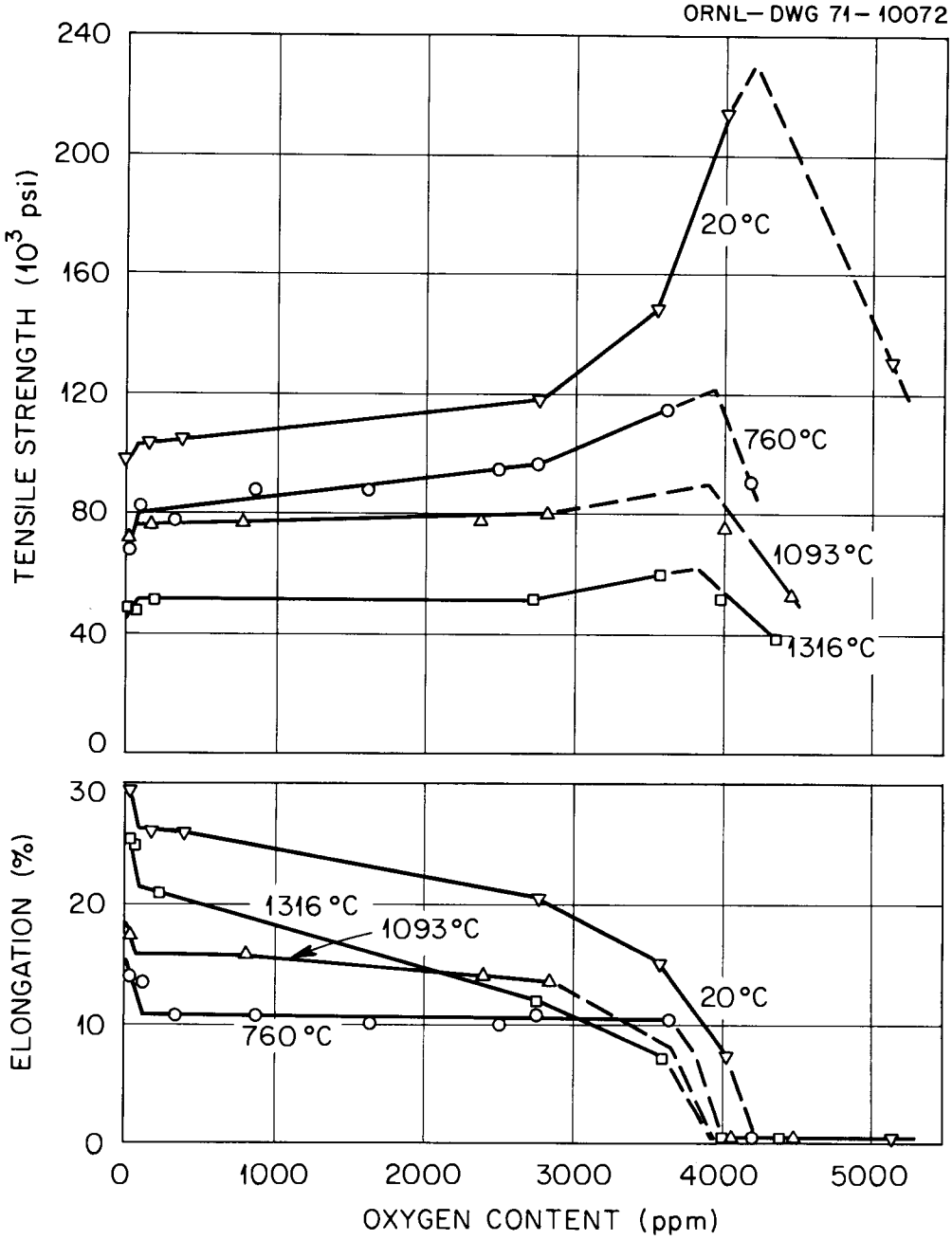

Fig. 12.1. Tensile Properties of 20 mil thick T-111 Heat-Treated 15 min 1700°C After Doping With Various Levels of Oxygen at 1000°C.

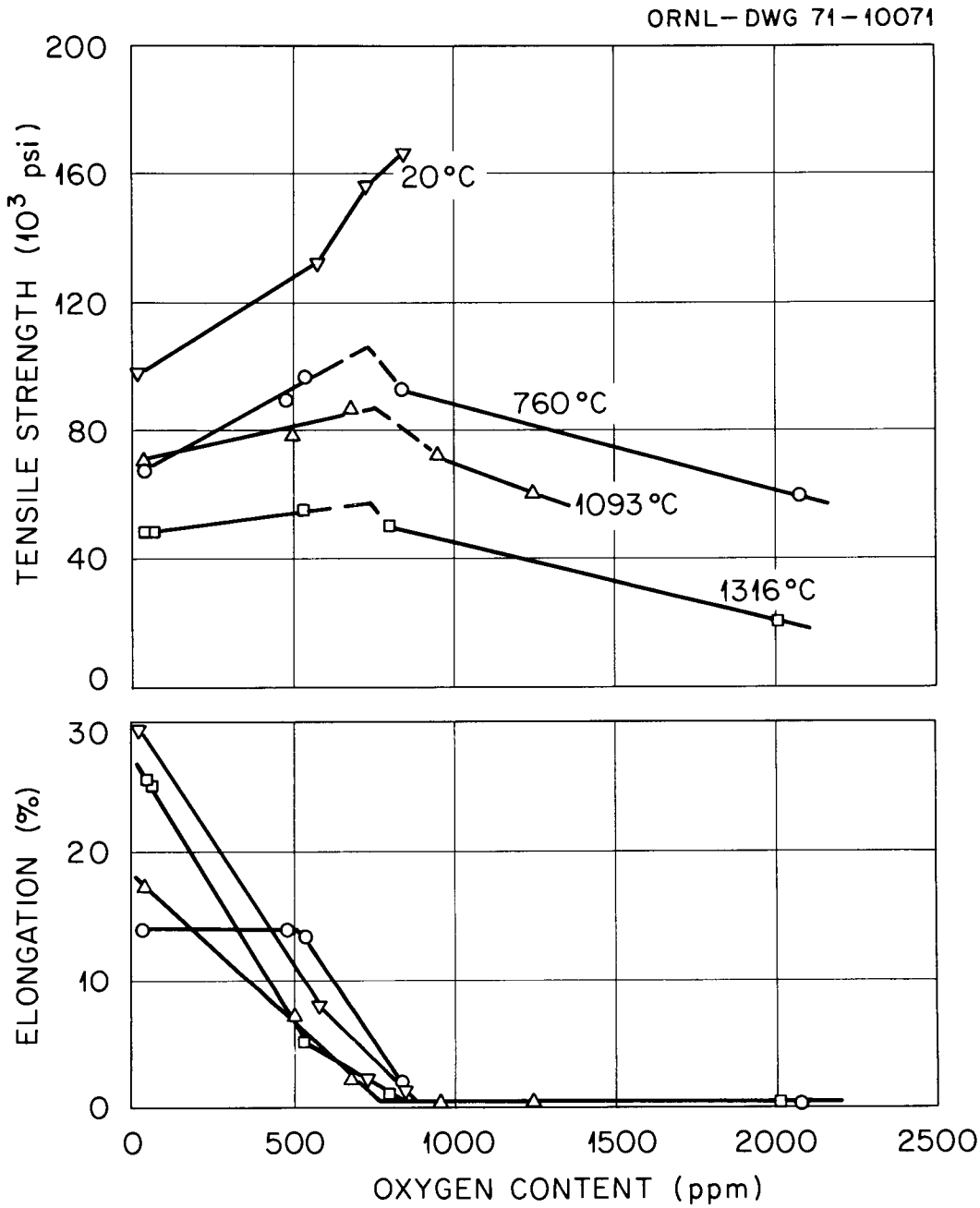

Fig. 12.2. Tensile Properties of 20 mil thick T-111 As-Doped With Various Levels of Oxygen at 1000°C.

3. T-111 loses its ductility completely when the oxygen content reaches a level of 3900 to 4200 ppm. In contrast to the usual effect of oxygen raising the ductile-to-brittle transition temperature of refractory metals and alloys, it appears that the T-111 can tolerate no more oxygen at 1316°C than at room temperature.

In contrast to the results in Fig. 12.1, we found that T-111 exhibits a much lower tolerance for oxygen contamination in the "as doped" condition. The results in Fig. 12.2 show a general increase of strength and decrease of ductility with oxygen content. At a level of 800 ppm and above, T-111 specimens completely lose their ductility.

In order to explain these results, the oxygen contaminated specimens were examined metallographically. Optical photomicrographs showed no difference in structure at all between the as-received ductile specimen containing 25 ppm oxygen (Fig. 12.3a) and the as-doped brittle specimens (Fig. 12.3b). However, the formation of hafnium oxide zones is observed in the as-doped specimens by transmission electron microscopy. The zones are less than 100 A in diameter and are coherent with the matrix. Based on these observations, it is believed that the brittleness of the as-doped specimens is due to the existence of a large amount of small, hard zones which effectively impede the motion of dislocations. From these zones coarse, spherical HfO_2 particles precipitate essentially on the grain boundaries (Fig. 12.3c) during the "ductilizing" treatment. With the increase of oxygen content the precipitates on the grain boundaries gradually connect into a network (Fig. 12.3d) which cause the brittleness of heat treated specimens at a level of about 4000 ppm.

Contamination Studies of T-111 in the Pioneer Heat Source Environment

H. Inouye

The Ta-10% W fuel liner and the T-111 strength member have been severely embrittled by oxygen contamination in test Pioneer heat sources operating at 825°C. Sources of the oxygen are thought to be the $^{238}PuO_2$ fuel, the graphite heat shield, and the asbestos-base Min-K 1301 insulation.

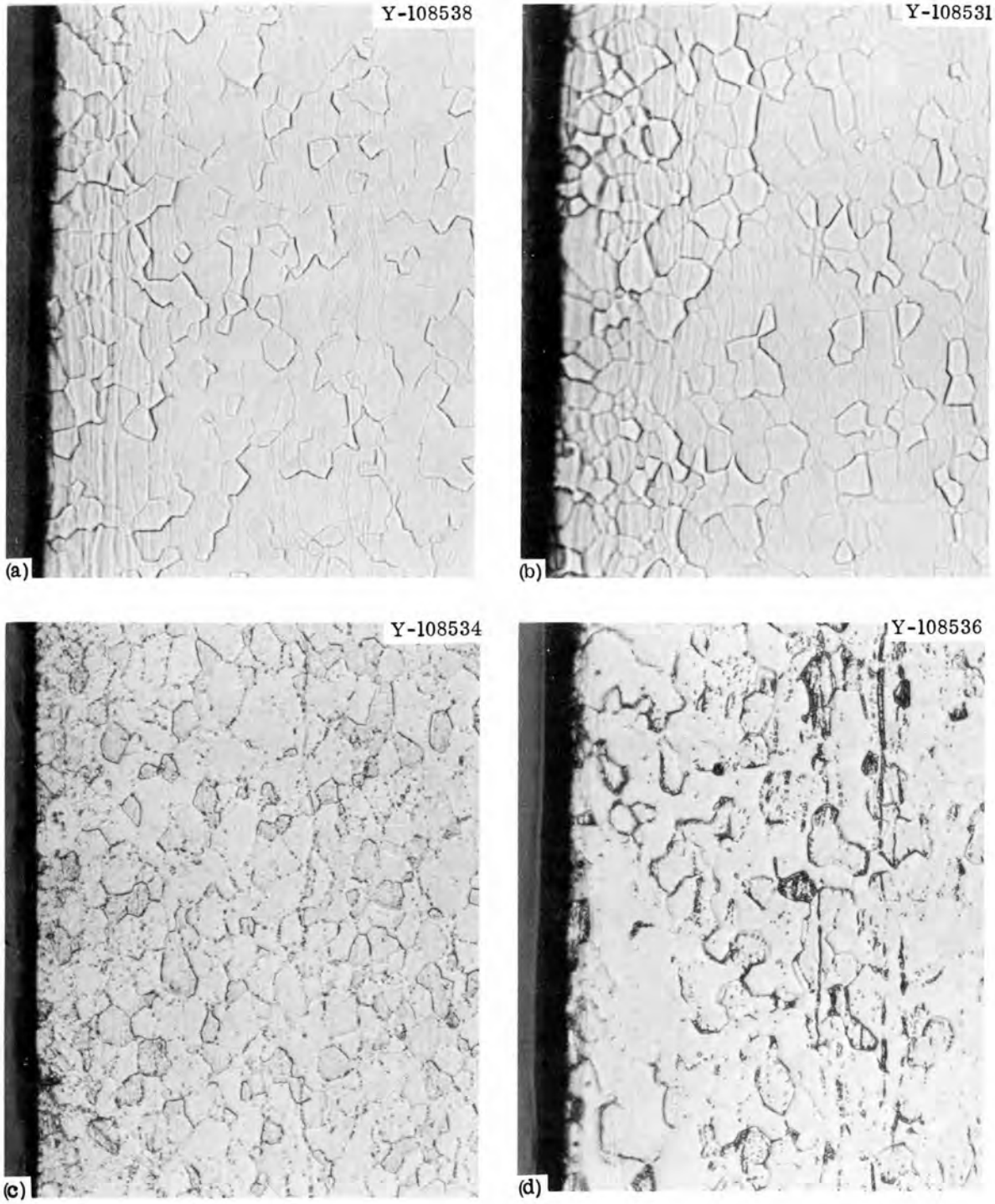

Fig. 12.3. Microstructure of T-111 Specimens Doped to Different Levels of Oxygen. (a) As-recrystallized, (b) as-doped with 800 ppm oxygen, (c) heat-treated 15 min at 1700°C after doping with 1640 ppm oxygen, and (d) heat-treated 15 min at 1700°C after doping with 4430 ppm oxygen.

Because H_2O, CO, H_2, and lesser quantities of CH_4, N_2, CO_2, hydrocarbons in the graphite,[1] and H_2O in the Min-K are degassed upon heating, it appears that gas transport from these components as well as from the fuel to the tantalum alloys is the principal mechanism of contamination. During this period, methods for minimizing the contamination of T-111 was investigated.

Effect of Barriers on T-111 Contamination

Tensile specimens wrapped in 0.003-in.-thick molybdenum foil or coated with 0.0002 in. of evaporated molybdenum were exposed to gases outgassed from ATJ graphite. The room-temperature tensile properties and the weight change of 0.020-in.-thick sheet specimens after exposure at 825°C to the gases are tabulated in Table 12.1. In terms of the weight gain of the specimens, the results shows (1) that wrapping T-111 with molybdenum foil lowers the contamination by a factor of 30; however, (2) if small holes are present in the foil, the contamination is about the same as the bare specimen, and (3) a molybdenum coating 0.0002-in.-thick deposited by vacuum evaporation lowers the 215-hr contamination level by a factor of approximately 200 and is a factor of approximately 7 better than the foil wrap.

Chemical analyses of the contaminated tensile specimens showing zero ductility after the 215-hr exposure are listed in Table 12.2. These results show that the principal contaminant in T-111 derived from the graphite environment is oxygen with lesser amounts of carbon and nitrogen. Thus, it appears that the level of oxygen contamination causing embrittlement of T-111 at 825°C is only about 400 ppm compared to about 800 ppm when contaminated at 1000°C.[2]

---

[1] D. S. Easton and R. E. Clausing, J. Vac. Sci. Tech. (7)6, pp. S116, S123 (November/December 1970).

[2] See Figure 12.2.

Table 12.1. The Effect of Molybdenum Barriers on the Contamination of T-111 at 825°C

Type of Barrier	Tensile Strength (psi)	Elongation (%)	Weight Gain (gr)	Contamination[a] (ppm)
		10 hr Exposures		
None	112,500	0	0.0020	530
0.003 in. molybdenum foil[b]	106,000	0	0.0021	550
0.0002 in. evaporated molybdenum	73,300	20.2	0.0004	108
		215 hr Exposures[c]		
None	---Not tested----		0.2793	68,600
0.003 in. molybdenum foil[d]	59,600	0	0.0099	2,680
0.0002 in. evaporated molybdenum	87,200	0	0.0014	392

[a]Based on weight gain.

[b]Two 1/16-in. diam holes in foil to support specimen.

[c]Graphite outgassed two hours at 800°C to pressure of 10^{-6} torr prior to exposures.

[d]Completely wrapped specimen.

Table 12.2. Chemical Analyses of T-111 Exposed 215 Hr at 815°C to Gases Outgassed from Graphite at 538°C

	As Received	Coated With 0.0002 in. Molybdenum	Wrapped With 0.003 in. Molybdenum Foil
Oxygen, ppm	62	440	3000
Carbon, ppm	60	62	90
Nitrogen, ppm	15	30	16
Hydrogen	6	2	4
Contamination Based on Weight Gain		392	2680

Effect of Outgassing Graphite and Zirconium Gettering on Contamination of T-111

In order to show the effect of the outgassing temperature of graphite and to show the effect of zirconium getters on contamination, specimens of T-111 were exposed to graphite outgassed at 800 and 1200°C, and also to graphite outgassed at 1200°C then gettered with 0.010-in. bare zirconium foil and 0.010-in. Zr foil wrapped with 0.001-in. foil of palladium. The impurity pickups based on the weight gain of 0.020-in.-thick T-111 specimens after approximately 200 hr at 825°C and a graphite temperature of 538°C are 68,600 ppm for graphite vacuum outgassed 2 hr at 800°C, 10,300 ppm for graphite vacuum outgassed 4 hr at 1200°C, and 6,400 ppm for graphite vacuum outgassed 4 hr at 1200°C with both bare and 0.001-in.-thick palladium-foil wrapped zirconium getters.

The T-111 specimens contaminated to approximately 7% were a brownish color, had swelled, and were grossly distorted. The specimens contaminated to 10,300 and 6,400 ppm showed no evidence of contamination and were as highly polished as they were before testing. Slight bending of the latter specimens at room temperature fractured the T-111 specimens in an extremely brittle manner.

The various test configurations outlined above, which represent potential "fixes" to the Pioneer contamination problem, show that outgassing the graphite at 1200°C rather than 800°C lowers the contamination by a factor of 7. Gettering combined with the 1200°C outgassing of graphite was disappointingly ineffective. Future tests will include recently received Min-K 1301 as well as graphite as sources of impurities, which will then be gettered by zirconium rings. Tests to 2000 hr are scheduled for bare T-111, molybdenum-coated T-111, TZM, and Mo–46% Re.

Effect of Oxygen Contamination on the Mechanical Properties of Molybdenum-Base Alloys

C. T. Liu

Because of its high melting point and reasonable strength at elevated temperatures, the molybdenum-base alloys are also considered as candidate materials for space power systems. For instance, TZM is currently the "backup" strength member material for the Pioneer heat source. The objective of this work is to evaluate the effect of oxygen contamination on the mechanical properties of TZM and Mo-Re alloys.

TZM, obtained from the Climax Molybdenum Company and initially containing 170 ppm C, 21 ppm O, 1 ppm N, and 1 ppm H, together with Mo–46% Re, prepared by electron-beam melting and warm rolling to sheet stock, were recrystallized at 1450 and 1600°C, respectively, and doped with oxygen at oxygen pressures of 1 to 4 x 10^{-5} torr at 825 and 1000°C. The status of the doping series is shown in Table 12.3. For each doping condition, two to five specimens are prepared in order to test them at various temperatures. Because of the evaporation of molybdenum oxide, the doped specimens show a small weight loss. Thus, the amount of oxygen in TZM cannot be calculated simply from the weight change. The results of tensile tests to date are presented in Table 12.4. The tensile properties of TZM are not sensitive to oxygen doping at 825°C in the time period of 500 hr. As compared with the as-recrystallized

Table 12.3. Status of Oxygen Doping on TZM and Mo–46% Re Specimens

Doping Condition			Status as of 9-30-71
Temperature (°C)	Time (hr)	Oxygen Pressure (torr)	
		TZM	
825	100	4×10^{-5}	Terminated
825	500	1×10^{-5}	Terminated
825	1000	1×10^{-5}	Not exposed
825	2000	1×10^{-5}	750-hr exposure
1000	200	1×10^{-5}	Terminated
		Mo–46% Re	
825	1000	1×10^{-5}	240-hr exposure
825	2000	1×10^{-5}	240-hr exposure

Table 12.4. Effect of Oxygen Contamination on the Room Temperature Properties of TZM

Specimen No.	Doping Condition			Ultimate Tensile Strength (psi)	Elongation (%)
	Temperature (°C)	Time (hr)	Oxygen Pressure (torr)		
1	-----As recrystallized-----			79,600	33.5
2	825	110	4×10^{-5}	81,200	35.3
3	825	500	1×10^{-5}	85,000	29.2
4	1000	207	1×10^{-5}	57,000[a]	0[a]

[a]Fracture within the elastic limit.

material, doping at 825°C causes a small increase of ultimate tensile strength. The doped specimens begin to show some reduction of ductility after 500 hr exposure at 825°C; however, after 207 hr exposure at 1000°C the TZM loses its ductility completely. Judging from these preliminary results and the chemical similarity between hafnium in T-111 and zirconium and titanium in TZM, we suspect that both alloys may behave similarly under oxygen contamination. However, due to the low rate of oxygen diffusion in molybdenum, it requires a longer doping time or higher doping temperature to embrittle TZM.

13. CLADDING MATERIALS FOR SPACE ISOTOPIC HEAT SOURCES

R. G. Donnelly H. Inouye

The purpose of this program is to develop alloys with a superior combination of properties to better assure reliable containment of radioisotope fuels such as $^{238}PuO_2$ and $^{244}Cm_2O_3$ under both operating and accident conditions for space thermoelectric generators. Ideally the encapsulating material should be insensitive to the operating environment and capable of surviving launch aborts, reentry heating, and earth impact as well as provide maximum post-impact containment of the fuel. At the same time it must be both fabricable and weldable.

We feel these goals can best be accomplished with high-strength, noble-based alloys having melting points above 2000°C. Presently, we are characterizing Pt-Rh-W alloys for this application.

Development of Improved Alloys

C. T. Liu

Ingots of the platinum-base alloy designated as Pt-3010, containing 26 to 30% Rh and 6 to 10% W (weight percent), are readily fabricable to sheet material by hot forging and hot rolling in air followed by cold rolling. Elevated-temperature tensile specimens stamped from 0.025 in. sheet stock were tested on an Instron machine with a vacuum induction furnace. The results for alloy specimens in the stress-relieved and recrystallized conditions are presented in Table 1. The data for TZM,[1] T-111,[1] and Pt-30 Rh[2] are included for comparison. The plot of the data in Figs. 13.1 and 13.2 as a function of testing temperature indicates that:

---

[1] General Electric Company, Multi-Hundred Watt, Radioisotopic Thermoelectric Generator Program, GESP-7034 (March 1970).

[2] C. T. Liu and H. Inouye, Fuels and Materials Development Program Quart. Progr. Rept. March 31, 1971, ORNL-TM-3416, p. 189.

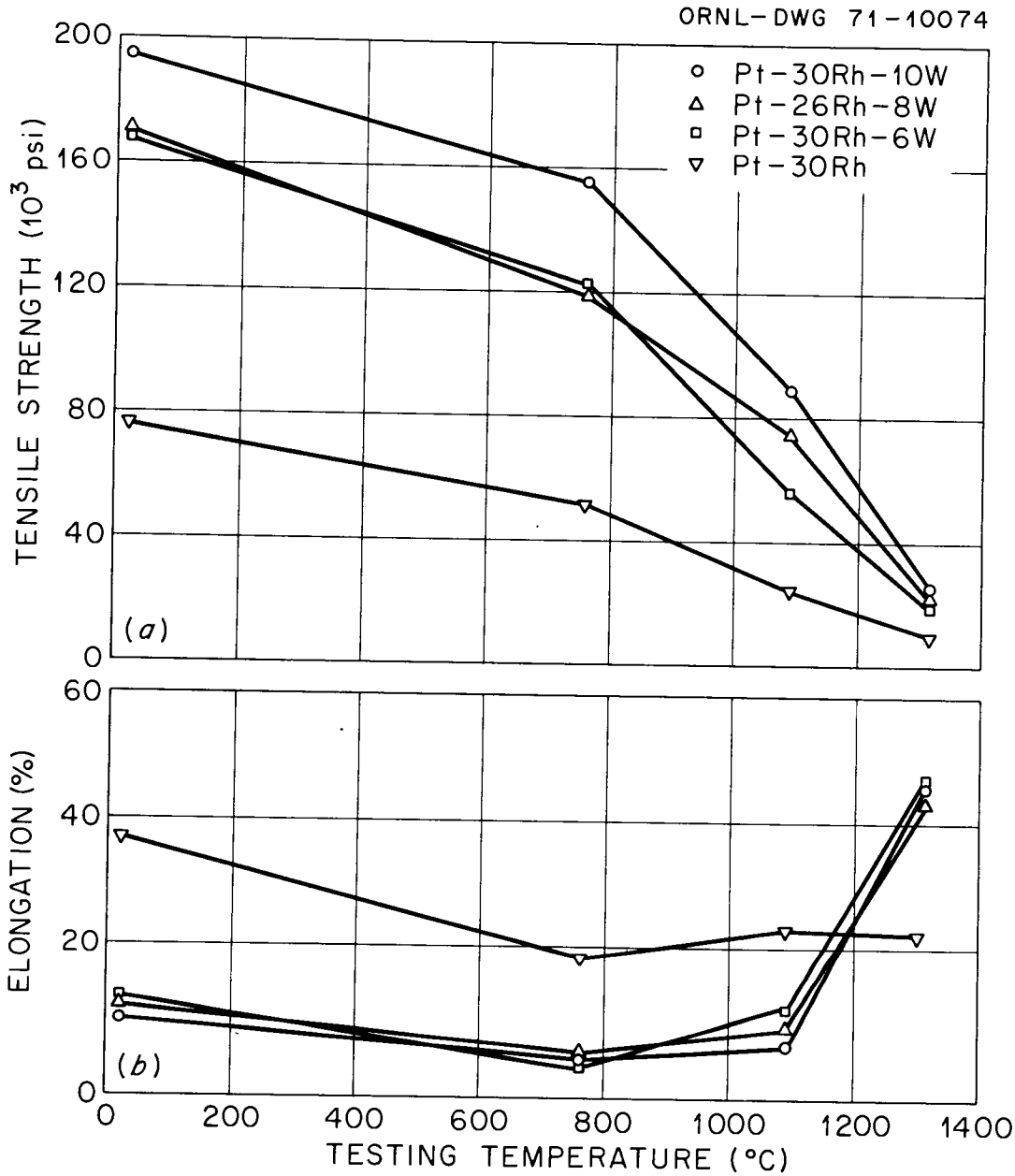

Fig. 13.1. Tensile Properties of Pt-Rh-W Alloys in the Stress-Relieved Condition.

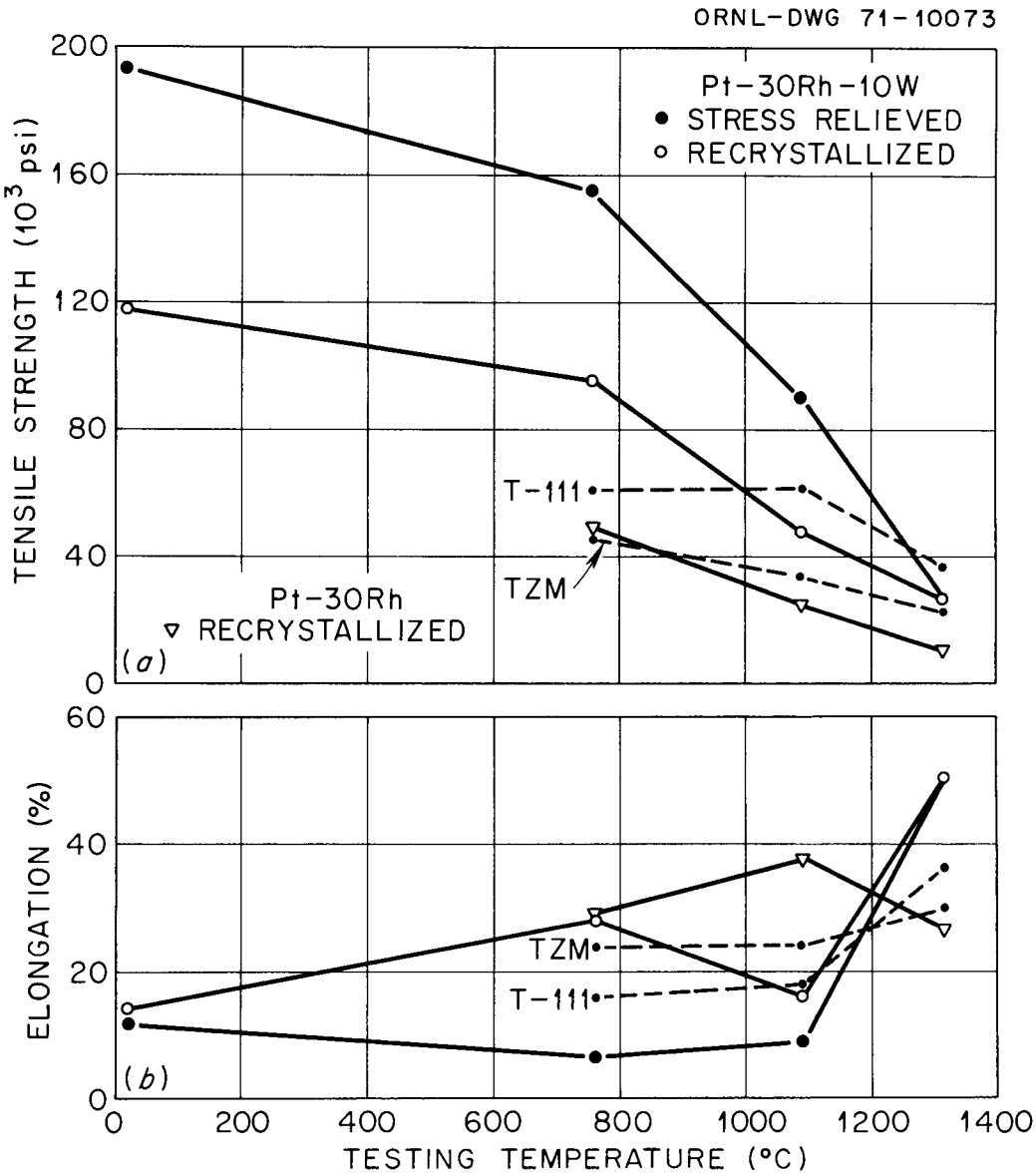

Fig. 13.2. Comparison of the Tensile Properties of Pt–30% Th–10% W with Pt–30% Rh, TZM, and T-111

1. The tensile strength of Pt-Rh-W alloys increases with tungsten level and this effect is more prominent at high temperature. In fact, the Pt–30% Rh–10% W alloy is stronger than the Pt–30% Rh by a factor of 2.5 at 1316°C.

2. The Pt-Rh-W alloys have low ductility in the stress-relieved condition, and the minimum elongation (about 6%) is obtained at 760°C.

3. The Pt-Rh-W alloys have good ductility in the recrystallized condition at all the testing temperatures. At 1316°C, the Pt-Rh-W alloys show about 50% elongation which is better than Pt-30% Rh, TZM, or T-111.

4. As compared with refractory alloys, Pt–30% Rh–10% W alloy is stronger than TZM at all temperatures, but is weaker than T-111 at temperatures above 1000°C.

Effects of the hafnium and titanium additions on the physical and mechanical properties of Pt-Rh-W alloys have been evaluated. Annealing studies on cold rolled Pt–26% Rh–8% W–1% Hf–0.2% Ti alloy sheet show that recrystallization begins at about 1050°C and is complete at 1200°C after a one-hour anneal. The 100% recrystallization temperature of the hafnium and titanium stabilized alloy is 150°C higher than the base ternary alloy.[2] The hardness of the stabilized alloy is also consistently higher than the base alloy. The hafnium and titanium are also effective to strengthen the base ternary alloys. At 1316°C (2400°F) the stabilized alloy has an ultimate tensile strength of 30,500 psi and elongation of 39% that indicate a superiority to the base Pt–26% Rh–8% W alloy (see Table 13.1).

Preparation of Pt-3010 Sheet

J. H. Irwin

In order to provide sufficient Pt-3010 sheet for further characterization and fabrication studies, we are preparing approximately 350 in.^{2} of nominally 0.025-in.-thick sheet. About 8.5 kg of platinum-rhodium scrap received from Mound Laboratory and 3 kg of virgin rhodium powder

Table 13.1. Room-Temperature and Elevated-Temperature Tensile Properties of the Platinum-Base Alloys, T-111 and TZM

Alloy Composition (wt %)	Ultimate Tensile Strength (psi)		Elongation (%)	
	Stress Relieved[a]	Recrystallized[b]	Stress Relieved[a]	Recrystallized[b]
		Room Temperature		
Pt-30 Rh	76,000	c	42	c
Pt-30 Rh-6 W	169,000	112,000	15.7	26
Pt-26 Rh-8 W	171,000	c	15	c
Pt-30 Rh-10 W	194,000	118,000	12.5	14.5
		760°C (1400°F)		
Pt-30 Rh	52,000	48,000	23	28.8
Pt-30 Rh-6 W	123,000	80,000	5.5	23.5
Pt-26 Rh-8 W	118,000	c	6.6	c
Pt-30 Rh-10 W	155,000	95,000	6.5	28
TZM[d]	c	45,000	c	24
T-111[d]	c	60,000	c	16
		1093°C (2000°F)		
Pt-30 Rh	24,400	24,000	28	38
Pt-30 Rh-6 W	56,000	36,000	15	33.3
Pt-26 Rh-8 W	75,000	38,000	12	18
Pt-30 Rh-10 W	89,000	47,000	9	15.5
TZM[d]	c	33,000	c	24
T-111[d]	c	61,000	c	18
		1316°C (2400°F)		
Pt-30 Rh	10,000	10,000	26.5	26.5
Pt-30 Rh-6 W	19,500	17,500	51.5	55
Pt-26 Rh-8 W	22,500	21,200	48	45
Pt-30 Rh-10 W	25,500	25,500	50.5	50.5
TZM[d]	c	33,000	c	30
T-111[d]	c	37,000	c	36

[a]Stress relieved at 1000°C.

[b]Recrystallization at 1200°C.

[c]Not determined.

[d]Data collected from General Electric Company, Multi-Hundred Watt, Radioisotope Thermoelectric

have been electron-beam melted and chemically analyzed. Prior to committing all this material to a given composition though, 500-g ingots of Pt–26% Rh–8% W, Pt–30% Rh–10% W, and Pt–30% Rh–10% W–1% Hf–0.1% Ti are being prepared and will be compared in bend, tensile, and forming tests to determine the most fabricable. The composition of the large sheet will be determined from these tests.

Previous reports in this series are:

ORNL-TM-920	Period Ending June 30, 1964
ORNL-TM-960	Period Ending September 30, 1964
ORNL-TM-1000	Period Ending December 31, 1964
ORNL-TM-1100	Period Ending March 31, 1965
ORNL-TM-1200	Period Ending June 30, 1965
ORNL-TM-1270	Period Ending September 30, 1965
ORNL-TM-1400	Period Ending December 31, 1965
ORNL-TM-1500	Period Ending March 31, 1966
ORNL-TM-1570	Period Ending June 30, 1966
ORNL-TM-1700	Period Ending September 30, 1966
ORNL-TM-1720	Period Ending December 31, 1966
ORNL-TM-1825	Period Ending March 31, 1967
ORNL-TM-1941	Period Ending June 30, 1967
ORNL-TM-2020	Period Ending September 30, 1967
ORNL-TM-2090	Period Ending December 31, 1967
ORNL-TM-2217	Period Ending March 31, 1968
ORNL-4330	Period Ending June 30, 1968
ORNL-4350	Period Ending September 30, 1968
ORNL-4390	Period Ending December 31, 1968
ORNL-4420	Period Ending March 31, 1969
ORNL-4440	Period Ending June 30, 1969
ORNL-4480	Period Ending September 30, 1969
ORNL-4520	Period Ending December 31, 1969
ORNL-4560	Period Ending March 31, 1970
ORNL-4600	Period Ending June 30, 1970
ORNL-4630	Period Ending September 30, 1970
ORNL-TM-3300	Period Ending December 31, 1970
ORNL-TM-3416	Period Ending March 31, 1971
ORNL-TM-3540	Period Ending June 30, 1971

INTERNAL DISTRIBUTION

1–3. Central Research Library
4. ORNL – Y-12 Technical Library
Document Reference Section
5–34. Laboratory Records Department
35. Laboratory Records, ORNL RC
36. ORNL Patent Office
37. G. M. Adamson, Jr.
38. S. E. Beall
39. J. A. Conlin
40. W. B. Cottrell
41. J. A. Cox
42. R. S. Crouse
43. F. L. Culler, Jr.
44. J. E. Cunningham
45. J. H. DeVan
46. R. G. Donnelly
47. W. P. Eatherly
48. J. I. Federer
49. D. E. Ferguson
50. J. H Frye, Jr.
51. R. J. Gray
52. B. L. Greenstreet
53. W. R. Grimes
54. W. O. Harms
55–57. M. R. Hill
58–59. F. J. Homan
60. H. Inouye
61–93. P. R. Kasten
94. G. W. Keilholtz
95. J. M. Leitnaker
96. H. R. Livesey
97. E. L. Long, Jr.
98. A. L. Lotts
99. T. S. Lundy
100. W. R. Martin
101. R. W. McClung
102–104. H. E. McCoy, Jr.
105. H. C. McCurdy
106. W. T. McDuffee
107. D. L. McElroy
108. J. R. McGuffey
109. C. J. McHargue
110. L. C. Oakes
111. R. E. Oakes
112. P. Patriarca
113. S. Peterson
114. P. L. Rittenhouse
115. M. W. Rosenthal
116. A. C. Schaffhauser
117. J. L. Scott
118. J. D. Sease
119–120. G. M. Slaughter
121. J. O. Stiegler
122. D. A. Sundberg
123. V. J. Tennery
124. D. B. Trauger
125. J. E. Van Cleve
126. T. N. Washburn
127. J. R. Weir, Jr.
128. G. D. Whitman
129. R. G. Wymer
130. H. L. Yakel

EXTERNAL DISTRIBUTION

AEC ADVISORY COMMITTEE ON REACTOR SAFEGUARDS, Washington, DC 20545

131–135. Executive Secretary

AEC DIVISION OF REACTOR DEVELOPMENT AND TECHNOLOGY, Washington, DC 20545

136. J. C. Crawford, Jr.
137. G. W. Cunningham
138. R. P. Denise
139. K. E. Horton
140. J. R. Hunter
141. E. E. Kintner
142. W. H. Layman
143. W. H. McVey

144. J. J. Morabito
145. E. C. Norman
146. R. E. Pahler
147. A. J. Pressesky
148. M. A. Rosen
149. S. Rosen
150. M. Shaw
151. J. M. Simmons
152. E. E. Sinclair
153. B. Singer
154. A. Taboada
155. A. N. Tardiff
156. A. Van Echo
157. C. E. Weber
158. M. J. Whitman

AEC DIVISION OF RESEARCH, Washington, DC 20545

159. L. C. Ianniello
160. P. W. McDaniel
161. D. K. Stevens

AEC DIVISION OF REACTOR LICENSING, Washington, DC 20545

162–164. P. A. Morris

AEC DIVISION OF REACTOR STANDARDS, Washington, DC 20545

165–166. E. G. Case

AEC DIVISION OF TECHNICAL INFORMATION EXTENSION, P.O. Box 62, Oak Ridge, TN 37830

167–168. Director

AEC OAK RIDGE OPERATIONS OFFICE, P.O. Box E, Oak Ridge, TN 37830

169. Laboratory and University Division

AEC-RDT SITE REPRESENTATIVES

170. R. H. Ball, Gulf General Atomic, P.O. Box 608, San Diego, CA 92112
171. D. F. Cope, Oak Ridge National Laboratory
172. Theodore Iltis, Westinghouse Advanced Reactors Division, Waltz Mill Site, P.O. Box 158, Madison, PA 15663
173. M. E. Jackson, Argonne National Laboratory, 9700 S. Cass Avenue, Argonne, IL 60439
174. C. L. Matthews, Oak Ridge National Laboratory
175. R. L. Morgan, Atomics International, P.O. Box 1446, Canoga Park, CA 91304
176. D. A. Moss, P.O. Box 2108, Idaho Falls, ID 83401
177. J. Sako, WADCO Corporation, P.O. Box 1970, Richland, WA 99352
178. Atomic Energy Commission Library, Room G-049, Washington, DC 20545

AEC DIVISION OF NAVAL REACTORS, Washington, DC 20360

179. R. H. Steele

AIR FORCE MATERIALS LABORATORY, Wright-Patterson Air Force Base, OH 45433

180. C. H. Armbruster
181. H. M. Burte
182. I. Perlmutter

AMES LABORATORY, USAEC, Iowa State University, Ames, IA 50010

183. M. S. Wechsler

ARGONNE NATIONAL LABORATORY, 9700 S. Cass Avenue, Argonne, IL 60439

184. B.R.T. Frost
185. J. H. Kittel
186. M. V. Nevitt
187. D. R. O'Boyle
188. P. G. Shewmon
189. R. C. Vogel

ATOMIC POWER DEVELOPMENT ASSOCIATES, 1911 First Street, Detroit, MI 48226

190. A. S. Shoudy, Jr.

ATOMICS INTERNATIONAL, P.O. Box 309, Canoga Park, CA 91304

191. J. G. Asquith
192. T. A. Moss
193. H. Pearlman
194. S. Siegel

BABCOCK & WILCOX COMPANY, Beaver Falls, PA 15010

195. William Buley

BABCOCK & WILCOX COMPANY, Lynchburg, VA 24505

196. C. J. Baroch
197. S. P. Grant
198. C. R. Johnson
199. L. R. Weissert

BATTELLE MEMORIAL INSTITUTE, 505 King Avenue, Columbus, OH 43201

200. D. Keller
201. S. J. Paprocki
202. Defense Materials Information Center

BROOKHAVEN NATIONAL LABORATORY, 29 Cornell Avenue, Upton, Long Island, NY 11973

203. D. H. Gurinksy
204. C. Klamut

BUREAU OF MINES, Albany Metallurgy Research Center, P.O. Box 70, Albany, OR 97321

205. Haruo Kato

BUREAU OF MINES, Boulder City, NV 89005

206. T. A. Sullivan

COMBUSTION ENGINEERING, INC., P.O. Box 500, Windsor, CT 06095

207. M. Andrews
208. W. P. Chernock

GENERAL ELECTRIC COMPANY, Nuclear Systems Programs, P.O. Box 15132, Cincinnati, OH 45215

209. H. C. Brassfield
210. E. E. Hoffman

GENERAL ELECTRIC COMPANY, Pleasanton, CA 94566

211. H. W. Alter

GENERAL ELECTRIC COMPANY, 175 Curtner Avenue, San Jose, CA 95125

212. R. Duncan
213. J. L. Krankota

GENERAL ELECTRIC COMPANY, 310 De Guigne Drive, Sunnyvale, CA 94086

214. R. E. Skavdahl
215. C. N. Spalaris
216. E. L. Zebroski
217. Technical Library

GEORGE C. MARSHALL SPACE FLIGHT CENTER, Huntsville, AL 35812

218. R. J. Schwinghamer

GULF GENERAL ATOMIC, P.O. Box 608, San Diego, CA 92112

219. L. J. Colby
220. A. J. Goodjohn
221. J. P. Howe
222. J. N. Lindgren
223. J. F. Watson
224. L. Yang

IDAHO NUCLEAR CORPORATION, P.O. Box 1845, Idaho Falls, ID 83401

225. W. C. Francis
226. W. A. Yuill

KNOLLS ATOMIC POWER LABORATORY, P.O. Box 1072, Schenectady, NY 12301

227. R. F. Wojciescak

LMFBR PROGRAM OFFICE, Argonne National Laboratory, 9700 S. Cass Avenue, Argonne, IL 60439

228. G. A. Bennet
229. P. F. Gast
230. J. M. McKee

LOS ALAMOS SCIENTIFIC LABORATORY, P.O. Box 1663, Los Alamos, NM 87544

231. R. D. Baker

MINE SAFETY APPLIANCES COMPANY, J. T. Ryan Memorial Laboratory, 100 N. Braddock Avenue, Pittsburgh, PA 15208

232. Library

MOUND LABORATORY, P.O. Box 32, Miamisburg, OH 45342

233. W. T. Cave
234. R. E. Vallée

NASA HEADQUARTERS, Code RN, 600 Independence Avenue, Washington, DC 20545

235. J. J. Lynch

NASA-LEWIS RESEARCH CENTER, 21000 Brookpark Road, Cleveland, OH 44135

236. G. M. Ault
237. J.W.R. Creagh
238. J. J. Lombardo
239. F. E. Rom
240. L. Rosenblum
241. N. T. Saunders
242. C. M. Scheuermann

NAVAL RESEARCH LABORATORY, Code 6390, Washington, DC 20360

243. J. R. Hawthorne

NUCLEAR MATERIALS AND EQUIPMENT CORPORATION, Apollo, PA 15613

244. K. H. Puechl

OHIO STATE UNIVERSITY, Columbus, OH 43212

245. R. W. Staehle

RENSSELAER POLYTECHNIC INSTITUTE, Troy, NY 12180

246. D. W. Dickinson
247. W. F. Savage

SANDIA CORPORATION, Albuquerque, NM 87115

248. J. R. Holland
249. P. D. O'Brian

SPACE NUCLEAR SYSTEMS OFFICE, AEC, Washington, DC 20545

250. R. E. Anderson
251. D. Beard
252. J. F. Griffo
253. H. Jaffe
254. C. E. Johnson
255. A. P. Litman
256. J. A. Powers
257. F. C. Schwenk

UNION CARBIDE CORPORATION, 270 Park Avenue, New York, NY 10017

258. J. A. Swartout

UNION CARBIDE CORPORATION, Carbon Products Division, Cleveland, OH 44101

259. C. F. Leitten, Jr.

UNITED NUCLEAR CORPORATION, Grasslands Road, Elmsford, NY 10523

260. A. A. Strasser

UNIVERSITY OF CALIFORNIA, LAWRENCE RADIATION LABORATORY, P.O. Box 808, Livermore, CA 94550

261. W. R. Holman
262. L. W. Roberts
263. A. J. Rothman

U.S. NAVAL AIR SYSTEM COMMAND (AIR-52031B), Washington, DC 20360

264. I. Machlin

USAEC SCIENTIFIC REPRESENTATIVE, American Embassy, P.O. Box 40, FPO New York, NY 09510

265. W.L.R. Rice

WADCO CORPORATION, P.O. Box 1970, Richland, WA 99352

266. E. A. Evans
267–280. J. N. Judy
281. F. J. Leitz
282–292. W. E. Roake
293. C. B. Shaw
294–303. W. F. Sheely

WESTINGHOUSE ADVANCED REACTORS DIVISION, Waltz Mill Site, P.O. Box 158, Madison, PA 15663

304. E. C. Bishop
305. A. Boltax
306. P. J. Levine
307. P. Murray
308. W. E. Ray
309. J. J. Taylor
310. G. A. Whitlow

WESTINGHOUSE ADVANCED REACTORS DIVISION, Cheswick Fuel Facility, P.O. Box 217, Cheswick, PA 15024

311. P. M. French

WESTINGHOUSE ASTRONUCLEAR LABORATORY, P.O. Box 10864, Pittsburgh, PA 15231

312. D. C. Goldberg

WESTINGHOUSE ATOMIC POWER DIVISION, P.O. Box 355, Pittsburgh, PA 15230

313. Technical Library

WESTINGHOUSE BETTIS ATOMIC POWER DIVISION, P.O. Box 79, West Mifflin, PA 15122

314. R. H. Fillnow
315. P. N. Gustafson
316. Technical Library

WESTINGHOUSE TAMPA DIVISION, Nuclear Energy Systems, P.O. Box 19218, Tampa, FL 33616

317. M. E. Eilbeck